TWO-DIMENSIONAL RANS SIMULATION OF FLOW INDUCED MOTION OF CIRCULAR CYLINDER WITH PASSIVE TURBULENCE CONTROL

by

Wei Wu

A dissertation submitted in partial fulfillment
of the requirements for the degree of
Doctor of Philosophy
(Naval Architecture and Marine Engineering)
in The University of Michigan
2011

Doctoral Committee:

Professor Michael M. Bernitsas, Co-Chair
Assistant Research Scientist Kevin J. Maki, Co-Chair
Professor Luis P. Bernal
Professor Armin W. Troesch

To my parents,
Shaoju Wang and Baocheng Wu

And my husband,
Dr. Jun Ma

ACKNOWLEDGEMENTS

First, I would like to sincere and deep gratitude to my academic advisors Professor Michael M. Bernitsas and Dr. Kevin J. Maki. I am grateful that I have the opportunity to join the group and work on this interesting research. It is their creative, beneficial discussions and suggestions that guide me to overcome the difficulties throughout the work. Without their instruction and guidance, I would not achieve what I have already. Without their support and patience, I would not have accomplished this thesis.

Special thanks are to Professor Armin W. Troesch and Professor Luis P. Bernal for serving on my doctoral committee and provide valuable guidance and suggestions on this thesis.

I appreciate that Dr. Shin Yung and Dr. Ge Wang provided opportunities for me to do internships in American Bureau of Shipping, where I had the opportunity to build working experience and get prepared for my career in the near future.

The following support is gratefully acknowledged: ONR, Naval Architecture and Marine Engineering department, University of Michigan.

My appreciation also goes to my friends and colleagues in VIVACE group, whom I spent the school life with in Ann Arbor and made it a memorable page in my life. In no particular order, I would like to thank Jingjing Li, Weiwei Yu, Yuxing Yun, Jiandao Zhu, Xiaoyan Yan, Rong Wu, Alton James Benjamin Luder III, Zhigang Tian, Aimin Wang, Zhen Li, Yanhui Xie, Chen Chen, Robert Ryan Oberlies, Bingbin Yu, Nabanita Datta. I would also thank the group mates Eun Soo Kim, Hongrae Park, Che-Chun Chang, Ajith Kumar for their friendship and their help in my research. I also would

like to thank other friends who are not from University of Michigan, Song Gao, Guangqiang Yang, Yu Fu, Bo Wang. Thank them all for being supportive.

Finally, I would express my deepest appreciation to my family. Without their love, I would never achieve this important stage of my life. Thank mom and dad, who love me unconditionally as always. It is their love gives me strength to face the challenges in my life. Thank my husband Dr. Jun Ma for always be there for me, for always comforting, supporting and encouraging me with his love, which accompany me to complete my work.

TABLE OF CONTENTS

LIST OF FIGURES

LIST OF TABLES

Chapter 1

INSTRODUCTION

1.1. Research background

Vortex-Induced Vibrations (VIV) is widely encountered hydrodynamic phenomenon caused by the excitations of the vortices shed from a bluff body. The vortex shedding process and resulting vortices create an asymmetric pressure distribution on the cylinder that can eventually cause the body to move. It is inherently a nonlinear phenomenon because the motion can enhance the strength of the shed vorticity and it occurs over a very broad and continuous range of frequencies. It is different from discrete natural frequencies as in linear resonance. It is normally treated as destructive phenomenon because of the fatigue damage it may potentially introduced.

VIVACE (Vortex Induced Vibration for Aquatic Clean Energy) converter is a hydrokinetic power generating device invented by Bernitsas and Raghavan (2005) and further developed by Bernitsas and his research group (Bernitsas et al. 2007, 2008, 2009) in the Marine Renewable Energy Lab (MRELab). It is based on the very simple idea of enhancing rather than suppressing VIV. It is designed to harnesses hydrokinetic energy from ocean and river currents as slow as 2 knots. The single VIVACE module can be treated as a circular cylinder mounted on springs with a PTO (Power Take Off) system. With entirely opposite objective to the other engineering problems, which are mainly focused on reducing vortex induced vibration effects, the goal of VIVACE team is to promote the oscillating amplitude and maximize the hydrokinetic energy. The highest lift coefficient and subsequently high VIV amplitude occur in the TrSL3 (fully turbulence shear layer: $2\times10^4\sim4\times10^4<Re<1\times10^5\sim2\times10^5$). To enhance VIV the flow properties of

TrSL3 must be extended to broader Reynolds number ranges. This has been achieved in the lab by implementing the passive turbulence control (PTC) by making it start earlier and go past the transition region from laminar to turbulent flow. By introducing Passive Turbulence Control (PTC), cylinder FIM was enhanced to reach back-to-back VIV and galloping.

Amplitude-to-diameter ratio (A/D) exceeds 3 and synchronization range is more than double that of VIV with no end within the capabilities of the Low Turbulence Free Surface Water Channel (LTFSWC) or the towing tank at the MRELab for $30{,}000<Re<120{,}000$. This subcritical range covers flow regimes TrSL2, TrSL3 (Zdravkovich 1997) for smooth stationary cylinders where 'TrSL' is short for Transition in Shear Layer.

In this thesis, numerical simulations are used to study enhanced motion of vortex induced vibrations. A numerical approach has several benefits. Firstly, the number of parameters that need to be investigated in this study is large, and the flexibility of numerical simulation to vary these parameters is effective to populate the test matrix and reveal functional dependence among the large number of parameters. Secondly, numerical simulation can go beyond the workable range in the lab and predict results without the limitations experienced in the experimental facility. In the MRELab, the maximum flow speed for the Low Turbulence Free Surface Water Channel is 2m/s and the test section is about 2.44m (length) × 0.8m (depth) × 1.0m (breadth). CFD can examine a higher flow-speed regime and investigate a larger working range of amplitude of motion for this device. In the experimental facility, the motion is physically restrained to prevent the cylinder from colliding with the bottom of the tank or from exiting the water. For cases in which passive turbulence control is used and the cylinder is in a galloping mode of motion, the oscillating cylinder hits the physical restraints indicating that potentially higher amplitude could be reached if more travel would be allowed. With a CFD tool, the maximum amplitude that the cylinder could potentially achieve without limitations of surface and bottom boundaries can be predicted. This is critical information in determining the needed spacing of the device when future generations of VIVACE are designed for an open-water environment.

The objective of this study is to establish the capability of a numerical tool to simulate the VIVACE system and investigate the system parameter effects that may potentially change the cylinder dynamics. Other properties of the flow such as vortex pattern, flow visualization, lift forcing and the phase angle are also provided as additional information that will be useful for future research and design. Finally, additional descriptive information such as boundary layer thickness, pressure distribution along the cylinder surface, drag force, separation point location, is also provided.

In Chapter 2, numerical simulations for the stationary cylinder flow using a two dimensional Reynolds-Averaged Navier-Stokes (RANS) method are presented. A range of turbulence models are examined and based on simulation accuracy the one-equation Spalart-Allmaras (SA) model is selected. Discretization requirements are established for this particular numerical method by computing the solution on various discretizations and comparing the results with experiments and other numerical results.

The case of a moving cylinder is studied in two steps: a smooth cylinder and cylinder with PTC (roughness). In Chapter 3, the smooth cylinder is first investigated in the low *Re* range (3,000~12,000) and the results are compared with Williamson's experiments (Khalak, Williamson 1996, 1999). The good agreement between current numerical study and the experiments demonstrates the capability of 2D RANS as a research and design tool for cylinder flow in VIV.

In Chapter 4, high *Re* range (30,000~80,000) is further studied. It is shown that current 2D RANS technology has limited ability to correctly predict some flow properties in the TrSL3 regime. The TrSL3 regime contains important three dimensional vortices in the shear layer of smooth cylinder, and two-dimensional nature of the current simulations cannot account for this important aspect of the flow in this regime.

In Chapter 5, Flow Induced Motion (FIM) of the circular cylinder with PTC is studied. PTC is applied in the spanwise along the cylinder surface. It is shown that the correlation length of the vortices in the spanwise direction is effectively elongated which acts to minimize three dimensional effects such that the resulting flow is "more" two-dimensional. Main features of the flow properties such as motion amplitude, oscillation

frequency and vortex structures are captured and agreement with experiments is satisfactory. The 2D RANS method is tested and verified as an effective numerical design tool for VIVACE system.

With the purpose of energy extracting and harnessing, the VIVACE system is in nature is employed with high system damping and high Reynolds number that is very difficult to study both experimentally and numerically. In order to investigate the effects of damping on the cylinder dynamics, different damping levels for cylinder with PTC cases are considered in Chapter 6. Also the spring constant, which is another important system parameter, is investigated to examine its effects on the system behavior.

The angle that describes the placement of the PTC with respect to the leading edge has been shown experimentally to be an essential factor in determining the cylinder dynamics. In Chapter 7, different angle values belonging to various zones according to PTC-to-FIM map (Park 2011 a,b) are tested. The numerical simulations agree strongly with the experimentally determined map, two entirely opposite body dynamics behaviors, FIM enhancement and FIM suppression, are found. One of the possible explanations for the different behaviors is proposed to be the phase angle variation. When the placement angle is in the suppression zone, the phase angle increases continuously till nearly π. This out-of-phase lift gradually loses driving power on the body and eventually leads to desynchronization. While the PTC is placed in the FIM promoting zone, the phase angle will be remarkably reduced (to less than 5 deg) at the end of VIV upper branch. This makes the best usage of the lift in exiting the in-phase motion and eventually leads to the galloping phenomenon.

1.2. Literature review

In this section, the literatures related to several areas that are important to this dissertation are presented, including: computational fluid dynamics (CFD), cylinder flow, vortex induced vibrations (VIV), effect of surface roughness on a cylinder, and passive turbulence control (PTC).

1.2.1. Computational Fluid Dynamics (CFD)

Direct numerical simulation (DNS) is a simulation technique in computational fluid dynamics in which the Navier-Stokes equations are numerically solved without any turbulence modeling and approximation. The entire range of spatial and temporal properties of the turbulence must be directly resolved, from the smallest energy dissipative scales to the largest kinetic energy carrying scales. The computational cost of DNS is very high, even at low Reynolds numbers and therefore the applications for this method are only limited to low *Re* range. Dong applied DNS to cylinder flow at a *Re* as high as 10,000 by employing a multilevel-type parallel algorithm in dealing with high computational requirements. The results are in good agreement with the experiments. Other DNS applications on cylinder flow are within much lower Re range. Batcho and Karniadakis (1991) researched on the cylinder flow at *Re*=500 and compared the 2D and 3D results. Ma et al. (2000) investigated at *Re*=3900. Extremely high working loads exclude the possibility of DNS to be developed as a design tool especially in high Re range of interest in this thesis.

Large eddy simulation (LES) is a numerical method used to simulate turbulent flow based on the idea that the large scale motions of the flow are calculated explicitly, while the effect of the smaller universal scales are modeled using a sub-grid scale (SGS) model. Navier-stokes equations are spatially filtered to obtain the LES governing equations. Comparing with DNS, the computational requirements are lower and therefore much many more applications and references are available in the scientific literature.

However, pure LES is still demanding especially in the near wall region. In an attempt to overcome this problem, a series of hybrid RAN/LES are developed and designed to combine the advantages of both methods achieving reasonable results with tolerable computational time. Detached Eddy Simulation (DES) is one type of this kind proposed by Spalart et al. (1997). DES approach modifies the production and destruction terms of the model to enable it to work accordingly in different flow regions. After spatial filtering, it functions like a RANS model in boundary layer regions and like LES in the separated flow region. Another type of hybrid RANS/LES is developed by Nichols and Nelson (Nichols 2005, 2006, Nichols and Nelson 2003, Morgan and Visbal 2006). This

type of approach solves the RANS turbulence model as usual and assesses the results afterwards by filtering the level of eddy viscosity and estimate the level of turbulence that should be contributing to the RANS equations. The technique was originally developed for the Menter-SST model and subsequently developed by Morgan and Visbal (2006) for a discretized form of *k*-*ε* model utilized with a high-order implicit LES approach. Travin et al. (1999) conducted a series of DES simulation cases for Reynolds numbers 1.4×10^5 and 3.0×10^6 using a fifth-order spatial upwind flow solver with structured grids. Reynolds number of 1.4×10^5 was simulated at both subcritical laminar separation (LS) and supercritical turbulent separation (TS) cases. When the entire boundary layer is assumed to be turbulent, the simulated flow properties of high subcritical flow are similar to those of supercritical flow.

Reynolds Averaged Navier-Stokes (RANS) are derived from time-averaging the Navier-Stokes equations. The Reynolds stress tensor is typically approximated using the product of an eddy-viscosity coefficient at the strain-rate of the time-averaged velocity field. In this type of solution method, practically all scales of the turbulent motion are required to be modeled and represented in the eddy-viscosity coefficient.

There are numerous studies of using RANS for the simulation of flow over a circular cylinder. Shur et al. (2008) performed a study comparing 2D RANS with 3D RANS on several different span lengths and using several different turbulence models. The simulation were conducted at $Re=5\times10^3$ and the conclusion was made that three-dimensional URANS can be more accurate than two-dimensional RANS with respect to the lift and drag coefficients, but is not as accurate as DES. Also, 3D RANS is unphysically sensitive to the spanwise length of the flow domain and also highly sensitive to the particular turbulence model.

Wanderley et al. (2008) uses numerical solution of the two-dimensional RANS to study stationary and Vortex-Induced Vibration (VIV) of an elastically mounted circular cylinder. An upwind-biased TVD scheme is used to discretize the convection term of the governing equations and the *k*-ε turbulence model is used to simulate the turbulent flow in the wake of the cylinder. For the stationary case, flow speeds based on Re =40, 100,

200 and 1000 are tested. The numerical results of lift and drag coefficient and Strouhal number agree well with the other numerical and experimental results at such low Re numbers.

Catalano (2003) performed cylinder flow simulation at Re=0.5×10^6 and 1×10^6 by using RANS and LES. The comparisons have been made between the two methods. This near-wall modified LES method estimates the cylinder flow well and the results are in good agreement with experiments in term of base pressure and drag, however, *Re*-dependent results are not fully achieved as expected. In comparison with the modified LES methods, the RANS results follow the same tendency with tolerable accuracy considering the time consumed in dealing with such a high *Re* range. The LES gave better agreement than RANS, however, as far as lift, drag and Stroubal number are concerned, the difference between these two methods make RANS a promising candidate in simulating cylinder flow from a design point of view. However, from the published literature results, researchers mostly apply RANS on the low *Re* range or higher range that are close to or after the drag crisis. This fact indicates the prediction for transition in the boundary layer is still challenging task for RANS.

1.2.2. Cylinder flow

This thesis is exclusively focused on flow over a cylinder. Although the geometry of the body is trival, the resulting flow is one of the most challenging problems that is encountered in many different engineering fields. The simple geometry produces complex flow phenomena that is highly Re-dependent, has an unsteady wake (vortex shedding), turbulent transition in various flow regimes depending on *Re*, and oscillating separation points and stagnation point.

One of the most challenging features for cylinder flow is the dominant dependence of many local aspects of the flow on Reynolds number. For example, Zdravkovich(1997, 2003), describes a succession of transitions from laminar to turbulent in various regions of the cylinder flow, namely, wake transition(TrW), shear layer transition(TrSL), boundary layer transition(TrBL). As the Re increases, the transition first occurs in the wake region and turbulence gradually develops and spreads out laterally along the wake.

This occurs when the Re is between 180~400. The next transition occurs in the shear layer. The transition region moves forward towards the separation as the Re increases. The TrSL regime occurs in Re ranges from 350 up to 2×10^5. In this regime, it can be subdivided into TrSL1 (Re=$350\sim2\times10^3$), TrSL2 (Re=1×10^3, $2\times10^3\sim2\times10^4$, 4×10^4), TrSL3 (Re=2×10^4, $4\times10^4\sim1\times10^5$, 2×10^5). The next transitional region is the boundary layer, which gains most of the attention in present day research. In this regime, the Re effect on the boundary layer can be classified into three categories. When the Reynolds number is smaller than 2×10^5, it is called the subcritical range. In this range of Reynolds numbers, the attached boundary layer is laminar, the separated layers are in the early stages of transition, and the wake is fully turbulent. The Reynolds number range from 2×10^5 to 3.5×10^6 is called the critical range. In this range, the boundary layer starts as laminar and gradually separates with turbulent reattachment, a separation bubble, and finally turbulent boundary layer separation. When the Reynolds number is greater than 3.5×10^6, it is called the supercritical region. The boundary layer starts as laminar, then transitions to turbulent before the separation point. Most numerical simulations are implemented at low subcritical Reynolds number range because at this range the attached boundary layer is laminar and relatively thick and can be resolved by the grids. For example, in the high subcritical or supercritical Reynolds number, the attached turbulent boundary layer becomes much thinner than in the low Reynolds number cases, nearly six times thinner for Re=1.4×10^5 than Re=3.9×10^3 (Lo 2005). Therefore, the computer resources and simulation time requirement is inversely proportional to the Reynolds number. This is way fewer CFD studies have been conducted for flows past a circular cylinder at high Reynolds numbers with respect to the number of studies at lower Reynolds number.

When simulating flow over bluff bodies, another important challenge is the accurate prediction of the transition point. Unlike DNS, a RANS method requires a special transition model with empirical relations for onset and length of the transition zone. A common practice when using RANS for a *Re* above the subcritical regime is to assume a fully turbulent condition. The position of the transition point and the flow status in the boundary layer can have a large influence on the lift and drag coefficient. When CFD is

used to simulate the turbulence with models based on transport equations, at least three different strategies can be used to predict or account for boundary layer transition (Shur 1996). Some methods use specific boundary conditions or initial conditions to achieve this, while some of the others need to modify the model. A method, called “trip-less”, is adopted in the following simulations of present study. It determines the transition by using specifically designed initial conditions. In this method, the initial conditions for eddy viscosity are specified to be zero upstream the determined separation point, and nonzero downstream of this coordinate. As the flow develops over the body, the turbulence level will be effectively laminar where the eddy viscosity is zero, and effectively turbulent and determined by the governing turbulence equations in the regions where it is nonzero.

1.2.3. Vortex induced vibrations

Vortex-induced vibrations are widely seen flow-structure-interaction problem. This inherently self-exciting, self-regulating, self-limiting highly nonlinear phenomenon has received extensive attention in the academia and industry for several decades. VIV commonly are excited by three-dimensional separated flow, and are influenced by a large number of system parameters including mass ratio, structure stiffness, damping, surface roughness. The body of literature related to VIV is massive, and covers experimental and numerical investigation methods, multi-degree or single degree of freedom motion, flexible or rigid body motion, and VIV in air, water, and other fluids.

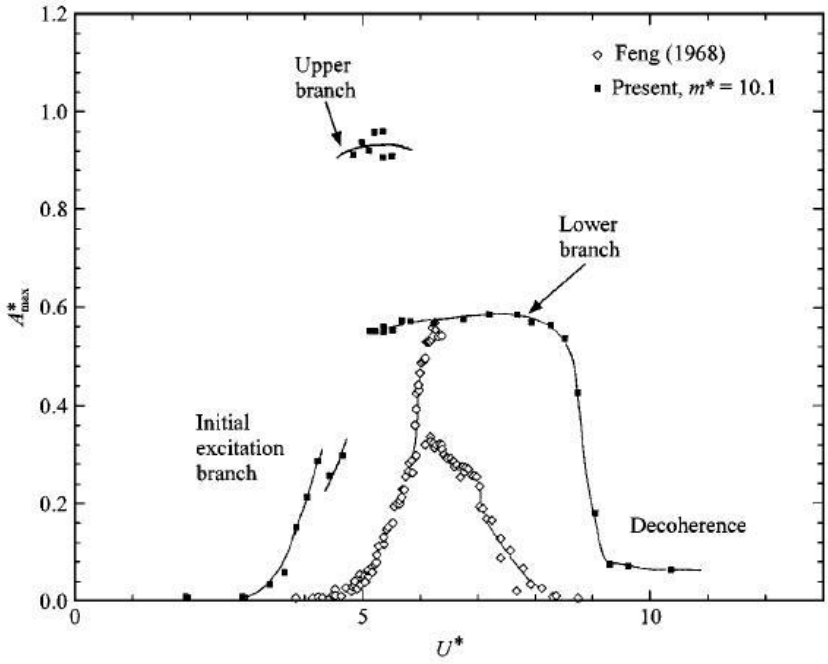

Figure 1.1. Maximum amplitude ratio plots by Feng (1968) with high mass ratio m^*=248 and by Khalak and Williamson (1999) with low mass ratio m^*=10.1(Reproduced from Khalak and Williamson 1999)

Amplitude

One of the most important measurements that can effectively describe and quantify VIV is the amplitude of motion. The important parameters that can potentially change the amplitude are the system stiffness, damping, mass ratio and surface roughness. In the VIVACE group, Lee (2010) investigated the damping and stiffness effects for a smooth cylinder in VIV. The large range of harnessing damping ratio (not including the structural damping) is 0~0.16. Chang (2010) further extended to research to the cylinder with passive turbulence control cases, and not only focused on the amplitude in VIV but also in other types of flow induced motion. Notably, galloping was found to be significantly affected by the stiffness and damping variation. In figure 1.1, the maximum amplitude ratio from Feng (1968) and Khalak and Williamson (1999) are compared. The effects of mass ratio to the response characteristics are well demonstrated. Feng conducted the experiments in air with a relatively low mass ratio m^*=248. The amplitude curve shows only initial and lower branches with a hysteretic switching mode in-between the two branches. The experiments performed by Khalak and Williamson are with a much lower

mass ratio of 10.1, mostly due to the water environment in which they tested. Clearly three different branches are exhibited in the amplitude curve, initial, upper, and lower branches. In Figure 1.1, the upper branch is present and has an amplitude value that is about 50% much greater than the maximum amplitude reported by Feng.

There are a large number of studies performed with the objective to reduce the amplitude of VIV. Most methods aim to alter the boundary layer, shear layer, or the wake flow such that the strongest vorticies are weakened, and thus the motion overall is reduced. For example, different type of surface roughness, surface protrusions, or other forms of wake stabilizers, such as the fairings used in the offshore structures, or a flat plate splitter, (Blevins 1990, Zdravkovich 1981, Raghavan, A.K et al 2008) have all been used to reduce the amplitude during VIV.

Frequencies

The frequency is another principally important characteristic that describes the body dynamics and flow status. The important variables that define the frequency of VIV are listed below, following the convention of Sarpkaya (2004):

$f_{n,air}$ – Natural frequency in air or vacuum: defined by $\frac{1}{2\pi}\sqrt{\frac{K}{m}}$

$f_{n,water}$ – Natural frequency in water: defined by $\frac{1}{2\pi}\sqrt{\frac{K}{m+ma}}$ and m_a is added mass.

f_{st} – Strouhal frequency: the vortex shedding frequency for fixed cylinder, it is closely related to the body dimensions as well as the flow speed over the body.

f_{vs} – vortex shedding frequency: when the cylinder body is fixed, this vortex shedding frequency is equal to the Strouhal frequency, while the body is undergoing VIV in the synchronization, the vortices are no longer shed at f_{st}, but at a frequency near to or equal to the natural frequency of the structure. Dominant shedding at this frequency is often referred to as "locked-in, locked-on, or synchronization". When synchronization ends, the vortex shedding frequency returns to f_{st}.

f_{ex} – Excitation frequency: Used in the case of self-induced and excited motion, this frequency is also called the oscillation frequency (Sarpkaya 2004).

f_{osc} – Oscillation frequency: The frequency of the primary oscillation mode. In the synchronization range, the ratio of $f_{osc}/f_{n,w}$ shows dependency on mass ratio, and tends to decrease as mass ratio increases. In Figure 1.2, Govardhan and Williamson (2000) show the frequency ratio as a function of reduced velocity for three different mass ratios. For the largest mass ratio of 10.3, the vortex shedding frequency is "locked-on" to the frequency very close to the natural frequency in water. For the intermediate mass ratio, the frequency of oscillation is still "locked" but to a relatively higher value comparing with $f_{n,w}$, and the ratio is about 2. For the lowest mass ratio of 0.52, the frequency continues to increase without synchronization. In Figure 1.3, Govardhan summarizes the effects of mass ratio on the oscillation frequency, and the range of the synchronization zone is also indicated.

Phase angle

Phase is defined as the angle in which the lift leads the motion in vortex-induced vibrations. It thus indicates the in-phase and out-of-phase components of the lift force. In Figure 1.4 (Sarpkaya 2004), *Ca* presents the inertia coefficient, which is the in-phase component of lift. It is clearly shown that it presents as phase angle is near to zero, indicating that the force is mostly in phase with the motion, and the inertia coefficient is large. For a reduced velocity of greater than 5.75, the phase angle suddenly moves to a value near 220 degrees, showing that the inertia coefficient is negative, and the drag coefficient is at its maximum positive value.

In the studies of Khalak and Willamson (1999), the phase angle behavior is well associated with different branches seen in the amplitude curve. Also, during the transition between branches, intermittent switching is often observed. In the upper branch, where the amplitude of motion is maximum, the phase angle is nearly 0 (Figure 1.5). The lift is almost perfectly in phase with the amplitude, which yields the high amplitude region. While at the end of upper branch, the phase angle shifts intermittently from 0 to 180 deg. The amplitude also indicates that the system is weakly "locked" onto both branches

(Khalak and Willamson1999) and spends part of the time in each mode according to the phase angle history. After the transition, the system is stabilized on the lower branch, and the phase angle is also remains consistently near 180 deg. The rapid decrease of the amplitude is very likely to be the resultant of the out-of-phase lift, which can no longer provide the system the energy it needed to sustain the high amplitude of motion.

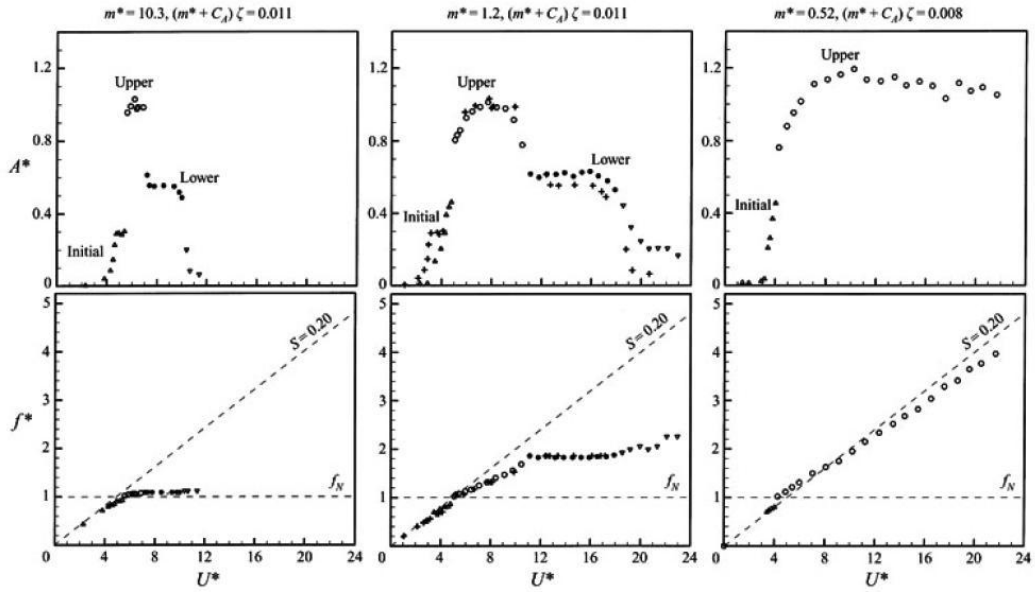

Figure 1.2. Amplitude and frequency ratio dependency on mass ratio (Reproduced from Govardhan and Williamson 2000)

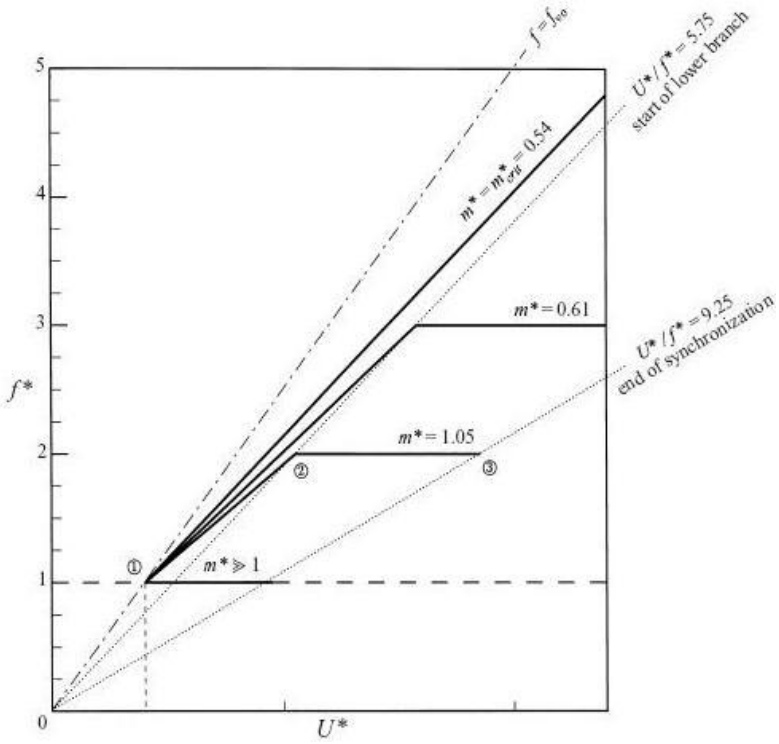

Figure 1.3. Schematic plot of frequency dependence on mass ratio (Reproduced from Govardhan and Williamson 2000)

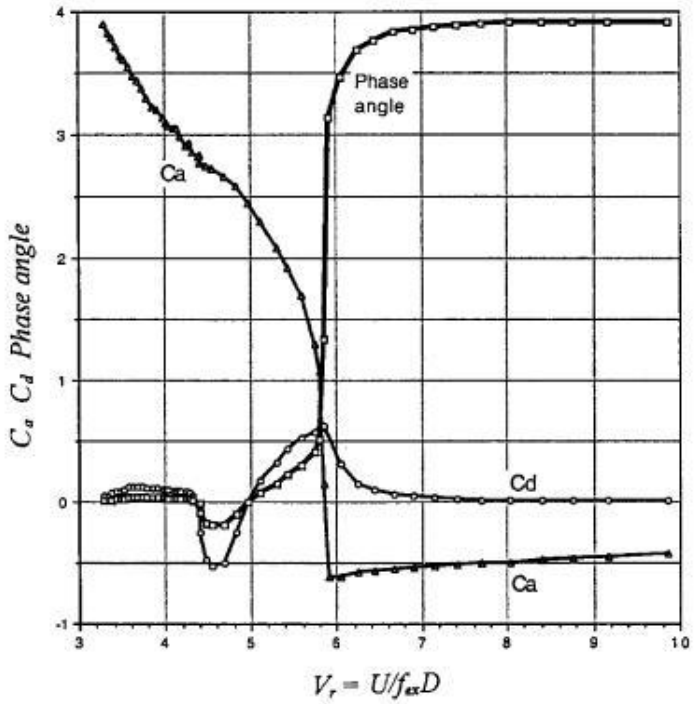

Figure 1.4. In-phase (*Ca*), out-of-phase components (*Cd*) of lift and phase angle plotted as a function of *Vr* (Reproduced from Sarpkaya 2004)

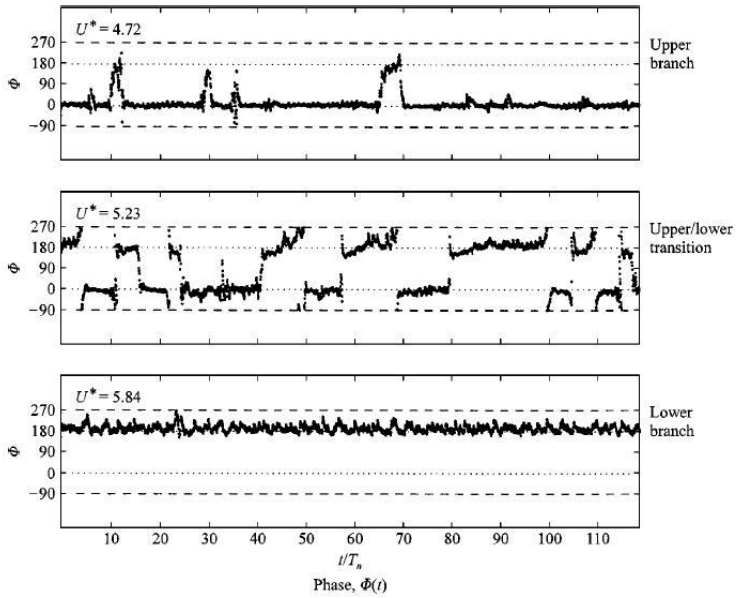

Figure 1.5. Phase angle history for different flow regimes (upper branch, upper/lower transition, lower branch) (Reproduced from Khalak and Willamson 1999)

Vortex patterns

There are certain forms of the vortex pattern related to vortex-induced vibration. Williamson and Roshko established the relations among oscillation amplitude and vortex modes and summarized experimental results in the Williamson-Roshko map of wake pattern regimes (Williamson and Roshko 1988; Khalak and Willamson 1999) (Figure 1.6). The different vortex patterns associated with the rigid-cylinder system in VIV with low mass-damping parameter has been described and labeled 2S, 2P, P+S, 2P+2S (Williamson 1985; Williamson and Roshko 1988; Govardhan and Williamson 1999; Jauvtis and Williamson 2003; Williamson and Govardhan 2004).

The vortex patterns are closely related to mass ratio, other degrees of freedom and surface roughness (Raghavan 2007). Flemming and Williamson (2005) mentioned that 2C mode is observed for a pivoted cylinder, which allows more degrees freedom. 2C refers to the case that for each cycle 2 single vortices with the same sign shed from each side of the cylinder. In addition, the 2T (Williamson and Jauvtis 2004) mode is discovered for cylinder in *X*-*Y* motion, and 2T refers to the pattern that for each half cycle

three vortices (Triplet) shed from one side of the cylinder, two with same sign rotating in one direction and the third one with opposite sign (or orientation of rotation). In Chapter 5, 6, 7 additional vortex patterns are well observed when PTC (surface roughness) is applied on the smooth cylinder, and the modes vary correspondingly as the PTC parameters change.

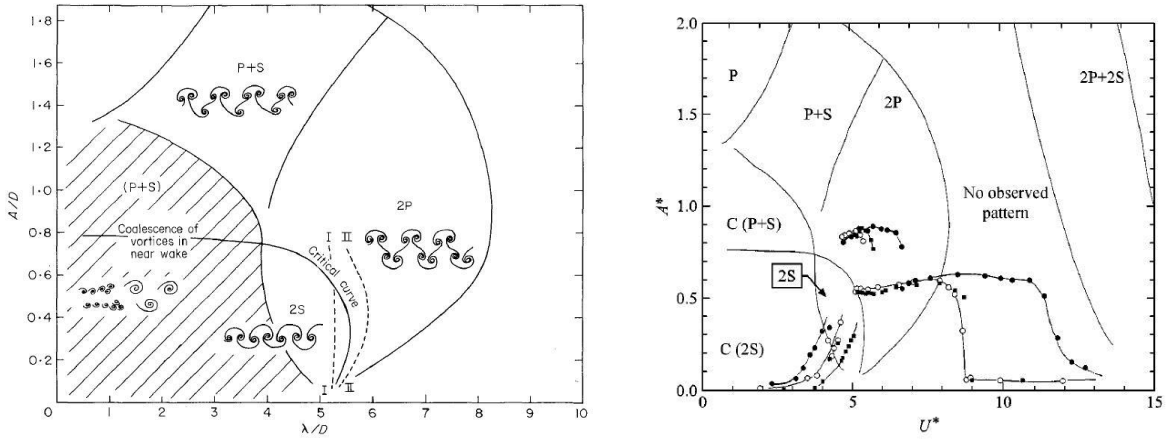

(a) Williamson-Roshko map in *A/d* (amplitude ratio) and *λ/D* (wave length) plane, (Reproduced from Williamson and Roshko 1988)

(b) Williamson-Roshko map in *A/d* (amplitude ratio) and U^* (reduced velocity) plane, (Reproduced from Khalak and Willamson 1999)

Figure 1.6. Williamson-Roshko map of wake pattern regimes

1.2.4. Roughness effect and Passive Turbulence Control (PTC)

Roughness on the cylinder can effectively change the flow properties. The alteration of the pressure distribution on the body results in the variation in the lift and drag on the cylinder body. Roughness introduced on the surface of smooth circular cylinder can effectively trigger boundary layer transition, and hence display postcritical flow properties in a pre-critical Reynolds number range. The literature is broad related to using roughness to alter VIV. Examples that show the different parameters that influence the roughness and motion include: roughness height, roughness density (send papers with close-packed particles it dispersed particles) (Ribeiro 1991), roughness coverage (fully or partially covered surface (Park 2011)), roughness shapes (hemi-sphere, pyramidal shape, irregular shape), roughness dimensions (one dimensional: spanwise ribs (Güven 1975,

Roulle 1980 and Ko et al. 1987), two-dimensional: mesh wire screen (Ribeiro 1991), three-dimensional: sandpaper)), arrangements (randomly distributed (Farell and Blessmann 1983, Farell et al.1977, Batham 1973) or orderly distributed (Fedeniuk 1982, Hove 1978, Achenbach 1977)). Ribeiro conducted experiments using roughness with different dimensions, and different roughness heights of each type. The conclusion is made that all of the types of roughness that were tested (spanwise ribs, mesh wire screen, sandpaper) are able to trigger boundary transition, however, with all with different effectiveness in doing so. The higher roughness height has the tendency to establish the supercritical phenomenon with a lower Reynolds number range, meaning the earlier transition will arrive (Ribeiro 1991). Many researchers were interested in the effect of surface roughness on flow around a circular cylinder (Achenbach 1971, Achenbach and Heinecke 1981, Nakamura and Tomonari 1982). Achenbach and Heinecke revealed the roughness height effects on the drag coefficient, Strouhal number, and transition point for stationary cylinder fully covered by pyramidal roughness case. Higher roughness yields earlier "drag crises" and brings the higher drag value at drag crises (Achenbach and Heinecke 1981).

By applying roughness on the circular cylinder surface, small vortices that are approximately of the size of the roughness are generated. The energetic tiny vortices help to mix the outer fluid of larger momentum with the lower momentum fluid close to the body in the laminar layer, or to enhance or invigorate the turbulent fluctuation in the turbulent boundary layer case (Ragvahan 2007). The vortex-shedding phenomenon becomes absent in TrBL0, TrBL1 and TrBL2 regimes where the cylinder flow is featured with separation bubbles attached on the surface (Zdravkovich 1997). Until the supercritical regime is achieved, the vortex shedding reappears in the wake region (Ribeiro 1991, Zdravkovich 1997). Roughness with dimension that is comparable to the boundary layer thickness can excite transition in the boundary layer and causes the vortex shedding to reappear at much lower Re range, possibly bridging the vortex-absent regime with a continuous synchronization zone.

Passive turbulence control (PTC) is successfully used as an effective way to enhance flow induced motion by VIVACE group in the University of Michigan MRELab. By

applying the PTC selectively on the cylinder surface throughout the spanwise direction, the flow over the cylinder surface is altering in a way that generates higher lift which is shown to be better synchronized with the motion. The effects of PTC used by VIVACE group can be summarized as followings (Chang 2010):

1. Trigger the boundary layer: cause the transition in the boundary layer at a lower Reynolds number.

2. Set the correlation length: By applying PTC continuously on the spanwise direction of the cylinder, it helps to regulate the dominant vortex, synchronize the flow properties on different locations of the cylinder, and lead to an elongated correlation length.

3. Stabilize the separation points and in some cases cause negative hydrodynamic damping.

Chapter 2

COMPUTIONAL METHOD

2.1. RANS governing equations

In this thesis the flow around a cylinder with or without motion and surface roughness is studied by seeking numerical solution of the unsteady Reynolds-averaged Navier–Stokes equations (RANS).

In the Reynolds-averaged approach to turbulence, practically all of the unsteadiness is modeled, and the slowly varying in time mean flow is solved for explicitly.

The basic tool required for the derivation of the RANS equations from the instantaneous Navier–Stokes equations is the Reynolds decomposition. Reynolds decomposition refers to separation of the flow variable (such as the velocity *u*) into the mean (time-averaged) component (*U*) and the fluctuating component (u'). Thus,

$$u_i(\vec{x},t) = U_i(\vec{x},t) + u_i'(\vec{x},t) \qquad (2.1)$$

Where the $\vec{x} = (x, y, z)$ is the position vector

$$U_i(\vec{x},t) = \lim_{T\to\infty} \frac{1}{T} \int_t^{T+t} u_i(\vec{x},t)dt \qquad (2.2)$$

In Equation 2.2, the period T is smaller than that of the slowest scales of motion that will be resolved explicitly in the discretization of the momentum equations, but larger than the greatest period describing the turbulent fluctuation.

Throughout this report the instantaneous variable is denoted by a lower-case symbol, the mean is denoted by the corresponding upper-case symbol and the fluctuating part is the lower-case symbol with a prime.

The Navier-Stokes equations of motion for an incompressible Newtonian fluid are:

$$\frac{\partial u_i}{\partial x_i} = 0 \tag{2.3}$$

$$\rho \frac{\partial u_i}{\partial t} + \rho u_j \frac{\partial u_i}{\partial x_j} = -\frac{\partial p}{\partial x_i} + \frac{\partial t_{ji}}{\partial x_j} \tag{2.4}$$

The vectors u_i and x_i are velocity and position, p is pressure, ρ is density and t_{ji} is the viscous tensor defined by

$$t_{ij} = 2\mu S_{ij} \tag{2.5}$$

Where μ is the molecular viscosity and S_{ij} is the strain rate tensor

$$S_{ij} = \frac{1}{2}\left(\frac{\partial u_i}{\partial x_j} + \frac{\partial u_j}{\partial x_i}\right) \tag{2.6}$$

To simplify the time-averaging process, we rewrite the convective term in conservation form

$$u_j \frac{\partial u_i}{\partial x_j} = \frac{\partial}{\partial x_j}(u_j u_i) - u_i \frac{\partial u_j}{\partial x_j} = \frac{\partial}{\partial x_j}(u_j u_i) \tag{2.7}$$

Where we take advantage of mass conservation in order to drop term $u_i \frac{\partial u_j}{\partial x_j}$.

Thus the Navier-Stokes equations in the conservation form are:

$$\rho \frac{\partial u_i}{\partial t} + \frac{\partial}{\partial x_j}(u_j u_i) = -\frac{\partial p}{\partial x_i} + \frac{\partial}{\partial x_j}(2\mu s_{ji}) \tag{2.8}$$

Substituting $u_i(\vec{x},t) = U_i(\vec{x}) + u_i'(\vec{x},t)$, $p(\vec{x},t) = P_i(\vec{x}) + p_i'(\vec{x},t)$, into above N-S equation yields the Reynolds-averaged Navier-Stokes equations of motion in conservation form

$$\frac{\partial U_i}{\partial x_i} = 0 \tag{2.9}$$

$$\rho \frac{\partial U_i}{\partial t} + \frac{\partial}{\partial x_j}(U_j U_i + \overline{u_j' u_i'}) = -\frac{\partial P}{\partial x_i} + \frac{\partial}{\partial x_j}(2\mu S_{ji}) \tag{2.10}$$

Aside from replacement of instantaneous variables by mean values, the only difference between the time-averaged and instantaneous equations is the appearance of the correlation term $\overline{u_j' u_i'}$. This is a time-averaged rate of momentum transfer due to the turbulent fluctuation. By using

$$\frac{\partial}{\partial x_j}(U_j U_i) = U_j \frac{\partial U_i}{\partial x_j} + U_i \frac{\partial U_j}{\partial x_j} \tag{2.11}$$

The resulting equation is

$$\rho \frac{\partial U_i}{\partial t} + \rho U_j \frac{\partial U_i}{\partial x_j} = -\frac{\partial P}{\partial x_i} + \frac{\partial}{\partial x_j}(2\mu S_{ji} - \rho \overline{u_j' u_i'}) \tag{2.12}$$

This is the equation which is usually referred as Reynolds-averaged Navier-Stokes Equation. The quantity $-\rho \overline{u_j' u_i'}$ is known as the Reynolds-stress tensor denoted by $\rho \tau_{ij}$. This term contains six components which need to be modeled.

2.2. Turbulence modeling

In order to solve the RANS equation for the mean-flow properties of the turbulent flow, we need to determine the value of the Reynolds stress tensor $-\rho\overline{u_j' u_i'}$. This is a second order symmetric tensor with 6 independent components. For general three dimensional flows, we have four unknown mean flow properties, viz., three velocity components and pressure. All together the six independent components from the Reynolds-stress tensor and the four mean-flow quantities result in ten unknowns. The equation of conversation of mass and three components of conservation of momentum equations yield only four equations to determine the ten unknowns. This means we need to find more equations to close the system.

The most widely used procedure to close the RANS equations is to use the concept of and eddy viscosity coefficient that is determined using the Boussinesq approximation. The eddy viscosity ν_t is a time and space dependent variable which is determined by the mean-flow value instead of being only a property of the fluid such as the molecular viscosity. The dependence of position is a consequence of variations in size and intensity of turbulence eddies. For wall bounded flow, as the wall is approached the eddy viscosity tends to increase first before the maximum ν_t value is reached, then falls to zero at the wall.

The Boussinesq eddy-viscosity approximation assumes that the principal axes of Reynolds stress tensor is the same as the principal axes of mean strain rate tensor, and the scalar eddy viscosity ν_t is the linear proportionality factor between these two quantities. Due to the simplification of this assumption, the modeling of Reynolds stress tensor can be finally be reached by modeling the eddy viscosity ν_t .

Spalart-Allmaras(S-A) turbulence model is a one-equation model, which is solving for one transport equation for eddy viscosity like variable $\tilde{\nu}$. The transport equation is assembled using empiricism and arguments of dimensional analysis. The S-A model is different from other one equation models and algebraic models in sense that it is

a local model, which means the equation in one location does not depend on the solutions of other points (Spalart et al. 1994). It is therefore compatible with grids of any structure. It is numerically forgiving, in terms of near wall resolution and stiffness. It is motivated by considerations of sensitivity to free stream values, which were not as explicit in the past, therefore comparing to other turbulence model like k-w and B-B which are suffer from excessive sensitivity to free steam values, the wall and free stream boundary conditions for S-A model are relatively trivial to prescribe.

The S-A model is given by following transport equation

$$\frac{\partial \tilde{\nu}}{\partial t} + u_j \frac{\partial \tilde{\nu}}{\partial x_j} = c_{b1}\tilde{S}\tilde{\nu} - c_{w1} f_w \left(\frac{\tilde{\nu}}{d}\right)^2 + \frac{1}{\sigma}\left[\frac{\partial}{\partial x_j}\left((\nu + \tilde{\nu})\frac{\partial \tilde{\nu}}{\partial x_j}\right) + c_{b2}\frac{\partial \tilde{\nu}}{\partial x_i}\frac{\partial \tilde{\nu}}{\partial x_i}\right] \tag{2.13}$$

And the turbulent eddy viscosity is computed from

$$\mu = \rho \tilde{\nu} f_{v1} \tag{2.14}$$

Where

$$f_{v1} = \frac{\chi^3}{\chi^3 + c_{v1}^3}$$

$$\chi = \frac{\tilde{\nu}}{\nu}$$

ρ is the density, $\nu = \mu / \rho$ is the molecular kinematic viscosity, and μ is the molecular dynamic viscosity. Additional definitions are given by following equations:

$$\tilde{S} = \Omega + \frac{\tilde{\nu}}{\kappa^2 d^2} f_{v2} \tag{2.15}$$

Where Ω is the magnitude of vorticity, d is the distance from the field point to the nearest wall, and

$$f_{v2} = 1 - \frac{\chi}{1 + \chi f_{v1}}$$

$$f_w = g\left[\frac{1 + c_{w3}^{\ 6}}{g^6 + c_{w3}^{\ 6}}\right]^{\frac{1}{6}}$$

$$g = r + c_{w2}(r^6 - r)$$

$$r = \min\left(\frac{\tilde{\nu}}{\tilde{S}\kappa^2 d^2}, 10\right)$$

The constants are

$$c_{b1} = 0.1335$$
$$\sigma = 2/3$$
$$c_{b2} = 0.622$$
$$\kappa = 0.41$$
$$c_{w2} = 0.3$$
$$c_{w3} = 2$$
$$c_{v1} = 7.1$$
$$c_{w1} = \frac{c_{b1}}{\kappa^2} + \frac{1 + c_{b2}}{\sigma}$$

2.3. Numerical schemes

2.3.1. Finite volume discretization

In this study, flow simulation is performed by using a solver built upon the open source CFD tool OpenFOAM. OpenFOAM is a collection of C++ libraries that are developed for the purpose of solving continuum mechanics problems with the finite-volume discretization procedure.

In order to solver the partial differential equations (PDE) that govern conservation of momentum, mass, and evolution of turbulence, a finite-volume procedure is used to transform the PDE's of continuous variables into sets of algebraic equations that describe the discrete or numerical solution of the governing equations.

The discretization procedure involves the discretising the continuous simulation domain and the equations governing the physical process. The entire domain is divided into a number of non-overlapping finite volumes on which the numerical solution of the governing equations is sought. The finite-volume method is based on integral form of continuity equations of mass and momentum. First, most volume integrals of spatial derivative terms are transformed into cell surface integrals by using Gauss's theorem. Gauss's theorem can be written as

$$\int_V \nabla * \phi dV = \int_S d\mathbf{S} * \phi \tag{2.16}$$

Where **S** is the surface area vector, *v* is the control volume surrounded by **S**, ϕ represents any tensor field, and the * sign is used to represent any tensor product, i.e., inner, outer, cross and respective derivatives. Then each term of the cell surface integral is discretised using an appropriate scheme.

2.3.2. Discretization schemes

As discussed previously, most spatial integral terms over a control volume can be converted to a cell surface integral. The generalized form of Gauss' theorem is applied to all the spatial terms that appear as:

$$\int_v \nabla \cdot a \; dV = \int_S dS \cdot a \tag{2.17}$$

$$\int_v \nabla \phi dV = \int_S dS \, \phi \tag{2.18}$$

$$\int_v \nabla a \, dV = \int_S dS \, a \tag{2.19}$$

Convection term

The convection term is integrated over the control volume and approximated as follows:

$$\int_v \nabla \cdot (\rho U \phi)\, dV = \int_S dS \cdot (\rho U \phi) = \sum_f S_f \cdot (\rho U)_f \phi_f = \sum_f F \phi_f \tag{2.20}$$

The face value ϕ_f can be calculated based on the volume field values by using different interpolation schemes, for current study linear interpolation is used for simulation, which is second order accuracy method in space.

Laplacian term

In the incompressible fluid dynamics, the Laplacian term is $\nabla \cdot \nu \nabla U$, where ν is the molecular viscosity and U is fluid velocity. Similarly as before, based on standard finite volume discretisation of Gaussian integration, the Laplacian term is evaluated as

$$\int_v (\nabla \cdot \nu \nabla U)\, dV = \sum_f S \cdot (\nu \nabla U)_f = \sum_f \nu_f S \cdot (\nabla U)_f \tag{2.21}$$

In this term, there are two quantities need to be evaluated from the cell center value, one is the viscosity and the other is the surface normal gradient $S \cdot (\nabla U)_f$, so two interpolation schemes need to be specified. For viscosity value, linear interpolation scheme is used and for the surface normal gradient term, the scheme is used as

$$S \cdot (\nabla U)_f = |S| \frac{U_N - U_P}{|d|} \tag{2.22}$$

Where P in U_P means current cell in which we are evaluating values for, N in U_N means the neighbor cell to the current cell. A correction scheme is selected to evaluate the surface normal gradient as follows, which improves the accuracy in the cases of non-orthogonal meshes. The entire is decomposed into two parts: orthogonal contribution and non-orthogonal contribution (Jasak, H. 1996),

$$S \cdot (\nabla U)_f = \underbrace{S_{orth} \cdot (\nabla U)_f}_{orthogonal\ contribution} + \underbrace{S_{non-orth} \cdot (\nabla U)_f}_{non-orthogonal\ contribution} \tag{2.23}$$

Splitting the term in this way is to make sure the main orthogonal term can be evaluated with second-order accuracy. For details of schemes used for this non-orthogonal term, refer to the thesis Jasak, H. (1996).

The governing equations derived from the RANS formulations are spatially discretised on finite-volumes of arbitrary polyhedral form. In this study, the open source CFD tool Open-FOAM has been used to perform all the simulations. For the spatial terms, the divergence, the gradient and Laplacian terms uses a second-order Gauss integration scheme with a linear interpolation for the face center values. The second-order backward Euler is adopted for the time integration. Accordingly, the numerical discretisation scheme gives second order accuracy in space and in time. Pressure implicit with splitting of operators (PISO) algorithm is used for solving momentum and continuity equations together in a segregated way. As for the iteration process, at least 20 vortex-shedding cycles, are taken to obtain reliable statistical information.

2.4. Equation of motion

Mathematically, the one degree of freedom dynamic system can be modeled as a cylinder with mass *m*, supported by a spring (spring constant *K*) and a damper (damping *c*). The one degree of freedom equation of motion for such a mass-spring-damper system can be presented as Equation 2.24:

$$m\ddot{y} + c\dot{y} + Ky = F_{fluid,y} \tag{2.24}$$

$$m\ddot{y} = F_{fluid,y} - c\dot{y} - Ky \tag{2.25}$$

$F_{fluid,y}$: Fluid force acting on the cylinder body in the perpendicular direction, which is integrated from pressure and viscous friction on the body obtained from Navier-Stokes equation solutions

$-c\dot{y}$: Damping force

$-Ky$: Spring force

The solutions of Equation 2.25 can be obtained by solving a system of 2 first-order differential equations 2.26 and 2.27:

$$m\dot{v} = F_{fluid,y} - c\dot{y} - Ky \tag{2.26}$$

$$\dot{y} = v \tag{2.27}$$

Mixed implicit explicit method is adopted to solve the equation of motion together with Navier-Stokes equations for velocity v and displacement y of the cylinder. Explicit time integration is used for velocity and implicit method is for displacement using predicted velocity at a new time level.

$$\dot{v}^n = \frac{v^{n+1} - v^n}{\Delta t} \tag{2.28}$$

$$v^{n+1} = v^n + \Delta t \cdot \left(\frac{F_{fluid,y}{}^n - cv^n - Ky^n}{m}\right) \tag{2.29}$$

$$y^{n+1} = y^n + \Delta t \cdot v^{n+1} \tag{2.30}$$

Where Δt is the time step.

2.5. Boundary conditions

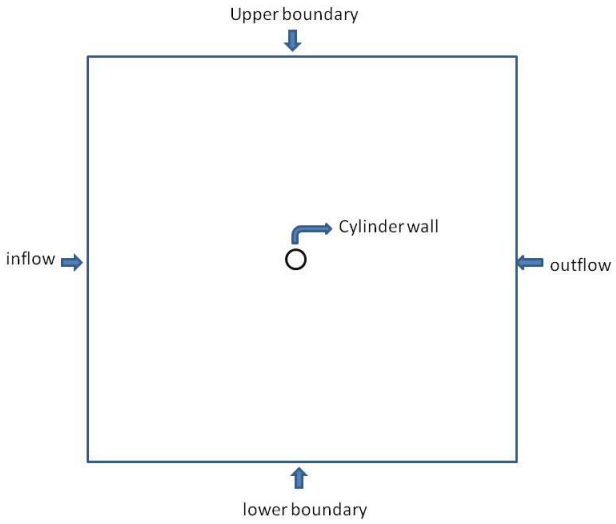

Figure 2.1. Boundaries of simulation domain

The simulation domain is 30D×30D for stationary cylinder and 50D×50D for cylinder in fluid induced motion. The entire domain is bounded by 5 boundaries in all, including upstream inlet boundary, outflow boundary, upper and lower boundary, and the cylinder wall. At the inlet boundary of the domain (see Figure 2.1), an inflow with uniform and constant velocity is specified for the fluid field. For the outflow, zero gradient is also imposed for velocity as well as ν_t and $\tilde{\nu}$. The specification of the outflow condition is justified because the distance from the cylinder to the outlet boundary is sufficiently long for this boundary condition to have negligible influence on the near-wake region of the cylinder flow. As for upper and lower boundaries, the flow field is assumed to not be disturbed by the existence of cylinder for all simulation variables since the distance from the cylinder to the boundary is large. From this point, the velocity is set to be the same as the inflow value and eddy viscosities are zero gradient. For the wall, two different types of boundary conditions are used for smooth and rough wall. Wall functions for ν_t and $\tilde{\nu}$ are used in order to count for the roughness effect while for smooth wall cases the zero gradient condition is applied for both quantities. No slip velocity boundary condition is used for smooth cases due to fact that the integration is implemented directly through the viscous sub layer down to the wall. When the flow-induced-motion cases are considered, a moving wall boundary condition

is applied. The grid is rigidly moving with the cylinder. This boundary condition equates the fluid velocity on the wall to the velocity of the moving cylinder which is calculated from the body dynamic motion solver at every time step. At the same time, zero gradient condition is used for pressure. The final condition is the inlet boundary condition.

In this thesis two approaches are used to prescribe the initial conditions of the eddy viscosity. The so-called 'trip-less approach' is used for the laminar separation case, following Travin et al. (1999). Trip-less means no trip term is included in the turbulence model. Here the trip-less method is used to simulate the subcritical regime in cylinder flow without transition information. The inflow eddy viscosity is zero, or much smaller than the molecular viscosity. The front part of the boundary layer then also has zero eddy viscosity. The recirculation region has non-zero eddy viscosity, and the small value eddy viscosity propagates upstream into the boundary region and separating shear layer. Travin (1999) explained the process of development of eddy viscosity as: due to the high strain rate and high vorticity in that layer, the production rate of eddy viscosity is rapid, which ensures more eddy viscosity goes into the recirculation region as feedback. The entire procedure is a "self-sustaining" process and the main advantage of this method is we don't need to provide any information about transition point before simulation. It occurs only if non-zero values were placed in the initial condition (Travin et al. 1999). More studies will be addressed in the following chapter about whether the simulation results are dependent on the initial values or the nonzero region setup. For the turbulent separation case, the model can provide fully turbulent results by setting the inflow value of eddy viscosity about 5 times the molecular viscosity, as well as the infield value with the same value. In using this setup, the turbulence model can simulate fully turbulent case in the sense that any regions that contain shear within simulation domain, including boundary layer, become fully turbulent.

2.6. Initial condition

As introduced in the previous session, different transition modes, namely turbulent separation (TS) and laminar separation (LS), are used to simulate subcritical and critical regime. The initial nonzero value of eddy viscosity has been set to molecular

viscosity and 5 time's molecular viscosity for LS and TS respectively. The non-zero domain is the downstream half of the cylinder and simulation area for LS, and the entire domain for TS cases. In order to further investigate how much the results are dependent on the initial nonzero values and the domain coverage, the results are compared for different initial values and regional setup in Chapter 3.

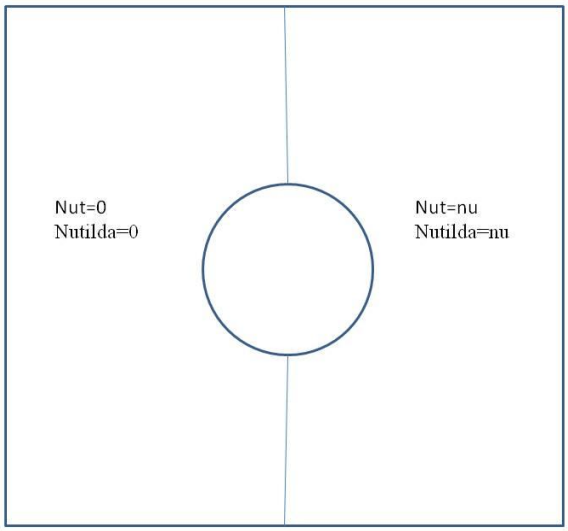

Figure 2.2. Domain setup for initial conditions of $\tilde{\nu}$ and ν_t in laminar separation cases

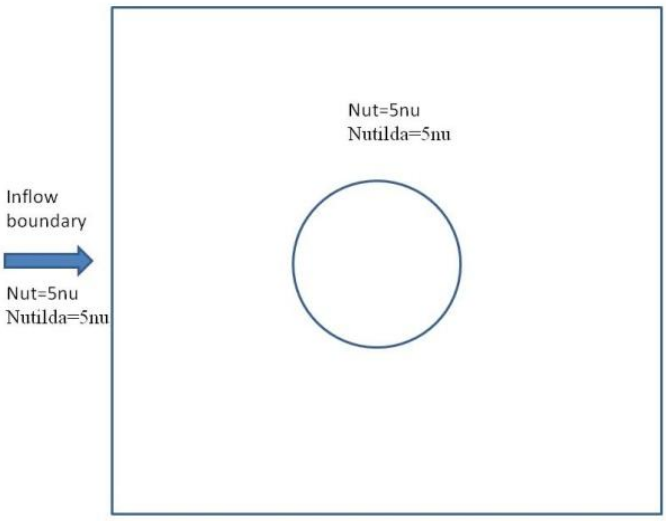

Figure 2.3. Domain setup for initial conditions of $\tilde{\nu}$ and ν_t in turbulent separation case

2.7. Grid requirement

Two-dimensional, structured and unstructured computational grids were generated for all cases using Gambit grid generating software. The computational domain is extended 15 times the cylinder diameter in fore and aft of the cylinder. The region also extended to 15 times the cylinder diameter in the vertical direction from the edge. This is to ensure that in the selected model, the numerical results are accurate and that the problem is solvable in a reasonable amount of time. The larger domain with 60D×40D has been also been used to make comparison for the stationary cylinder cases and the results from this larger grid does not offer obviously better results, therefore, the grid domain size is selected as 30D×30D for stationary case. For the purposes of grid construction, the computational domain for cylinder is divided into two regions: the boundary layer near wall region and the far from the wall region. Dividing the domain in this way is a common practice in problems where the effects of the viscous boundary layer near the body are expected to significantly affect the flow field and where enhanced grid resolution in the vicinity of the boundary layer is important. For the far from the wall

region, the grids are more clustered near the cylinder and have a higher resolution within a circular region whose radius is 4 times cylinder diameter D. In order to determine the overall grid resolution required to provide a grid independent solution, a grid sensitivity study was conducted on three different grid levels for smooth stationary cylinder cases (the results are summarized in chapter 3). When the smooth cylinder is studied the grid is sufficient to resolve the viscous sublayer. The wall variable for distance from the wall $y+$ at the wall-adjacent cell should be on the order of 1. However, a higher y+ is acceptable as long as it is well inside the viscous sublayer. Some work has been done regarding this first grid spacing topic and more results can be found in next chapter. In the grid for rough cylinder, the paper component of Passive Turbulence Control (PTC) is modeled as part of cylinder surface, and treated as wall boundary. The roughness effects are modeled by wall functions. Comparing with smooth cylinder grids, no fine boundary layer cells are used and first grid spacing $y+$ is about 20-70, depending on the Reynolds number. The grid used for cylinder with PTC in flow-induced-motion also has enhanced grid density near cylinder wall and the total cell number is about 45,600 (circumferential × radial: 240 × 190). This is the same as the medium structured grid used for smooth cylinder. Due to the high amplitude of motion induced by the PTC, the domain size is increased to 50D×50D.

Chapter 3

STATIONARY CYLINDER

In this chapter, results from numerical simulations for the flow over a stationary cylinder are summarized. The numerical method is based on solving 2D-RANS equations and employs the Spalart-Allmaras turbulence model. The force acting on the body and the Strouhal frequency are investigated for a wide range of Reynolds number from 1,000 to 10^6. Wall resolving grids are been used for this smooth cylinder case and grid resolution requirements are determined by comparing the flow solution on a series of grids of different discretization of the fluid domain. The different grids vary in size of the discretization, and are of structured and unstructured topology. Performance quantities such as drag and lift coefficients, Strouhal number are compared with experimental measurements and with other existing numerical simulation data.

3.1. Grid dependency study

Two types of grid dependence studies were completed to define a baseline grid.

1. "*y*+ study" for the plat plate
2. Grid resolution study
3. Structured grids versus unstructured grids

3.1.1. y+ study on flat plate

The first study examined the near-wall spacing aspect of the grid resolution. The implementation of the Spalart-Allmaras model used in this thesis for most of the smooth-wall cases requires that the numerical grid resolve the body-boundary layer with the first grid point deep in the viscous sublayer. Using the wall normal distance of the wall-

adjacent cell measured dimensionlessly in wall units, the first cell should have a value of $y+$ close to 1.

In order to test the sensitivity of the results to this requirement on the near-wall spacing, a set of grids for the flow over a flat plate are used to compute the wall shear stress. For this case, the simulation is run at $Re=10^6$ and is performed over a 9 meter long flat plate. The computational domain is 9m×2.5m using a 2D grid with approximately 8,000 cells. Nine grids are used with different values of the near-wall spacing. The *posteriori* average values of the $y+$ on the nine grids are 3, 7, 18, 31, 48, 86, 150, 294 and 727 respectively. These grids are obtained by changing the stretching rates for the cells in the wall normal direction with total number of cells fixed. The wall shear stress is plotted over plate for each grid and compared with the empirical formulas from White (2005). All the results are presented in figure 3.1, where one can see that the grid with $y+=3$ has the closest agreement with White. Also, the smaller average value of $y+$ is, the better agreement is. This confirms the near wall model guideline which need the first grid point to be located within the viscous sublayer and should be close to the value of 1.

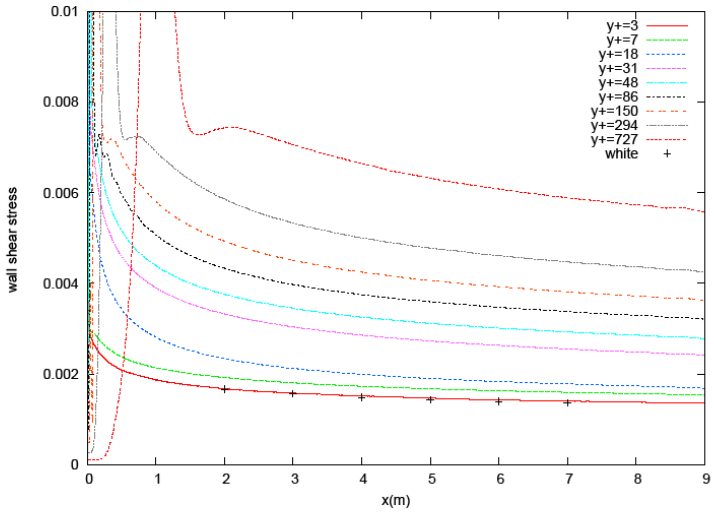

Figure 3.1. Flat plate wall shear stress with different $y+$ according to different grids

3.1.2. Grid density study

In order to determine the overall grid resolution required to get a grid independent solution, a grid sensitivity study is conducted on three different grids. Structured grids are used in this study. The three levels of grids are namely structured coarse (S1), structured medium (S2), structured fine (S3). The refinement is achieved by increasing the number of cells in circumferential and radial direction by a factor of approximately 1.5 between successive grids. For each case the wall integration grid requirement is satisfied by ensuring $y+$ for the wall cells is on order of $O(1)$. The detailed parameters are listed in Table 3.1.

Table 3.1. Parameters of grids used in the resolution study

Grid	Grid resolution (circumferential x radial)
Structured-coarse (S1)	180 x 160 = 28,800
Structured-medium (S2)	240 x 190 = 45,600
Structured-fine (S3)	360 x 220 = 79,200
Unstructured	~ 44,000 cells

3.1.3. Structured vs. unstructured grids

The third grid dependence study compares the results based on using unstructured grid topology with the structured discretization. This investigation is motivated by the fact that unstructured grids provide great flexibility in tackling complex geometries. As the VIVACE system evolves, more complex configurations such as a fish-tail device may be utilized. Structured quadrilateral meshes will generally force cells to be placed in regions where they are not needed. On the other hand, unstructured quadrilateral grids may use far fewer cells due to the fact that it allows clustering of cells in selected regions of the flow domain.

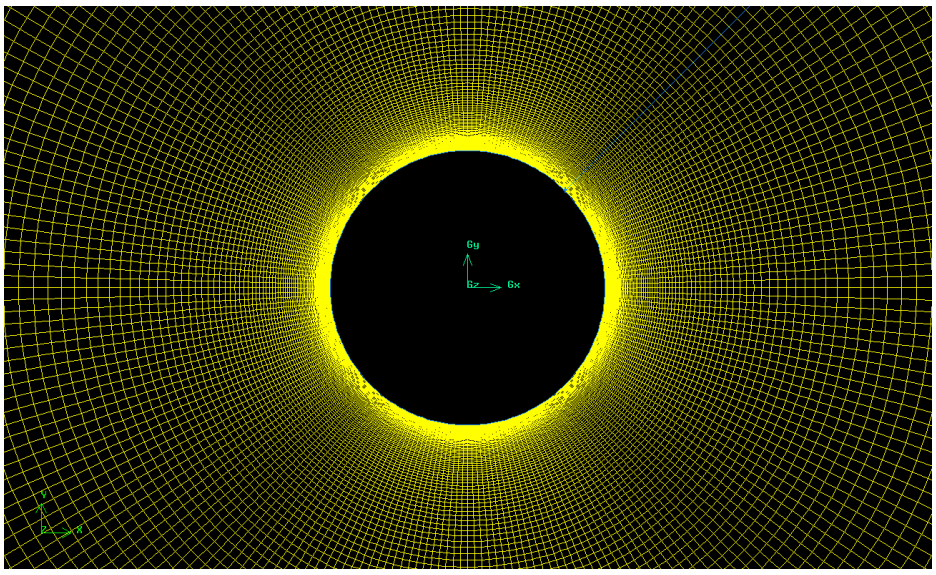

Figure 3.2. Close look of the structured medium grid (S2)

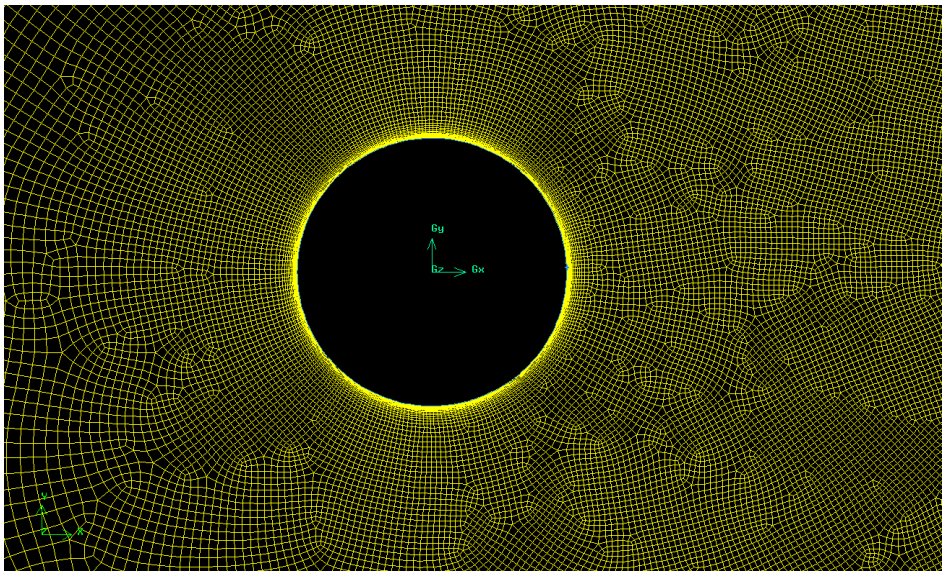

Figure 3.3. Close look of the unstructured grid

Table 3.2. Comparison with references for smooth stationary cylinder Re=1.4×10^5

Reference	Methods	Cd	Cl
Morgan and Visbal (2006)	2D-RANS	0.58	/
Morgan and Visbal (2006)	3D-hybrid RANS/ILES	0.52	/
Morgan and Visbal (2006)	3D-ILES	0.46	/
Travin et al. (1999)(Laminar Separation)	DES	0.87/1.08	0.1/0.29
Travin et al. (1999)(Turbulent Separation)	DES	0.57/0.65	0.06/0.1
Travin et al. (1999)(Turbulent Separation)	2D-RANS	0.56	/
Breuer (2000)	LES	0.38/1.45	/
Cantwell and Coles(1983)	experimental	1.237	/
Wieselsberger et al.(1921)	experimental	1.2	/
Roshko(1961)	experimental	0.62/0.74	/
Present Study	2D-RANS(coarse-S1)	0.4856	0.1338
Present Study	2D-RANS(medium-S2)	0.5428	0.1403
Present Study	2D-RANS(fine-S3)	0.5615	0.1432
Present Study	2D-RANS(Unstructured)	0.5423	0.122

The parameters describing the discretization of the three structured and the single unstructured grid are summarized in Table 3.1. The results of the root-mean square of the lift coefficient and drag coefficients for smooth stationary cylinder case Re=1.4×10^5 are shown in Table 3.2 together with both experimental and numerical results from the literature. In Table 3.2, the scatter in lift and drag coefficient from the previous studies is easily observed. The challenges in simulating smooth stationary cylinder flow in such high *Re* are well demonstrated in the sense that all numerical results listed have measureable differences when compared to experimental results. As for the results of current study, relatively small differences are present in the lift and drag coefficients from all three structured grids for this *Re* number. The unstructured grid with similar cell number of S2 also yields comparable results. Additional results for cases at different Reynolds numbers are summarized in Section 3.3.

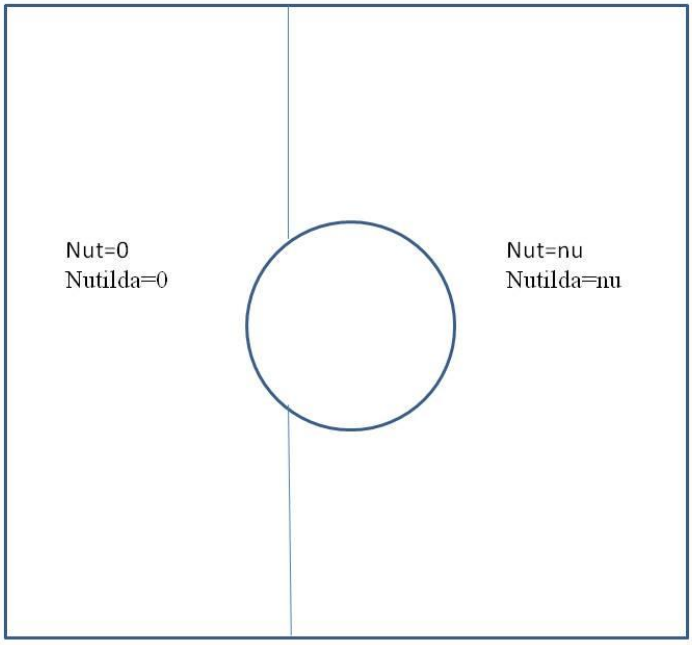

Figure 3.4. Regional setup A

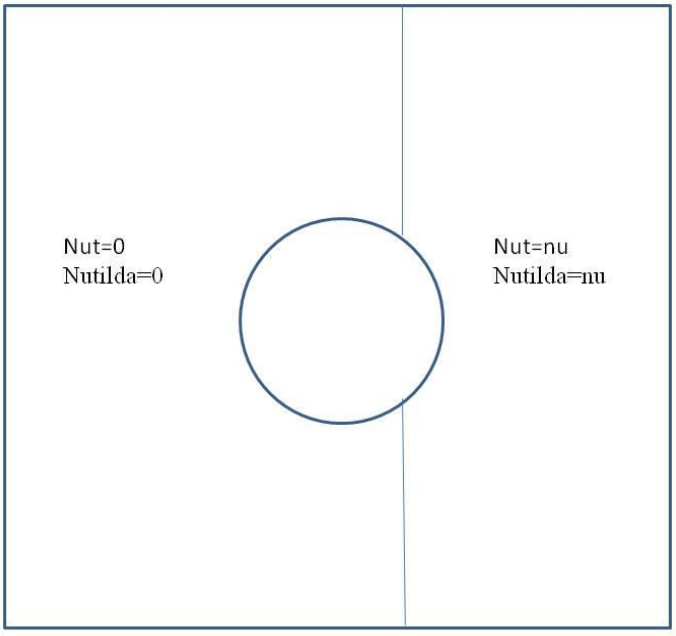

Figure 3.5. Regional setup B

3.2. Initial condition study for nut (ν_t) and nutilda ($\tilde{\nu}$)

A critical aspect of the flow over the circular cylinder is the laminar or turbulent character of the body boundary layer. The Spalart-Allmaras model used in this study is to model turbulence, and will not automatically produce a laminar flow result. There are two strategies to allow for a laminar body boundary layer. The first is to include a "trip" term in the model that will enforce the position of the transition. The second strategy uses a regional description of the initial and far-field boundary condition on the eddy viscosity to produce laminar or turbulence flow in the body boundary layer.

3.2.1. Regional setups

The basic idea of the regional setup to enforce laminar or turbulent flow in the body boundary layer relies on the fact that the production of eddy viscosity is proportional to the product of the eddy viscosity itself and the strain-rate of the mean flow. Thus, if the eddy-viscosity is zero, it will remain so even in the presence of large strain rate. To allow for laminar flow on the upstream portion of the cylinder, the initial condition and the upstream boundary condition on the eddy-viscosity variable is set to zero. In order for the model to be active in the wake, a non-zero value is used as an initial condition in a region downstream of the body.

For the laminar separation case, the regional dividing line between the regions of zero and non-zero eddy viscosity is chosen to be the line goes through the center of cylinder. In order to investigate the effect of the position of the dividing line on the simulation results, 3 different regional setups are simulated and the results of C_D and C_L are compared for cases corresponding to *Re*=10,000 and 50,000. Setup A (as shown in Figure 3.4) places the dividing line one half radius upstream of the center, setup B (as shown in Figure3.5) places the line one half radius downstream of the center of the cylinder. Setup C is the original case in which the line is located at the center of the cylinder.

In Figures 3.6 and 3.7, the time series of the lift and drag coefficient for each Reynolds number the three different regional setups are shown. It can be seen that after the flow becomes fully developed, the results for laminar separation cases based on the trip-less method are not sensitive to the initial regional setup.

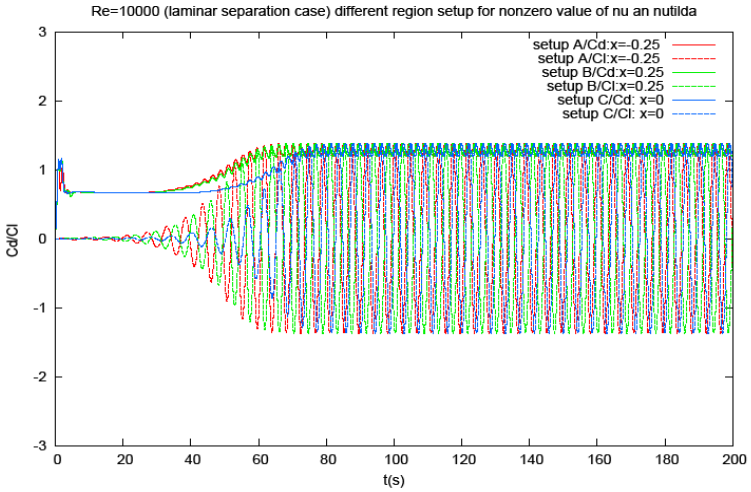

Figure 3.6. C_D and C_L comparison for 3 different regional setups (Re=10,000)

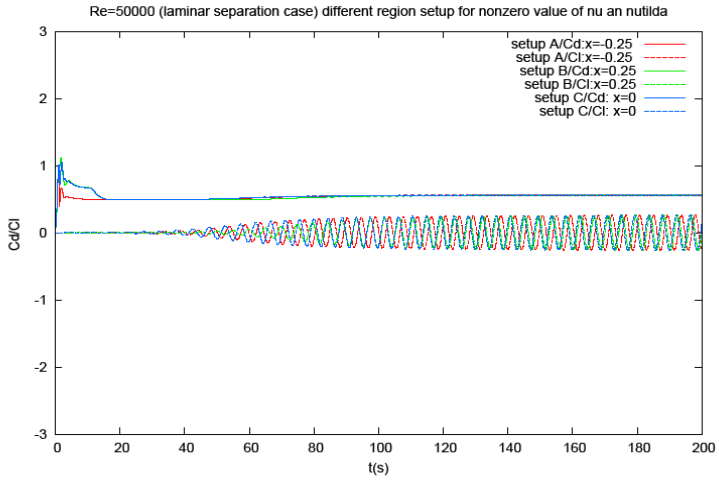

Figure 3.7. C_D and C_L comparison for 3 different regional setups (Re=50,000)

3.2.2. Effect of the initial values of ν_t and $\tilde{\nu}$

LS (laminar separation)

For the laminar separation case, the effect of initial values for eddy viscosity ν_t and modified eddy viscosity $\tilde{\nu}$ are studied to estimate the sensitivity on these values. In the paper by Travin (1999), the inflow eddy viscosity is zero, or much smaller than the

molecular viscosity. The front part of the boundary layer then also has zero eddy viscosity. Travin explained the procedure that "The recirculation region has non-zero eddy viscosity, and these finite values propagate upstream to the separation region. There, eddy viscosity diffuses into the separating shear layer. The vorticity in that layer causes rapid production of eddy viscosity, which then enters the recirculation region." Based on empirical value, the same value as molecular viscosity ν has been selected for the nonzero zone and 0.1 times ν as well as 0.5 times ν also have been used to make comparison for the lift and drag coefficient.

In Figures 3.8- 3.10, the time series of the lift and drag coefficient for the different initial value of the eddy viscosity is shown for each Reynolds number. After the flow becomes fully developed, the initial value of the eddy viscosity is seen to have very little influence on the force coefficient. Thus it is concluded that only a very small value is necessary to ensure that the eddy viscosity production is activated and that the eddy viscosity can propagate via diffusion into the shear layers.

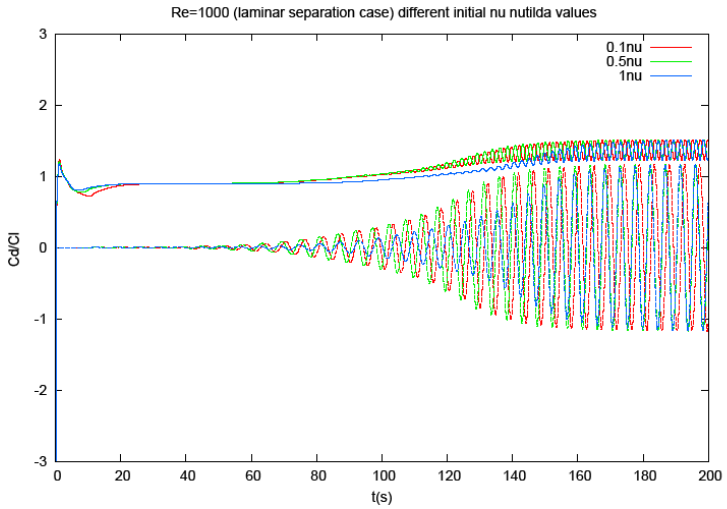

Figure 3.8. C_D and C_L comparison with 3 different initial values for $\tilde{\nu}$ and ν_t (*Re*=1,000/structured-coarse grid)

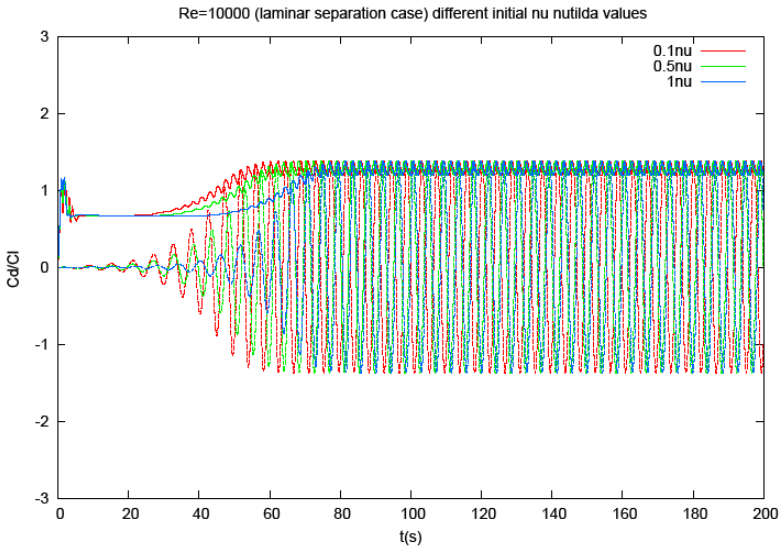

Figure 3.9. C_D and C_L comparison with 3 different initial values for $\tilde{\nu}$ and ν_t (*Re*=10,000/structured-medium grid)

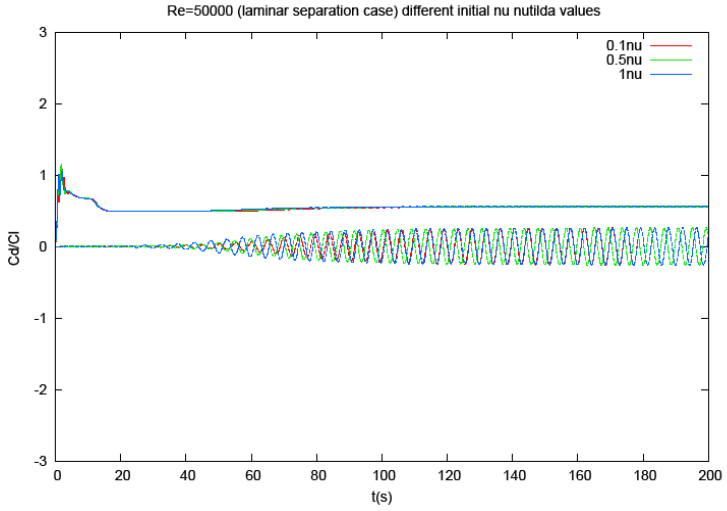

Figure 3.10. C_D and C_L comparison with 3 different initial values for $\tilde{\nu}$ and ν_t (*Re*=50,000/structured-medium grid)

TS (turbulence separation)

For the turbulent separation case, the model can provide fully turbulent results by setting the inflow value of eddy viscosity to a value that is about 5 times the molecular viscosity. The use of a large value of the eddy viscosity in the freestream allows the turbulence model simulate fully turbulent flow in regions that contain shear within simulation domain, including boundary layer. The value recommended by Travin (1999) is five times the molecular viscosity. In the study, investigations are performed using twice and ten times the molecular value, together with the recommended value of 5.

Time series of the force coefficeints are shown in Figures 3.11 and 3.12. In Figure 3.11, Reynolds number 5×10^5 has been simulated with 3 different initial values. The results for C_D and C_L do not vary much and the only obvious difference is time required to arrive to a fully developed state. The largest value of the freestream eddy velocity converges faster than the other two. This can be explained by the fact that this value is closer to the fully developed value. For Reynolds number 10^6 (see Figure 3.12), values of 5ν and 10ν converge to the same fully developed state, but for the 2ν case, it arrives to a different state.

From this study, the conclusion is made that, just as laminar separation case, for turbulent separation, different initial values also have little effect in varying the results as long as a sufficiently large value of the freestream eddy viscosity is provided. In this thesis, 5ν will be selected as the initial value for turbulence separation cases.

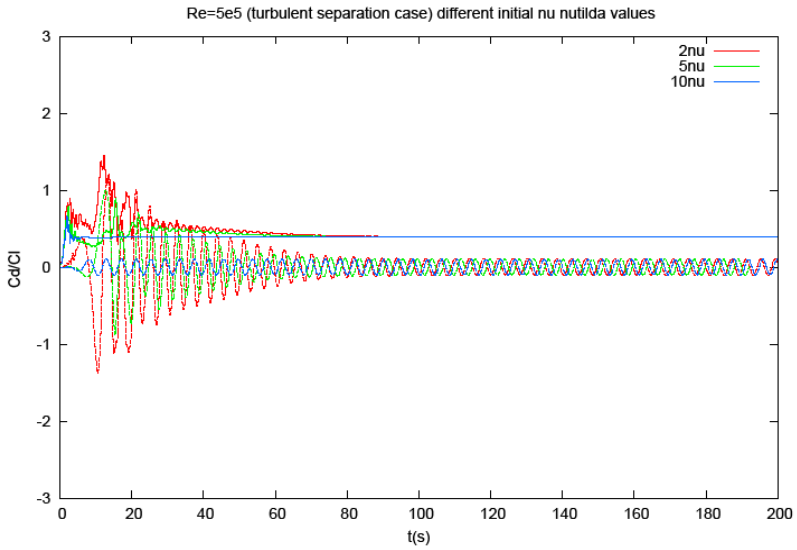

Figure 3.11. C_D **and** C_L **comparison with 3 different initial values for** $\tilde{\nu}$ **and** ν_t **(**Re**=5×10^5**/structured-medium grid)**

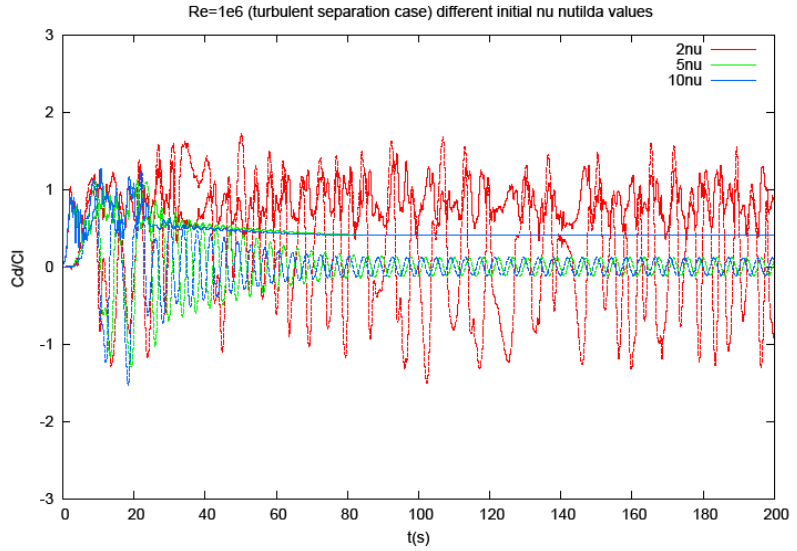

Figure 3.12. C_D **and** C_L **comparison with 3 different initial values for** $\tilde{\nu}$ **and** ν_t **(Re=10^6/structured-medium grid)**

3.2.3. Laminar separation vs. turbulent separation

In this section, the laminar separation case and turbulent separation case are compared for the Re=1.4×10^5which are in the transition range of cylinder flow. When the Reynolds number is below $\sim2\times10^5$, it is called the subcritical range. At this range of Reynolds numbers, the attached boundary layer is laminar, the separated shear layers are in the early stages of transition, and the wake is fully turbulent. The Reynolds number range from $\sim2\times10^5$ to $\sim3.5\times10^6$ is called the critical range. Based on drag coefficient distribution, Roshko (1961) subdivided this region into lower transition (Re=2.5×10^5 $\sim5\times10^5$) and upper transition (Re=1×10^6 $\sim3.5\times10^6$) regions. In this range, the boundary layer begins as laminar and subsequently separates with turbulent reattachment, a separation bubble, and finally turbulent boundary layer separation. The TS situation could be obtained experimentally by tripping the boundary layer well ahead of separation point. If this is done, the results for Reynolds number in the transitional region should have similar flow properties as those in supercritical region. This idea is tested numerically by using the laminar separation regional set-up and the turbulent separation set-up on the same Reynolds number. The times series of force coefficient is shown Figure 3.13. It can be seen that the almost identical and the tripped effects are not well captured. This is possibly due to the fact that the current two-dimensional numerical method has limitations in predicting the fully developed three-dimensional flow characters.

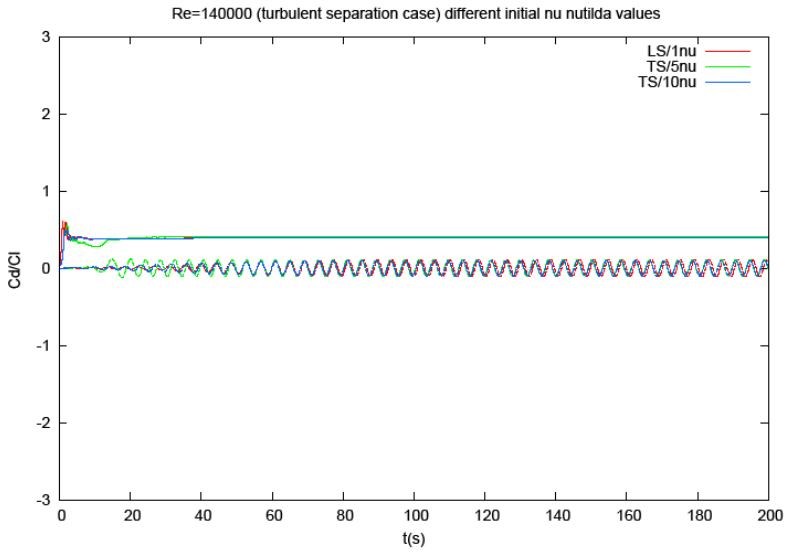

Figure 3.13. C_D and C_L comparison for LS and TS initial conditions (Re=1.4×10^5/structured-medium grid)

3.3. Results

Drag, lift coefficients and Strouhal number from 4 sets of grids are compared with literature results over a wide Reynolds number range from 1000 up to 10^6. LS is used for *Re* lower than and equal to 1.4×10^5, and TS initial condition is used for other cases. The numerical data are tabulated in Tables 3.3 and 3.4 for the results from the literature and from current numerical study, respectively. In Figure 3.14, drag coefficient results are presented. Experimental curve from Weiselsberger (1921) is plotted with a black broken line and other experimental results are plotted separately with black dots. Singh and Mittal (2005) conducted a series of simulations on a stationary cylinder for a wide range of Re (100~10^7) using a finite-element based method. Their 2D numerical results are listed separately from numerical data from other researchers (in blue dots) and presented in blue hollow squares. In comparison with experiments, 2D RANS over predicts the drag coefficients in the lower Re range (1,000~3×10^4) and yields earlier transition (drag crises) then the experimental results show. When Re is close to 5×10^4, the predictions for drag coefficients drop quickly and are lower than the experimental values. By tracking

the locations of mobile separation points and the motion of stagnation point for each *Re* case, the moving ranges of both separation points are found decrease rapidly from around 70 deg at $Re=2\times10^4$ (range is 80~150 deg), to around 10 deg (range is 85~95 deg) at $Re=5\times10^4$. The sharp drop of the lift occurs coincidently with the loss of mobility of separation points. It is possibly the incapability of capturing the separation-point motion that causes the early drag crises. The loss of correct tracking the mobility of separation points indicates the local flow properties are not well captured, therefore the integral properties of the cylinder the lift and the drag are no longer in good agreement with experiments. Although current numerical results have differences when compared with experiments, they are in the range covered by the other existing numerical simulations due to the wide scattering of the other numerical results. In comparison with results with Singh and Mittal (2005) who cover a relatively wide Reynolds number range solving 2D equations, the results from current study are in closer agreement with the experimental drag coefficients in the *Re* range from 1,000 to 2×10^4. When examining the results for the four sets of grids, the finest grid offers slightly better results in transition prediction, however at a cost of much more computational time required. Over all the C_D values generated by those grids with different resolutions are comparable. Therefore the grid density similar to medium grid is adopted for most of the simulations in this thesis. As for the lift and Strouhal number, fewer reference results can be found over such a broad range of Reynolds number. The empirical lift coefficient C_L from Nordberg (2001) is presented continuously in black line and other numerical and experimental results are presented by discrete blue or black dots in Figure 3.15. As is clearly shown in the plots, the lift is over predicted in the *Re* range lower than 2×10^4. After a sudden drop around *Re* $=5\times10^4$, the lift stays lower than 0.4 which is under predicted comparing with Nordberg's functions, but still comparable with other numerical results. As for the Strouhal number, it is the one of the best predicted quantities with comparison with experimental as well as other numerical solutions.

Table 3.3. C_D , C_L and St summary from the literature

	case	model	C_D	C_L	St
Re=1,000	Wanderley(2008)	2D-RANS(k-ε)	0.9600	0.2200	0.1930
	Herfjord(1995)	FEM	1.4700	1.4500	0.2340
	Rengel(1999)	FVM	1.6000	1.7000	0.2250
	Nordberg(2003)	exp	/	0.0800	0.2100
	Weiselsberger(1921)	exp	0.9900	/	/
Re=5,000	Shur(2005)	2D-URANS(SA)	1.68		
	Shur(2005)	3D-URANS	1.24/1.7		
	Shur(2005)	3D-DES	1.26		
	Cantwell and Coles(1983)	exp	1.24		
Re=10,000	Dong(2005)	DNS	1.11-1.208	0.448-0.574	0.195-0.209
	Weiselsberger(1921)	exp	1.1430	/	/
	Bishop and Hassan(1964)	exp	/	0.4630	0.2010
	Moeller andLeehey(1984)	exp	/	0.5320	/
	Gopalkrishnan(1993)	exp	1.1860	0.3840	0.1930
	West and Apelt(1993)	exp	/	0.4610	/
	Nordberg(2003)	exp	/	0.3940	0.2020
Re=50,000	Travin(1999)(Lam.Sep.)	DES	1.05/1.32	0.21/0.66	0.19/0.22
	Travin(1999)(Lam.Sep.)	2D-RANS	1.8	1.47	0.22
	Travin(1999)(Lam.Sep.)	2D-DES	1.77	1.39	0.14/0.20
Re= 140,000	Morgan(2006)	2D-RANS	0.58	/	0.31
	Morgan(2006)	hybrid RANS/ILES	0.52	/	0.29
	Morgan(2006)	ILES	0.46	/	0.23
	Travin(1999)(Lam.Sep.)	DES	0.87/1.08	0.1/0.29	0.21/0.23
	Travin(1999)(Turb.Sep.)	DES	0.57/0.65	0.06/0.1	0.28/0.31
	Travin(1999)(Turb.Sep.)	2D-RANS	0.56	/	/
	Breuer(2000)	LES	0.38/1.45	/	0.20/0.33
	Cantwell and Coles(1983)	exp	1.237		0.179
	Wieselsberger et al.(1923)	exp	1.2		0.2
	Roshko(1961)	exp	0.62/0.74		0.27
Re=10^6	Catalano(2003)	LES	0.3100	/	0.3500
	Catalano(2003)	URANS	0.3900	/	/
	Catalano(2003)	URANS	0.4000	/	0.3100
	Shih et al(1993)	exp	0.2400	/	0.2200
	Others(see Zdravkovich1997)	exp	0.17-0.4	/	0.18-0.5
	Published experimental	exp	0.21-0.63	0.03-0.15	0.18-0.5

Table 3.4. Summery of C_D , C_L and St results from different grids

	Re	C_D	C_L	St
structured-coarse	1,000	1.383	0.832	0.217
	3,900	1.555	1.091	0.228
	5,000	1.596	1.145	0.231
	10,000	1.690	1.278	0.234
	50,000	0.758	0.291	0.237
	140,000	0.486	0.134	0.249
structured-medium	1,000	1.373	0.819	0.216
	3,900	1.574	1.214	0.249
	5,000	1.604	1.164	0.231
	10,000	1.698	1.288	0.234
	50,000	0.738	0.231	0.232
	140,000	0.543	0.140	0.246
	500,000	0.524	0.098	0.235
	1,000,000	0.536	0.111	0.243
structured-fine	3,900	1.518	1.058	0.211
	5,000	1.524	1.067	0.219
	10,000	1.615	1.221	0.227
	30,000	1.680	1.331	0.221
	50,000	1.011	0.353	0.232
	100,000	0.612	0.175	0.242
	140,000	0.561	0.143	0.267
unstructured	1,000	1.373	0.819	0.216
	5,000	1.604	1.164	0.214
	10,000	1.698	1.288	0.234
	50,000	0.815	0.424	0.243
	140,000	0.542	0.122	0.246
	500,000	0.524	0.098	0.246
	1,000,000	0.536	0.110	0.243

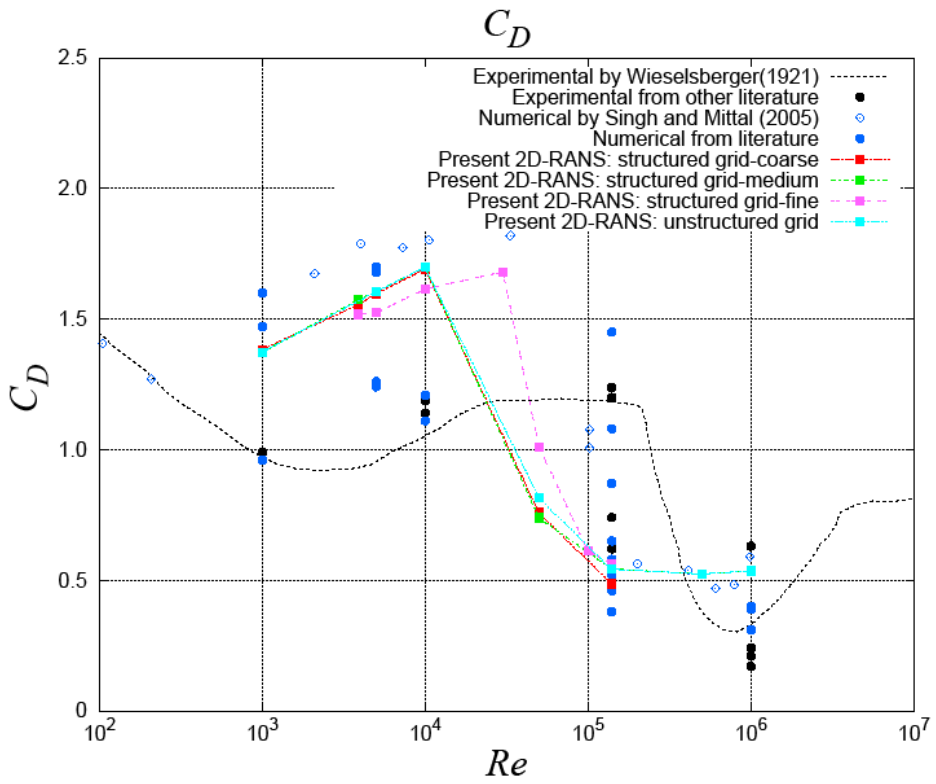

Figure 3.14. C_D **results from different grids in comparison with literature**

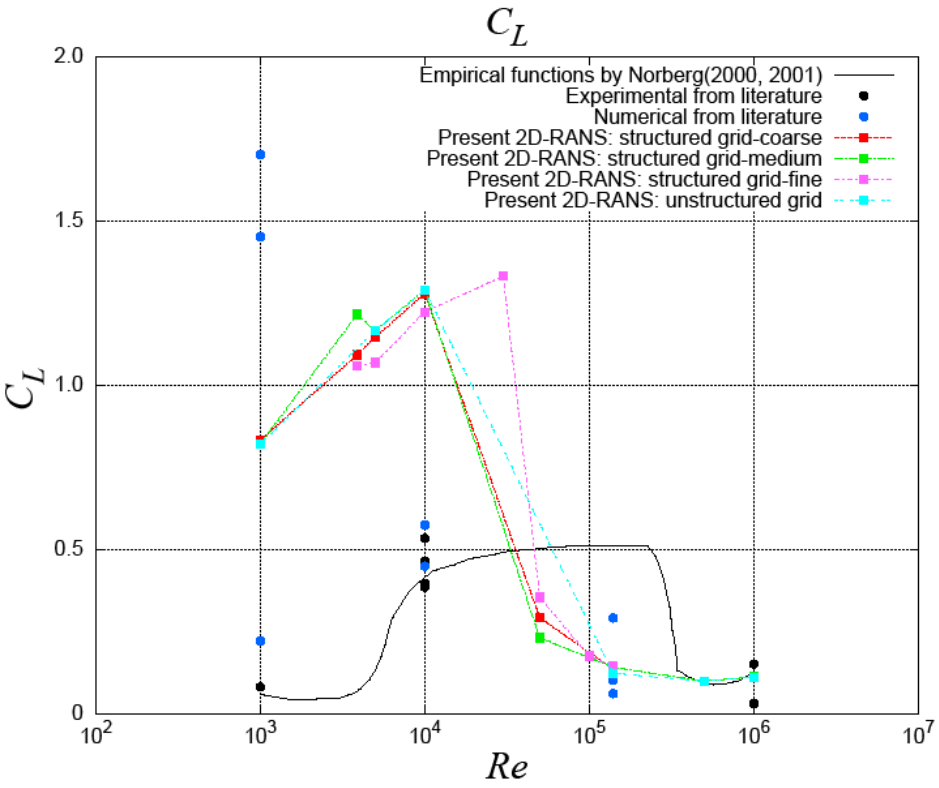

Figure 3.15. C_L **results from different grids in comparison with literature**

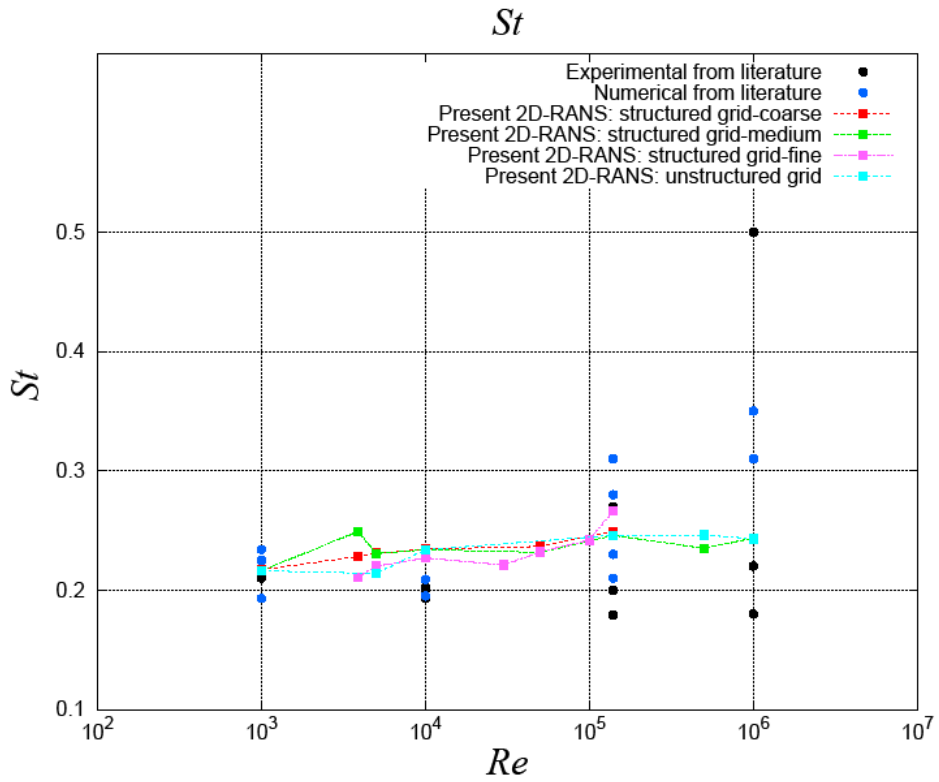

Figure 3.16. *St* results from different grids in comparison with literature

3.4. Conclusions

In this chapter, flow over a stationary circular cylinder problem has been studied using two dimensional RANS methods with Spalart-Allmaras turbulence model. The forces acting on the body and the Strouhal frequency are investigated over a series of *Re* cases ranging from 1,000~10^6.

The wall integration grids are adopted over this smooth stationary cylinder situation and the grid study has been conducted firstly with three steps in order to establish the baseline for grid requirements for this flow. The grid studies include the wall grid spacing investigation over a flat plate case, and grid density convergence study (including both structured and unstructured grid topologies). From the investigations, the conclusion is confirmed that in order to resolve the near wall flow structure correctly, in combination with the non-slip wall boundary condition, the first grid spacing must be such that the wall unit $y+$ is near one. In addition, three grids are used to clarify the total cell number that is needed in order to achieve grid number independent solutions. It turns out the dependency of the solution on the grid resolution is weak as long as the total cell number

is above ~3×10^4. This conclusion applies only under the condition that *Re* is below 1.4×10^5 since the coarse grid (S1) is only tested for the *Re* range up to 1.4×10^5, where the results have negligible differences with those from higher resolution grids. The results generated using the unstructured grid show that current RANS solver can handle unstructured grid well and can yield comparable results if property wall spacing and cell number are given.

Studies that investigate the importance of initial conditions are conducted in order to ensure proper initial conditions are applied. Following Shur (1996) and Travin (1999), a "trip-less" initial condition is shown to be effective to produce reasonable solutions in subcritical flow regime for laminar separation cases. Different regional setups are tested for laminar separation case, and various initial values that are within the vicinity of the recommended value are investigated for both laminar and turbulent separation cases. The results confirmed that the results are not sensitive to the regional setups, or to the initial turbulence level, as long as the value is not too far from the recommended value. For LS, the initial eddy viscosity in the non-zero zone could be 0.1~1 times molecular viscosity. While for TS case, the value of more than 5 times the amount of molecular viscosity is appropriate for entire domain.

The studies with 4 different grids show the capability of 2D RANS in deriving comparable results with other numerical simulations, however comparing with the experiments, the obvious differences still exist and demonstrate that improvements are needed for completely solving this challenging physical problem. Slight improvement in accuracy for the flow over a circular cylinder flow is possibly using more complex turbulence models, but all of these require much greater computational resources and are not practical and applicable from design point of view.

Chapter 4

CYLINDER IN VIV

4.1. Introduction

The first prototype for VIVACE module uses a smooth cylinder. A large number of experiments have been conducted on a smooth cylinder in VIV in the MRELab (Raghavan (2007) and Lee (2010)). In this chapter an elastically mounted smooth cylinder undergoing VIV is investigated by RANS numerical tool at two Reynolds number ranges. The aim is to establish the capability of numerical tool for simulating the VIVACE system and to assess the effective working range for this tool. From the results, the capabilities and the limitations of current approach are identified and discussed. Additional properties of the flow such as vortex pattern, flow visualization, lift forcing and the phase angle are also investigated.

In this chapter, the smooth cylinder is first investigated in the low *Re* range (3,000~12,000) and the results are compared with the experiments of Williamsom and his colleagues and students (Khalak, Williamson 1996, 1999), as well other numerical results from Guilmineau and Queutey (2004). Good agreement between the current numerical study and the experiments manifest the capability of 2D RANS as a research and design tool for cylinder flow in VIV in a lower *Re* range. As *Re* increases up to 30,000~80,000 (which is the TrSL3 regime), three dimensional eddies in the shear layer become dominant, and the agreement is not as strong with experiments in terms of the amplitude of motion and other properties that are well predicted when *Re* is lower, such as the branch coverage.

4.2. Low *Re*'s simulation results (3,000≤*Re*≤12,000)

In this section, the experiment from Khalak and Williamson (1996) is select for comparison. An elastically mounted rigid cylinder undergoing vortex-induced excitation is studied. The experiments of Williamson use a very low mass-damping ratio with respect to the values used in the VIVACE group. Comparison is also made with the classical studies from Feng (1968) and Brika (1993), which were conducted in air and also with relatively very low mass-damping ratio. Values of 0.36 and 0.41 were used in Feng's and Brika's work, and the mass-damping parameter m*ζ used in Khalak and Williamson's is 0.013.

Table 4.1. Definition of dimensionless and dimensional variables

A^*	A/D	Amplitude ratio
m_d	$\frac{\pi}{4}\rho D^2 L$	The displaced fluid mass
m_a	$C_a m_d$	Added mass
m_o		Oscillating system mass
m^*	$m_o/(m_d)$	Mass ratio
f_{osc}		Oscillating frequency of cylinder
$f_{n,water}$	$\frac{1}{2\pi}\sqrt{\frac{K}{(m+m_a)}}$	System natural frequency in water
$f_{n,air}$	$\frac{1}{2\pi}\sqrt{\frac{K}{m}}$	System natural frequency in air
$U_{r,air}$	$\frac{U}{f_{n,air}D}$	Reduced velocity based on natural frequency in air
$U_{r,water}$	$\frac{U}{f_{n,water}D}$	Reduced velocity based on natural frequency in water
ϕ		Phase angle by which lift leads the displacement

Table 4.2. Experimental system properties

Mass ratio	m^*	2.4
Damping ratio	ζ	0.0054
Mass-damping parameter	$m^* \zeta$	0.013
Diameter of circular cylinder	D [inch]	1.5
Length of cylinder	L [inch]	15
Natural frequency in air	$f_{n,air}$ [Hz]	0.7846

The numerical simulations use the identical values of the system parameters as reported in the experimental references (see Table 4.2). The simulations are conducted on the medium structured grid with 30D×30D domain size. The cylinder body is set free from a neutral position with zero initial velocity, although this condition is different from what is used in the experiments. In Williamson's paper, they measure the oscillation amplitude while the flow speed is slowly increasing, which means the initial displacements and velocities were not zero for any given Reynolds number.

Table 4.3. Run cases summary

Re	***U*(m/s)**	$U_{r,air}$	$U_{r,water}$
3000	0.0897	3.00	3.57
3800	0.1136	3.80	4.52
4000	0.1196	4.00	4.76
4500	0.1345	4.50	5.36
4800	0.1435	4.80	5.71
5000	0.1495	5.00	5.95
5200	0.1554	5.20	6.19
5500	0.1644	5.50	6.55
6000	0.1794	6.00	7.14
7000	0.2092	7.00	8.33
7860	0.2350	7.86	9.36
8000	0.2391	8.00	9.52
9000	0.2690	9.00	10.71
10000	0.2989	10.00	11.90
10500	0.3139	10.50	12.50
12000	0.3587	12.00	14.28

A series of simulations (see Table 4.3) are performed for validating the ability of RANS to predict hydrodynamic loads and further the responses for spring-mounted smooth cylinder undergoing vortex-induced vibration. The classical experiments from

Khalak and Williamson (1996, 1999) are selected for validation. The comparison is also conducted between present work and the numerical study from Guilmineau and Queutey (2004) for the lift and drag coefficients, who also simulate the same problem using 2D RANS.

4.2.1. Amplitude ratio (A- Re)*

Figure 4.1 shows the comparison between the present simulation and the experimental measurements. The data corresponding to the measurements of Khalak and Williamson shows three branches, namely, the initial branch, the upper branch and the lower branch. The amplitude ratio data from the RANS simulations follows the same trend as in the experiments, but the maximum amplitude does not as large as the experimental value, and RANS simulations does not predict the upper branch properly. This can be explained partly because the "at rest" initial condition is used here, while the experiment Khalak and Williamson were use and "increasing velocity" initial condition for those cases. This same issue has been documented by Guilmineau (Guilmineau and Queutey 2004). Guilmineau et al. used "from rest" and "increasing velocity" initial conditions in simulating the same problem. Although their results from "increasing velocity" conditions do not match the upper branch entirely, the amplitude ratio goes up to nearly unity for a narrow band of reduced velocity, and agrees well with the maximum value in experimental results. However, their results with "from rest" initial condition show that only the lower branch is well predicted and no upper branch value is detectable.

The lowest value of Reynolds number simulated is 300 ($U_{r,air}$=3, $U_{r,water}$ =3.57). The amplitude ratio is approximately is 0.4 and is relatively high with respect to the experiment data. The amplitude increases with increasing Reynolds number. At Re=4000 ($U_{r,air}$=4, $U_{r,water}$ =4.76), the amplitude of oscillation rapidly increases to a value of 0.82, which is the maximum amplitude along the curve. The increase at around Re=4000 agrees well with the transition to the upper branch in the experiment. For Reynolds number that is greater than that for the value in which the amplitude of motion is maximum, the amplitude decreases gradually with further increase in Reynolds number. As shown in Figure 4.1, in the range from Re=6000 ($U_{r,air}$=6, $U_{r,water}$ =7.14) to Re=10500 ($U_{r,air}$=10.5, $U_{r,water}$ =12.5), the RANS results follow the lower branch that is observed in

the experiments and also have an accurate prediction of the Reynolds number in which desynchronization occurs.

4.2.2. Oscillation frequency ratio (f_o / $f_{n,water}$ - Re)

In Figure 4.2, the frequency ratio f_o / $f_{n,water}$ is plotted as a function of Reynolds number. From Re=3000 ($U_{r,air}$=3, $U_{r,water}$ =3.57) to Re=4000 ($U_{r,air}$=4, $U_{r,water}$ =4.76), frequency ratio is relatively low and below 1, which means in this range the oscillating frequency is lower than the structure natural frequency. In the range 3000<Re<5800, comparing with values after Re=6000 ($U_{r,air}$=6, $U_{r,water}$ =7.14), the curve shows the obvious increasing trend as velocity increases. After Re=6000, frequency ratio stabilizes around 1.35~1.45 and the curve shows a nearly flat slope. As the Reynolds number reaches 12000, the frequency ratio jumps up to 2.42. This sudden increase is accompanied with the rapid drop of oscillating amplitude, and illustrates the end of synchronization range. It is important to note that when in the lower velocity range Re<4500 ($U_{r,air}$<4.5, $U_{r,water}$<5.36) some reduced velocity cases show two or more major oscillating frequencies in the simulation results. This occurs right before the mode switch from the initial branch to the upper branch in the experiment. Interestingly, as observed by Khalak and Williamson (1999), the quasi-periodic and periodic sub-branches are also well captured in the initial branch of current study. At Re=3000, the oscillation amplitude spectra (Figure 4.3 (a)) show distinct two peaks. One is corresponding to the structure natural frequency in water, which gives the frequency ratio near 1, while the other one is the vortex shedding frequency of stationary cylinder (Strouhal frequency). As the velocity goes up, the curve switches from the quasi-periodic sub-branch to the periodic sub-branch (see Figure 4.3 (b)). This also agrees with experiments from Khalak and Williamson (1999). This is easily observed in the FFT spectral analysis of the amplitude time series. At Re=3000, there are two major frequencies, while as the Reynolds number increases to 3800, only one prevailing frequency exits in the response amplitude.

4.2.3. Mode transition and vortex structure

Although the upper branch is not well captured from the amplitude point of view with the current RANS simulation, some other results are still very encouraging in the

sense that the oscillating frequency agrees well with the experiments, and also the branch transitions are correctly predicted (initial branch→upper branch, upper branch→lower branch). The first transition from initial branch to upper branch occurs around Re=4000 ($U_{r,air}$=4, $U_{r,water}$=4.76) , and it features a sudden change in the amplitude of oscillation. There is also an obvious vortex pattern switch from the 2S to 2P-mode associated with this branch change. Here 2P and 2S indicate two single and two pairs of vortices shed per cycle, respectively. Figures 4.4 (a) and (b) show contours of vorticity for two cases corresponding to Re=3800 and 4000, and the 2S and quasi-2P modes can be observed. Two vortices are clearly shown in the first vorticity plot, while the second shows a quite different pattern which is a "quasi-2P" in the sense that there are two pairs of vortices per cycle. In Figure 4.4 (b), each pair of vortices is of different strength so this mode is labeled "quasi-2P" since it is transitional between 2S and 2P. This "quasi-2P" mode lasts during the upper branch range until the beginning of the lower branch, where 2P (Figure 4.4 (c)) is clearly established. During the transitional regime from the upper to the lower branch, the phase angle also shifts between 0 and 180 degrees indicating the displacement is in phase or out phase with lift. When the Reynolds number reaches 5200 ($U_{r,air}$=5.2, $U_{r,water}$=6.19), the lift is almost completely out of phase with the displacement throughout the time trace, which is the signal of the end of the upper branch. Finally, at a Reynolds number of 5500 ($U_{r,air}$=6, $U_{r,water}$=7.14), the system stabilizes on the lower branch with the 2P vortex pattern. There is another difference between these two branches that is clear in the current analysis, related to the uniformity of amplitude of oscillation. In the upper branch (Re =4200~5200) (see Figure 4.5 (a)) the amplitude is relatively non-uniform, while from Re =5500 to the end of synchronization zone, the amplitude is highly uniform (see Figure 4.5 (b)) and associated with a 2P vortex mode.

4.2.4. Lift coefficient C_L and drag coefficient C_D

In Figure 4.6, the lift and drag coefficients are compared with the results from Guilmineau (Guilmineau and Queutey 2004) for each of the two initial conditions. The maximum lift coefficient curve from present study agrees well with Guilmineau overall, but over predicts the lift coefficient at the lower Reynolds number near 3000. In comparing with the mean drag coefficient corresponding to Guilmineau's results for the

"from rest" initial condition, the values from present study are relatively higher, but within the range covered by the two curves from "increasing velocity" and "from rest".

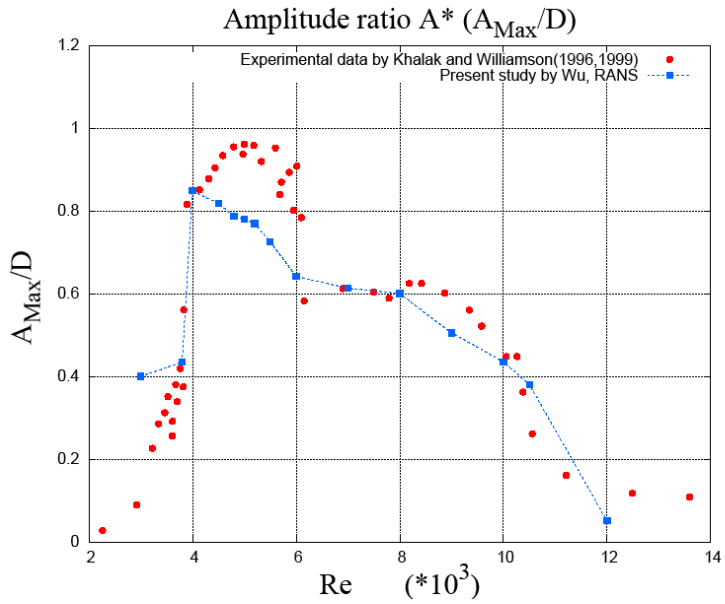

Figure 4.1. Amplitude ratio *A (*A/D*) plot (*m*ζ*=0.013, *m**=2.4) comparing with Khalak and Williamson (1996)**

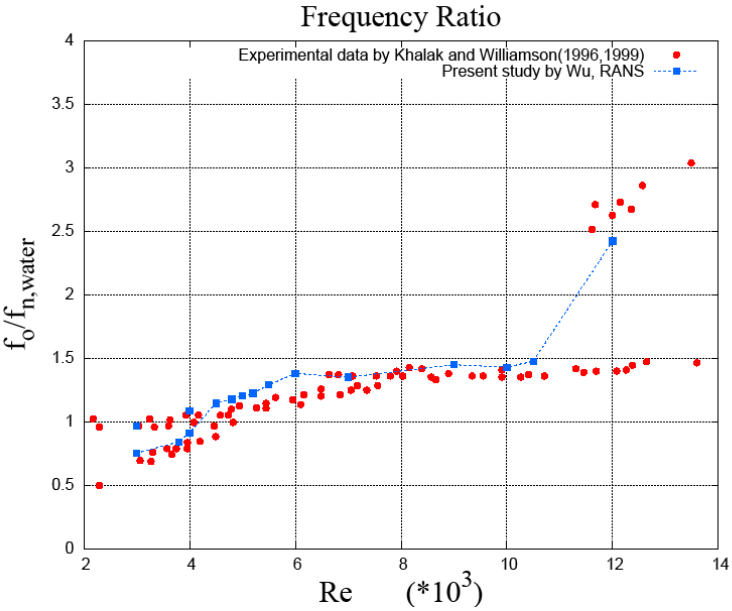

Figure 4.2. Frequency ratio $f_o/f_{n,water}$ vs. $U_{r,air}$ (*m*ζ*=0.013, *m=2.4) comparing with experimental data from Khalak and Williamson(1999)**

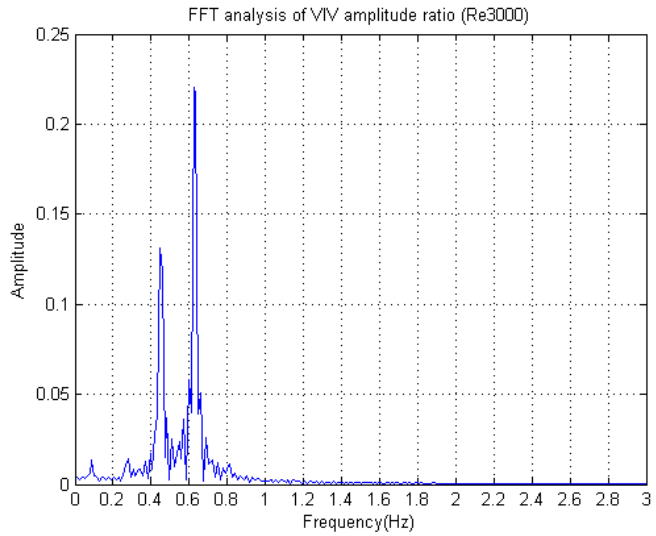

(a)

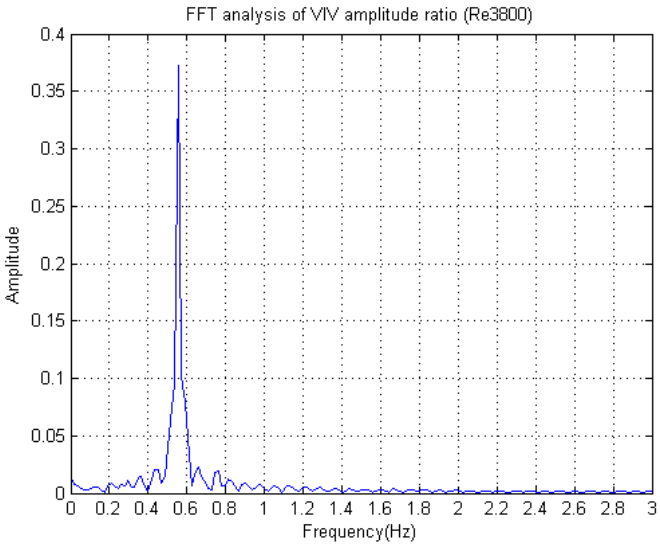

(b)

Figure 4.3. (a) Double-peaked spectra of oscillation amplitude *Re*=3000 ($U_{r,air}$=3, $U_{r,water}$ =3.57) in Quasi-periodic sub-branch; (b)Single-peaked spectra of oscillation amplitude Re=3800 ($U_{r,air}$=3.8, $U_{r,water}$ =4.52) in periodic sub-branch

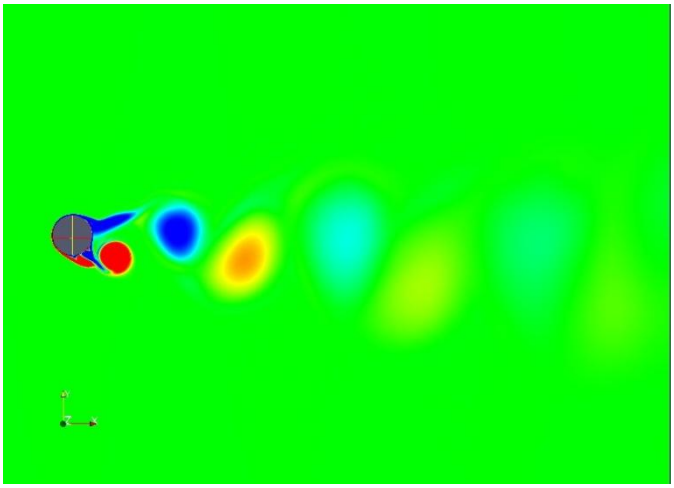

(a) 2S mode for initial branch Re=3,800 ($U_{r,air}$=3.8, $U_{r,water}$ =4.52)

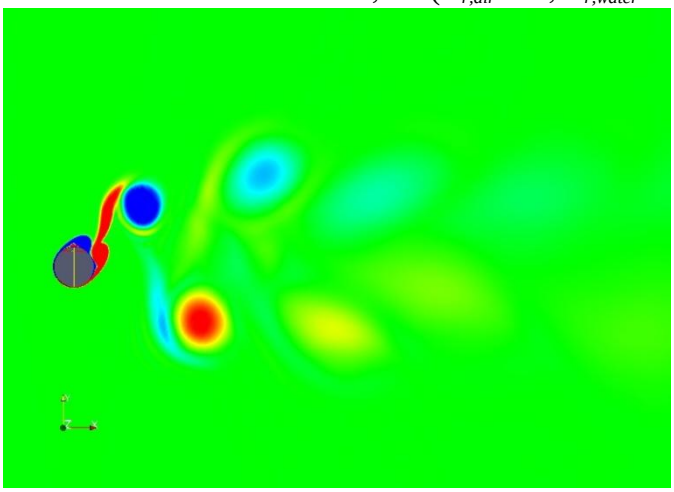

(b) Quasi-2P mode for upper branch Re=4,000 ($U_{r,air}$=4, $U_{r,water}$ =4.76)

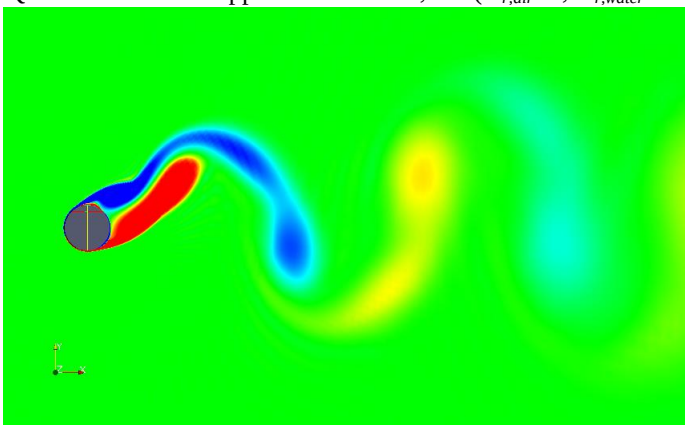

(c) 2P mode for lower branch Re=8,000 ($U_{r,air}$=8, $U_{r,water}$ =9.52)

Figure 4.4. Different vortex patterns for smooth cylinder in VIV ($m^*\zeta$=0.013, m^*=2.4)

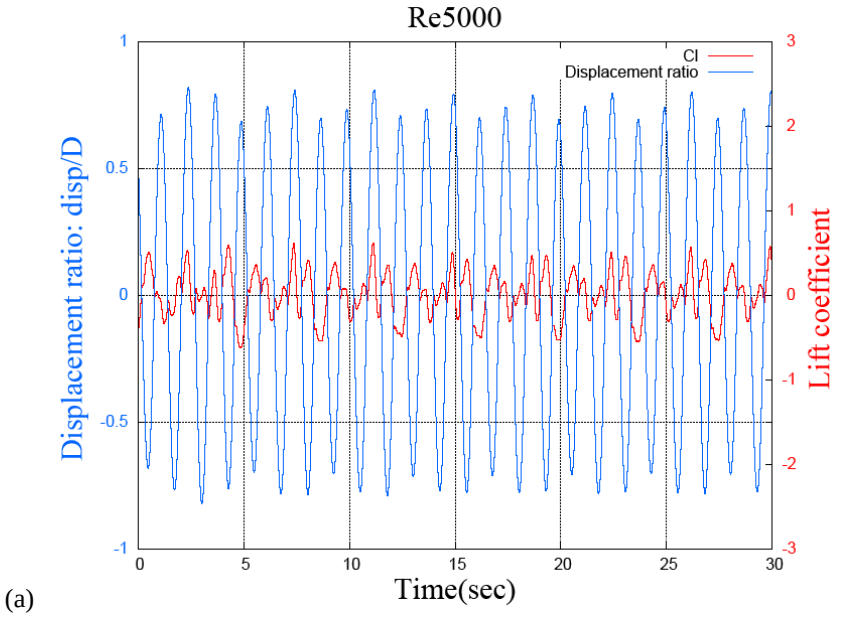

(a)

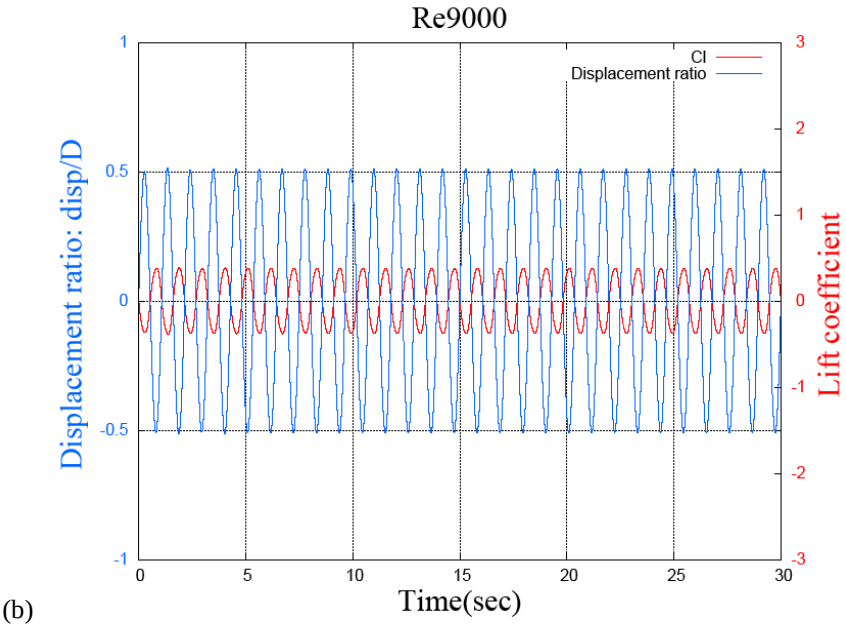

(b)

Figure 4.5. Time traces of displacement and lift coefficient (a). Re=5000 ($U_{r,air}$=5, $U_{r,water}$ =5.95) and (b). Re=9000 ($U_{r,air}$=9, $U_{r,water}$ =10.71)

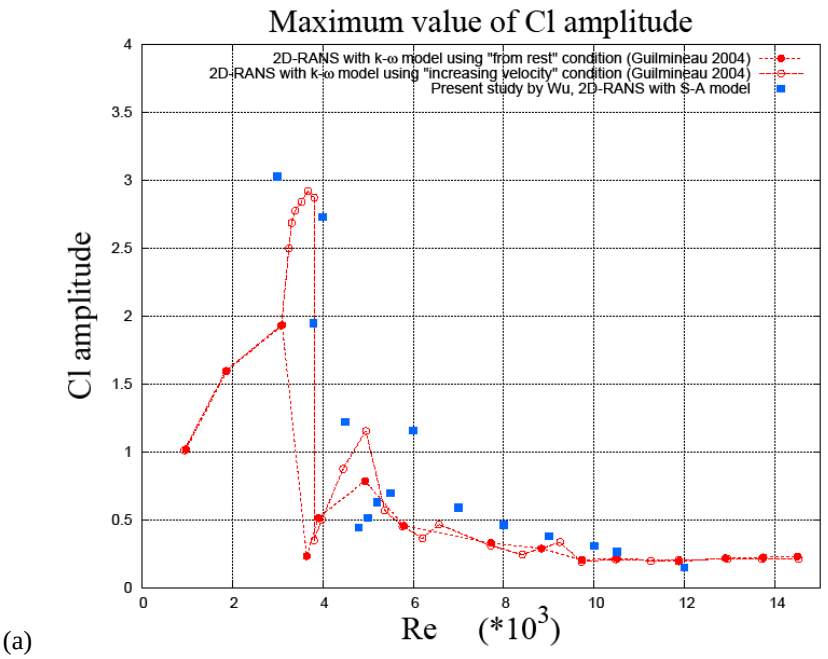

(a)

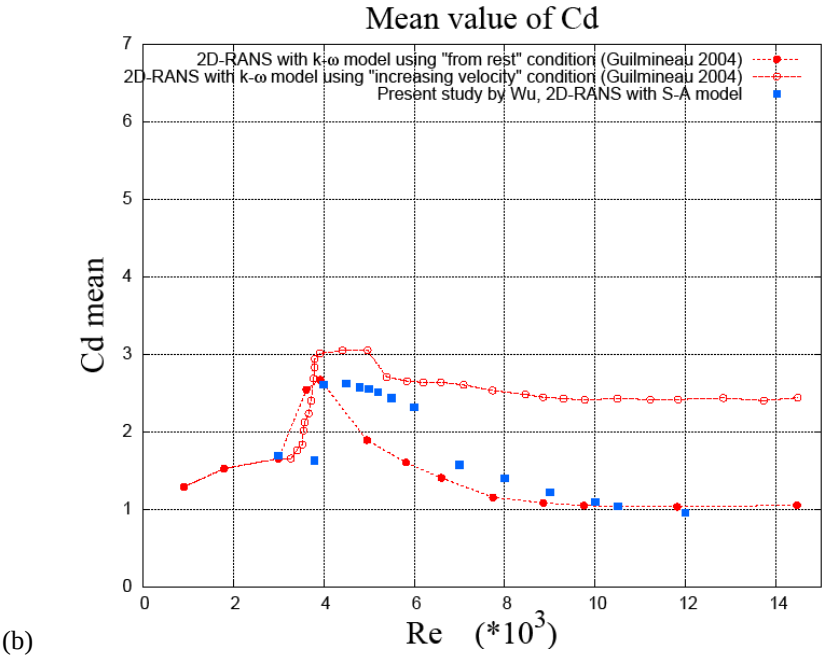

(b)

Figure 4.6. Forces comparison between current study and results from Guilmineau and Queutey (2004) (2D-RANS with *k-w*): (a) Maximum lift coefficient, (b) Mean drag coefficient

4.3. High *Re*'s simulation results (25,000≤*Re*≤80,000)

The VIVACE group is interested in much higher Reynolds numbers that belong to the TrSL3 regime (*Re* from 20k-40k to 100k-200k) and in the future values high enough to fall in the TrBL0 regime (*Re* from 100k-200k to 300k-340k) (Zdravkovich, 1997) may

be used. One of the remarkable events that marks the beginning of the TrSL3 regime is the disappearance of the dominantly two dimensional eddies in free shear layer (Zdravkovich, 1997). Also, the near wake structure becomes highly three-dimensional. Because of the temporal and spatial unsteadiness in the shear layer, it can be expected that the flow properties at different spanwise locations are no longer in phase with each other and the spanwise correlation breaks down, this is in sharp contrast with lower Reynolds number flow regimes. Shimizu and Kawamura (1972) studied the relation between the spanwise correlation length and Reynolds number. It turns out the correlation length for cylinder flow decreases rapidly after $Re=10^4$ (Zdravkovich, 1997, Shimizu and Kawamura, 1972), and becomes even shorter in TrSL3 regime. All these facts make the cylinder flow in this regime a very challenging problem for the two-dimensional RANS approach adopted here.

In this section, the capability of current 2D-RANS method is investigated in predicting the elastically mounted smooth cylinder undergoing VIV. The Reynolds number range is from 25,000 to 80,000 and the simulation results are compared with the experiments of VIVACE group conducted by Lee (Lee, 2010). Two cases are simulated with stiffness K=400N/m and harness damping ratio ζ_{harn}=0 and 0.04. The complete list of system parameters is shown in Table 4.4.

Table 4.4. Experimental system properties (Smooth cylinder in High *Re* flow regime)

Mass ratio	m^*	1.89
External damping ratio for energy harnessing	ζ_{harn}	0; 0.04
Diameter of circular cylinder	D [m]	0.0899
Total mass of oscillation	M [kg]	10.94
Spring constant	K [N/m]	400
Structural damping	$C_{structure}$ [Ns/m]	4.4
Natural frequency in water	$f_{n,water}$ [Hz]	0.778

For the smooth cylinder in VIV experiments conducted by Lee, the principal results are the amplitude and frequency ratio. In Figure 4.7 and 4.8, the maximum amplitude ratio and frequency ratio for the case with K=400N/m and harness damping ratio ζ_{harn}=0 are compared with experiments. Within the test range of experiments, the three branches are shown in the amplitude curve. It is noted that the character of the three

branches shows some differences with that from the experiments of Khalak and Williamson. In the amplitude curve from VIVACE MRELab, a shorter range of initial branch is presented with a greater rate of increase. The upper branch covers relatively broader range with a maximum value at around 1.4 times the diameter, which is greater than the maximum value found in Khalak's experiments. The RANS results are not capturing the maximum amplitude values in this case just as they did not in the lower *Re* number range. In addition, the ranges of Reynolds number corresponding to the different branches are not in strong agreement with the experiments. The synchronization starts much earlier, and same tendency is shown for the upper and the lower branches. From the simulations, the upper branch appears in the *Re*=~30,000, where the lift is well in phase with displacement. While from *Re*=~40,000, the phase angle starts to increase and accordingly the displacement affected in that the amplitude decreases. Similar results are observed in Figure 4.9 for the case with ζ_{harn}=0.04, and even larger differences in amplitude are seen.

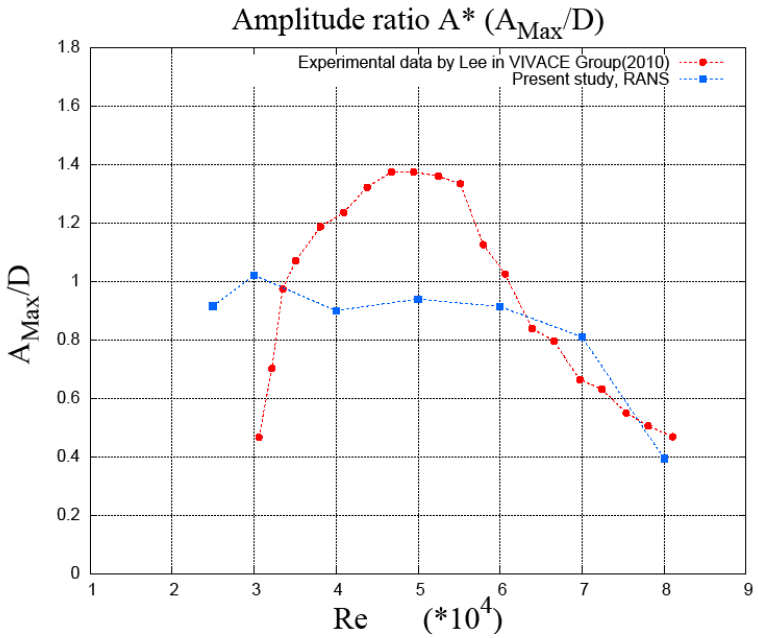

Figure 4.7. Maximum amplitude ratio comparison between present 2D-RANS and experiments by Lee (2010) for *K*=400N/m, ζ_{harn} =0

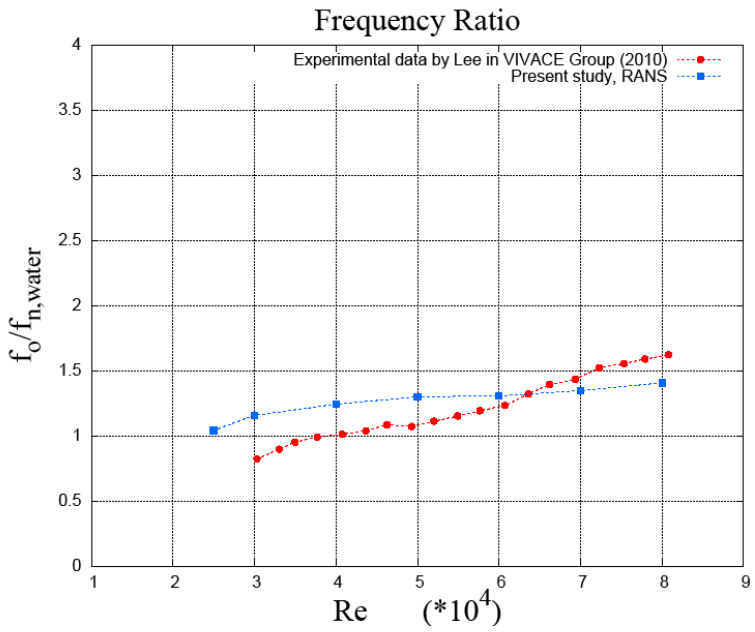

Figure 4.8. Frequency amplitude ratio comparison between present 2D-RANS and experiments by Lee (2010) for *K*=400N/m, ζ_{harn} =0

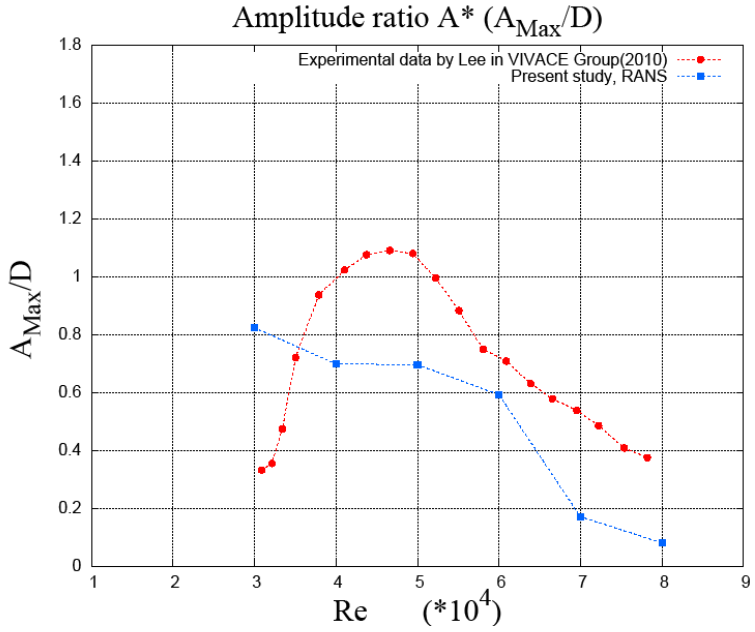

Figure 4.9. Maximum amplitude ratio comparison between present 2D-RANS and experiments by Lee (2010) for *K*=400N/m, ζ_{harn} =0.04

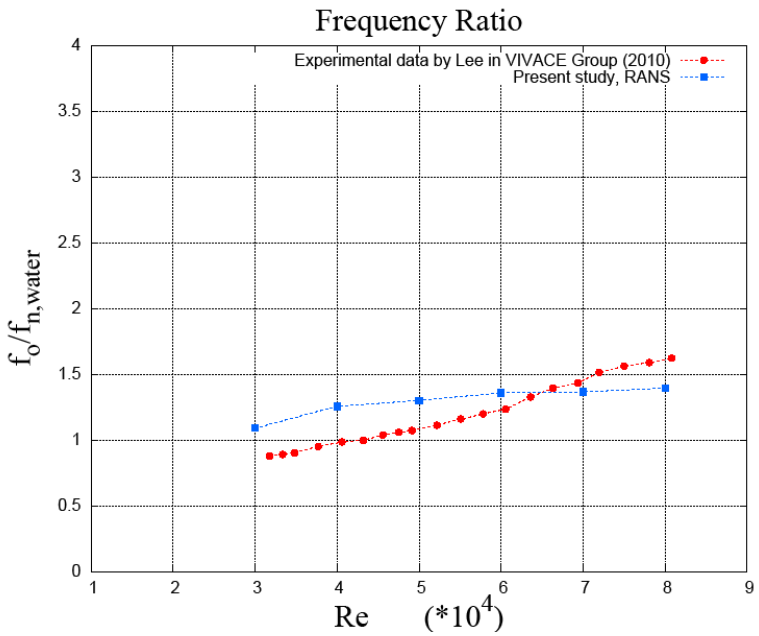

Figure 4.10. Frequency amplitude ratio comparison between present 2D-RANS and experiments by Lee (2010) for K=400N/m, ζ_{harn} =0.04

4.4. Conclusions

In this chapter, the smooth cylinder in VIV problem is investigated with the 2D-RANS numerical tool for two ranges of Reynolds number. The relatively lower Reynolds number range (3,000~12,000) is studied first with a "from rest" initial condition, and results of maximum amplitude ratio, frequency ratio and vortex pattern are compared with experimental data from Khalak and Williamson. The transitional regime between different branches is also discussed. Although the upper branch of the amplitude is not well captured by numerical simulation, the amplitude in the initial and lower branch strongly agrees with experimental measurement. In addition, the frequency of oscillation agrees well with the experiments, and the Reynolds number of the transition between different branches is well captured.

Two series of simulations are conducted with different damping levels for higher Reynolds number cases. With respect to the the simulation results for lower range, the numerical results are not satisfactory in predicting amplitude of motion. Premature synchronization is shown in the simulation and the maximum value of amplitude occurs at Re=~25,000, instead of in the Reynolds number range of the upper branch (40,000 <

Re < 55,000). The coverage of different branches is not well captured. The values of the frequency of oscillation are within the range covered by experiments, but the curve from the simulations shows slower rate of increase. The differences between numerical and experimental results is attributed primarily to the the highly three dimensional nature of the flow in TrSL3 regime. Inherently, 2D-RANS is not capable to well capture flow properties with strong three dimensional effects, and therefore 2D-RANS is better to be utilized within the Re range lower than TrSL3 regime for smooth cylinder in VIV case, where three dimensional transition eddies start to prevail in the shear layer.

Chapter 5

CYLINDER WITH ROUGHNESS IN FIM

5.1. Introduction

Recent developments in the Marine Renewable Energy Laboratory (MRELab) at the University of Michigan, on passive turbulence control (PTC) of elastically mounted rigid circular-cylinders, have improved dramatically the hydrodynamics of hydrokinetic energy harnessing using flow-induced motions (FIM). The VIVACE (Vortex Induced Vibration for Aquatic Clean Energy) converter is a hydrokinetic power generating device invented by Bernitsas and Raghavan (2005) and further developed by Bernitsas and his research group in the Marine Renewable Energy Lab (MRELab) since then. It is designed to harnesses hydrokinetic energy from ocean and river currents as slow as 2 knots. The single VIVACE module can be modeled as a circular cylinder mounted on springs with a PTO (Power Take-Off) system. With entirely opposite objective to the other engineering problems, which are mainly focused on reducing vortex induced vibration effects, the goal of the VIVACE team is to enhance the oscillating amplitude and maximize the hydrokinetic energy converted to mechanical energy. By introducing Passive Turbulence Control (PTC), cylinder FIM was enhanced to reach back-to-back VIV and galloping. Amplitude-to-diameter ratio (A/D) exceeds 3 and synchronization range is more than double that of VIV of a smooth cylinder. No end to the synchronization range and A/D was reached within the capabilities of the Low Turbulence Free Surface Water (LTFSW) Channel or the towing tank at MRELab for $30{,}000<Re<120{,}000$. This subcritical range covers flow regimes TrSL2, TrSL3 (Zdravkovich 1997) for smooth stationary cylinders, where 'TrSL' is short for Transition in Shear Layer. With the purpose of hydrokinetic energy converting to mechanical and harnessing, the VIVACE system is in

essence an FIM problem with high system damping and high Reynolds number, which is setting rarely studied in previous experimental as well as numerical studies. In the MRELab, ζ_{harn} is up to 0.16 (external damping only) compared with 0.0054 used by Williamson et al. (Khalak and Williamson 1996).

The present study is aimed to numerically model the single-cylinder VIVACE unit with PTC. Reynolds-Averaged Navier-Stokes equations (RANS) with the Spalart-Allmaras one-equation turbulence model are solved numerically for two-dimensional flows over a circular cylinder. The cylinder on springs is free to move only in a direction transverse to the flow and the cylinder axis and is restricted in in-line direction. Apart from time requirement concerns, using two dimensional rather than three-dimensional analyses takes advantage of the specific geometry of the VIVACE cylinder with PTC. Although it is a well-known fact that flow over a circular cylinder is a highly three-dimensional phenomenon, the spanwise correlation length of vortices is highly increased by applying straight sand-strips continuously along the cylinder, which helps to some extent in organizing vortices in the spanwise direction and limiting the three-dimensional effects. Two-dimensional RANS simulation of circular-cylinder flows for Re>20,000 is challenging and results are at best approximate of experimental measurements. Nevertheless, with proper modeling of PTC, RANS simulations exhibit several of the salient features of experiments and can provide complementary flow information, which would be difficult to measure experimentally at such high speeds and turbulence levels.
A series of cases are simulated and the results are compared with experimental results derived in the Low Turbulence Free Surface Water Channel of the MRELab. Amplitude ratio (A/D) curves show clearly 3 different branches, including the VIV initial branch, the VIV upper branch and a galloping branch, similar to those observed experimentally. Frequency ratio, vortex pattern, transitional behavior and lift are also investigated. The system parameters are: Mass ratio m^*=1.88, damping ratio ζ_{harn}=0.08, and spring constant K=1,600 N/m. Reynolds number ranges from 35,000 to 130,000. In order to investigate the potential effective working range of galloping, the higher Re cases are further studied with maximum Re=200,000.

Table 5.1. Experimental system parameters

Mass ratio	m^*	1.88
External damping ratio for energy harnessing	ζ_{harn}	0.08; 0.12
Mass-damping parameter	$m^* \zeta_{harn}$	0.0752; 0.1504; 0.2256
Diameter of circular cylinder	D [inch/cm]	3.5/0.0899
Total mass of oscillation	M [kg]	10.75
Spring constant	K [N/m]	1,600; 2,000
Structural damping	$C_{structure}$ [Ns/m]	3.2
Natural frequency in water	$f_{n,water}$ [Hz]	1.5650; 1.7497

Table 5.2. PTC parameters (P60 sand paper)

Strip placement angle	α_{PTC} [degree]	20 ~ 36, -20 ~ -36
Strips coverage	[degree]	16
Sand paper thickness	P [mm]	0.587
Average height of sand grits	K [mm]	0.26
Total thickness	$T=P+K$ [mm]	0.847

5.2. Cylinder amplitude ratio *(A_{RMS}* - Re)*

For cylinder with PTC, due to the specifically modified surface geometry, the wall-function is used in the simulations to account for the roughness effect. In the MRELab, the PTC device, which is made of two straight trips of sandpaper, is selectively applied to the smooth cylinder surface on specific circumferential locations. The sandpaper with roughness designation P60 is composed of paper (with thickness p) and sand grits, with roughness height K (Chang 2010). In the computational grid for rough cylinder, the paper component of PTC is modeled as part of the cylinder surface, and treated as wall boundary. The rough sand grits effects are modeled by wall-functions. Comparing with smooth cylinder grids, no fine boundary layer cells are used and first grid spacing $y+$ is about 30-70 for different Re's. Similar to S2, R1 grid also has enhanced grid density near the cylinder wall and the total number of cells is 45,600 (circumferential*radial: 240*190), same as S2.

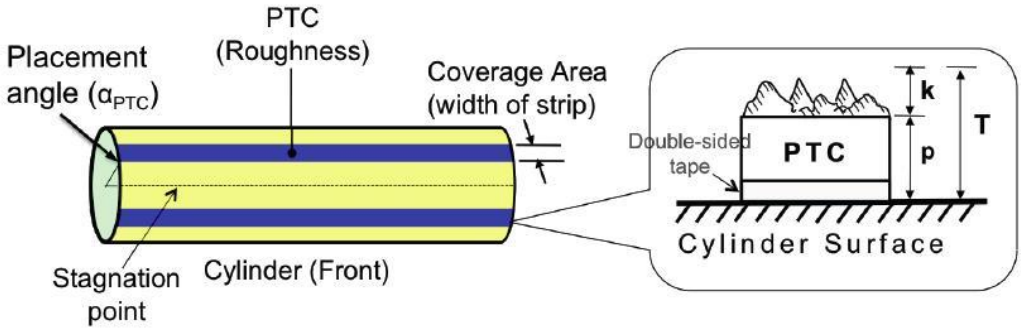

Figure 5.1. Configuration of sandstrips (PTC) along the cylinder (Reproduced from Chang 2010)

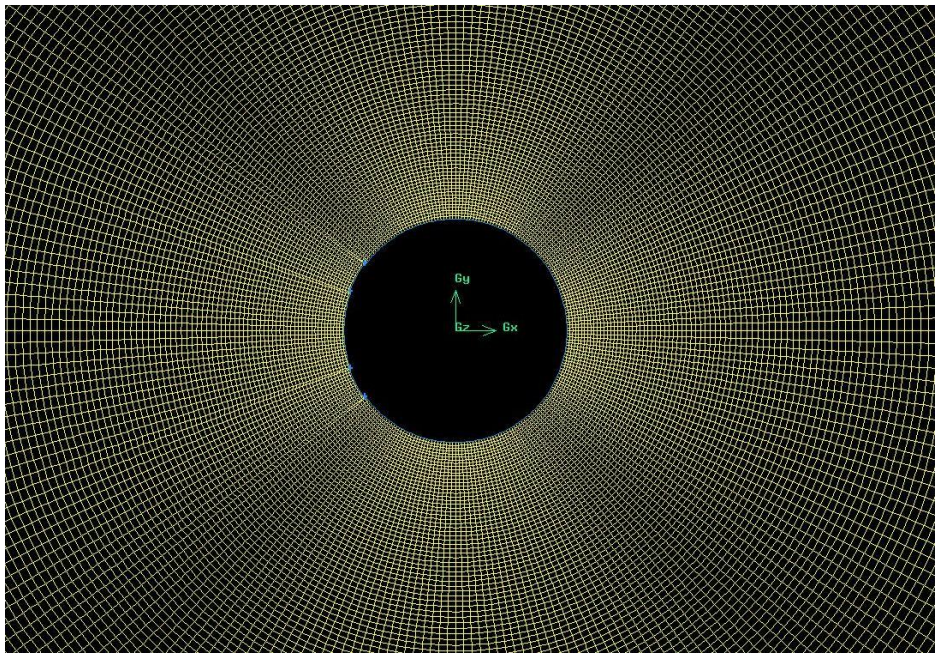

Figure 5.2. Grid R1 for cylinder with PTC

The system parameters and PTC details are the same as those tested in the MRELab, as listed in Tables 5.1 and 5.2. For the experimental conditions, the ratio of cylinder diameter D to channel depth d is about 12% (D/d=3.5/29). The ratio of cylinder length L over channel width w is nearly 1 (L/w=36/38). The boundary blocking (side-to-side, top-to-bottom) and free surface effects are not considered in current numerical study. The entire computational domain is two dimensional with a 50D×50D size. The upper and lower boundaries are assumed to be far enough from the cylinder so the

boundary conditions of velocity conditions on them are set to be equal to the inflow velocity value. It is anticipated that this discrepancy between experiments and simulations will lead to some differences in the results.

A series of simulations have been conducted with K=1,600 N/m, ζ_{harn}=0.08. The *Re* varies from 35,000 to 130,000 and the corresponding $U_{r,w}$ ranges from 3.15 to 11.71. Figure 5.3 presents the comparison of amplitude ratio A_{RMS}^{*} (A_{RMS}/D), which is based in the Root Mean Square value of oscillating amplitude, between current the numerical study and experimental data from MRELab. RANS results follow the basic trend of experimental data very well, presenting clearly different branches including the VIV initial branch, the VIV upper branch, as well as galloping, where the amplitude ratio shoots up to 4. However, the amplitude ratio is over predicted throughout the simulation range compared with experimental data. This is partly due to the fact that the free surface effect and bottom blockage effect are not considered in the present simulations. In the MRELab, the ratio of cylinder diameter D to channel depth d is about 12% (D/d=3.5/29). In galloping, cases with high amplitude ratio, the oscillating cylinder hits the stoppers, at both ends of the travel, indicating that higher amplitude could be reached if more space was allowed. One of the characteristics of galloping is the ever increasing amplitude with increasing velocity of flow until structural collapse.

As shown in Figure 5.3, there are clearly three branches of amplitude ratio curve, namely the VIV initial branch, the VIV upper branch and the galloping branch. The range from *Re* 35,000 to 60,000 is the VIV initial branch. The amplitude ratio slowly picks up from 0.18 at *Re*=35,000 and reaches 0.88 around *Re*=60,000. The following branch is the VIV upper branch ranging from approximately *Re*=~60,000 to *Re*=~100,000. It initiates with a small jump of the amplitude at *Re*=65,000 and again the amplitude increases in a relatively slow rate until *Re* reaches 100,000, where galloping starts and the amplitude begins to climb with a steeper slope. By the end of the simulation range, *Re*=130,000, the amplitude ratio still keeps increasing and reaches up to 4. In Figure 5.5, time histories of displacement ratio and lift coefficient for different *Re*'s are plotted together. Interestingly, comparing with smooth cylinder case, in which there is an obvious sudden phase change

from 0 to 180 degrees near the end of upper branch (Khalak and Williamson 1999, Wanderley et al. 2009), there is limited amount of change in the phase angle between lift and oscillation and the peaks of them for each cycle are well synchronized in the upper and the galloping branches (see Figure 5.5). This might be a good reason to keep the amplitude going up throughout the whole synchronization range for cylinder with PTC cases, without a sudden amplitude drop as it happened after phase change in upper branch for smooth cylinder.

5.3. Mode transition and vortex structure

The following observations are made in the results of numerical simulations and are typically observed in experiments: the shape of any amplitude curve is closely related to the vortex dynamics and wake pattern throughout the three branches. During transition between branches, which is typically accompanied with vortex pattern switch, the amplitude of oscillation tends to be non-uniform which is the resultant of appearance of an additional frequency in the FFT (see Figures 5.6 (d), (f)) caused by additional vortices shed per cycle. On the contrary, while the cylinder is well associated with certain vortex pattern, the chance is that the amplitude is relatively uniform throughout the time history (see Figures 5.5(e), (h)).

In the initial branch, 2S and 2P vortex patterns are observed. 2S occurs at *Re*=35,000 (see Figure 5.11 (a)) and at *Re*=50,000 and 55,000 2P (see Figure 5.11(b)). In the range from *Re*=~60,000 to *Re*=~75,000, the beginning of VIV upper branch, the vortex pattern associated with each *Re* in this range is unstable, in the sense that the number and format of the vortices shed during each cycle are not exactly the same throughout the time history, and the system switches back and forth between different vortex patterns. This makes it difficult to generalize the vortex pattern over all. At *Re*=65,000, in most cycles the 2P pattern are observed 2P (see Figure 5.11(c)), while in others cycles one pair plus one single vortices are shed on one side and one single vortex is found from the other side, which gives 1P+2S in total (see Figures 5.11(d) and (e)). At *Re*=70,000, for some cycles, P+S is observed on one side while S on the other side, which is similar as in some cycles at *Re* 65,000 (see Figure 5.11(f)); and for some other

cycles, P+S can be found on both sides, however, with different vorticity strength for the counterparts from each side. For *Re*=73,000 and 75,000, P+S on each side is found. The single S and pair P shed from bottom side are shown in Figures 5.11 (g) and (h). In this transitional range between the VIV initial branch and upper branch, the vortex pattern is also showing transitional behavior and unstable features. For each *Re*, the vortex pattern switches back and forth as time goes on, and in addition, it is sensitive to *Re* variation, small change in *Re* can lead to pattern shift. For each *Re* case in this range (transition for the VIV initial branch → the VIV upper branch), the amplitude also shows oscillatory behavior and lack of uniformity throughout the time history. In the experiments conducted in the MRELab, no lower branch presents in the amplitude curve for high *Re* range, which is different from Williamson's low *Re* VIV cases. In our case, the upper branch expands and takes over the lower branch. As *Re* reaches up to 78,000, a 2P+4S pattern starts to prevail till the end of the VIV upper branch and clearly two vortex streets are shown in the wake structure. For each side of the cylinder, one pair of vortices (P) sheds first and two single ones (S+S) follow next (see Figure 5.12 (a)). The two singles are almost formed at the same time and shed together. Comparing with the transitional range, this 2P+4S is a more stable mode in the sense that it lasts over a wider *Re* range and exhibits remarkable uniformity of amplitude and stability. In the galloping branch, initially, there is a range of transition (the VIV upper branch→galloping) and *Re*=110,000 and 120,000 are in this range. The mode is 2P+4S, which is the same number of vortices (see Figure 5.12 (b)). The difference from the upper VIV branch is the ordering of the vortices. When the cylinder passes the mean position on its way up, the single vortex (S) is shed firstly and followed closely by a pair (P) and then a second single (S). Same is the shedding sequence on the other side of the cylinder. Thus, the ordering is S+P+S+S+P+S (see Figure 5.12 (b)), differing from the P+S+S+P+S+S (see Figure 5.12(a)), which is the case in upper branch. When *Re* reaches 130,000, the vortex mode is 2P+8S and amplitude goes back to high uniformity (see Figure 5.13(c)). The vortex pattern and corresponding regimes are summarized in Table 5.3.

5.4. Oscillation frequency ratio ($f_o / f_{n,water}$ - *Re)*

In Figure 5.4, frequency ratio $f_o/f_{n,water}$ is plotted along with experimental results for comparison. The major oscillating frequency for each *Re* is used in this plot. In the numerical simulation results, the frequency increases during the VIV initial branch and encounters a drop-off when switching to the VIV upper branch. From *Re*=60,000, another frequency in lift, in addition to the major one, shows up due to extra vortices, but at this time the secondary frequency is very weak in FFT analysis (see Figure 5.6 (d)). The major frequency tends to increase again after the sudden drop at the beginning of this upper branch. After the transition from the initial to the upper branch, at *Re*=78,000, the second and third harmonic frequencies in lift show up clearly, and occur approximately at 3 times and 5 times the first major frequency (see Figure 5.6 (e)). Stepping into the galloping branch, one of the features in galloping is well demonstrated by the drop of the major frequency of oscillation. f_o drops from 1.58 at *Re*=100,000 to 1.49 at *Re*=110,000 and further to 1.33 at *Re*=120,000. Instead of the distinct second and third frequencies in lift, many irregular frequency peaks show up and are unevenly distributed throughout a wide frequency range, which explains the non-uniformity of the amplitude for these *Re*'s. At *Re*=130,000, the major frequency f_o increases a little to 1.56.

Table 5.3. Summary of regimes according to vortex pattern (*K*=1,600 N/m, ζ_{harn}=0.08)

Regime	Vortex pattern	*Re*
VIV initial branch	2S: 2 single vortices per cycle	35,000
VIV initial branch	Transitional mode	40,000~45,000
VIV initial branch	2P: 2 pairs of vortices per cycle	50,000~55,000
VIV upper branch	Transitional mode	60,000~75,000
VIV upper branch	2P+4S: 2 pairs and 4 single vortices per cycle	78,000~100,000
Galloping branch	2P+4S: 2 pairs and 4 single vortices per cycle	110,000~120,000
Galloping branch	2P+8S: 2 pairs and 8 single vortices per cycle	130,000

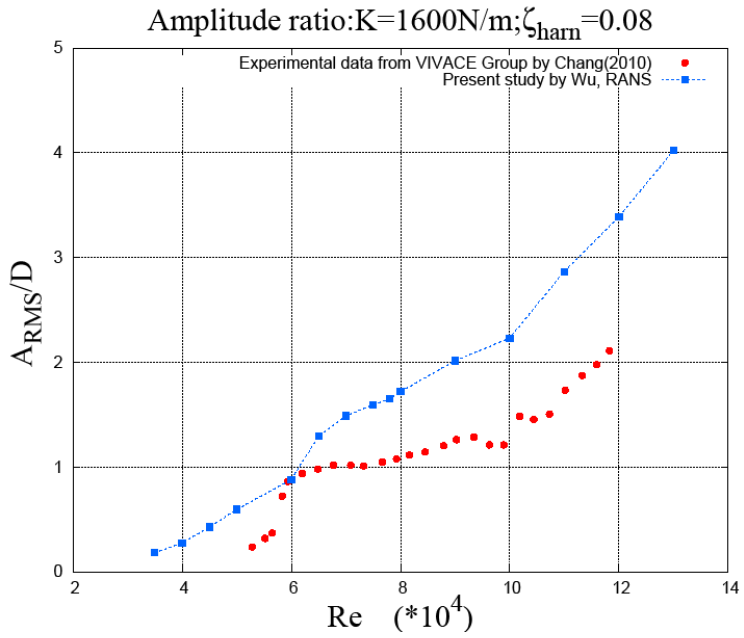

Figure 5.3. Amplitude ratio (A_{RMS}^{*}) comparison between present study and Chang (2010), MRELab, University of Michigan (K=1,600 N/m, ζ_{harn}=0.08)

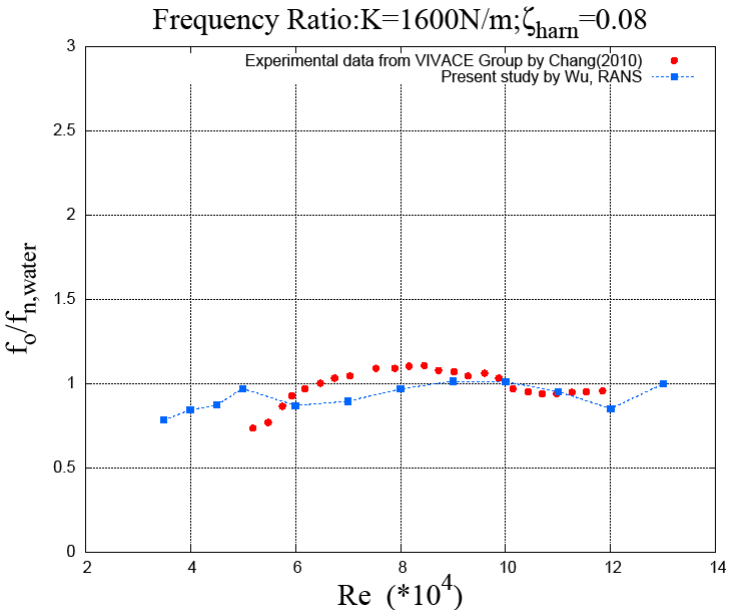

Figure 5.4. Frequency ratio comparison between present study and Chang (2010), MRELab, University of Michigan (K=1,600 N/m, ζ_{harn}=0.08)

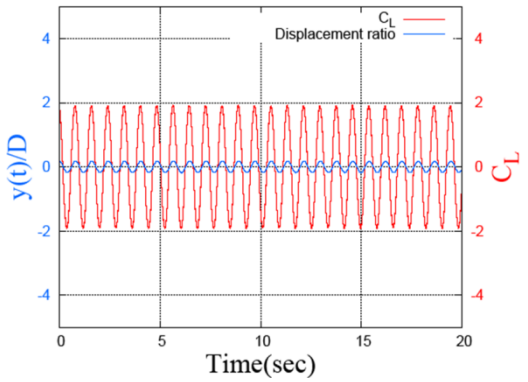

(a) *Re*=35,000; $U_{r,water}$=3.15

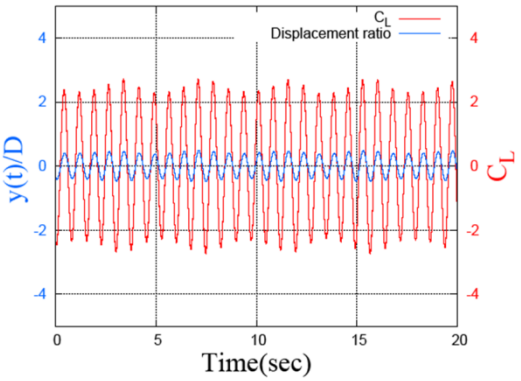

(b) *Re*=45,000; $U_{r,water}$ =4.05

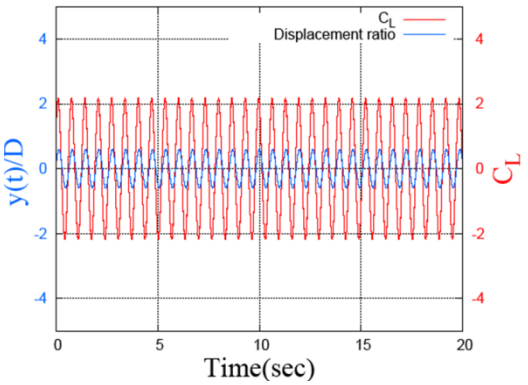

(c) *Re*=50,000; $U_{r,water}$ =4.5

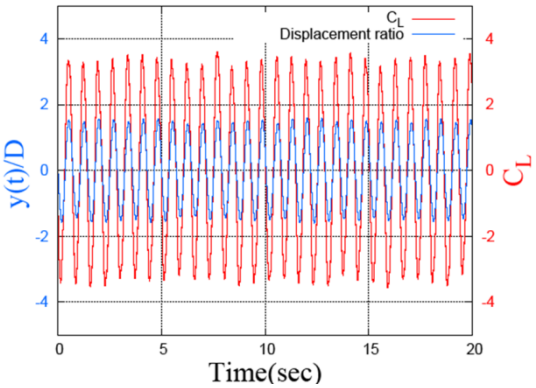

(d) *Re*=70,000; $U_{r,water}$ =6.3

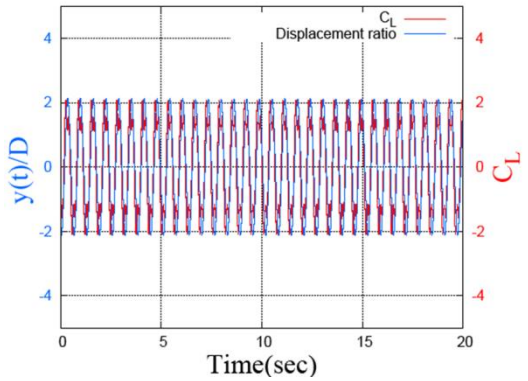

(e) *Re*=95,000; $U_{r,water}$ =8.55

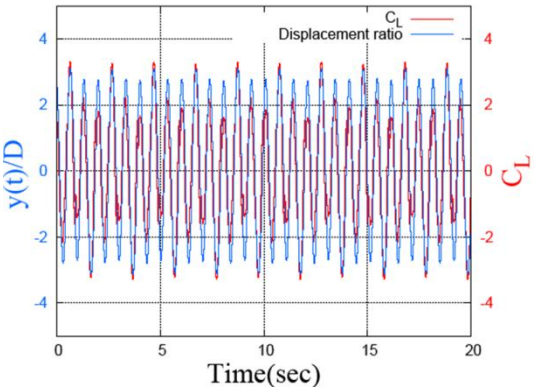

(f) *Re*=110,000; $U_{r,water}$ =9.91

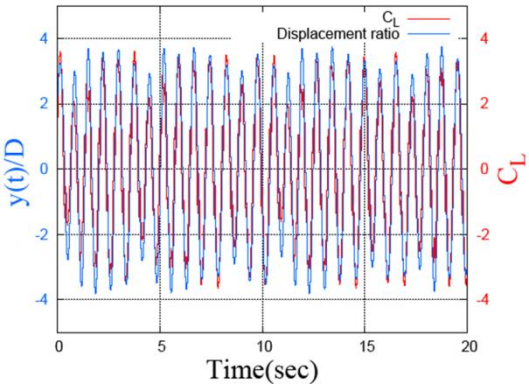

(g) *Re*=120,000; $U_{r,water}$ =10.81

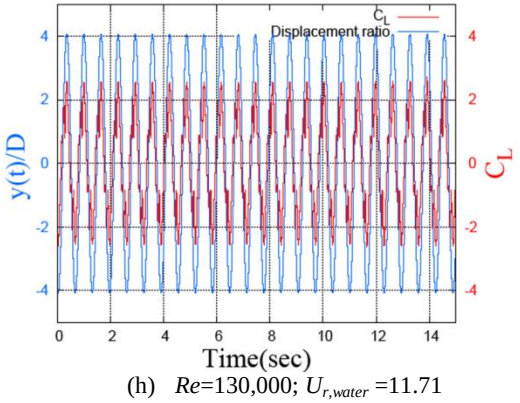

(h) *Re*=130,000; $U_{r,water}$ =11.71

Figure 5.5. Displacement ratio (*y(t)/D*) and lift coefficient for different *Re* (*K*=1,600 N/m, ζ_{harn}=0.08)

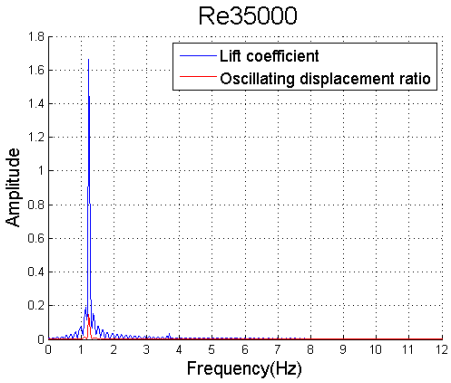

(a) *Re*=35,000; $U_{r,water}$=3.15

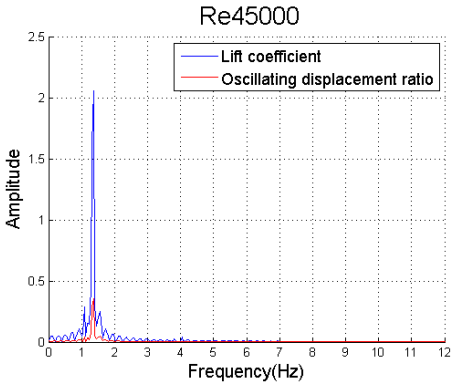

(b) *Re*=45,000; $U_{r,water}$ =4.05

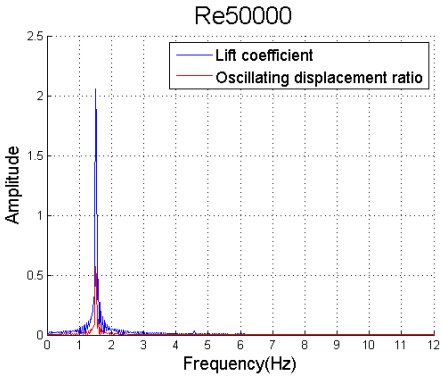

(c) *Re*=50,000; $U_{r,water}$ =4.5

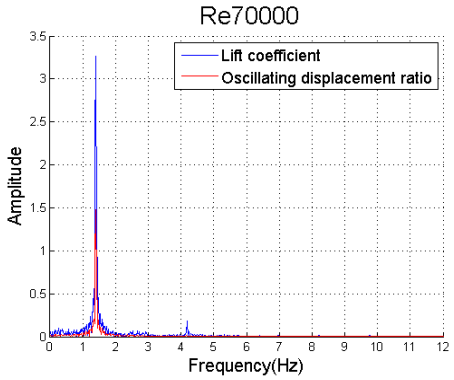

(d) *Re*=70,000; $U_{r,water}$ =6.3

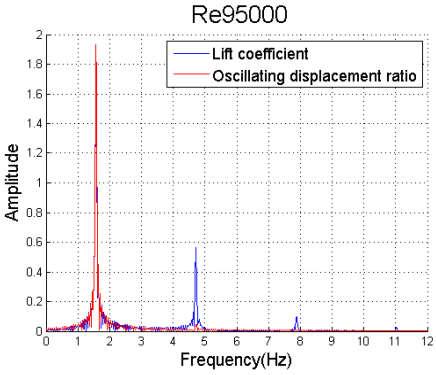

(e) *Re*=95,000; $U_{r,water}$ =8.55

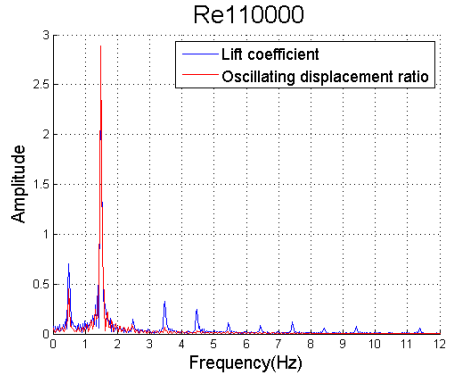

(f) *Re*=110,000; $U_{r,water}$ =9.91

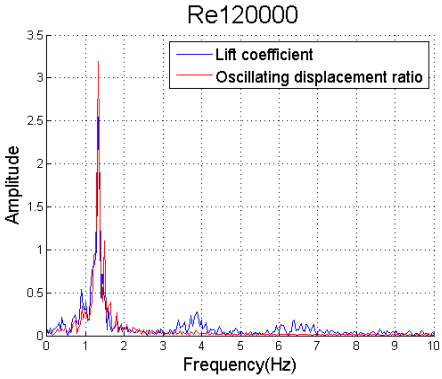

(g) *Re*=120,000; $U_{r,water}$ =10.81

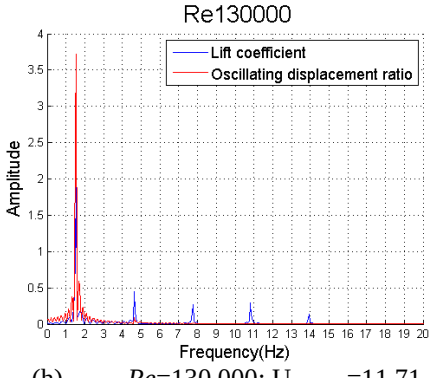

(h) *Re*=130,000; $U_{r,water}$ =11.71

Figure 5.6. FFT analysis of displacement ratio (*y(t)/D*) and lift coefficient for different *Re* (*K*=1600 N/m,ζ_{harn}=0.08)

5.5. Investigate the range for galloping

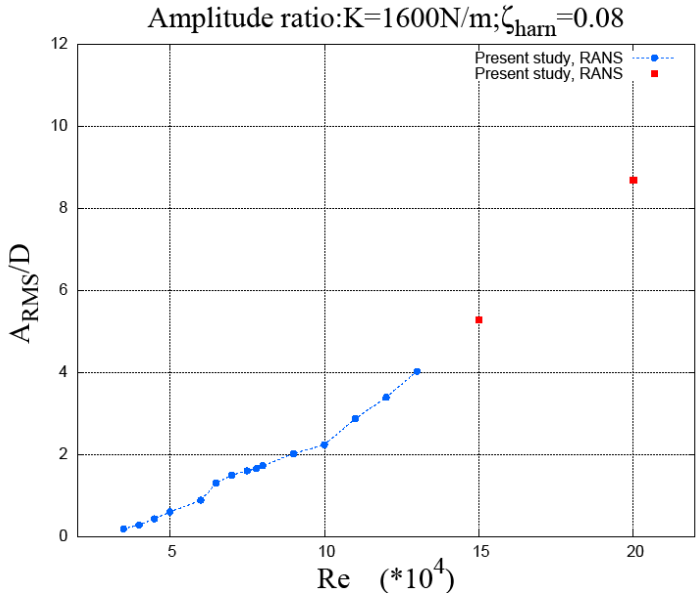

Figure 5.7. Amplitude ratio (A_{RMS}^{*}) for additional cases on *Re*=150,000 and *Re*=200,000 (in red dots) in comparison to the other previous cases (in blue dots) (*K*=1,600 N/m, ζ_{harn}=0.08)

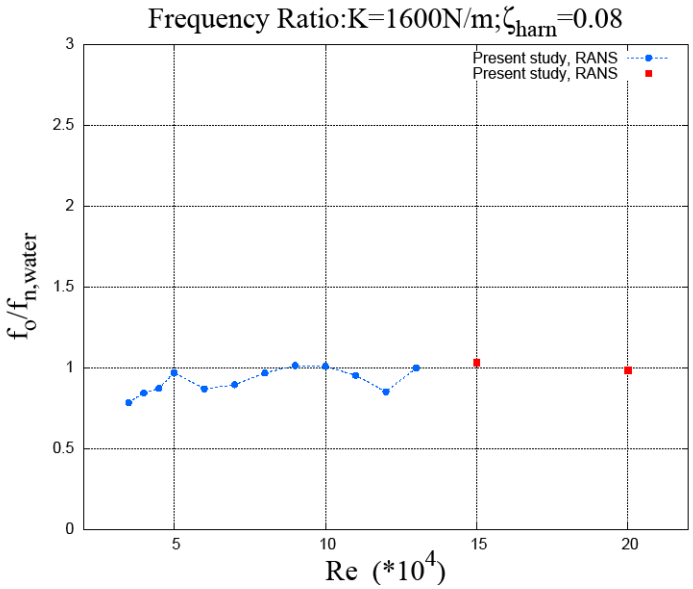

Figure 5.8. Frequency ratio for additional cases at *Re*=150,000 and *Re*=200,000 (in red dots) in comparison to the other cases (in blue dots) with *K*=1,600 N/m, ζ_{harn}=0.08

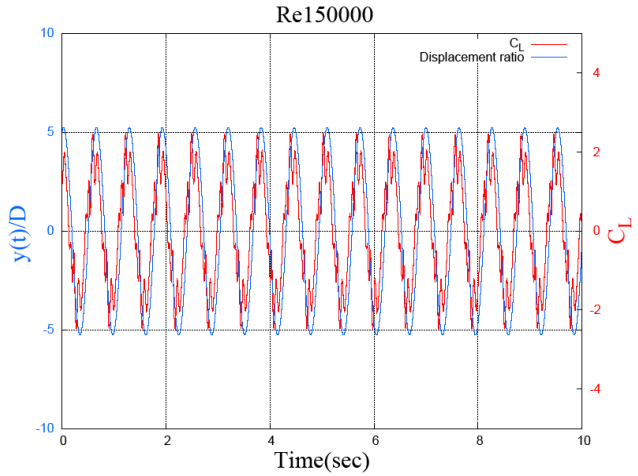

(a) Lift coefficient and displacement ratio history, *Re*=150,000

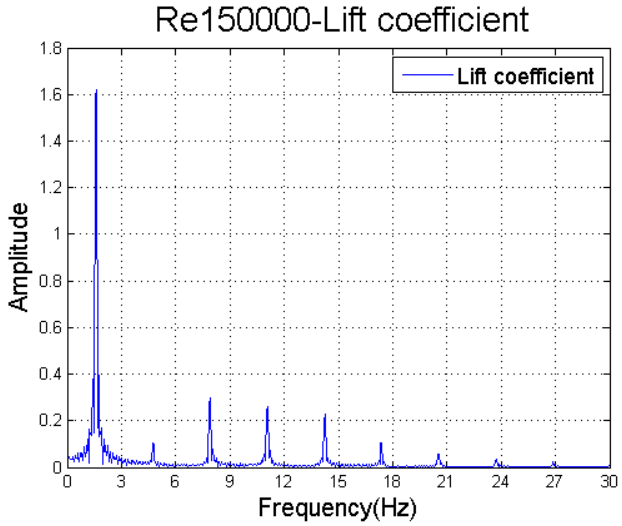

(b) FFT analysis for lift coefficient, *Re*=150,000

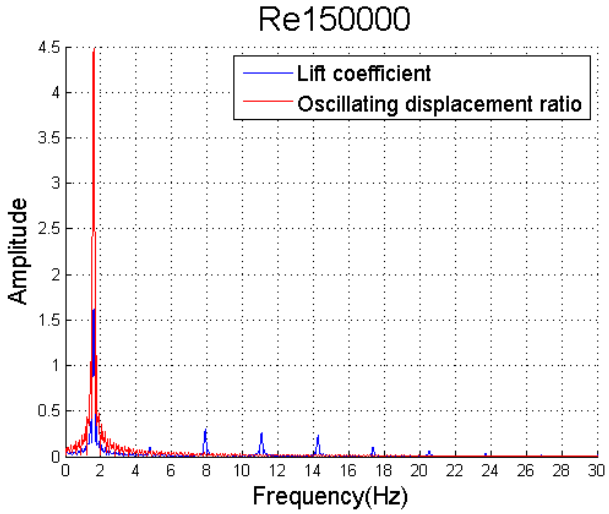

(c) FFT analysis for lift coefficient and displacement ratio, *Re*=150,000

Figure 5.9. Time history and spectra of lift coefficient (C_L) and displacement ratio ($y(t)/D$) for *Re*=150,000 and *K*=1,600N/m, ζ_{harn}=0.08.

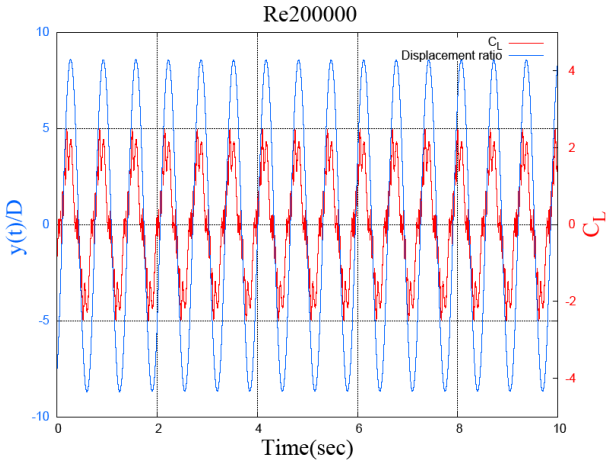

(a) Lift coefficient and displacement ratio history, *Re*=200,000

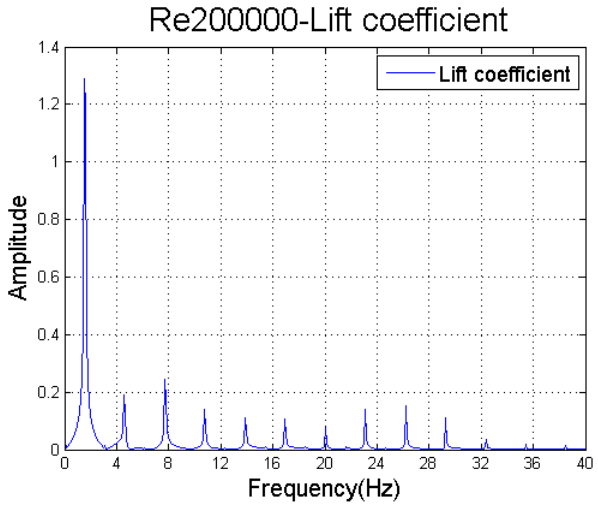

(b) FFT analysis for lift coefficient, *Re*=200,000

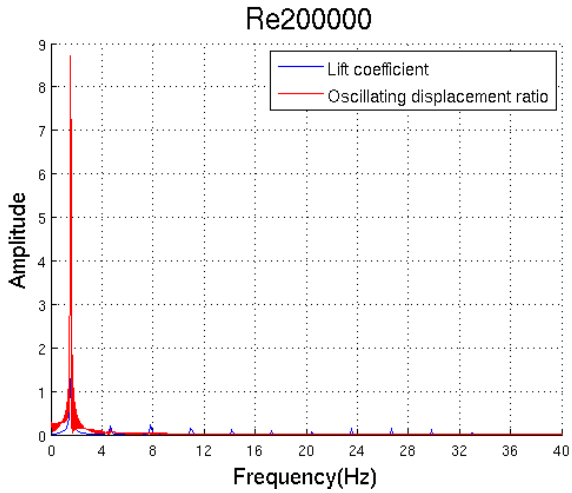

(c) FFT analysis for lift coefficient and displacement ratio, *Re*=200,000

Figure 5.10. Time history and spectra of lift coefficient (C_L) and displacement ratio ($y(t)/D$) for *Re*=200,000 and *K*=1,600N/m, ζ_{harn}=0.08.

In experiments, limited by the capabilities of the experimental facility, the synchronization lasts till the end of test range with no end found in the galloping branch. In order to investigate the potential extent of the galloping range, two higher *Re* cases are studied with *Re*=150,000 and *Re*=200,000.

In Figure 5.7, the amplitude ratios of these two new cases are plotted together with the previous cases. The amplitude keeps growing as *Re* increases and the amplitude ratio (A_{RMS}^{*}) reaches 5.27 and 8.68 respectively. Therefore up to *Re*=200,000, the galloping behavior still exists and more cases are needed in order to find the end of synchronization. As for the frequency, the major oscillating frequency is similar to the natural frequency in water and no substantial changes are present in the frequency ratio compared with *Re*=130,000 which also resides in the fully developed regime of galloping. In Figures 5.9 and 5.10, the displacement and lift coefficient history and spectra are listed for *Re*=150,000 and *Re*=200,000. Both cases are featured with a single-peaked displacement spectrum and a multi-peaked lift spectrum. For *Re*=200,000, there are around 13 notable peaks appearing in the lift spectrum. Totally 16 and 24 vortices are generated per cycle in these two cases (see Figures 5.13 (a) and (b)). The vortices shed alternatingly with opposite sign vorticity from the two sides of the cylinder. The only exception appears when the maximum displacement is reached with two successive vortices with the same sign shedding almost at the same time. This observation agrees well with other cases in the fully developed galloping branch (Figures 5.13(a), (b)).

5.6. Conclusions

(a) Two-dimensional RANS faces for smooth cylinders – stationary or in FIM – fails completely in predicting all essential flow features when *Re* goes to a higher range (35,000~200,000) in the subcritical regime. By introducing PTC, which is made of two straight strips of sandpaper, the correlation length of vortices is set close to the spanwise dimension of the cylinder while the vortices are shedding. This makes two-dimensional RANS work better in such a high *Re* range.

(b) R.M.S. values of the oscillating amplitude and frequency ratios are compared with results from the MRELab by the VIVACE group. The three branches in the

amplitude curve are well captured as derived in the experiments. However, the numerical results tend to over-predict the amplitude throughout the simulation range. This is partly due to the fact that the free surface and bottom boundary blocking effects are not considered in the present numerical study. It is known that boundaries reduce FIM amplitudes.

(c) The frequency ratio curve also shows variations in different branches (see Figure 5.4). When in the VIV initial branch, the frequency keeps increasing and ends with a sudden drop around the transition between the initial and the upper branches. There is another sudden drop of the frequency observed, which occurs right with the onset of galloping.

(*d*) The vortex pattern switches throughout the three branches and various vortex patterns are indentified including 2S, 2P, 2P+4S and 2P+8S.

(e) Other transitional patterns during the branch-shift were also discussed together with other transitional features, like the uniformity of amplitude and the frequency change.

(f) When *Re* goes up to 200,000, the synchronization is not ended and galloping is still observed. Up to 24 vortices are found to shed per cycle and at least 13 peaks are show in the lift spectrum. Therefore, within the range of current investigation, the end of synchronization is still not unveiled and even higher *Re* numbers should be investigated. This is consistent with the galloping characteristic of the amplitude ever increasing with increasing velocity till structural failure.

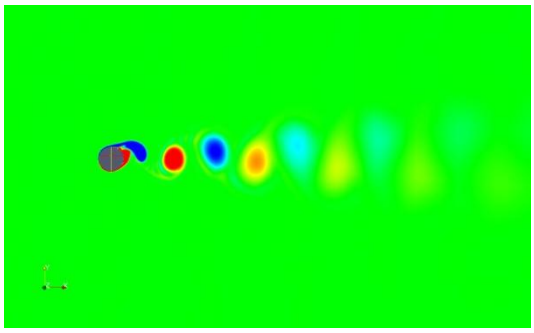

(a) "2S" mode (*Re*=35,000)

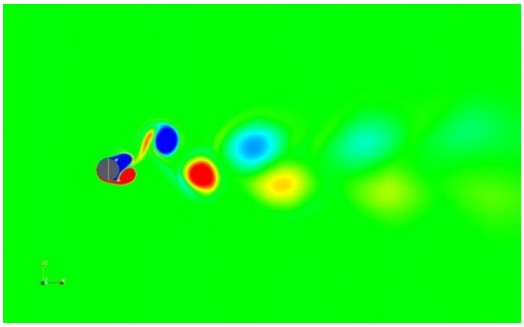

(b) "2P" mode (*Re*=50,000)

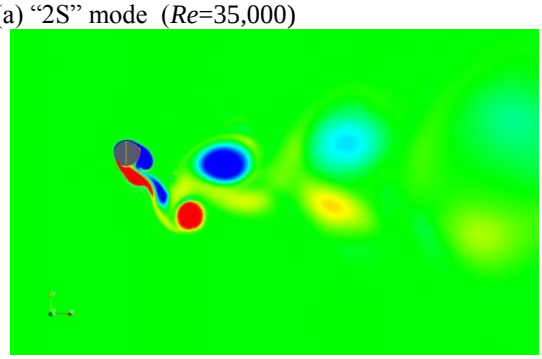

(c) P of "2P" mode (*Re*=65,000, mode2P/P+2S)

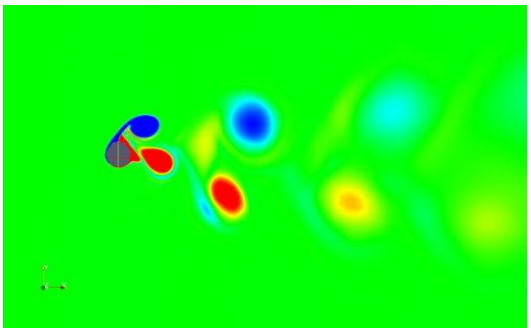

(d) two S of "P+2S" mode shed from lower and upper sides (*Re*=65,000, mode 2P/P+2S)

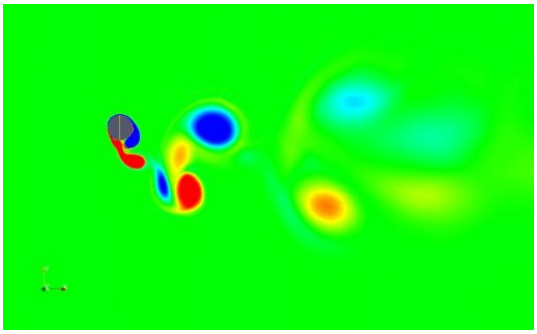

(e) P and S of "P+2S"mode shed from lower side of the cylinder (*Re*=65,000, mode 2P/P+2S)

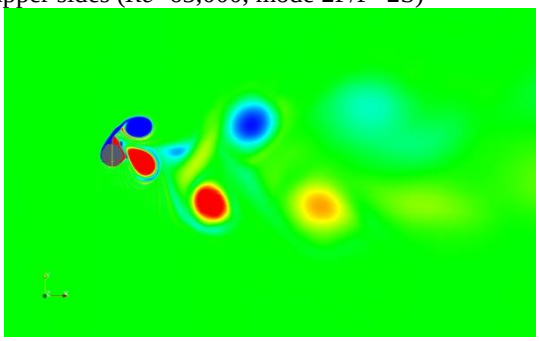

(f) two S of "P+2S" mode shed from lower and upper sides (*Re*=70,000, mode P+2S/2P+2S)

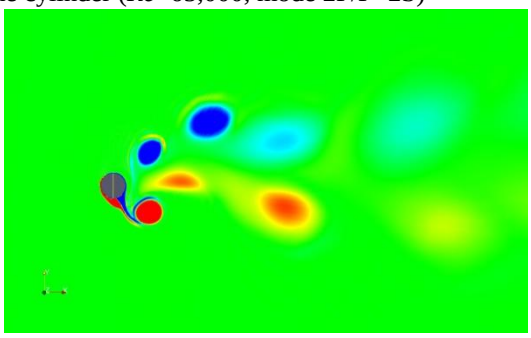

(g) P of "2P+2S"mode shed from lower side of the cylinder (*Re*=73,000, mode 2P+2S)

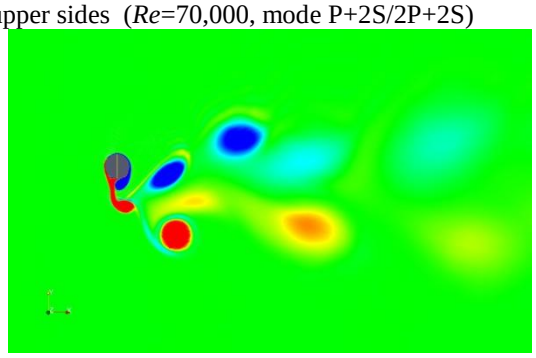

(h) S of "2P+2S"mode shed from lower side of the cylinder (*Re*=73,000, mode 2P+2S)

Figure 5.11. Vortex pattern for the initial and upper branch (developing regime), and *K*=1,600N/m, ζ_{harn}=0.08.

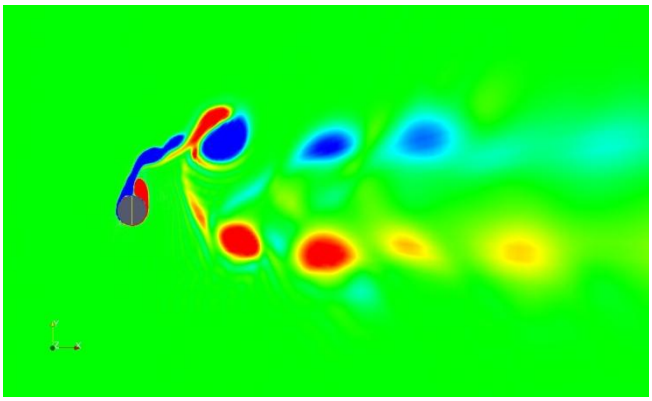

(a) P+S+S+P+S+S mode: upper branch *Re*=95,000

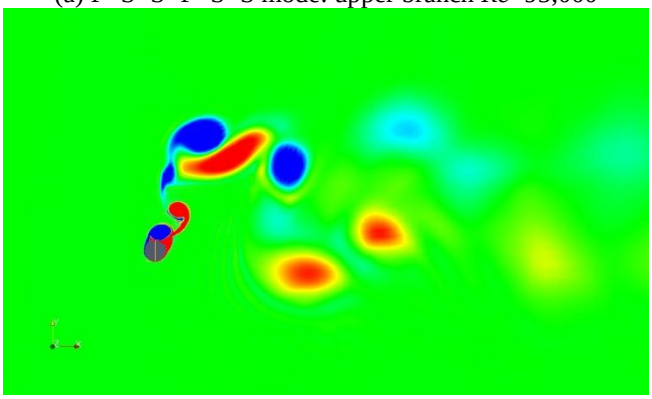

(b) S+P+S+S+P+S mode: transition upper branch to galloping; *Re*=110,000

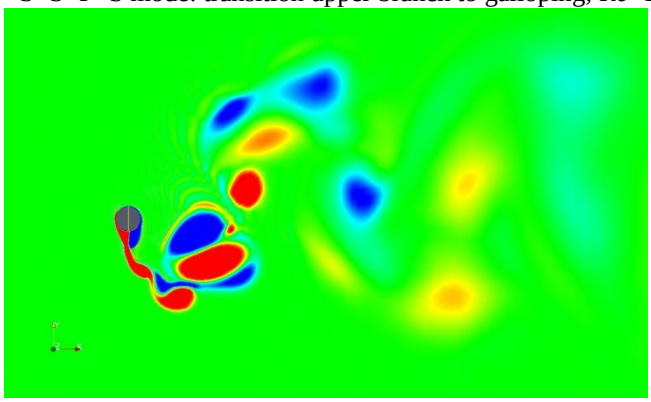

(c) 2P+8S mode: galloping *Re*=130,000

Figure 5.12. Vortex pattern for the upper branch (fully developed regime) and galloping branch, and *K*=1,600N/m, ζ_{harn}=0.08.

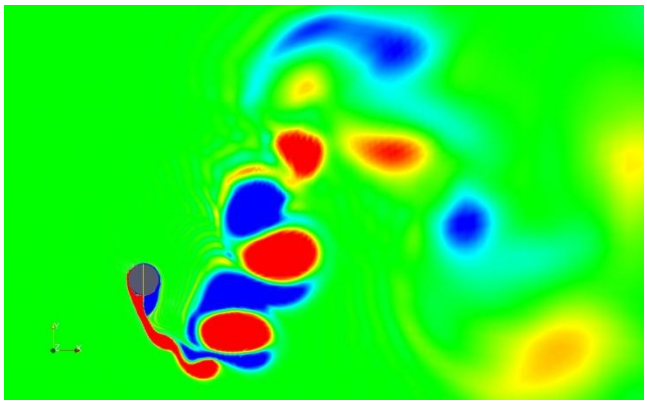

(a) 16 vortices (*Re*=150,000)

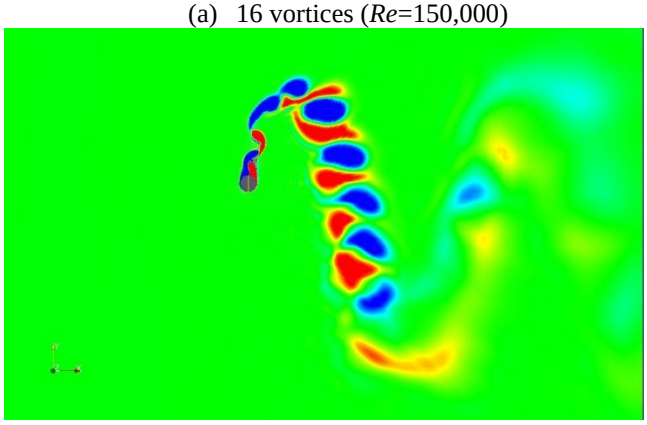

(b) 24 vortices (*Re*=200,000)

Figure 5.13. Vortex patterns for *Re*=150,000 and *Re*=200,000

Chapter 6

EFFECT OF DAMPING AND STIFFNESS ON FIM OF CYLINDER WITH PTC

6.1. Background

In Chapter 5, the Flow-Induced Motions of a circular cylinder with passive turbulence control (PTC) has been studied. High damping is mandatory for the purpose of energy conversion and harnessing using the VIVACE energy converter. When VIVACE is linked with a power take-off system, additional damping is introduced to this dynamic system to harness energy. Therefore, how the system will perform under various damping levels and moreover how those system parameters will affect the cylinder FIM dynamics are two very important questions from the system design point of view.

The VIVACE group has conducted series of experiments aiming to study systematically the effect of damping and stiffness for both smooth and cylinder with PTC cases. The early stage VIVACE prototype was in the form of a smooth cylinder. J. H. Lee proposed and verified a virtual damper/spring (V_{ck}) apparatus with a motor-controller system (Lee 2009). This device was designed to allow changing of the system damping and stiffness for the VIVACE system by dialing in the appropriate values. A 3.5inch cylinder model is used for the smooth cylinder case. The test Reynolds number ranges from 40,000 to 120,000 depending on the synchronization range for different system parameters. Extensive experiments have been performed with combinations of various damping ($\zeta_{harn} \in [0,0.16]$) and stiffness ($K \in [400,1800]$ N/m) values. The effects on several important properties associated with oscillations are discussed, which include the range of synchronization, oscillation amplitude and frequencies. For lower damping ratio the synchronization range tends to be broader with a slightly earlier onset and a later end. As damping level increases, the sudden stop of the synchronization zone is no longer

observed for high damping cases as it is in the low damping. Instead, the amplitude decreases gradually till the end of the "locked-in" region. For certain spring stiffness *K*, the amplitude shows clear declining tendency as damping goes up and the consistency of the this trend is well observed for different stiffness levels. Comparing to the damping effects, the system stiffness has more obvious effects in changing the synchronization range. As stiffness increases, the entire synchronization zone shifts to higher *Re* numbers, but not necessarily with a broader synchronization range.

In order to enhance the oscillating amplitude and further extend the synchronization range, PTC was applied recently by the VIVACE group in the MRELab. Cylinder FIM is successfully enhanced to reach back-to-back VIV and galloping, synchronization range of more than double that of VIV with no end within the capabilities of the Low Turbulence Free Surface Water (LTFSW) Channel. More investigation of the effect of damping and stiffness on this new generation of VIVACE prototypes is beening conducted. In those studies, the same virtual damper/stiffness apparatus developed by Lee is adopted first time in such a high damping, high amplitude condition (Chang 2010). The Reynolds number ranges from 30,000 up to 130,000. Spring constant *K* varied from 400 to 2,000N/m and harnessing damping ratio ζ_{harn} varied from 0 to 0.16. Beyond the working scope of amplitude, frequency and VIV synchronization range, more information is provided though his research, such as galloping branch behavior, the transition to galloping, and vortex structure description for a few cases.

In this chapter, the stiffness and damping effects are studied with the 2D-RANS numerical tool developed in this thesis for the VIVACE system and the investigations cover the amplitude ratio, frequency ratio, lift and displacement spectra, and vortex patterns. For each property the comparisons are made for different flow regimes as well as for different system damping and stiffness. The transitional behavior, from the VIV lower branch to the upper branch and from the VIV upper branch to galloping branch, is also discussed.

6.2. Effect of stiffness on FIM of a cylinder with PTC

6.2.1. System parameters

In this section, a series of simulations are performed to investigate the effect of system spring constant on cylinder with PTC in FIM. The simulation results are compared with experimental results from the VIVACE group (Chang, 2010). The cylinder with 0.0899 meter diameter (3.5 inch) is used, the values for spring constant K are 1,200, 1,600, 2,000 N/m. The damping is composed of two parts as described in the experiments, namely structural damping $C_{structure}$ and harnessing damping C_{harn} (additional damping). The damping ratio for the harnessing damping in the present simulations is ζ_{harn} =0.08. All the system parameters are listed in Table 6.1. For PTC, all parameters are kept consistent with those used in Chapter 5, and they are listed in Table 6.2.

Table 6.1. Experimental system parameters

Mass ratio	m^*	1.88
External damping ratio for energy harnessing	ζ_{harn}	0.08
Mass-damping parameter	$m^* \zeta_{harn}$	0.1504
Diameter of circular cylinder	D [m]	0.0899
Total mass of oscillation	M [kg]	10.75
Spring constant	K [N/m]	1200/1600/2000
Additional damping for harnessing	C_{harn} [Ns/m]	18.2/21.0/23.5
Structural damping	$C_{structure}$ [Ns/m]	3.2
Natural frequency in water	$f_{n,water}$ [Hz]	1.3553/1.5650/1.7497

Table 6.2. PTC parameters (P60 sandpaper)

Strip placement angle	α_{PTC} [degree]	20 ~ 36, -20 ~ -36
Strips coverage	[degree]	16
Sand paper thickness	P [mm]	0.587
Average height of sand grits	k [mm]	0.26
Total thickness	$T=P+k$ [mm]	0.847

6.2.2. Cylinder displacement (A_{RMS}- Re)*

The RMS amplitude ratio curves are plotted over Re and compared with experimental results for all three stiffness values (see Figures 6.1, 6.2 and 6.3). Similarly to the results in Chapter 5, the RANS results over-predict amplitude compared to

experimental results though out the three branches of response. However, numerical simulation results do show features observed experimentally, and the effect of the spring constant K on the system response is also well supported by the experiments.

For all three cases, the entire response range can be subdivided into 3 parts, same as founding Chapter 5: VIV initial branch, VIV upper branch, and galloping branch. In Figure 6.5, the cylinder oscillation displacement $y(t)$ is plotted together with the lift coefficient $C_L(t)$ for different Reynolds number cases for K=1,200N/m, allowing easy observation of phase lag between lift and dispacement for each Re case. In addition, the FFT analyses for $y(t)$ and $C_L(t)$ are also performed for corresponding cases.

As shown in Figure 6.1, for the K=1,200kN/m case, the simulation cases Re=40,000 and Re=45,000 are in the range of the VIV initial branch. Similarly, as discussed in Chapter 5 for the K=1,600N/m and ζ_{harn}=0.08 case, in the initial branch, the amplitude of lift and displacement is relatively uniform, and the FFT plot of lift shows a single major peak. The VIV upper branch starts from Re=50,000 for K=1,200N/m. The initiation of this branch not only features an increase in amplitude response, but most importantly, as found from the present numerical studies, is associated with another characteristic: the drop-off of oscillation frequency. The VIV upper branch ranges from Re=50,000 to Re=90,000 and the RMS amplitude increases in a relatively high rate compared to experiments and the RMS amplitude ratio changes from about 0.83 to 2.26. In the entire VIV upper branch, the two sub-domains can be identified by different behaviors in lift and oscillating amplitude. At the beginning of the upper branch, from Re=50,000 to 65,000, non-uniform amplitude shows in both lift and displacement (see Figures 6.5 (c1), (d1), (e1) and (f1)). A second harmonic peak and even more frequency peaks for lift start to appear and gradually gain strength, and the value of the second major frequency is about twice that of the first harmonic frequency at this time (see Figures 6.5 (c2), (d2), (e2) and (f2)). For the fully developed VIV upper branch, from Re=70,000 to 90,000, the amplitude for both lift and displacement goes back to nearly perfectly periodic status (see Figures 6.5 (g1), (h1) and (i1)). The second and third harmonic frequencies for lift become stronger and conspicuous, and are about 3 times and 5 times that of first harmonic frequency, respectively (see Figures 6.5 (g2), (h2) and (i2)). For Re=100,000,

this case is located in the transitional regime from the VIV upper branch to galloping branch. As seen in Figure 6.5 (j1), the amplitude and lift coefficient both show obvious non-uniformity, which indicate the initiation of the galloping branch. As *Re* goes up to 110,000, the fully developed state of galloping branch is reached and the RMS amplitude ratio shoots up to nearly 4, and it goes even beyond 4 when *Re* gets higher (see Figure 6.5 (k1)). The amplitude of oscillation comes back to a relatively uniform state, which can be easily identified by the displacement FFT plot. The frequency of displacement for *Re*=110,000 shows a narrow-banded first major peak. The second harmonic peak appears, but in a much weaker way (see Figure 6.5 (k2)).

In Figure 6.4, the RMS amplitude ratio plots are compared for the three values of *K* tested (1200, 1600 and 2000N/m) under the same damping ratio ζ_{harn}=0.08. All curves have three branches, and they share similar features for different regimes. There are resemblances in the results from different *K* values. The following differences among the three setups can be observed:

1. For each Re case, higher values of *K* tend to yield lower response amplitude, and the range of VIV synchronization and galloping shifts to higher *Re* numbers. This is predictable, since lower values of *K* correspond to lower values of additional damping for harnessing C_{harn}, given the same damping ratio ζ_{harn}. The results satisfy engineering intuition that the system with the softer springs and lower damping tends to have larger response motions.

2. The system with a lower *K* has an earlier transition from the VIV initial branch to the VIV upper branch. For these three systems, the transition occurs at approximately *Re*=50,000 for *K*=1200N/m; *Re*=60,000 for *K*=1600N/m; and *Re*=70,000 for *K*=2000N/m.

3. The lower *K* not only tends to lead to an earlier transition to the VIV upper branch, but also results in an early transition to the galloping branch. In addition, for higher *K*, the transition from the VIV upper branch to galloping lasts relatively longer. For *K*=1200N/m, the transition to galloping starts at *Re*=100,000, and only this Re is in the transitional regime. For *K*=1600N/m, the transition is from

Re=110,000 to *Re*=120,000. While for *K*=2000N/m, both *Re*=120,000 and 130,000 are located in this transition regime.

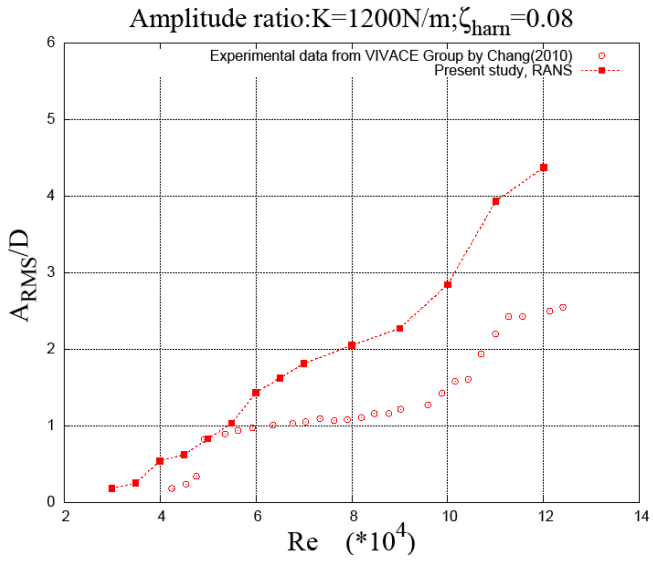

Figure 6.1. RMS amplitude ratio comparison with experiments from MRELab by Chang (2010) (*K*=1200N/m, ζ_{harn}=0.08)

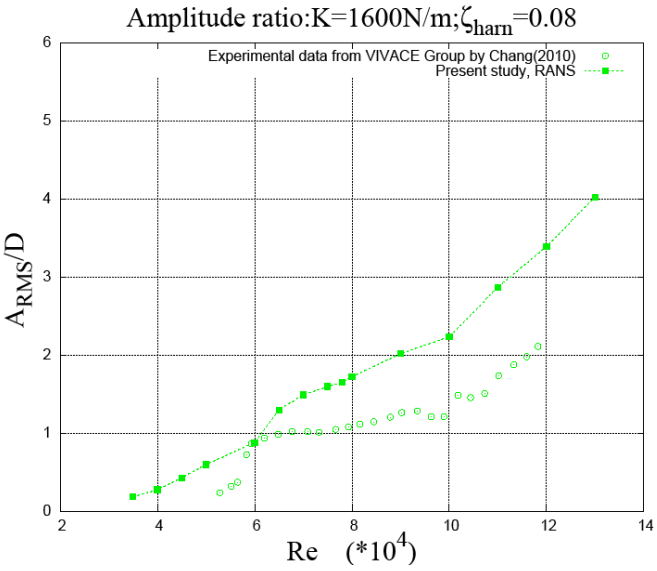

Figure 6.2. RMS amplitude ratio comparison with experiments from MRELab by Chang (2010) (*K*=1600N/m, ζ_{harn}=0.08)

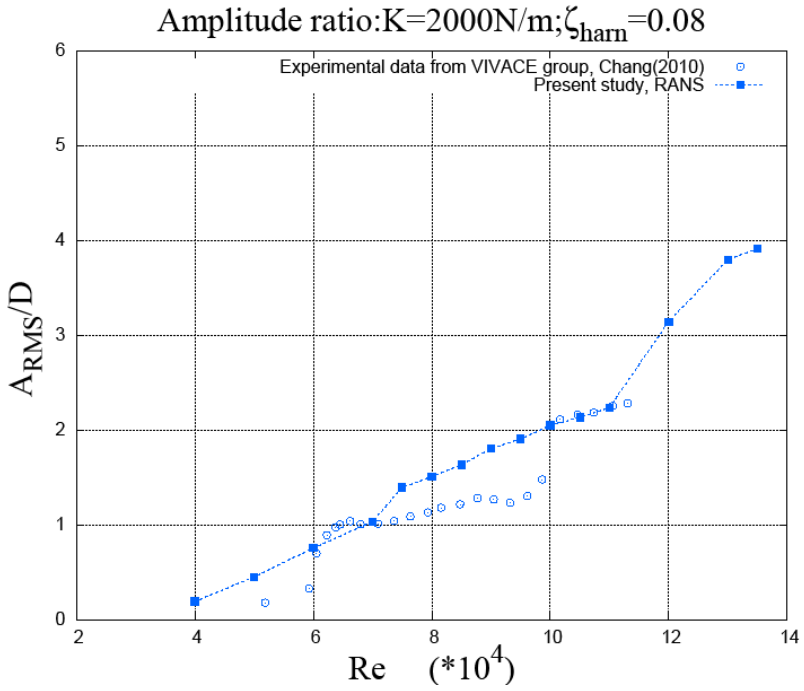

Figure 6.3. RMS amplitude ratio comparison with experiments from MRELab by Chang (2010) (*K*=2000N/m, ζ_{harn}=0.08)

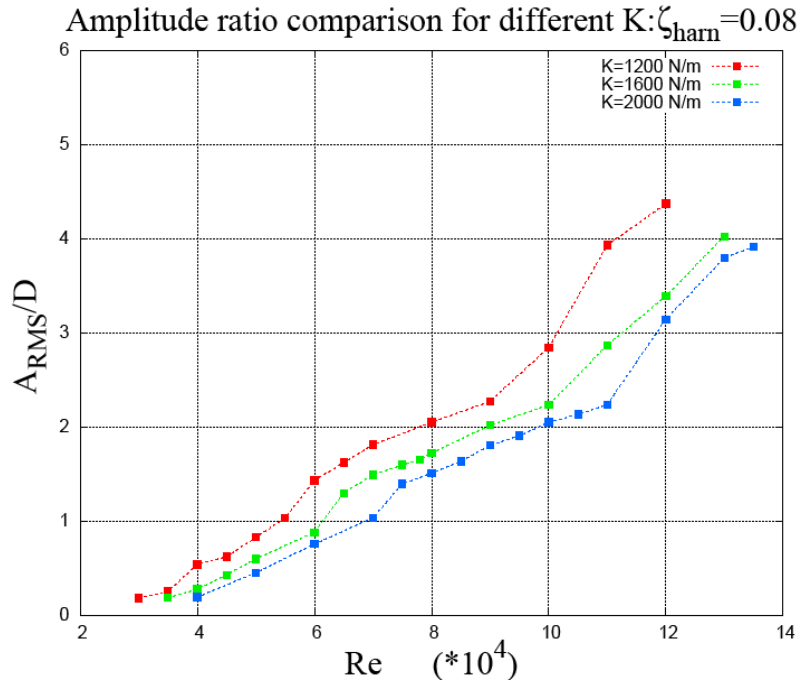

Figure 6.4. RMS amplitude ratio comparison for different *K* values (*K*=1200, 1600 and 2000N/m, ζ_{harn}=0.08)

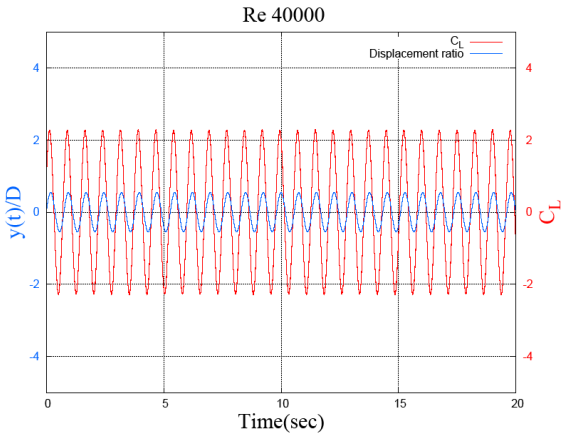

(a1) Lift coefficient and displacement ratio history, *Re*=40,000

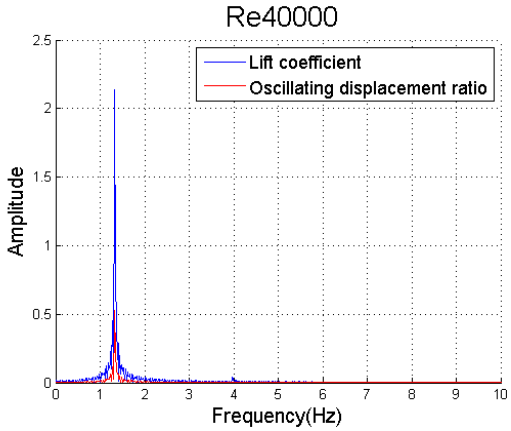

(a2) FFT analysis for lift coefficient and displacement ratio, *Re*=40,000

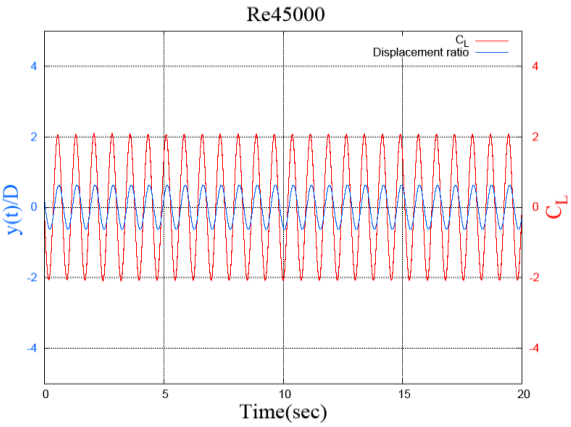

(b1) Lift coefficient and displacement ratio history, *Re*=45,000

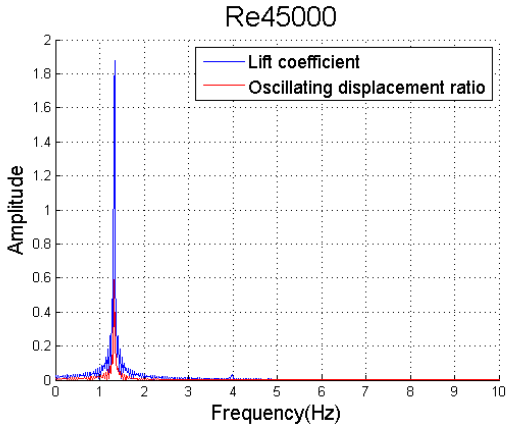

(b2) FFT analysis for lift coefficient and displacement ratio, *Re*=45,000

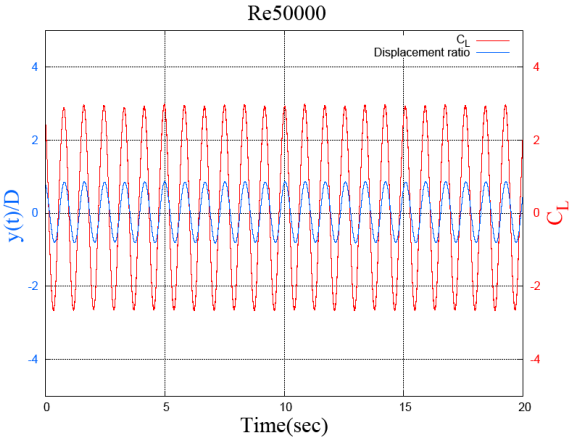

(c1) Lift coefficient and displacement ratio history, *Re*=50,000

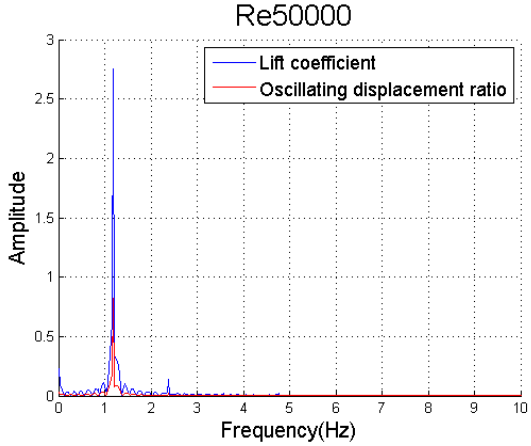

(c2) FFT analysis for lift coefficient and displacement ratio, *Re*=50,000

Figure 6.5. Time history and spectra of lift coefficient (C_L) and displacement ratio($y(t)/D$) for different *Re* cases (40,000≤*Re*≤120,000) (*K*=1200N/m, ζ_{harn}=0.08)

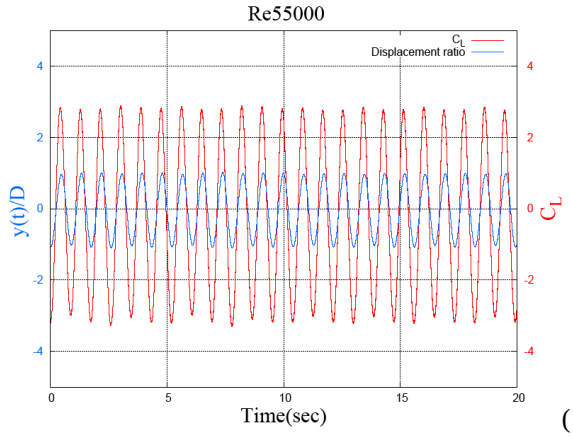

(

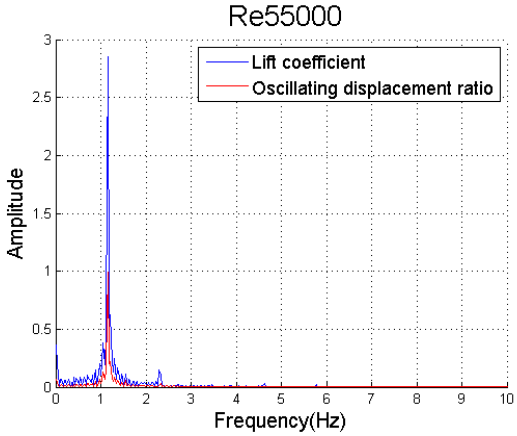

d1) Lift coefficient and displacement ratio history, *Re*=55,000

(d2) FFT analysis for lift coefficient and displacement ratio, *Re*=55,000

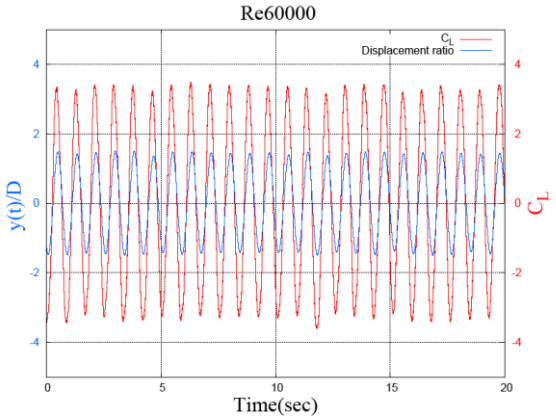

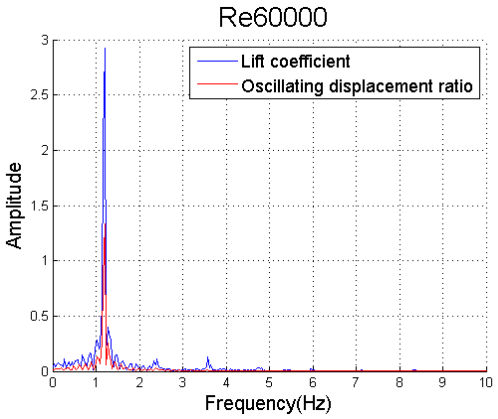

(e1) Lift coefficient and displacement ratio history, *Re*=60,000

(e2) FFT analysis for lift coefficient and displacement ratio, *Re*=60,000

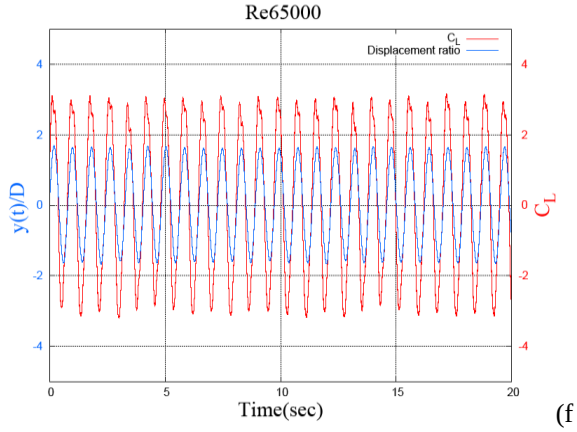

(f

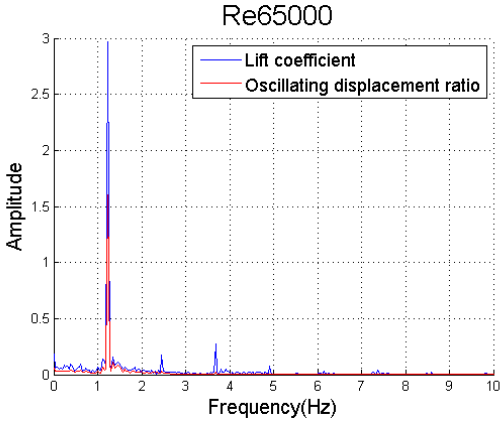

1) Lift coefficient and displacement ratio history, *Re*=65,000

(f2) FFT analysis for lift coefficient and displacement ratio, *Re*=65,000

Continue Figure 6.5

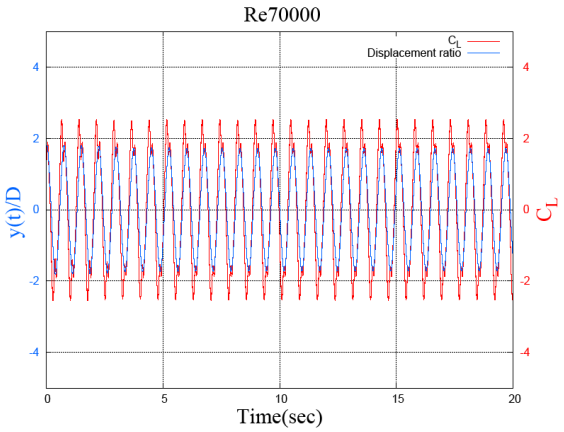

(g1) Lift coefficient and displacement ratio history, *Re*=70,000

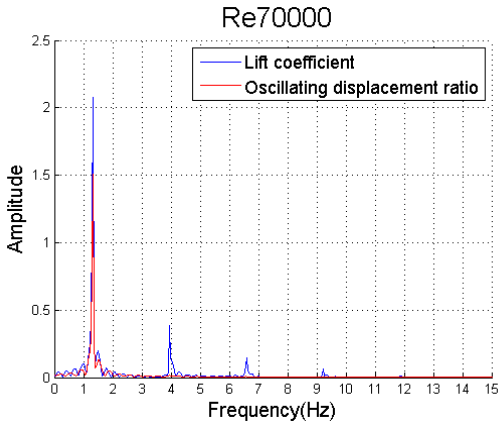

(g2) FFT analysis for lift coefficient and displacement ratio, *Re*=70,000

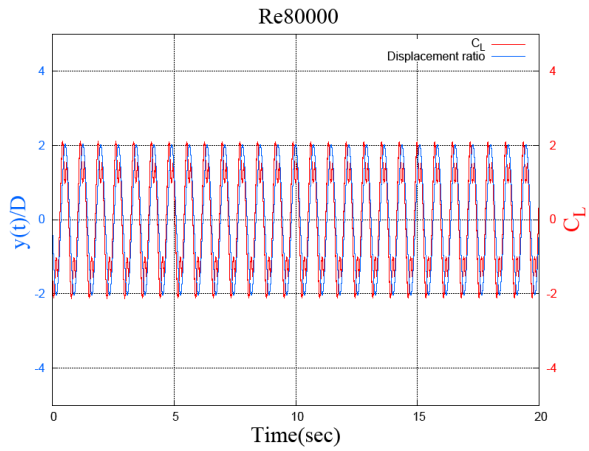

(h1) Lift coefficient and displacement ratio history, *Re*=80,000

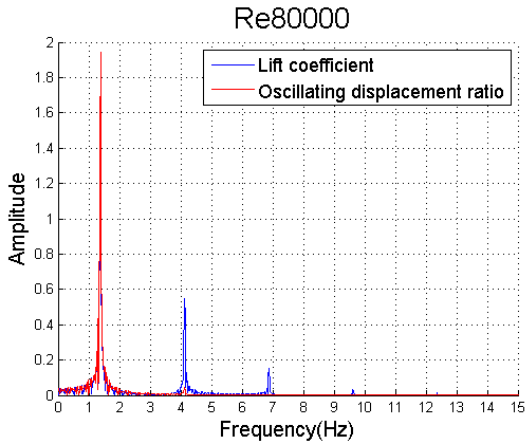

(h2) FFT analysis for lift coefficient and displacement ratio, *Re*=80,000

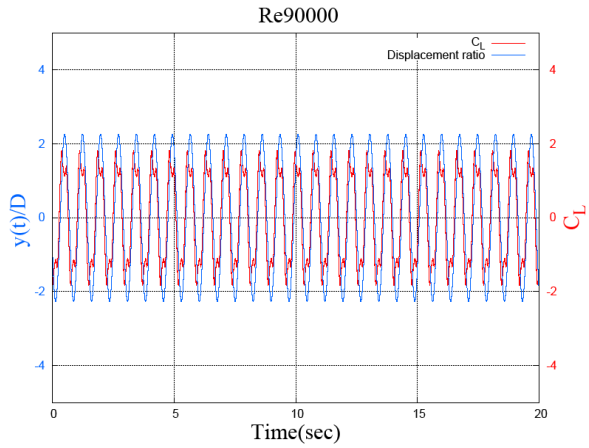

(i1) Lift coefficient and displacement ratio history, *Re*=90,000

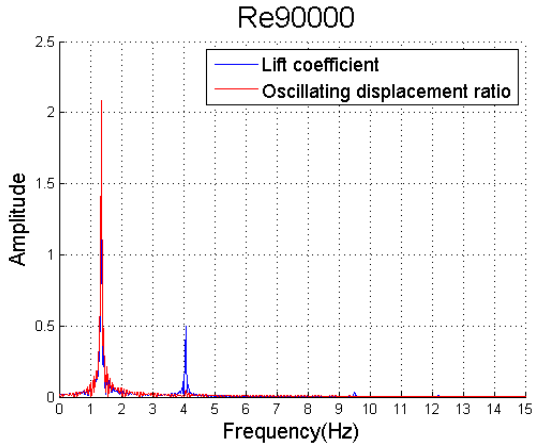

(i2) FFT analysis for lift coefficient and displacement ratio, *Re*=90,000

Continue Figure 6.5

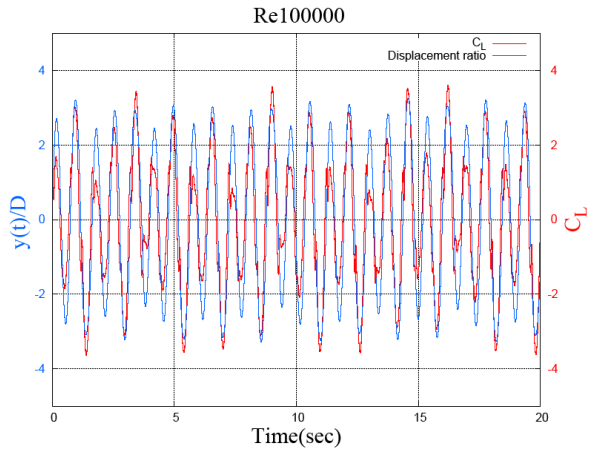

(j1) Lift coefficient and displacement ratio history, *Re*=100,000

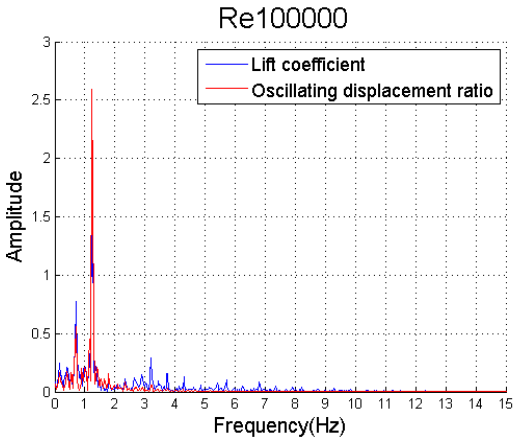

(j2) FFT analysis for lift coefficient and displacement ratio, *Re*=100,000

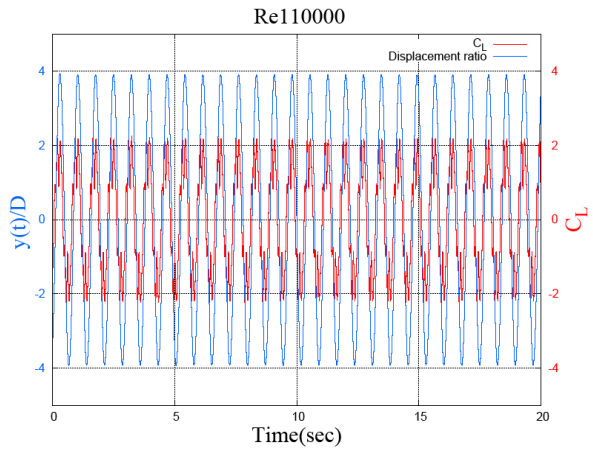

(k1) Lift coefficient and displacement ratio history, *Re*=110,000

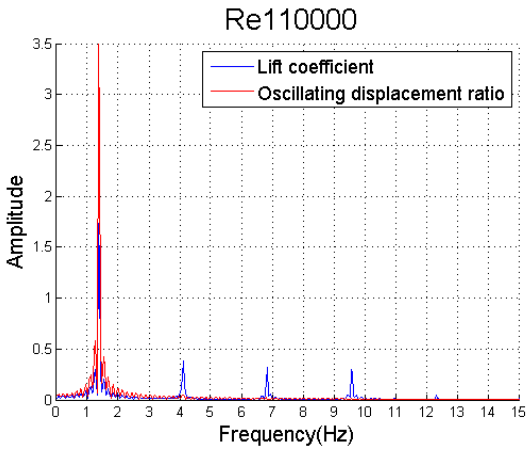

(k2) FFT analysis for lift coefficient and displacement ratio, *Re*=110,000

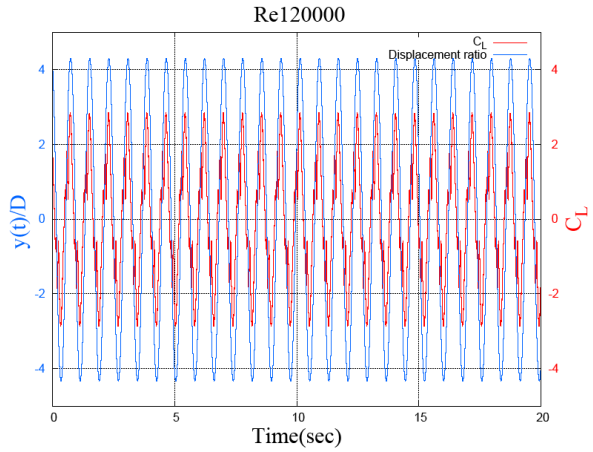

(l1) Lift coefficient and displacement ratio history, *Re*=120,000

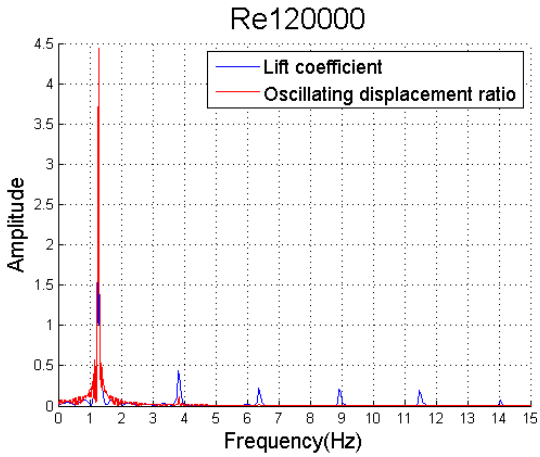

(l2) FFT analysis for lift coefficient and displacement ratio, *Re*=120,000

Continue Figure 6.5

6.2.3. Frequencies and vortex patterns

In Figures 6.6, 6.7, and 6.8, the frequency ratio is plotted over Re and compared with experimental results for three spring constant values, respectively. Comparing with experimental results, the major harmonic frequency in the VIV initial branch are higher and has larger differentiation with the corresponding experimental value. In numerical results, the frequency plots also exhibit three distinct branches and they are consistent with the way that the three branches are defined by amplitude. In the VIV initial branch, the oscillation frequency increases throughout the entire branch. For the K=1200N/m, the increasing trend in the initial branch is similar to what is shown in the cases of K=1600N/m and 2000N/m. Once transition into the upper branch has occurred, a prominent drop-off shows first in the curve, and then the frequency increases again at a modest rate. For the K=1200N/m case, the Re corresponding to the maximum frequency in the plot is Re=80,000 which is about the same as derived in the experiments, however, the numerical value is relatively low. For K=1600N/m and 2000N/m, the frequency peaks shift to higher Re values compared with experiments, and also the frequencies are under-predicted in this VIV upper branch. Transition to the galloping branch is manifested by the second drop-off in the frequency curve. In addition, the frequency keeps decreasing until the fully developed galloping state is reached. In Figure 6.9, all three frequency ratio curves are plotted together to make comparison. Each curve has the similar frequency ratio value range from ~0.8 to ~1. Similarly to what was observed in amplitude behavior, from frequency plots, the conclusion can also be derived that as K goes higher, the transition to the VIV upper branch and to galloping are shifted to higher Re numbers, which is clearly demonstrated in Figure 6.9.

In Figure 6.5, FFT analyses for different Re cases with K=1200N/m are presented. This plotting shows easily how the motion responds to the lift and how Re affects the behavior of lift and motion amplitude throughout the entire synchronization range. Frequencies of lift and displacement for K=1600N/m and ζ_{harn}=0.08 have been discussed in Chapter 5.

Generalities can be easily observed by making comparisons among the results from all those three K cases with relatively high damping level (ζ_{harn}=0.08, $m^*\zeta_{harn}$=0.1504).

The main features for vortex pattern and spectra of lift and displacement are shared with the system with different *K* value. They are summarized below classified per branch:

1. In the VIV initial branch, normally there are two types of vortex structures associated with this regime, namely the 2S and 2P modes. Due to the fact that frequencies of the lift and displacement are resultants of the vortex patterns, they are closely related to each other. When the vortex structure is a 2P or a 2S mode, for both cases, only one dominant major frequency peak shows up in both the lift and displacement spectra. In contrast, for the cases in between 2S and 2P, in other words, in the transition from 2S to 2P, due to additional vortices, the lift spectrum becomes broad-banded with multiple peaks and the displacement spectrum also has additional peaks and the displacement time history is no longer sinusoidal in this time.

2. In the VIV upper branch, from the wake structure point of view, the branch can be subdivided into two phases. The first is the developing phase and the second is the fully developed phase. The fully developed phase is the higher Reynolds number half-branch, where the 2P+4S pattern is dominant. The developing phase is relatively unstable from the point of view of the wake vortex structure. This phase bridges 2P and 2P+4S, and 4 more vortices develop and grow within a limited velocity range. The vortex pattern associated with each *Re* case in this phase is transient state in the sense that no exact pattern is well associated with each *Re* and the pattern switches throughout the time history. For the *K*=1,200N/m and *Re*=55,000 case, the vortex pattern shifts between 2P and P+2S, which is P+S observed from one side of the cylinder and S from the other side. When Re increases to *Re*=60,000, the wake patterns of P+2S, 2P+2S are formed. 2P+2S is the dominant pattern which means P+S shed on both sides per cycle (see Figure 6.10 (a)). For Re=65,000, even more vortices are generated per cycle, P+3S, 2P+2S and even 2P+3S are observed in different cycles. 2P+3S refers to the case with P+S on one side and P+2S on the other, where the first S closely following P is much weaker than the second S and gets struck into the P very quickly right after forming. The show-up of additional vortices explains well the additional multiple peaks in the lift spectrum (see Figures 6.5 (e2), (f2)). Unlike the fully

developed phase, where additional harmonic peaks of lift frequency occur at about 3 times and 5 times of the major frequency (see Figures 6.5 (g2) and (h2)), in the developing phase the frequency spectra are broader and peaks are located at relatively lower frequency about 2 and 3 times the major frequency (see Figures 6.5 (e2), (f2)). The fully developed phase is associated with 2P+4S pattern, which is stable in the sense that it prevails over a relatively broader *Re* range until the end of the upper branch. The lift and displacement during this time are highly periodic (see Figures 6.5 (g1), (h1) and (i1)) and the wake has clearly two vortex trails (see Figure 6.10 (b)).

3. Transition to galloping exhibits a declining trend in the oscillation frequency and the frequency keeps decreasing until the galloping branch is fully developed. The lift and displacement spectra become obviously broad-banded in comparison with previous cases. The vortex pattern is 2P+4S (*Re*=100,000, Figure 6.10(c)). Although the number of singles and pairs of the vortices are the same as those in the upper branch, the differences are dramatic. Firstly, the wake trail is no longer regular two streets, but becomes "S" shape due to the larger displacement and faster convection speed down to the wake (see Figure 6.10 (c)). Secondly, the order of the vortices is different. Instead of shedding a pair and then two singles, in the transition to galloping, one single is generated right before the pair, and then another single follows closely after the pair, shedding almost at the same time with it (see Figure 6.10 (d)). This has also been discussed in Chapter 5 (see Figures 5.12). In addition, the vortex strength for the pairs in this case is much higher compared to other single vortices, which contributes more driving lift force leading to the higher amplitude.

4. In the galloping branch, more harmonic peaks of lift frequency become prominent, namely, 4^{th}, 5^{th} and even 6^{th} in some cases (see Figures 6.5 (k2), (l2)). However, in the displacement FFT, only the first and second peaks are noticeable, no 3^{rd} harmonic is noticeable, which makes the displacement time history nearly sinusoidal (see Figures 6.5 (k2), (l2)). As expected, the number of vortices increases again and the wake pattern changes to 2P+8S (*Re*=120,000, Figure

6.10(d)). Counting the vortices from past the mean position (y=0), one pair of vortices sheds first and four singles follow closely. Interestingly, the vortices always shed alternatively with opposite vorticity. The only exception is when the maximum displacement is reached, two successive vortices with the same vorticity sign are generated almost at the same time and shed together. This observation also applies to other cases in the galloping branch with higher *Re* and more vortices.

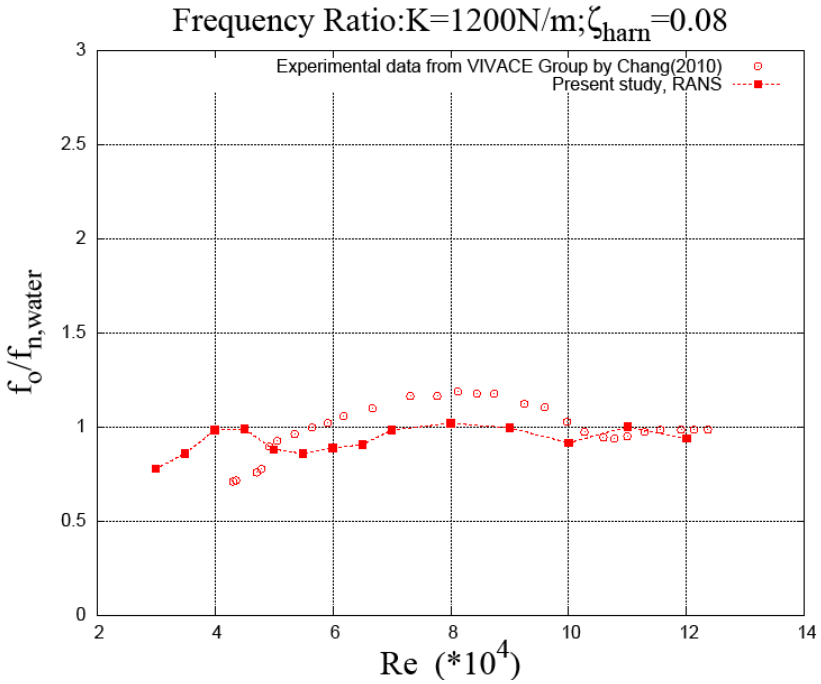

Figure 6.6. Frequency ratio comparison with experiments from MRELab by Chang (2010) (*K*=1200N/m, ζ_{harn}=0.08)

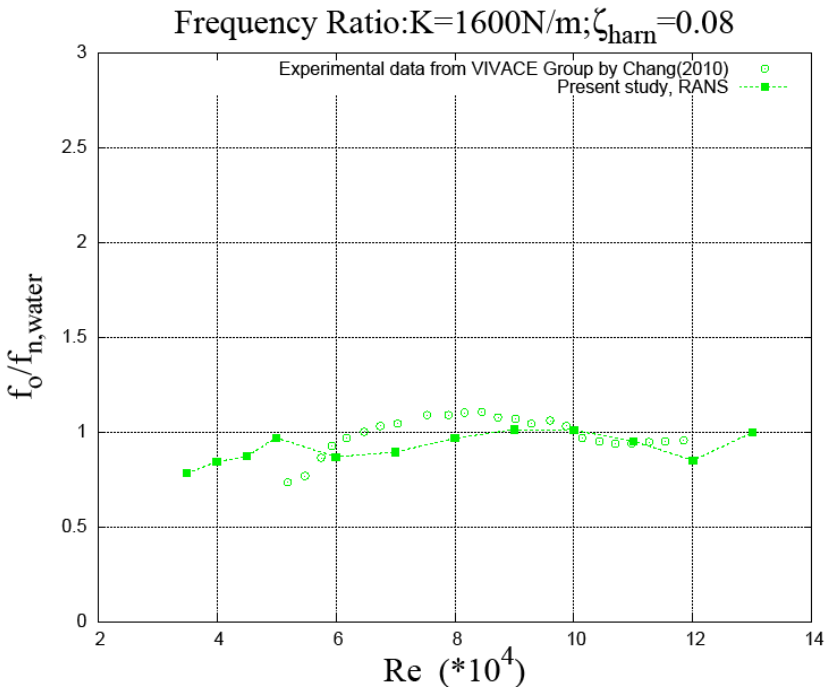

Figure 6.7. Frequency ratio comparison with experiments from MRELab by Chang (2010) (*K*=1600N/m, ζ_{harn}=0.08)

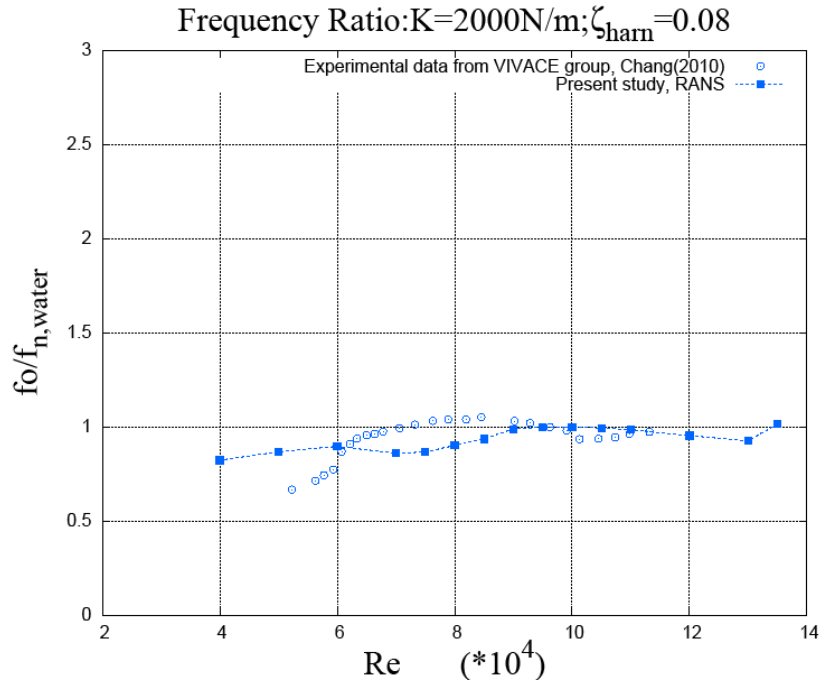

Figure 6.8. Frequency ratio comparison with experiments from MRELab by Chang (2010) (*K*=2000N/m, ζ_{harn}=0.08)

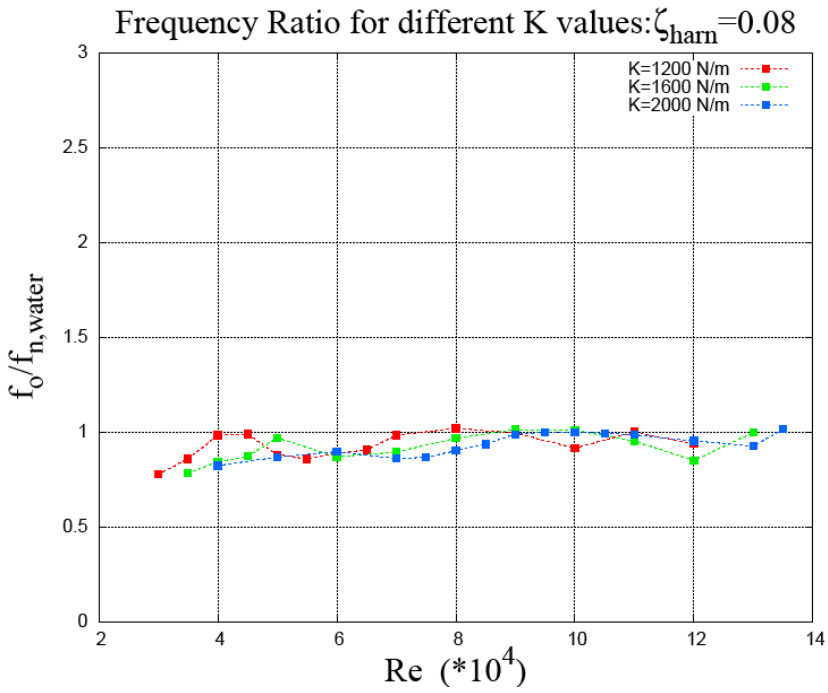

Figure 6.9. Frequency ratio comparison for different *K* values (*K*=1200, 1600, 2000N/m, ζ_{harn}=0.08)

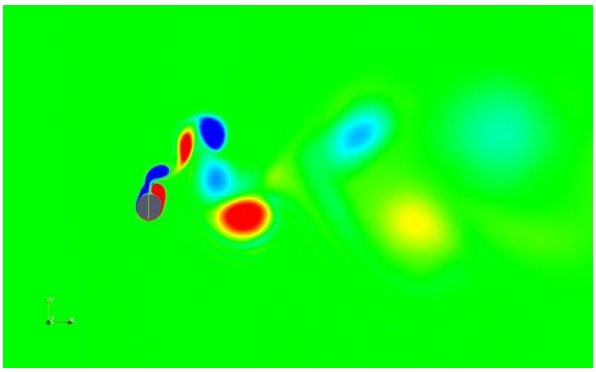

(a) P+2S/2P+2S mixed mode for *Re*=60,000 (P+S is shed for current half cycle, developing regime in upper branch)

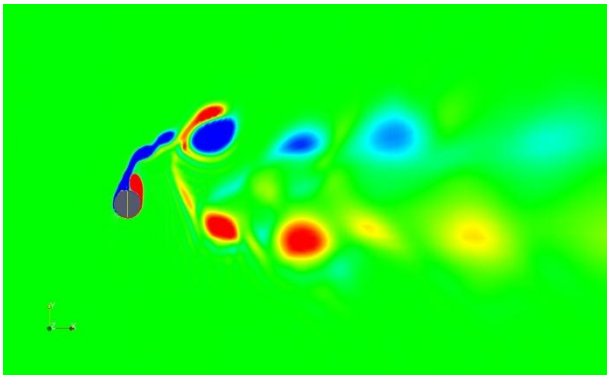

(b) 2P+4S (two streets shown in the wake, *Re*=80,000, developed regime in upper branch)

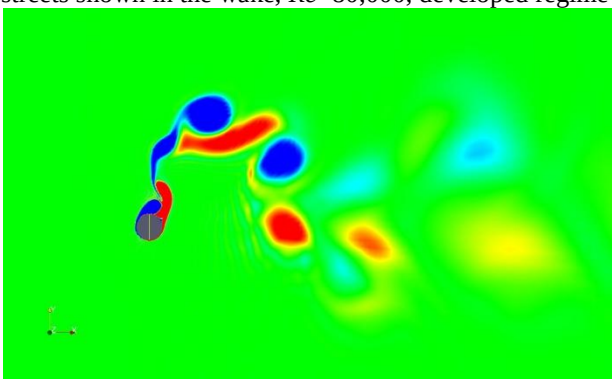

(c) 2P+4S ("S" shape wake, *Re*=100,000, transition to galloping branch)

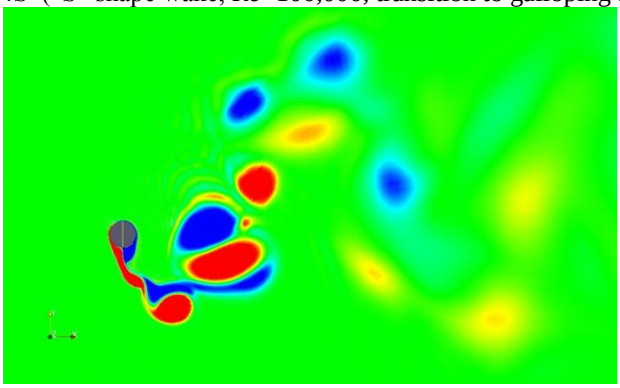

(d) 2P+8S (*Re*=120,000, galloping branch)

Figure 6.10. Different vortex patterns associate with various flow regime (*K*=1200N/m, ζ_{harn}=0.08)

6.3. Effect of damping on FIM of a cylinder with PTC

6.3.1. System parameters

In this section, a series of simulations are performed to investigate the effect of damping on a cylinder with PTC in FIM. The simulation results are compared with those from the VIVACE group for the same experimental parameters (by Chang, 2010). The cylinder with 0.0899 meter diameter (3.5 inch) is used, the spring constant K is 1,600 N/m. The damping is composed of two parts as described in the experiments, namely structural damping $C_{structure}$ and harnessing damping C_{harn} (additional damping). Damping ratios for the harnessing damping ζ_{harn} selected in the current simulations are 0, 0.04, 0.08 and 0.12. All the system parameters are listed in Table 6.2. For PTC, all parameters are kept consistent with those used in Chapter 5, and they are listed in Table 6.3.

Table 6.3. Experimental system parameters

Mass ratio	m^*	1.88
External damping ratio for energy harnessing	ζ_{harn}	0/0.04/0.08/0.12
Total damping ratio	ζ_{total}	0.0122/0.0522/0.0922/0.1322
Mass-damping parameter	$m^* \zeta_{harn}$	0/0.0752/ 0.1504/0.2256
Diameter of circular cylinder	D [cm]	0.0899
Total mass of oscillation	M [kg]	10.75
Spring constant	K [N/m]	1600
Structural damping	$C_{structure}$ [Ns/m]	3.2
Natural frequency in water	$f_{n,water}$ [Hz]	1.5650

Table 6.4. PTC parameters (P60 sandpaper)

Strip placement angle	α_{PTC} [degree]	20 ~ 36, -20 ~ -36
Strips coverage	[degree]	16
Sand paper thickness	P [mm]	0.587
Average height of sand grits	k [mm]	0.26
Total thickness	$T=P+k$ [mm]	0.847

6.3.2. Cylinder displacement (A_{RMS}- Re)*

The RMS amplitude curves of different damping ratios are plotted in comparison with experimental results from the VIVACE group (see Figures 6.11, 6.12, 6.13 and

6.14). The numerical simulations for amplitude are compared with each other in the Figure 6.15. From the plots, it can be observed that differences exist between numerical and experimental outcomes and become larger as the damping decreases. For the case with damping ratio ζ_{harn}=0, in which case only limited structural damping is present, the amplitude shoots up to more than 5 times the cylinder diameter in the galloping branch, double what recorded in the experiments. This is mainly caused by the facts that, firstly, in experiments stoppers are placed on both sides of the mean position with a distance around 2.8 times the diameter, which sets the experimental limit; secondly, the free surface and bottom boundary are not modeled as boundary conditions. These boundary conditions limit FIM in experiments.

In Figure 6.15, RMS amplitude ratios are compared for different damping values. It clearly demonstrates the trend that, for every *Re* considered the case with higher damping shows lower response amplitude. For different branches throughout the entire curve, the sensitivity to damping also varies, which can be presented by the different amount of amplitude increments for all branches. In the VIV initial branch, where the amplitude just starts to increase, the differences among the response in Figure 6.15 are small and this is partly caused by the limited amplitude itself at the beginning of the synchronization. As *Re* increases, the differences become obvious and finally become significant when the galloping branch is reached.

When damping decreases, one feature becomes quite conspicuous and has not been observed before. It is the "beat" like behavior in lift and displacement. In Figure 6.16, the cases in different branches for the system with K=1600N/m, ζ_{harn}=0, ζ_{total}=0.0122 are studied. The displacement and lift are plotted together, and FFT analyses are also performed for each *Re* case. For the previous cases, the damping level is relatively high, with ζ_{harn}=0.08, ζ_{total}=0.091~0.094. In comparison with those higher damping systems, the major differences show in the VIV initial branch. As discussed in Chapter 5 as well as in Section 6.2, the VIV initial branch is normally associated with two types of vortex patterns, which are 2S and 2P. When a *Re* case is well identified as a 2S or 2P mode, the lift and displacement spectra are single-peaked and narrow-banded, which gives a sinusoidal like profile for both of the lift and displacement history, while the lift for the cases between these 2S and 2P modes are relatively broadband with

multiple peaks around the major frequency. Quite different from these observations, when damping decreases to a certain level, the lift and displacement spectra are multi-peaked, and the "beat" like lift and displacement profiles start to become notable and last throughout the VIV initial branch until the upper branch (see Figures 6.16 (b1), (c1), (d1) and (e1)). This phenomenon is similar to another low damping smooth cylinder case from Williamson discussed in Chapter 4. The similarities between the two cases are low damping and multi-peak lift and displacement spectra in the VIV initial and upper branches. The damping is ζ_{total}=0.0054, which is even lower than in our cases. The VIV initial branch is featured with a double-peaked displacement spectrum region and single-peaked region (see Figure 4.3). Moreover, from the RANS simulations of this system in present study, the case of *Re*=4000, which is in the initial branch right before transition to the upper branch, presents "beat" like lift and displacement profiles (Figure 6.19). This beating behavior in the low flow speed regime related to low damping was also observed by Brika (1993) and Xu (2009). Although there are resemblances in the initial branch for these two low damping systems, the modified cylinder surface geometry leads to a bifurcation in the behavior of the upper branch. For the smooth cylinder case, the phase angle changes from 0^o to about 180^o in the upper branch. This out-of-phase lift can no longer provide a lift driving force in time for higher amplitude, in which case after having reached the maximum value the amplitude drops and the lower branch follows. For the cylinder with PTC, during the upper branch, the lift is always in phase with the displacement, which allows the lift forces to be utilized effectively throughout the moving process. As expected, it further brings in the galloping branch with even higher amplitude (see Figures 6.16 (h1) and (i1)).

The effect of damping on amplitude can be well observed when all 4 sets of data are analyzed together. In Figures 6.17 and 6.18, the cases of the VIV initial branch and transitioning to the VIV upper branch for the system with *K*=1600N/m, ζ_{harn}=0.04, ζ_{total}=0.0522 and *K*=1600N/m, ζ_{harn}=0.12, ζ_{total}=0.1322 are presented for comparison. The plots of displacements and lift coefficient for the system with *K*=1600N/m, ζ_{harn}=0.08 can be found in Chapter 5 (see Figure 5.5, 5.6). For ζ_{harn}=0.04 case, the initial branch is approximately in the range from *Re*=30,000 to 45,000. At the beginning of this branch, for *Re*=30,000 the lift spectrum is single-peaked. Afterwards, the beating behavior starts

to appear in the lift and displacement time histories and lasts throughout the rest of the initial branch similarly to what was found in ζ_{harn}=0 case (see Figures 6.17 (a1), (b1), (c1) and (d1)). When ζ_{harn} increases to 0.12, no "beat" like lift and displacement profile appear in the initial branch. Even no multi-peaked lift spectrum exists for the mode switching cases between 2S and 2P, as it does in the ζ_{harn}=0.08 case. The spectra for lift and displacement are all single-peaked narrow-banded (see Figure 6.18). From the results above, there is clearly a trend of energy dissipating and frequency filtering in the initial branch as damping goes up. Energy dissipating obviously means reduction in displacement. Frequency filtering refers to the fact that as damping increases the response with frequency components other than the major one are dissipated, which eliminates the beating behavior in motion and returns the single frequency response.

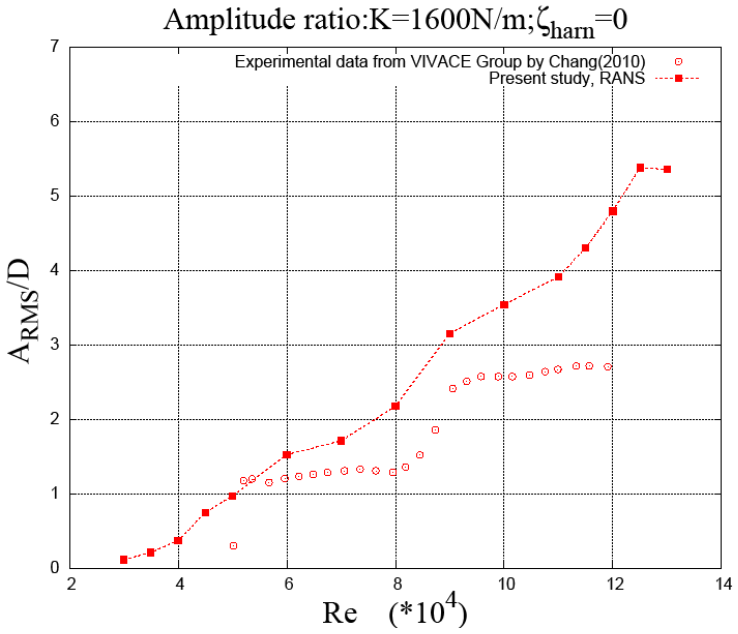

Figure 6.11. RMS amplitude ratio comparison with experiments from MRELab by Chang (2010) (*K*=1600N/m, ζ_{harn}=0)

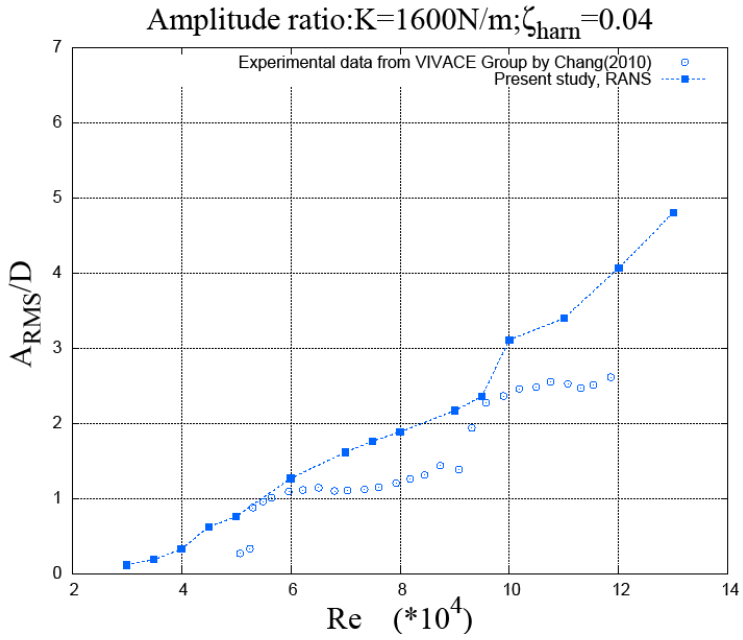

Figure 6.12. RMS amplitude ratio comparison with experiments from MRELab by Chang (2010) (*K*=1600N/m, ζ_{harn}=0.04)

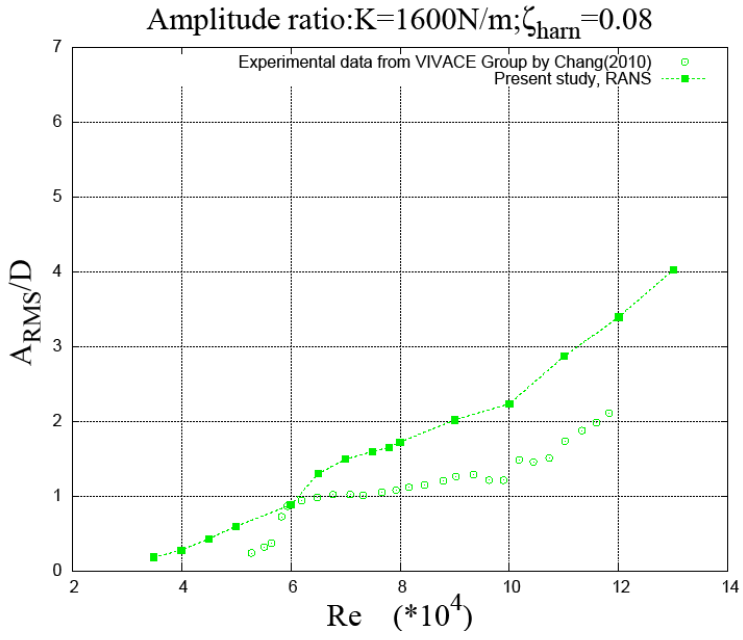

Figure 6.13. RMS amplitude ratio comparison with experiments from MRELab by Chang (2010) (*K*=1600N/m, ζ_{harn}=0.08)

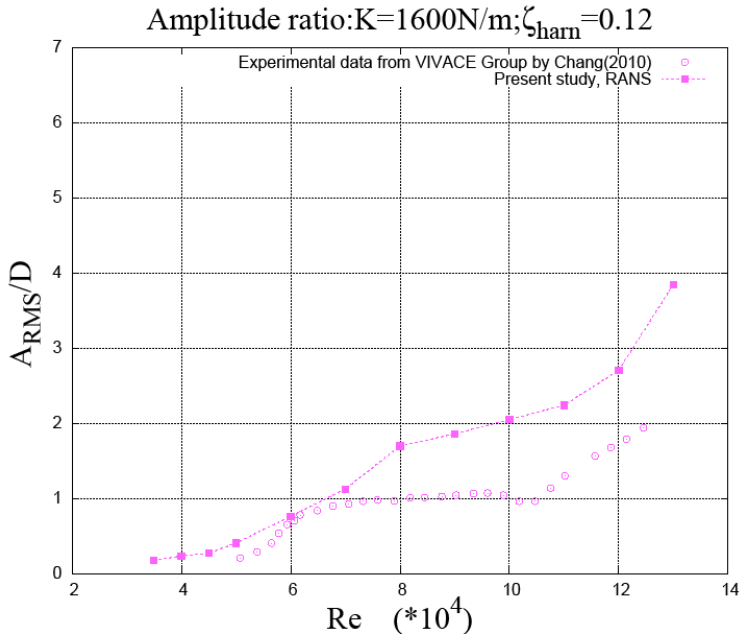

Figure 6.14. RMS amplitude ratio comparison with experiments from MRELab by Chang (2010) (*K*=1600N/m, ζ_{harn}=0.12)

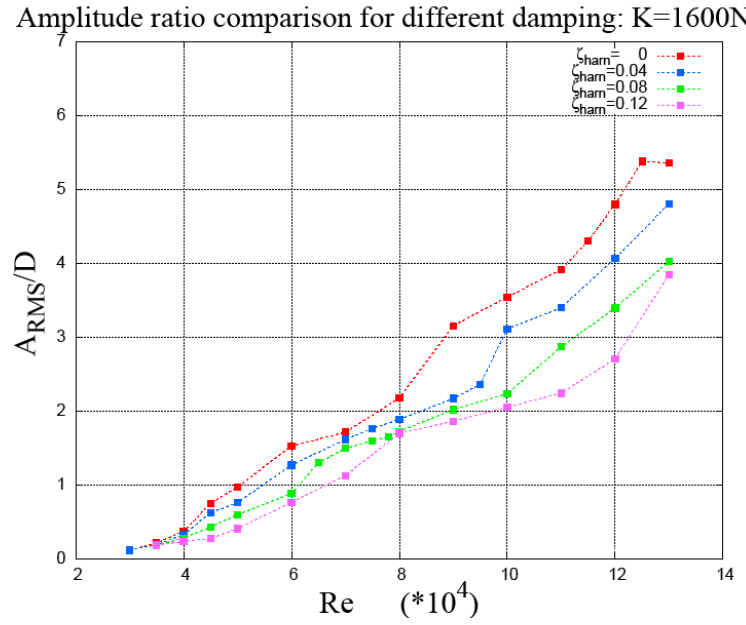

Figure 6.15. RMS amplitude ratio comparison for different damping ζ_{harn} levels (*K*=1600N/m, ζ_{harn}=0, 0.04, 0.08 and 0.12)

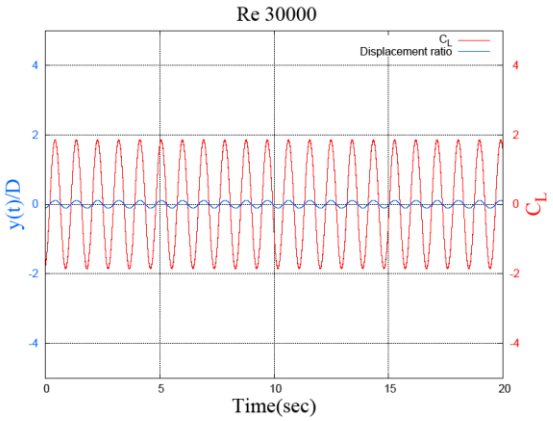

(a1) Lift coefficient and displacement ratio history, *Re*=30,000

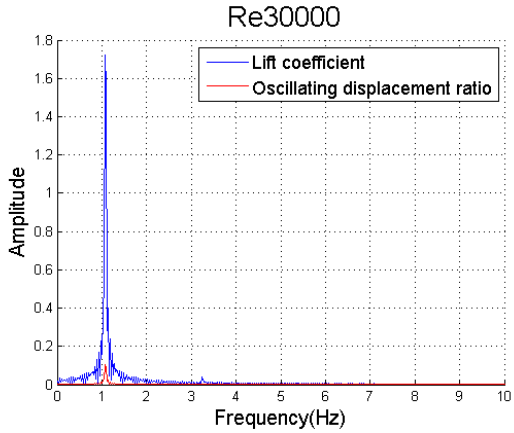

(a2) FFT analysis for lift coefficient and displacement ratio, *Re*=30,000

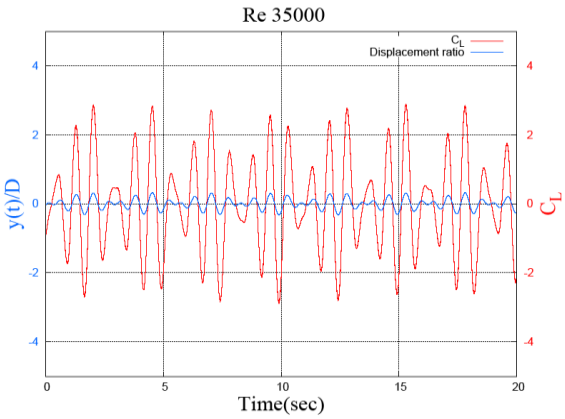

(b1) Lift coefficient and displacement ratio history, *Re*=35,000

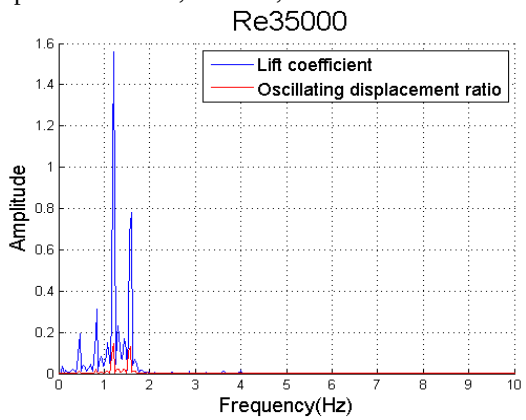

(b2) FFT analysis for lift coefficient and displacement ratio, *Re*=35,000

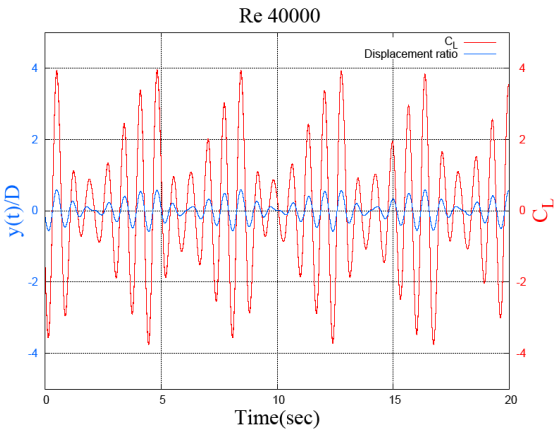

(c1) Lift coefficient and displacement ratio history, *Re*=40,000

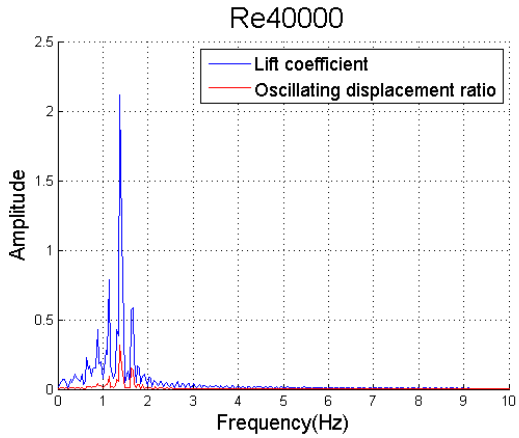

(c2) FFT analysis for lift coefficient and displacement ratio, *Re*=40,000

Figure 6.16. Time history and spectra of lift coefficient (C_L) and displacement ratio ($y(t)/D$) for different *Re* cases (30,000≤*Re*≤130,000) (*K*=1600N/m, ζ_{harn}=0)

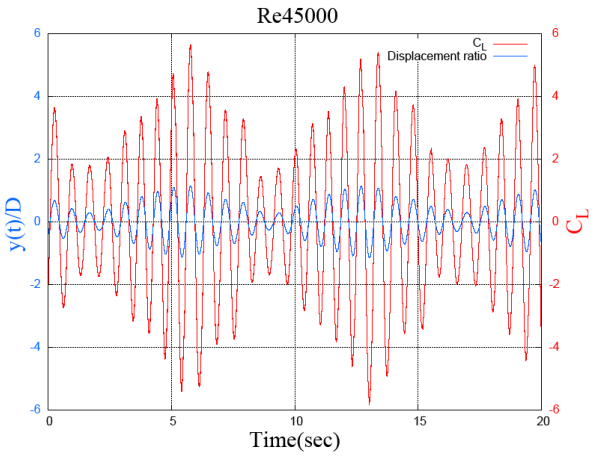

(d1) Lift coefficient and displacement ratio history, *Re*=45,000

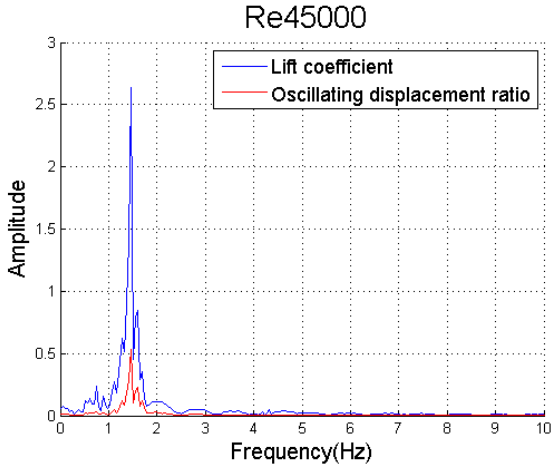

(d2) FFT analysis for lift coefficient and displacement ratio, *Re*=45,000

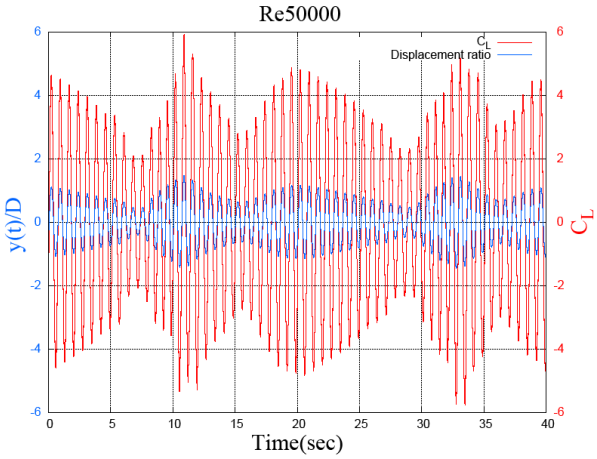

(e1) Lift coefficient and displacement ratio history, *Re*=50,000

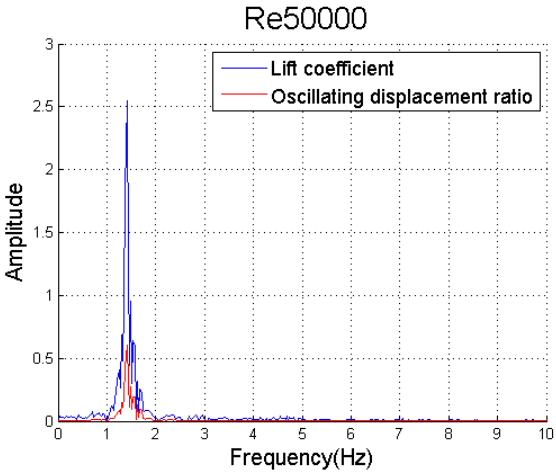

(e2) FFT analysis for lift coefficient and displacement ratio, *Re*=50,000

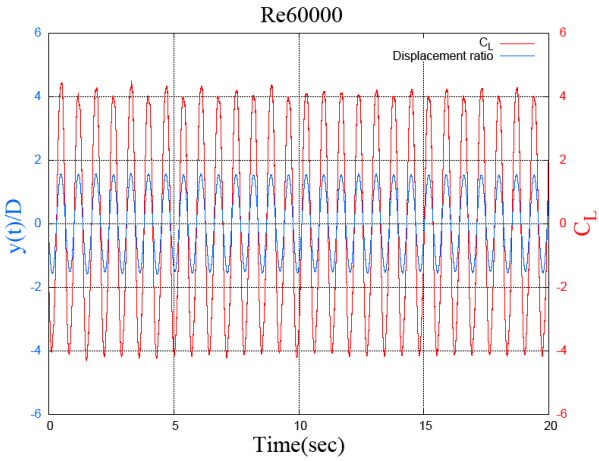

(f1) Lift coefficient and displacement ratio history, *Re*=60,000

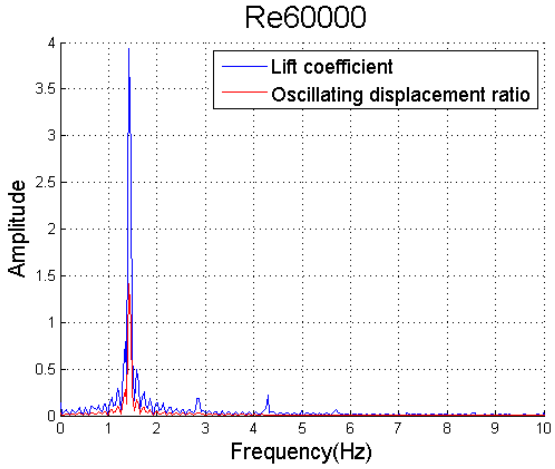

(f2) FFT analysis for lift coefficient and displacement ratio, *Re*=60,000

Continue Figure 6.16.

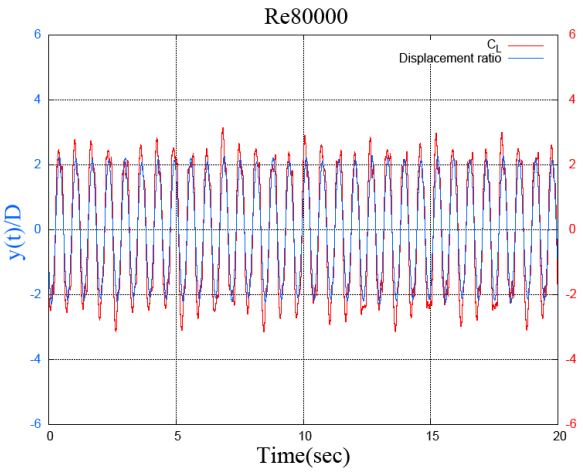

(g1) Lift coefficient and displacement ratio history, *Re*=80,000

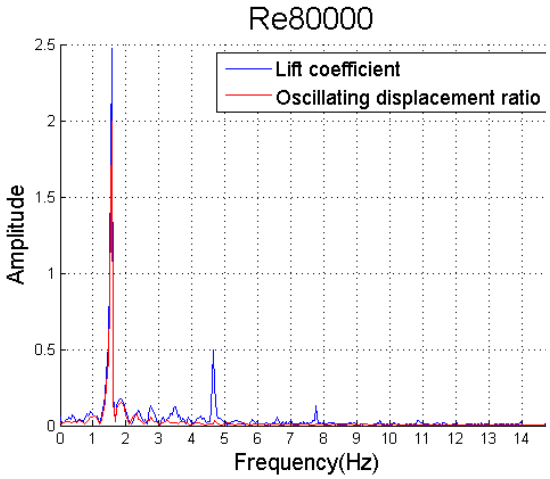

(g2) FFT analysis for lift coefficient and displacement ratio, *Re*=80,000

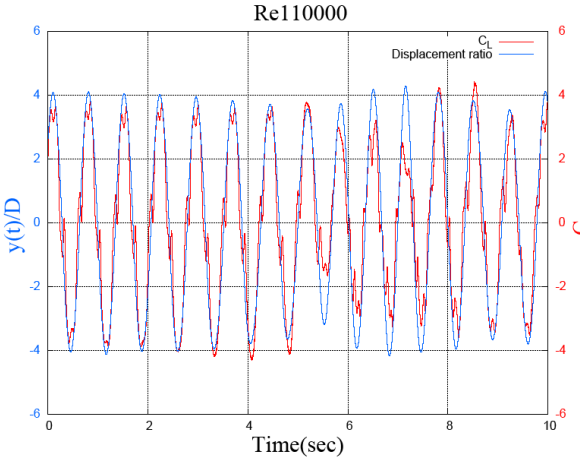

(h1) Lift coefficient and displacement ratio history, *Re*=110,000

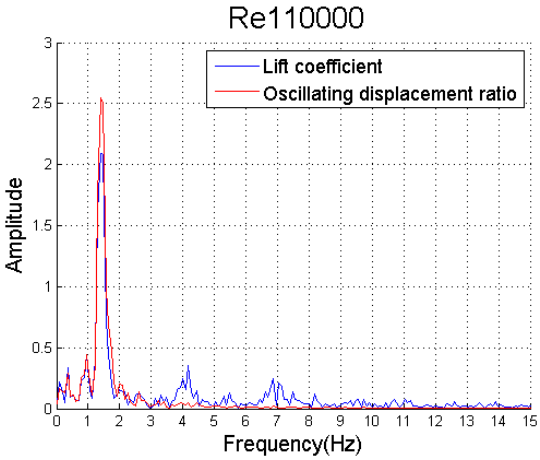

(h2) FFT analysis for lift coefficient and displacement ratio, *Re*=110,000

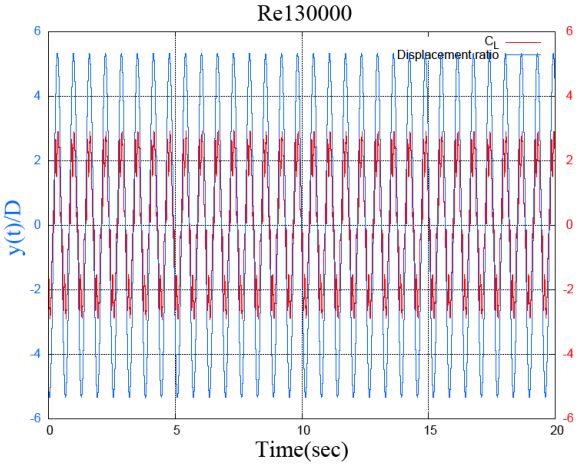

(i1) Lift coefficient and displacement ratio history, *Re*=40,000

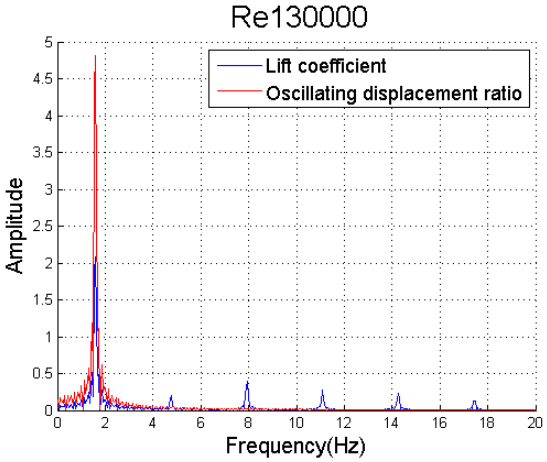

(i2) FFT analysis for lift coefficient and displacement ratio, *Re*=130,000

Continue Figure 6.16

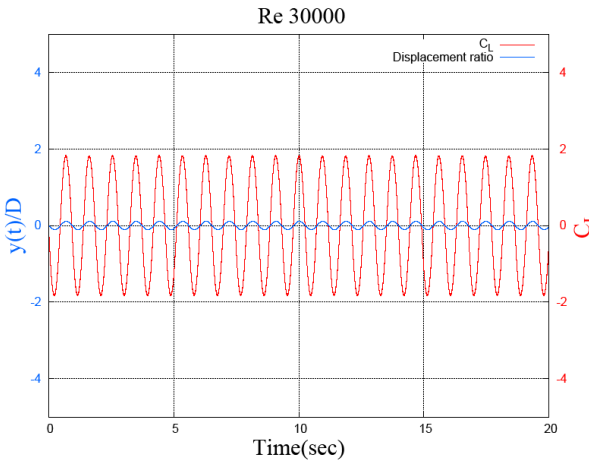

(a1) Lift coefficient and displacement ratio history, *Re*=30,000

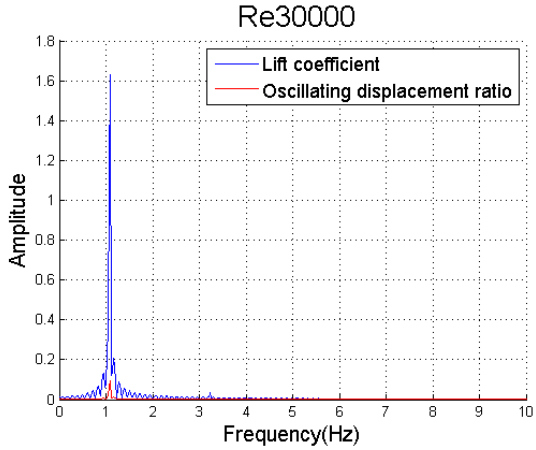

(a2) FFT analysis for lift coefficient and displacement ratio, *Re*=30,000

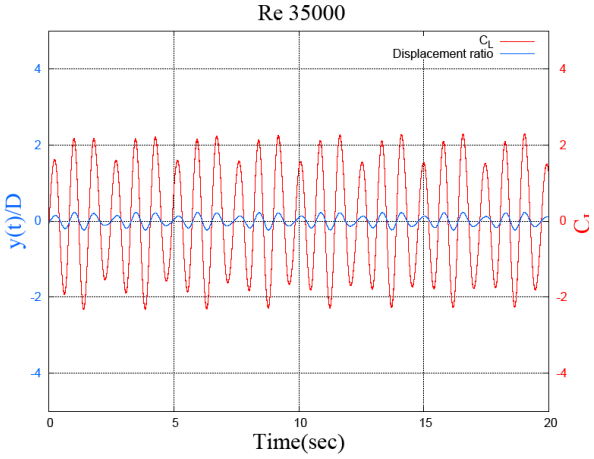

(b1) Lift coefficient and displacement ratio history, *Re*=35,000

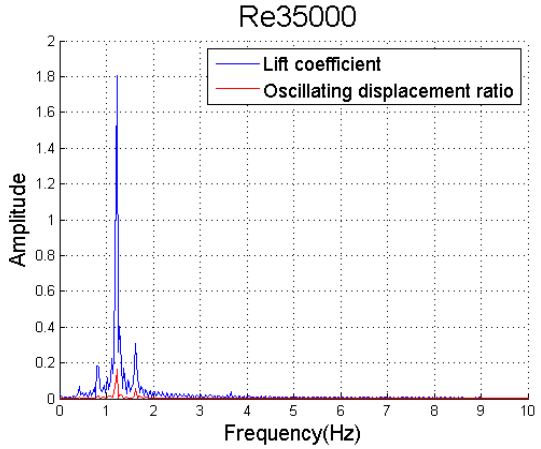

(b2) FFT analysis for lift coefficient and displacement ratio, *Re*=35,000

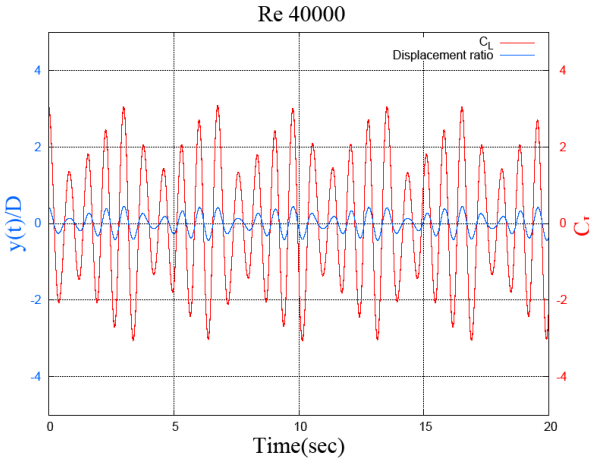

(c1) Lift coefficient and displacement ratio history, *Re*=40,000

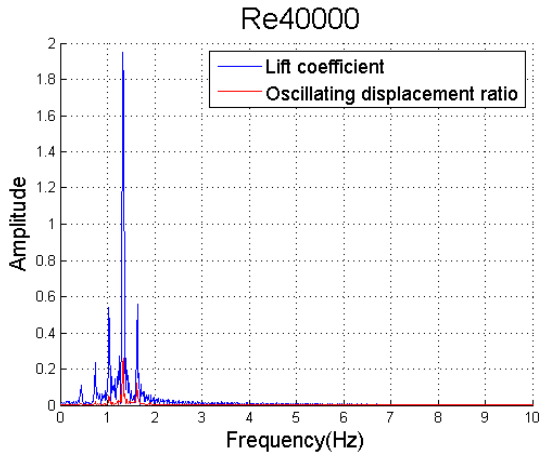

(c2) FFT analysis for lift coefficient and displacement ratio, *Re*=40,000

Figure 6.17. Time history and spectra of lift coefficient (C_L) and displacement ratio ($y(t)/D$) for different *Re* cases (30,000≤*Re*≤60,000) (*K*=1600N/m, ζ_{harn}=0.04)

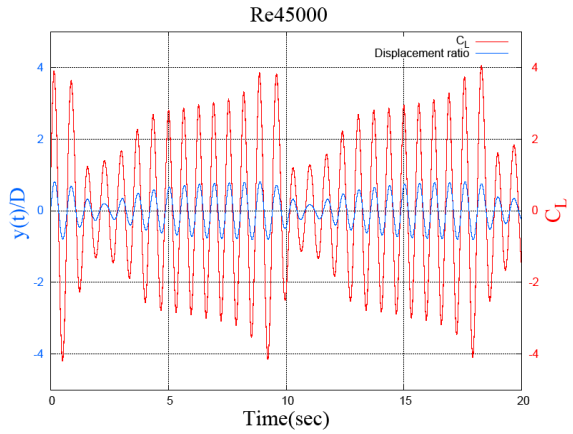

(d1) Lift coefficient and displacement ratio history, *Re*=46,000

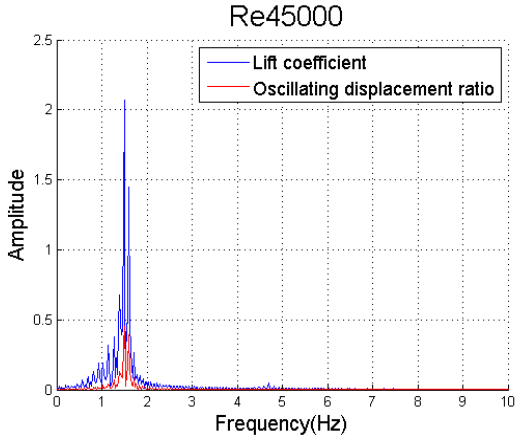

(d2) FFT analysis for lift coefficient and displacement ratio, *Re*=45,000

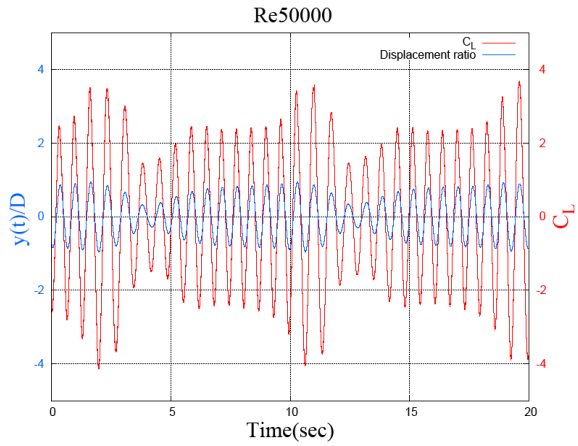

(e1) Lift coefficient and displacement ratio history, *Re*=50,000

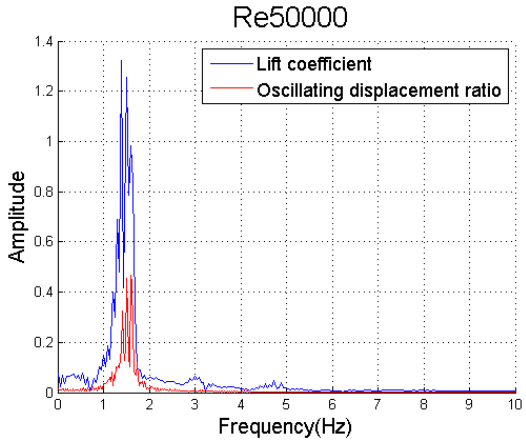

(e2) FFT analysis for lift coefficient and displacement ratio, *Re*=50,000

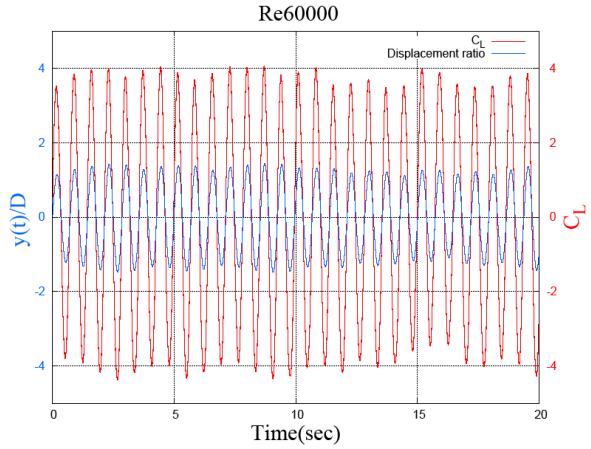

(f1) Lift coefficient and displacement ratio history, *Re*=60,000

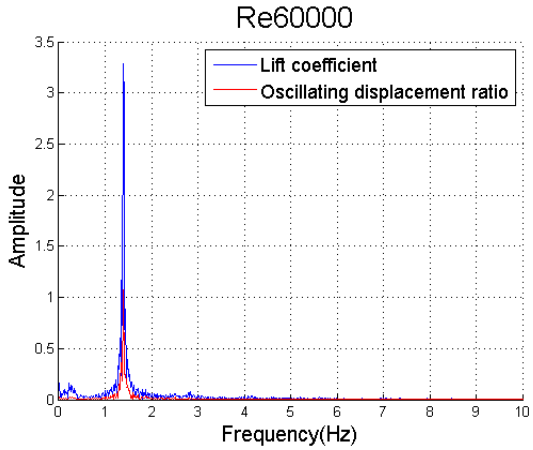

(f2) FFT analysis for lift coefficient and displacement ratio, *Re*=60,000

Continue Figure 6.17

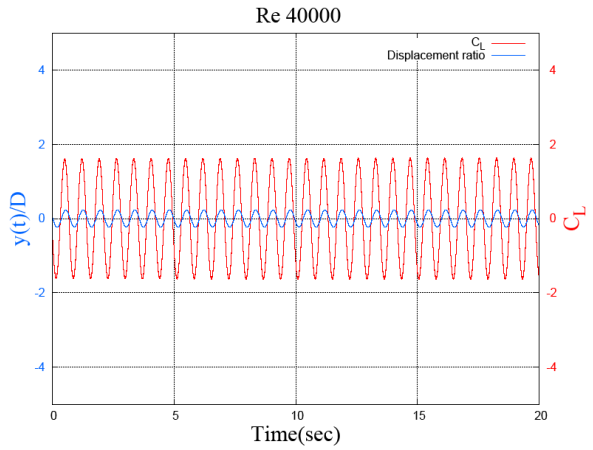

(a1) Lift coefficient and displacement ratio history, *Re*=40,000

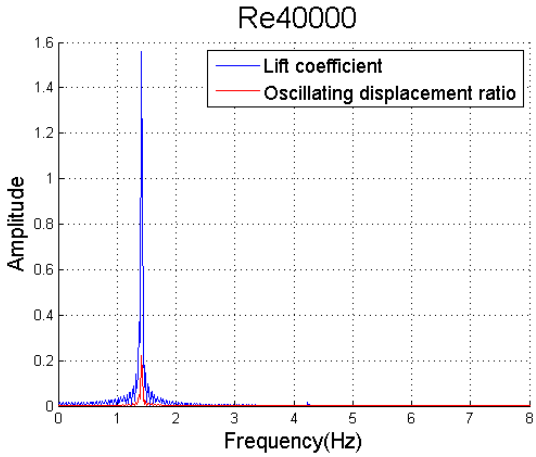

(a2) FFT analysis for lift coefficient and displacement ratio, *Re*=40,000

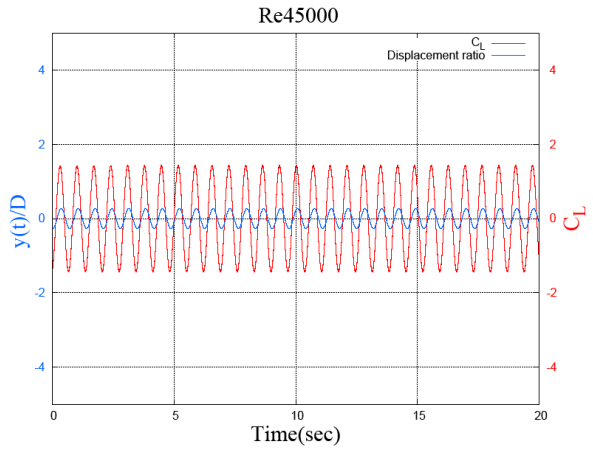

(b1) Lift coefficient and displacement ratio history, *Re*=45,000

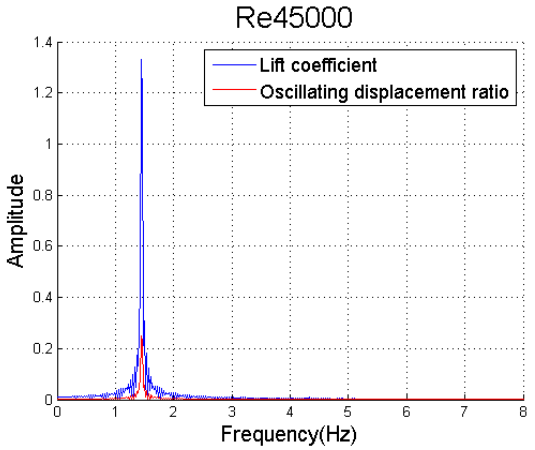

(b2) FFT analysis for lift coefficient and displacement ratio, *Re*=45,000

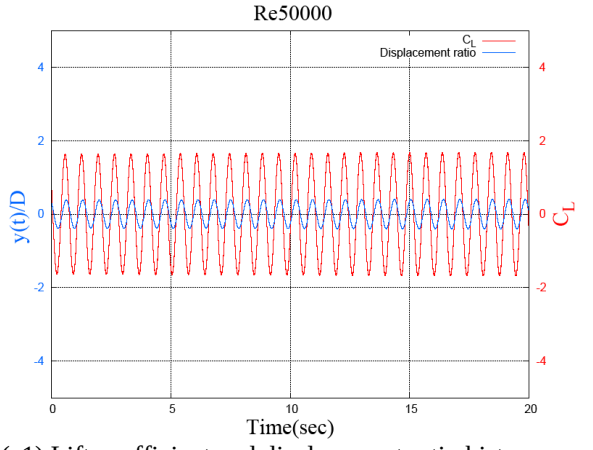

(c1) Lift coefficient and displacement ratio history, *Re*=50,000

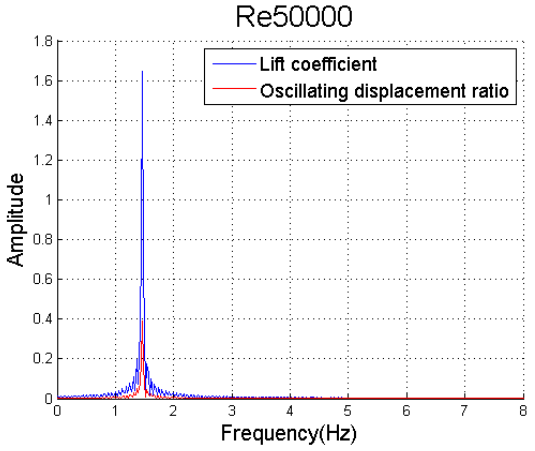

(c2) FFT analysis for lift coefficient and displacement ratio, *Re*=50,000

Figure 6.18. Time history and spectra of lift coefficient (C_L) and displacement ratio ($y(t)/D$) for different *Re* cases (40,000≤*Re*≤50,000) (*K*=1600N/m, ζ_{harn}=0.12)

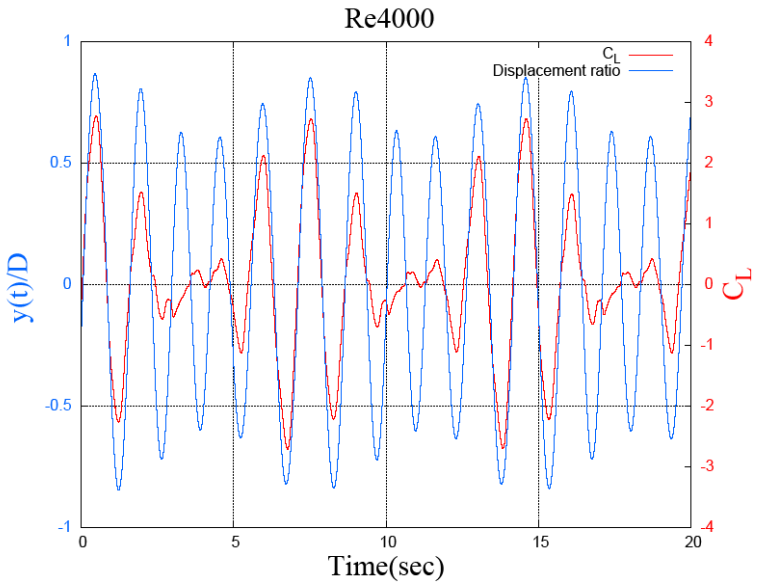

Figure 6.19. Time history of lift coefficient (C_L) and displacement ratio ($y(t)/D$) for $m^*\zeta$=0.013, m^*=2.4; Beating behavior is found for lift and displacement in this low damping case (the system parameters are the same as in Khalak and Williamson 1999)

6.3.3. Damping effect on different branches

As damping changes, there are not only variations in the behavior of displacement, but also in the transition between branches and branch coverage. The sensitivity to damping varies when different regimes are considered. The damping does not have much effect on the coverage of the initial branch. The end point of this region does not change much for different systems. For ζ_{harn}=0 and 0.04, it is around Re=~45,000, and for ζ_{harn}=0.08 and 0.12 the initial branches end at Re=~50,000. However, the transition points to the galloping branches are remarkably changed for different damping values. The higher the damping is, the longer the upper branch lasts (see Figure 6.15) and, the shorter the transition to the galloping branch becomes. In the case of ζ_{harn}=0, the transition takes place around Re=~90,000, in comparison with around 100,000, 110,000 and 120,000 for ζ_{harn}=0.04, 0.08 and 0.12, respectively.

When damping is low, in the case of ζ_{harn}=0, the lift spectrum in the upper branch shares the same features as in the ζ_{harn}=0.08 case. At first, in the developing regime, the second and third harmonic frequencies occur at 2 and 3 times the major frequency. However, as Re goes higher, after switching to the developed upper branch regime, the second and third harmonic frequencies shift to 3 and 5 times the major frequency. In

addition to these similarities, the lift and displacement show distinctions for the low damping case. It has broader band around the major frequencies, which is demonstrated by non-periodic displacement and lift time history. This also can be attributed to the frequency filtering effect of a higher damping system, which is comparable to what happened in the initial branch.

6.3.4. Frequencies of lift and oscillation

In Figures 6.20, 6.21, 6.22 and 6.23 the ratio of major oscillation is plotted versus *Re* and compared with experimental results for ζ_{harn}=0, 0.04, 0.08 and 0.12, respectively. As observed before, the three branches of the frequency ratio are found in each case. The similar characteristics shared by different damping can be summarized as follows:

1. The frequency ratio for the VIV initial branch increases monotonically until the end of the branch.

2. The first reduction in the frequency manifests the initiation of the upper branch, and this point is not sensitive to the damping level.

3. In the transitional regime to galloping, the frequency ratio decreases again until the fully developed galloping branch is reached (see Figures 6.20, 6.21, 6.22 and 6.23). However, the location of this second time reduction and the coverage of this decreasing frequency range vary with different damping levels, indicating that the transition to galloping regime is remarkably affected by damping.

4. The value ranges of the oscillation frequency ratio for different damping are comparable with the maximum value around 1.

As discussed in previous sections, when the damping is low enough, the beating phenomenon shows in the displacement and the lift time traces in the initial branch. This is caused by multiple frequency peaks in the lift and displacement spectra, which are very close to each other. There is another interesting trend worth to mention for the frequencies in this region. For a certain damping value, for example ζ_{harn}=0, when increasing *Re*, the peaks tend to get even closer to each other and more frequency peaks

show up. At the end of the initial branch, the peaks finally become connected with each other and the spectra turn into broad-banded.

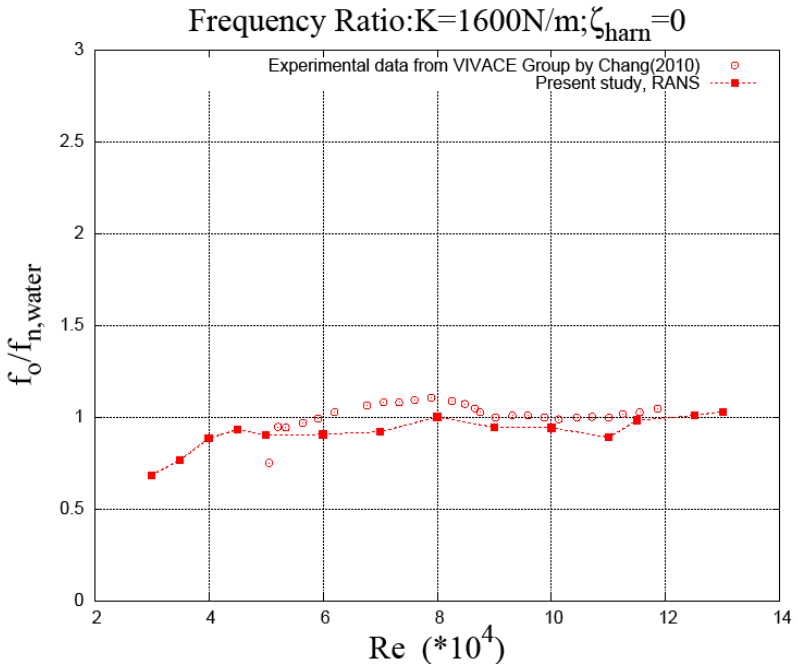

Figure 6.20. Frequency ratio comparison with experiments from MRELab by Chang (2010) (*K*=1600N/m, ζ_{harn}=0)

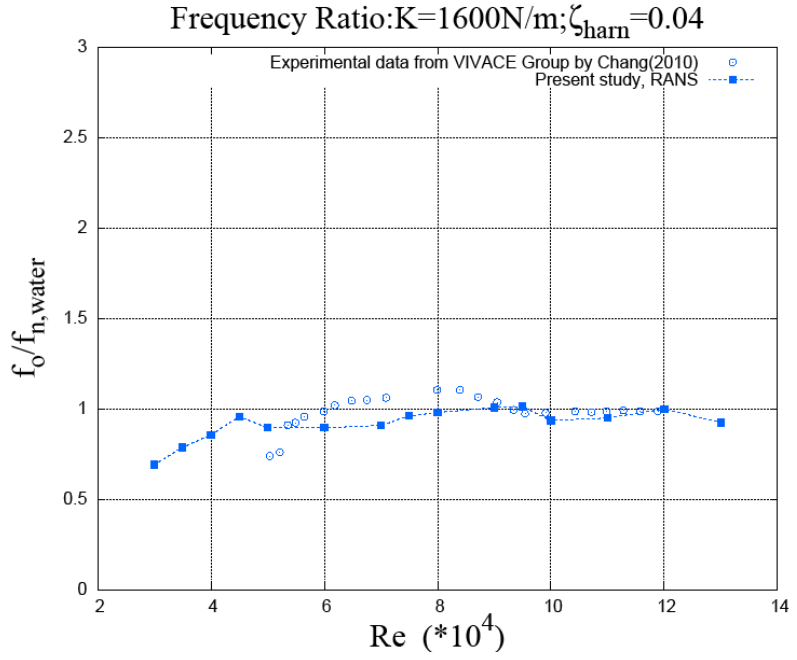

Figure 6.21. Frequency ratio comparison with experiments from MRELab by Chang (2010) (*K*=1600N/m, ζ_{harn}=0.04)

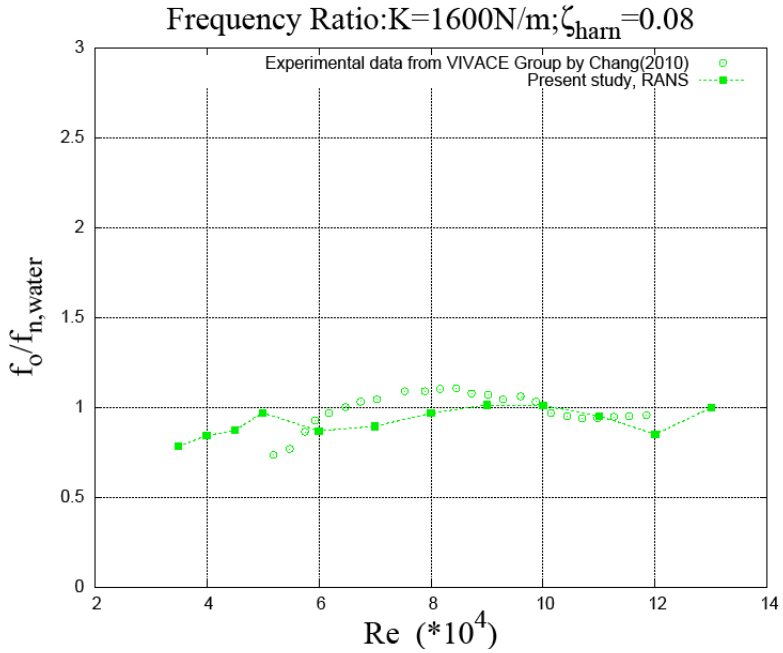

Figure 6.22. Frequency ratio comparison with experiments from MRELab by Chang (2010) (*K*=1600N/m, ζ_{harn}=0.08)

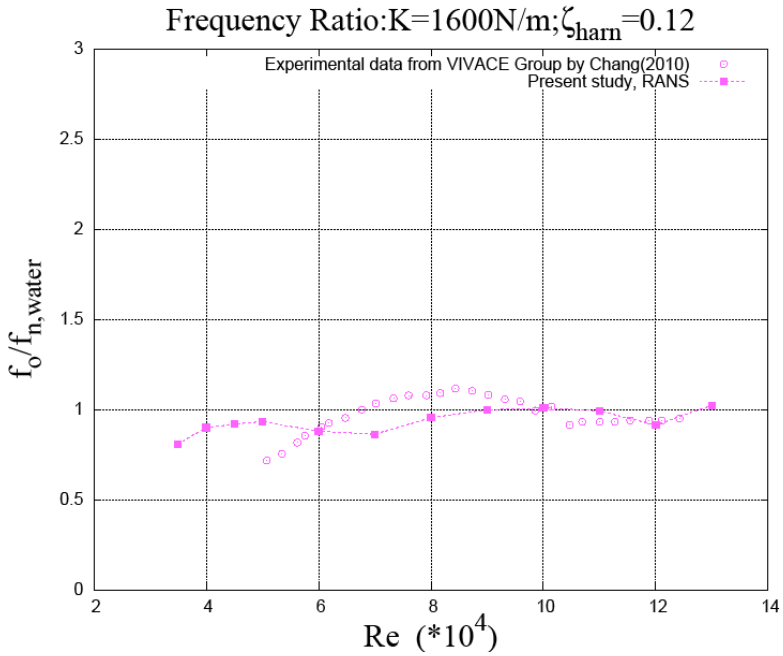

Figure 6.23. Frequency ratio comparison with experiments from MRELab by Chang (2010) (*K*=1600N/m, ζ_{harn}=0.12)

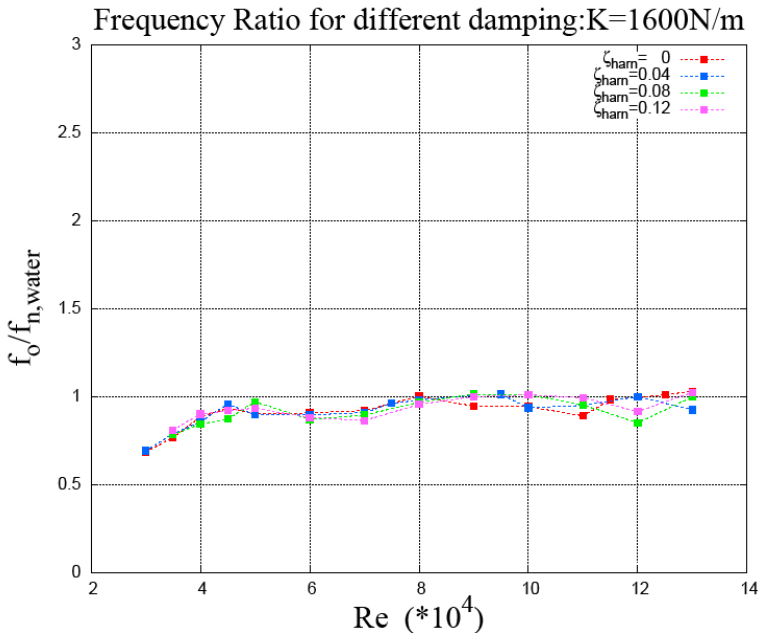

Figure 6.24. Frequency ratio comparison for different damping ζ_{harn} levels (K=1600N/m, ζ_{harn}=0, 0.04, 0.08, 0.12)

6.4. Conclusions

In this chapter, from the numerical investigations on the FIM of a circular cylinder with PTC (α_{PTC}=20), the following main findings were derived:

Stiffness (K) effects:

For the different stiffness cases that have been tested, it was found that there are significant resemblances in the results in terms of amplitude curve branches, frequency variation tendency, lift and displacement spectra features within 3 different branches, as well as the vortex pattern in the wake associated with different flow regimes. These similarities are summarized below:

1. For different system stiffness, the amplitude curves are all composed of three branches, the VIV initial branch, the VIV upper branch, and the galloping branch.

2. The entire frequency curve also can be identified as three branches and the resultant ranges of different branches are consistent with the way they are defined by the amplitude curve. The frequency curve shows nearly monotonic behavior in the initial and upper branches. Moreover the frequency reduction phenomenon is observed when the transition to galloping begins.

3. The upper branch can be further divided into developing regime and fully developed regime from the lift spectrum point of view. In the VIV upper branch developing regime, the lift and displacement time histories are non-sinusoidal and not perfectly periodic. The 2^{nd} and 3^{rd} harmonic peaks of lift spectrum approximately occur at twice and three times the value of the first major one. On the contrary, when the fully developed regime is reached, the displacement recovers the nearly sinusoidal form and the lift time trace also becomes remarkably periodic. The 2^{nd} and 3^{rd} harmonic peaks in the lift spectra are 3 and 5 times that of the first major peak, respectively.

4. The vortex patterns associated with different branches are very similar to each other comparing with various *K* values.

The major effects exhibited by changing *K*, or in other words, the main variations caused by different system stiffness are listed here:

1. For each Re case, higher values of *K* tend to yield lower response amplitude.

2. The lower *K* not only tends to lead to an earlier transition to the VIV upper branch, but also results in an early transition to the galloping branch. In addition, for higher *K*, the transition regime from VIV upper branch to galloping last relatively longer.

Damping (ζ_{harn}) effects:

There are many properties that are subject to obvious changes when the damping level is different.

1. The amplitude reduces as the damping increases because of more energy being dissipated.
2. Just as observed by other experiments of cylinder flow in VIV, when the system damping is low, the oscillating amplitude at the onset of the synchronization, which also refers to the initial branch, is found to associate with beating like that in the displacement history. For 4 different levels of system damping, the gradual development of the damping effects is well observed. The lower damping values cases with ζ_{harn}=0 and 0.04, the beating prevails throughout the initial branch. For ζ_{harn}=0.08, the non-sinusoidal profiles of lift and displacement are only notable in

the initial branch when the *Re* is associated with a vortex pattern switch. While for the case of ζ_{harn}=0.12, even during the wake pattern shift, the lift and displacement are relatively sinusoidal-like and with limited unevenness and irregularity in the lift and motion amplitude.

3. Damping does not have much effect on the coverage of the initial branch but the transition points to the galloping branches are remarkably changed by different damping values. The higher the damping is, the longer the upper branch lasts, and moreover, the shorter the transition to the galloping branch is.

Beyond those differentiations, there are still properties that are not sensitive to the damping variations:

1. The major features of lift and amplitude time traces in the upper branch, the transition to galloping, and the galloping branch are similar in spite of damping variation.
2. Frequency curves with different damping are found to be similar in the ranges of the three FIM branches.
3. Vortex patterns and wake dynamics are similar in the same branch for different damping.

Chapter 7

EFFECT OF LOCATION OF PTC ON CYLINDER WITH PTC IN FIM

7.1. Introduction

In Chapters 5 and 6, a circular cylinder with PTC excited in FIM has been studied. The FIM enhancement using PTC and its robustness were established well over broad ranges of system damping and stiffness parameters.

Although in the MRELab PTC consisting of selectively applied roughness on the cylinder surface, focused only on enhancing motion amplitude and convert more hydrokinetic energy to mechanical, the opposite effect is revealed by varying the circumferential location of the PTC. Systematic studies have been conducted by Park et al. (2011) regarding different effects from varying placement angles, PTC coverage, roughness height, PTC configuration and arrangement (straight, staggered or helical strips) and etc. One of the most dominant factors in determining the FIM behavior is the placement angle α_{PTC} where the leading edge (the edge closer to the upstream stagnation point) of the PTC is located. The possible α_{PTC} range for each PTC device is tested and 4 robust zones are discovered, namely weak suppression, strong suppression, hard galloping, and soft galloping (Park et. al. 2011). In Figure 7.1, the PTC-to-FIM maps for two different sandpapers P60 and P180 are shown. Only slight differences of zonal coverage can be observed between the two sandpapers. For both PTC configurations, there are two major regions with entirely opposite FIM type, that is enhancement for α_{PTC} <~60^o and suppression for α_{PTC}>~60^o.

In this Chapter, the placement angle effect is studied by the 2D-RANS numerical tool developed in this thesis. Different grids are generated to cover the locations of PTC and model PTC appropriately. The grids utilized in this chapter are consistent with the

one used in Chapters 5 and 6 in number of cells and near wall spacing. The only difference is the PTC placement angle. Beyond the case α_{PTC}=20^o, which has been studied in previous chapters with details, four other values are investigated and compared in this chapter, these are 50^o, 70^o, 90^o and 114^o degrees located in various zones according to the PTC-to-FIM map in Figure 7.1. The numerical results are in good agreement with the experimental observations by Park et al. (2011).

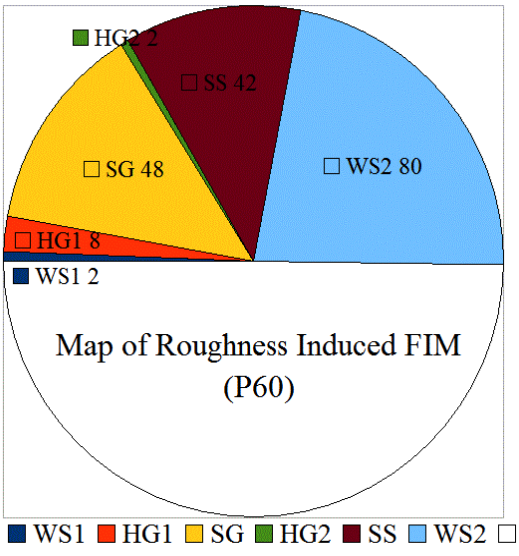

(a) Map of FIM for P60

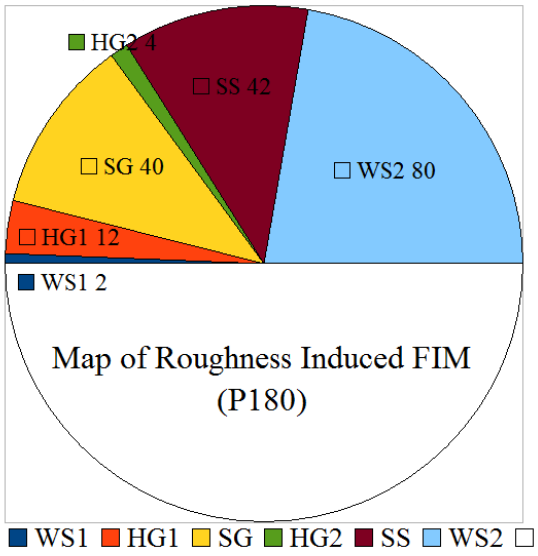

(b) Map of FIM for P180

Figure 7.1. Map of roughness induced FIM showing weak suppression (WS), hard galloping (hg), soft galloping (SG), strong suppression (SS) response zones (Reproduced from Park et al. 2011)

7.2. Placement angle (α_{PTC}) effect

7.2.1. System parameters

In this section, the effect of PTC placement angle is investigated through a series of simulations. The VIVACE system parameters selected have the same values as in Chapter 5, with K=1600N/m and ζ_{harn}=0.08. More detailed information on the system parameters is provided in Table 7.1. As in Chapters 5 and 6, P60 sandpaper is used. Sand grit roughness height *k*, backup sandpaper thickness *P*, and the placement angle values used are specified in Table 7.2. Beyond the placement angle α_{PTC}=20^o, which has been investigated in Chapter 5, α_{PTC}=50^o, 70^o, 90^o and 114^o are also considered in this chapter. According to the PTC-to-FIM map in Figure 7.1, these angle values fall into different FIM zones. α_{PTC}=20^o and 50^o degrees are in the SG (soft galloping) zone, 70^o and 90^o are located in SS (strong suppression) zone, and 114^o is in WS (weak suppression) zone.

Table 7.1. Experimental system parameters

Mass ratio	m^*	1.88
External damping ratio for energy harnessing	ζ_{harn}	0.08
Mass-damping parameter	$m^* \zeta_{harn}$	0.1504
Diameter of circular cylinder	D [m]	0.0899
Total mass of oscillation	M [kg]	10.75
Spring constant	K [N/m]	1,600
Structural damping	$C_{structure}$ [Ns/m]	3.2
Natural frequency in water	$f_{n,water}$ [Hz]	1.5650

Table 7.2. PTC parameters (P60 sandpaper)

Strip placement angles	α_{PTC} [degree]	20 ~ 36, -20 ~ -36 ; 50 ~ 66, -50 ~ -66 ; 70 ~ 86, -70 ~ -86 ; 90 ~ 106, -90 ~ -106 ; 114 ~ 130, -114 ~ -130
Strips coverage angle	[degree]	16
Sand paper thickness	P [mm]	0.587
Average height of sand grits	k [mm]	0.26
Total thickness	$T=P+k$ [mm]	0.847

7.2.2. FIM enhancement (α_{PTC} 20 deg,50deg)

The amplitude ratio for different placement angles is plotted in Figure 7.2. There are clearly two trends appearing in these curves. One is that the amplitude increases as the *Re* increases, which demonstrates the FIM enhancement effects. It has been discussed in Chapter 5 and 6, with a PTC placement angle α_{PTC}=20^o. The second trend is the opposite, as *Re* increases the amplitude decreases, showing obvious FIM suppression. In this section, the FIM enhancing cases are discussed and compared regarding the motion, lift, and wake structures in different branches, while the FIM suppression cases are discussed in the Section 7.2.3.

The RMS amplitude plots for α_{PTC}=50^o exhibit similar features as those for α_{PTC}=20^o (see Figure 7.2). The data ranges are comparable with each other and different branches are also shown. The VIV initial branches for both placement angles are similar from the RMS amplitude point of view. The VIV upper branch for α_{PTC}=50^o is relatively short and soon is taken over by the succeeding transition to galloping around *Re*=80,000, which explains the amplitude overshoot for α_{PTC}=50^o in this region (see Figure 7.2). In Figure 7.4, the displacement traces and FFT analyses are compared side by side for 4 different *Re* cases, which represent 4 different regimes, namely the VIV initial branch, the VIV upper branch, transition to galloping, and the fully developed galloping branch. From the FFT analysis, the developing stage of the VIV upper branch, in other words the early part of the upper VIV branch, is absent which is characterized by the first reduction of frequency and additional lift harmonic frequencies with values about twice and three times that of the first major frequency. Except for this, the features for different regimes are in good agreement with previous observations regarding the FFT frequency analysis and amplitude. Even though many similarities are shared for different angles in the same FIM map zone, variations for each angle can be unveiled when other results are analyzed, such as frequency ratio and the vortex pattern in the wake. These variations are due to the effects of PTC location change.

In Figure 7.3, the frequency ratios are compared over *Re*. Instead of three different branches in the frequency ratio curve found in previous simulations (see Figures 5.4, 6.6-6.8, 6.20-6.23), for α_{PTC}=50^o, there is no drop-down around the transition from the initial VIV to the upper VIV branch. The frequency keeps climbing until reached the

transition from the VIV upper branch to galloping. However, the amount of frequency reduction is limited in comparison to α_{PTC}=20^o case and the curve shows flatness around unity after entering the VIV upper branch.

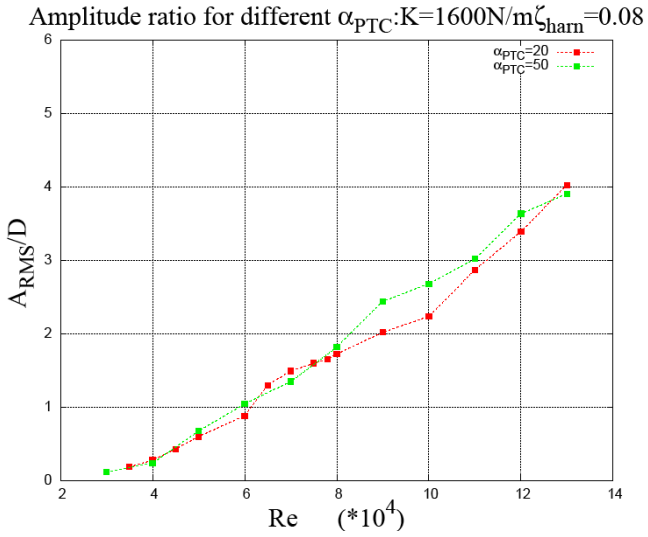

Figure 7.2. RMS amplitude ratio comparison for α_{PTC}=20^o and 50^o, with K=1600N/m, ζ_{harn}=0.08

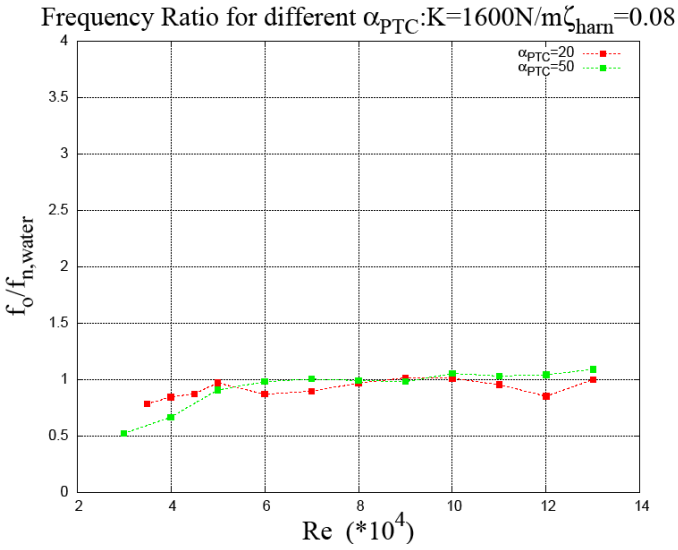

Figure 7.3. Frequency ratio comparison for α_{PTC}=20^o and 50^o, with K=1600N/m, ζ_{harn}=0.08

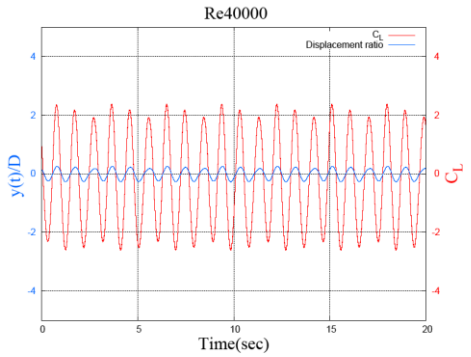

(a1) Lift coefficient and displacement ratio history, *Re*=40,000

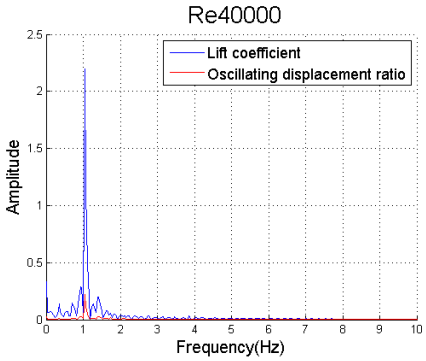

(a2) FFT analysis for lift coefficient and displacement ratio, *Re*=40,000

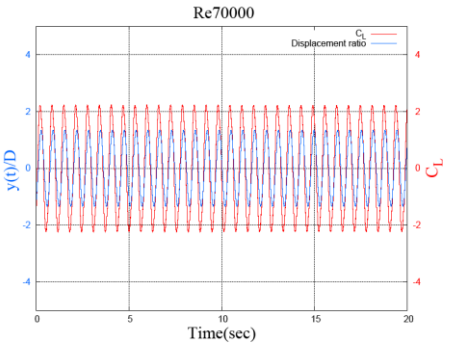

(b1) Lift coefficient and displacement ratio history, *Re*=70,000

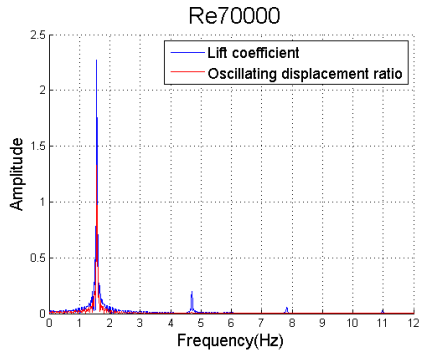

(b2) FFT analysis for lift coefficient and displacement ratio, *Re*=70,000

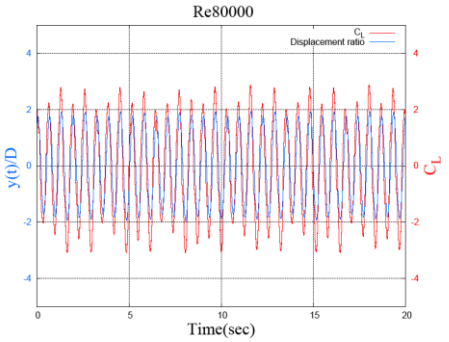

(c1) Lift coefficient and displacement ratio history, *Re*=80,000

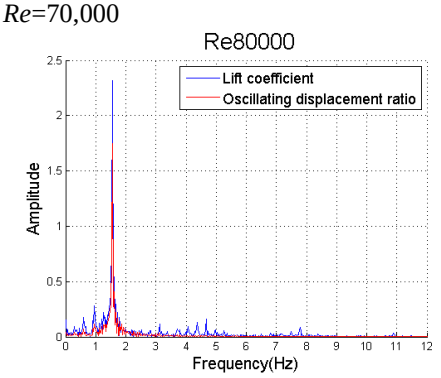

(c2) FFT analysis for lift coefficient and displacement ratio, *Re*=80,000

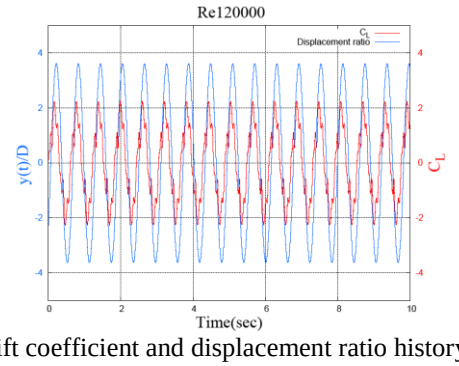

(d1) Lift coefficient and displacement ratio history, *Re*=120,000

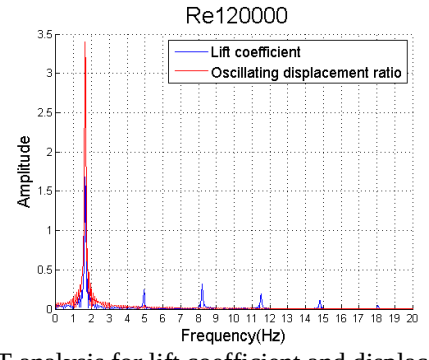

(d2) FFT analysis for lift coefficient and displacement ratio, *Re*=120,000

Figure 7.4. Time history and spectra of lift coefficient (C_L) and displacement ratio ($y(t)/D$) for different *Re* cases (40,000≤*Re*≤120,000) (α_{PTC}=50°, *K*=1600N/m, ζ_{harn}=0.08)

The wake structure for each Re case undergoes dramatic changes as α_{PTC} varies, especially in the initial and upper branches. This can be further confirmed by the other α_{PTC} cases considered in the suppression zone, which are all associated with different wake structures. In the initial branch, the 2S (*Re* at 30,000 and 40,000 see Figure 7.5 (a) and (b)) and 2C (*Re* at 50,000, Figure 7.5(c)) vortex modes are found. The 2C mode has not been observed in previous cases in the present numerical study. It has been observed experimentally, however, in the VIV flow wake by other researchers. It is a well-known wake vortex pattern attributed to the VIV phenomenon of a cylindrical structure (Williamson 2004), and it has been found in the pivoted cylinder case (Flemming and Williamson 2005, see Figure 7.6). The 2C mode refers to the case where during each cycle 2 singe vortices with the same vorticity sign shed from each side of the cylinder, and the vorticity signs for the vortices from the two sides are opposite. The 2C mode in this case shows even more interesting behavior that after the two vortices from one side are formed successively rotating in the same direction, get closer and finally combine into one as they move downstream. In the VIV upper branch, at Re=70,000, 2P+4S is found (Figure 7.5(d)). Comparing with the 2C case, an additional one pair of vortices is generated on each side between the two singles. One of the two vortices in the pair is formed very closely with the first S before it, and they get separated until the first S is merged with the second S from the same side. When in the transition regime to galloping, the number of vortices is the same and vortex pattern is still 2P+4S (*Re*=80,000, Figure 7.5(e)). The timing of shedding of the vortices, however, varies which make the wake looks different. The displacement increases sharply during this period, therefore, more spatial and temporal gaps are allowed between successive vortices. As a result, the singles no longer merge quickly and the pair is also formed separately from the single one. In the galloping branch, 2P+6S (*Re*=100,000, Figure 7.5(f)) and 2P+8S are formed.

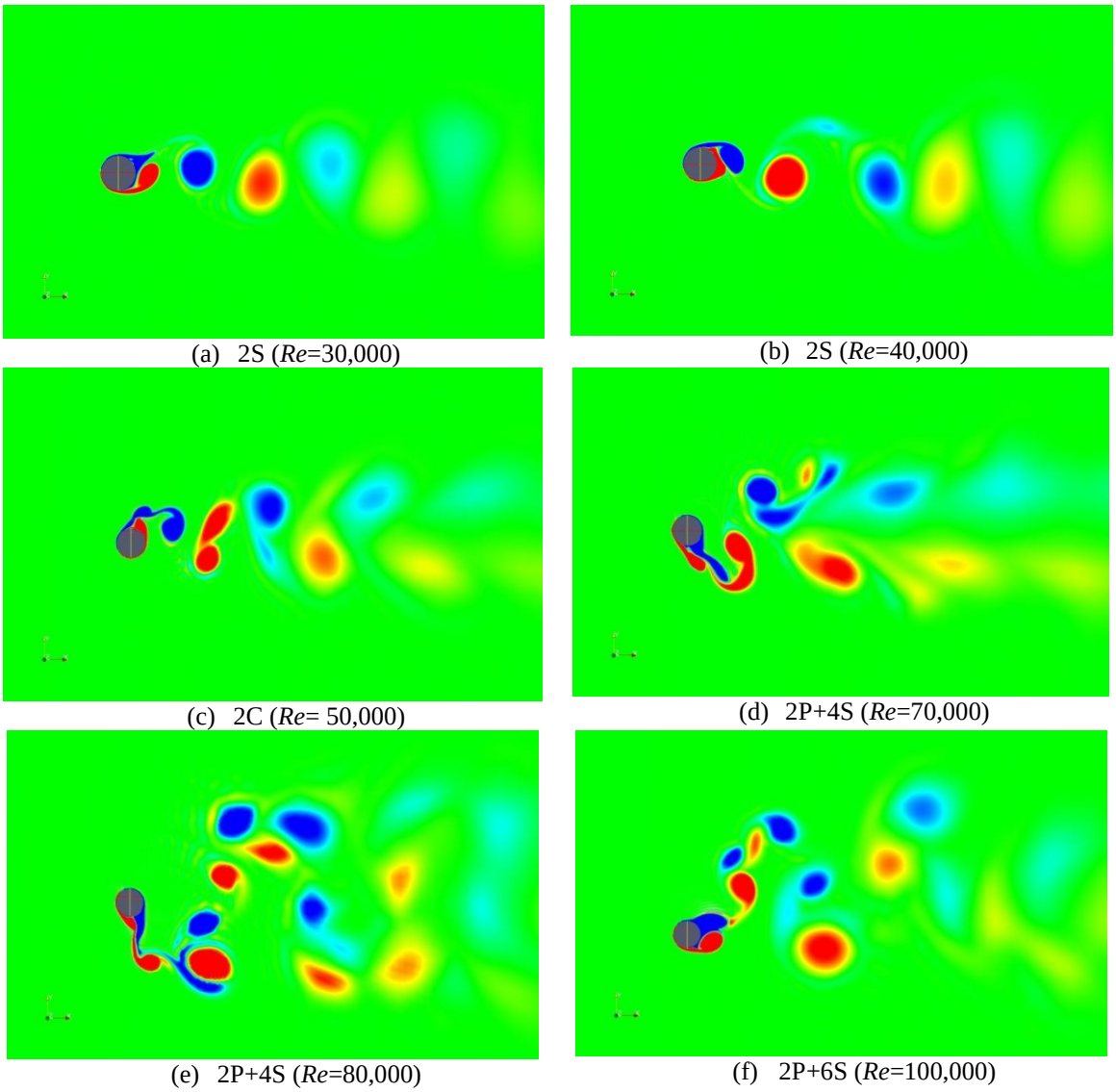

(a) 2S (*Re*=30,000) (b) 2S (*Re*=40,000)

(c) 2C (*Re*= 50,000) (d) 2P+4S (*Re*=70,000)

(e) 2P+4S (*Re*=80,000) (f) 2P+6S (*Re*=100,000)

Figure 7.5. Different vortex patterns associate with various flow regime for FIM enhancing (α_{PTC}=50^o, *K*=1600N/m, ζ_{harn}=0.08)

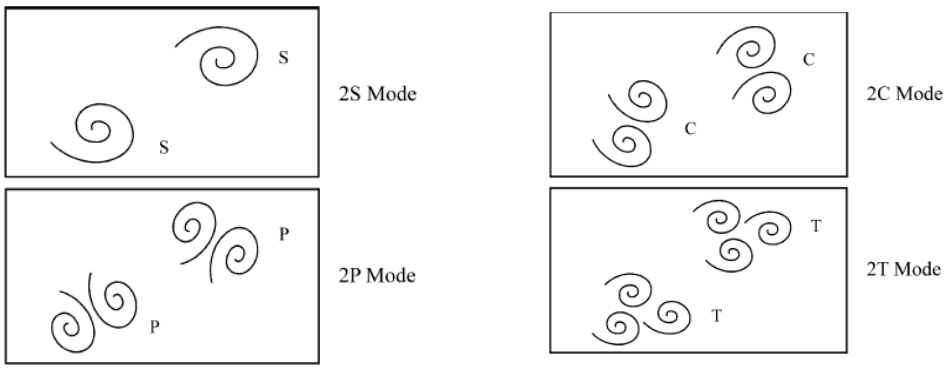

Figure 7.6. The sets of {2S, 2P, 2C, 2T} modes associated with VIV (Reproduced from Flemming and Williamson 2005)

7.2.3. FIM suppression (α_{PTC} =70deg,90deg,114deg)

PTC devices for the VIVACE system are designed to enhance the oscillation amplitude and FIM range and eventually enable the converter to generate more power. VIVACE group tests in the MRELab, however, show that the motion of the cylinder exhibits dramatic changes when PTC locations are varied along the cylinder circumferential direction. Beyond certain zones, where galloping occurs with a dramatic increase in amplitude, there are specific locations, where FIM suppression is quite obvious (see maps in Figure 7.1). In this section, several other α_{PTC} values are further investigated by using the numerical tool developed in this thesis. Under the guidance of PTC-to-FIM map (see Figure 7.1), 3 angles located in the suppression zone are chosen: 70^o, 90^o, 114^o.

The parameters of the VIVACE system and PTC are the same as those specified in Section 7.2.2 and listed in Tables 7.1 and 7.2.

α_{PTC} =70deg

This angle falls in the suppression zone in the PTC-to-FIM map and therefore the FIM suppression effect is expected to prevail in the cylinder motion behavior. In this case, three branches are observed in the amplitude curve, the VIV initial branch, the VIV upper branch as well as the suppression branch (Park et. al. 2011), where the new branch is taking the place of the galloping branch. As expected, certainly there are changes in the initial and upper branch cases compared with FIM enhancing situations. However, the most remarkable changes are found in the region where suppression effects become prominent, the suppression branch.

The amplitude ratios of different PTC angle locations are plotted together in Figure 7.7 and the results from FIM enhancement (section 7.2.2) are also included to make comparison. Compared with α_{PTC}=20^o and 30^o, the results for the other 3 angles clearly show FIM suppression. For α_{PTC}=70^o, the amplitude values in the VIV initial branch are at about same level as those cases for FIM enhancement. In addition, the *Re* range for the initial branch is also about the same. This demonstrates that, from the behavior of the VIV initial branch, the PTC effect on FIM cannot be easily identified a priori as enhancement or suppression effect. When the upper branch begins, in

comparison with the amplitude enhancement cases, the amplitude increases at a slower rate, and by the end of this branch, Re=100,000 for this case, the amplitude is reduced 11%~26% comparing to the FIM enhancement cases (α_{PTC}=20^o and 50^o) (see Figure 7.7). After this point, amplitude drops rapidly throughout the rest of range and for all test cases, and the galloping branch is replaced by the suppression branch (Park et al. 2011), which is characterized by a small amplitude and a much more complex wake structure than 2S.

In Figure 7.8, the frequency ratio for 5 different angles in various zones is plotted. At first, in the VIV initial branch, the frequency keeps climbing steeply as in all cases studied so far. The speed of increasing drops quickly after the transition to the VIV upper branch. Slightly higher frequency ratio values are noted compared with the FIM enhancement situations and even more obvious increment occurs as the suppression branch is reached. From FFT analysis, the initial branch still has relatively unsteady amplitude with beating showing in the lift and displacement time history. The multiple peak spectra manifest the onset of the transition to the upper branch. It is easily observed that the first major frequency increases and moves closer to the secondary frequency, at the same time, more peaks appear in-between. In the VIV upper branch, the developing regime is absent and only the developed regime appears with a range from *Re*=~60,000 to ~100,000. The rest is the suppression branch. From the frequency ratio point of view, the frequency picks up much faster beyond *Re*=100,000, where the amplitude begins to drop sharply. For both the VIV upper branch and the suppression branch, the 2nd and 3rd harmonic frequencies exist with values about 3 and 5 times the major frequency, and higher order harmonic frequencies are also found as in the FIM enhancement cases. Vortex patterns 2S and 2C are found to be associated with the VIV initial branch, and 2P+4S with the beginning of the VIV upper branch, similarly to what was observed for α_{PTC} =50^o. A new pattern - 2T mode - has been observed in the upper and supression branch, which is discovered for the first time (see Figure 7.9 (a)). 2T refers to the pattern where during each half cycle three vortices (Triplet) shed from one side of the cylinder, two with same sign rotating in one direction and the third one with opposite vorticity sign rotating in the other way. 2T was previously found experimentally in a two-degree of freedom VIV motion case (Williamson 2004). The sketch of 2T can be found in Figure 7.6 together with 2S, 2P, and 2C vortex structure. Altough for α_{PTC} =70^o 2T is found at different Re cases, it seems

that the configuration and relative position for the triplets vary and to some extend they depend on the timing of vortex shedding and wake breadth. Different 2T configurations are shown in Figure 7.9. As *Re* reaches higher values up to 120,000 and 130,000, the 2S mode appears again.

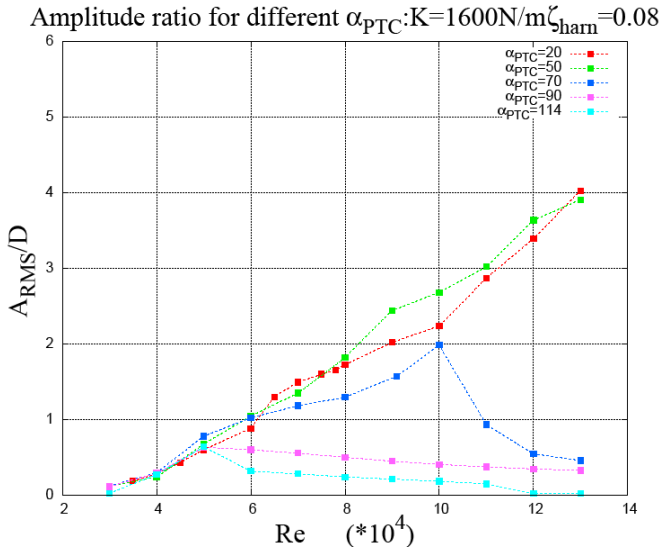

Figure 7.7. RMS amplitude ratio comparison for different placement angle values (α_{PTC}=20, 50, 70, 90, 114 deg ; *K*=1600N/m, ζ_{harn}=0.08)

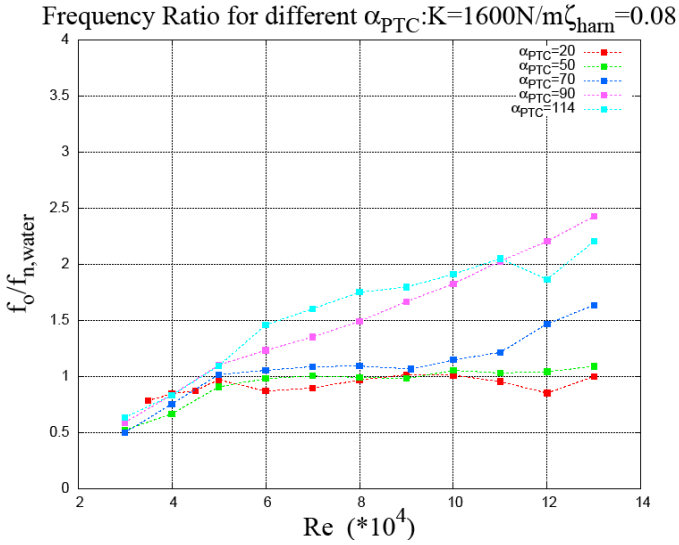

Figure 7.8. Frequency amplitude ratio comparison for different placement angle values (α_{PTC}=20, 50, 70, 90, 114 deg; *K*=1600N/m, ζ_{harn}=0.08)

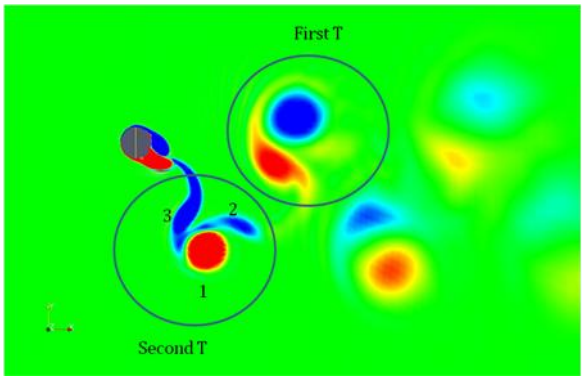

(a) 2T mode at *Re*=91,000

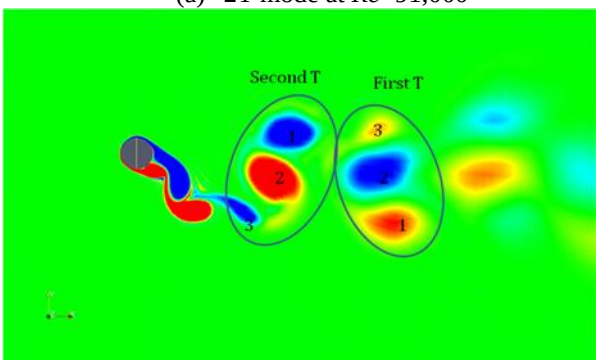

(b) 2T mode at *Re*=110,000

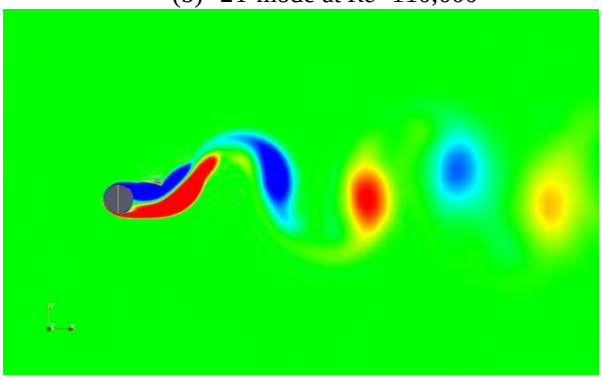

(c) 2S at *Re*=120,000 and 130,000

Figure 7.9. Different vortex patterns associate with various flow regimes for FIM suppression (α_{PTC}=70^o, *K*=1600N/m, ζ_{harn}=0.08)

α_{PTC} =90deg

In this case, the placement angle is 90^o, which means the leading edge of the sandpaper is right at the top and bottom points of the cylinder. The results exhibit remarkable effects of suppression. Only two obvious branches of amplitude are shown (see Figure 7.7), and the frequency keeps climbling throughout the entire test region (see Figure 7.8).

The amplitude ratio for this angle is showing only two obvious branches, the VIV initial branch and the suppression branch. From *Re*=~30,000 to ~50,000 is the VIV initial branch. The beating phenomenon appears and is associated with the lift and amplitude profile for *Re*=30,000 and 40,000, which gives broad-band lift and displacement spectra (see Figure 7.12 (a1), (b1), (a2), (b2)). In the initial branch region (30,000<*Re*<50,000), the RMS values of oscillation amplitude are comparable for systems with different values of α_{PTC} (see Figure 7.8). Past *Re*=50,000, the amplitude (α_{PTC}=90^o) drops fast and demonstrates the onset of the suppression branch. The decreasing continues until the last test case *Re*=130,000 with amplitude ratio=0.32.

As shown in Figure 7.8, the frequency ratio for α_{PTC}=90^o keeps increasing at two different rates in these two branches. In this initial branch, the frequency increases relatively rapidly showing comparable curve slope as the other curves. After the turning point at *Re*=50,000, frequency continues climbing without decrement at any point. This phenomenon is also well observed experimentally in the MRELab by the VIVACE group. As for the spectra for lift and amplitude, broad-banded spectra are well observed in the initial branch (*Re*=30,000~40,000), and for the end of the initial branch, Re=50,000, the 2nd and 3rd major peaks in the lift spectrum are found at twice and 3 times of the first frequency (see Figure 7.11 (c2)). For the rest of the cases on the suppression branch (*Re*=60,000~130,000) the lift spectrum is featured with the regular 2nd and 3rd hamonic frequencies with values of 3 and 5 times first major one (see Figure 7.11 (d2)).

In Figure 7.10, various vortex patterns in the wake region associated with this placement angle are presented. Three main modes are found: 2S (Figure 7.10(a)), T+S (Figure7.10 (b)) and 2C (Figure 7.10 (c)). In the initial branch (*Re*=30,000~40,000) the 2S mode is found. As *Re* goes up to 50,000, an asymmetric wake structure is formed with different modes shed on the two sides. At the top side of the wake, the triplet is composed of two negative vortices at the beginning shed from the upper half of the cylinder and followed closely by another positive one shed from the cylinder bottom. At the lower side of the wake, a positive single shed from cylinder bottom is the only one showing in the wake. Interestingly, the asymmetric vortex mode is very stable, and moreover it is able to yield relatively symmetric lift and displacement history traces. In the suppression branch, the number of vorices is not changed, however, the strength of the vortices varies

(see Figure 7.10 (c), (d), (e), (f)). The third vortex with positive vorticity of "T" at Re=50,000 is no longer following closely to the other two on top side of the wake, on the contrary, the gap between it and the other two is enlongated and more time is allowed for it to grow stronger before it is shed. In addtion, the other positive vortex which is formed from the same side is getting closer to it and eventually the vortex mode switches from T+S into 2C, which has two same sign vortices shed on both sides of the cylinder.

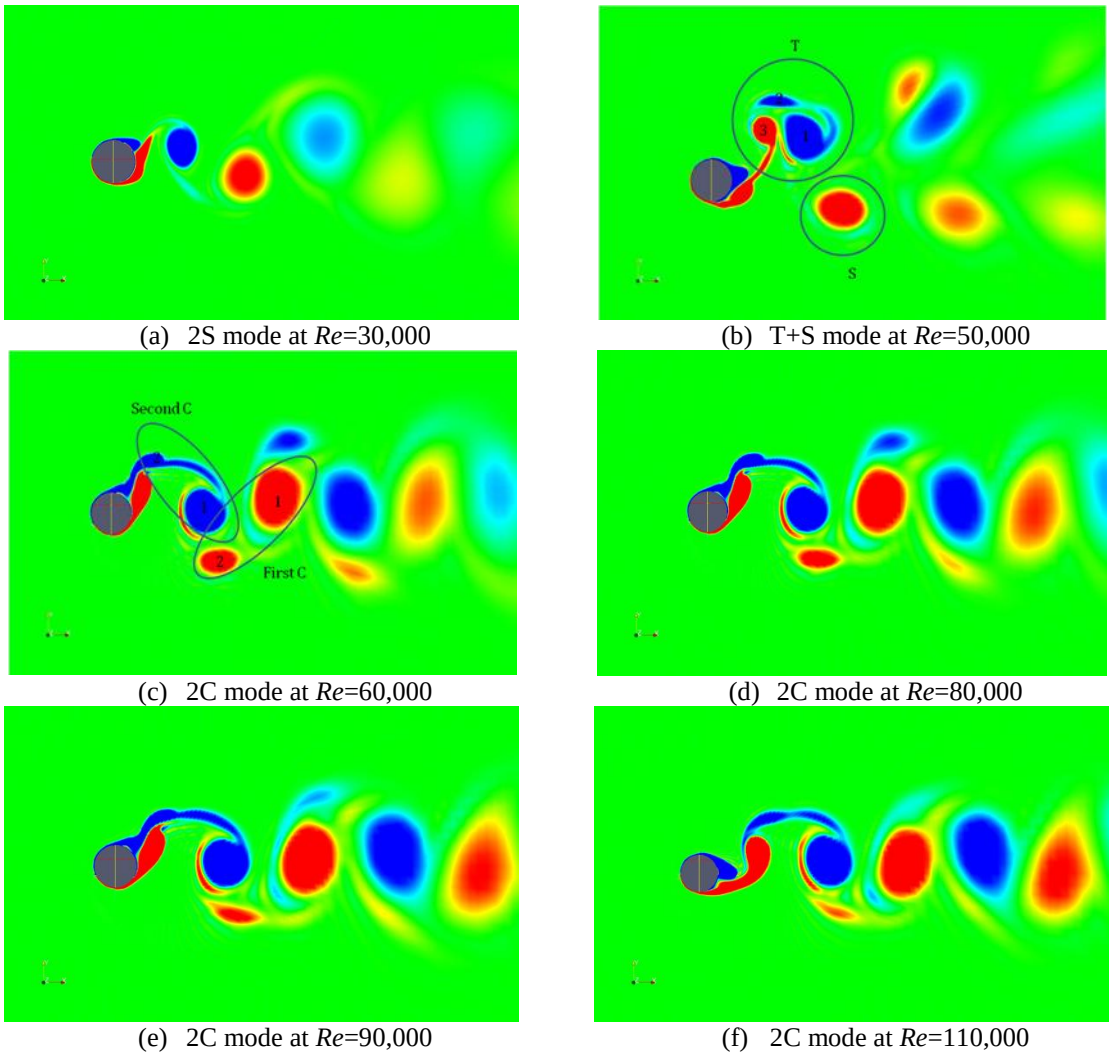

(a) 2S mode at *Re*=30,000 (b) T+S mode at *Re*=50,000

(c) 2C mode at *Re*=60,000 (d) 2C mode at *Re*=80,000

(e) 2C mode at *Re*=90,000 (f) 2C mode at *Re*=110,000

Figure 7.10. Different vortex patterns associate with various flow regime for FIM suppression (α_{PTC}=90^o, *K*=1600N/m, ζ_{harn}=0.08)

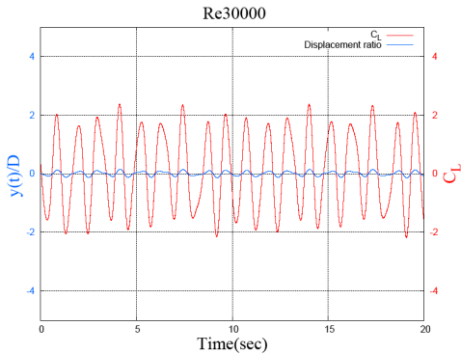

(a1) Lift coefficient and displacement ratio history, *Re*=30,000

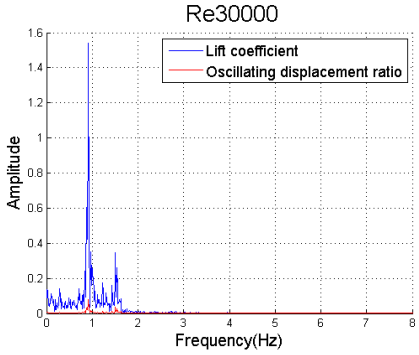

(a2) FFT analysis for lift coefficient and displacement ratio, *Re*=30,000

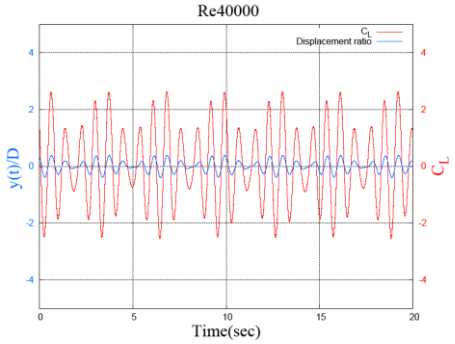

(b1) Lift coefficient and displacement ratio history, *Re*=40,000

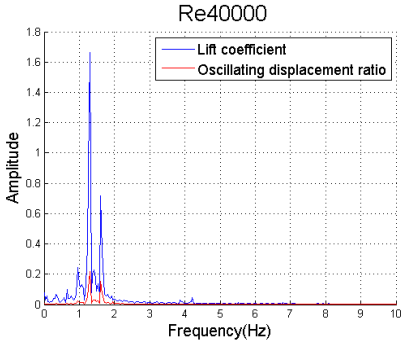

(b2) FFT analysis for lift coefficient and displacement ratio, *Re*=40,000

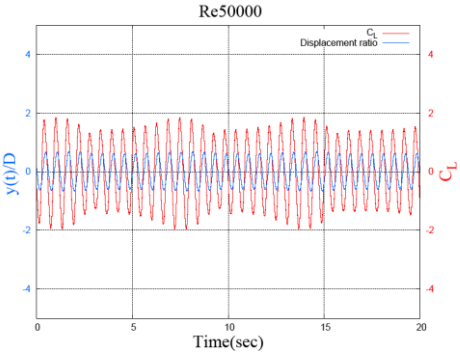

(c1) Lift coefficient and displacement ratio history, *Re*=50,000

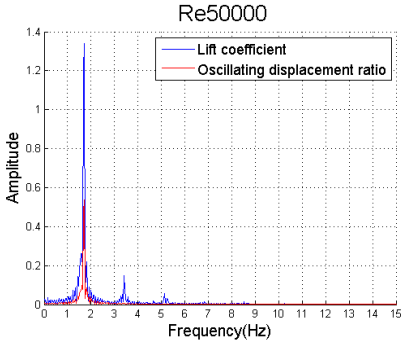

(c2) FFT analysis for lift coefficient and displacement ratio, *Re*=50,000

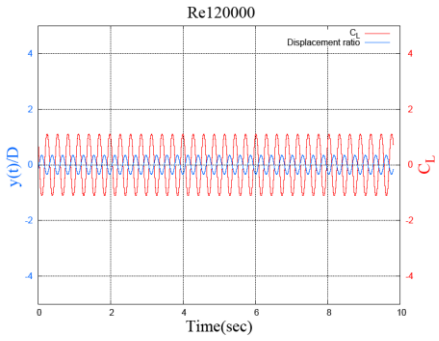

(d1) Lift coefficient and displacement ratio history, *Re*=120,000

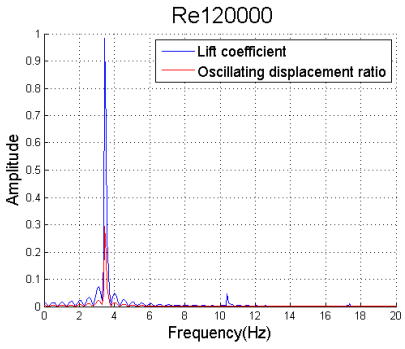

(d2) FFT analysis for lift coefficient and displacement ratio, *Re*=120,000

Figure 7.11. Time history and spectra of lift coefficient (C_L) and displacement ratio($y(t)/D$) for different *Re* cases (30,000≤*Re*≤120,000) (α_{PTC}=90°, *K*=1600N/m, ζ_{harn}=0.08)

α_{PTC} = 114deg

When the PTC moves to the back side of the cylinder, the leading edges of the sandpaper strips are placed on 114^o in this case. More sever effects of suppression are found from current numerical simulations in the sense that in addition to the suppression branch the desynchronization is found as well within the test range, for the case *Re*=120,000 and Re=130,000 (see Figure 7.7).

The amplitude ratio curve is shown in Figure 7.7. It exhibits even more remarkable surpression effects compared with the previous two cases when the placement angles are 70 and 90 degrees. The initial and suppression branches are found to be similar to the case of α_{PTC} =90, with Re in the range from Re=~30,000 to 50,000 and from Re=~50,000 to 110,000, respectively. In addtion, the desynchronization is reached at around Re=120,000 and only limited oscillations can be observed beyond that point with amplitude ratio about 0.016~0.017. At the same time, the frequency also goes back around the Strouhal frequency level which further proves the occurrence of desynchroniztion (see Figure 7.8).

As for the frequency ratio, it increases almost throughout the entire range. In the initial branch, the curve overlaps with that part of α_{PTC} =90^o case. After entering the suppression branch, at *R*e=60,000, the frequency ratio is higher than the values in α_{PTC} =90^o curve, but with a lower increasing rate. There is a drop when the synchronization range ends around Re=120,000. The lift time histories for all cases are remarkablely sinusoidal especially at the beginning of the initial branch at *Re*=30,000 (see Figure 7.13(a1), (a2)) and in the end of the test range from *Re*=90,000 to ~130,000 (see Figure 7.13(d1), (d2)), where the lift spectrum is single-peaked and narrow-banded for each case. For the rest of cases in-between, only weak 2^{nd} and 3^{rd} peaks can be found in the lift spectra with values of 3 and 5 times that of base frequency(see Figure 7.13(b2), (c2)).
For the wake structure modes, at *Re*=30,000 and 40,000, the 2S mode appears. Afterwards, 2 more vortices are developed to give a quasi-2P mode at *Re*=50,000, which means that for each pair, the vorticity strength for thess two vortices with opposite sign are different. From *Re*=60,000 to 80,000, the 2C mode prevails through this range. At first, 2 singles shed from the same side with same sign are detached from each other, but come closer as Re increases, and finally combined into one at *Re*=90,000, which make

the vortex pattern identified as the 2S mode. Finally, when the FIM desynchronizes, no obvious vortices can be found in the oscillatory wake (see Figure 7.12 (f)).

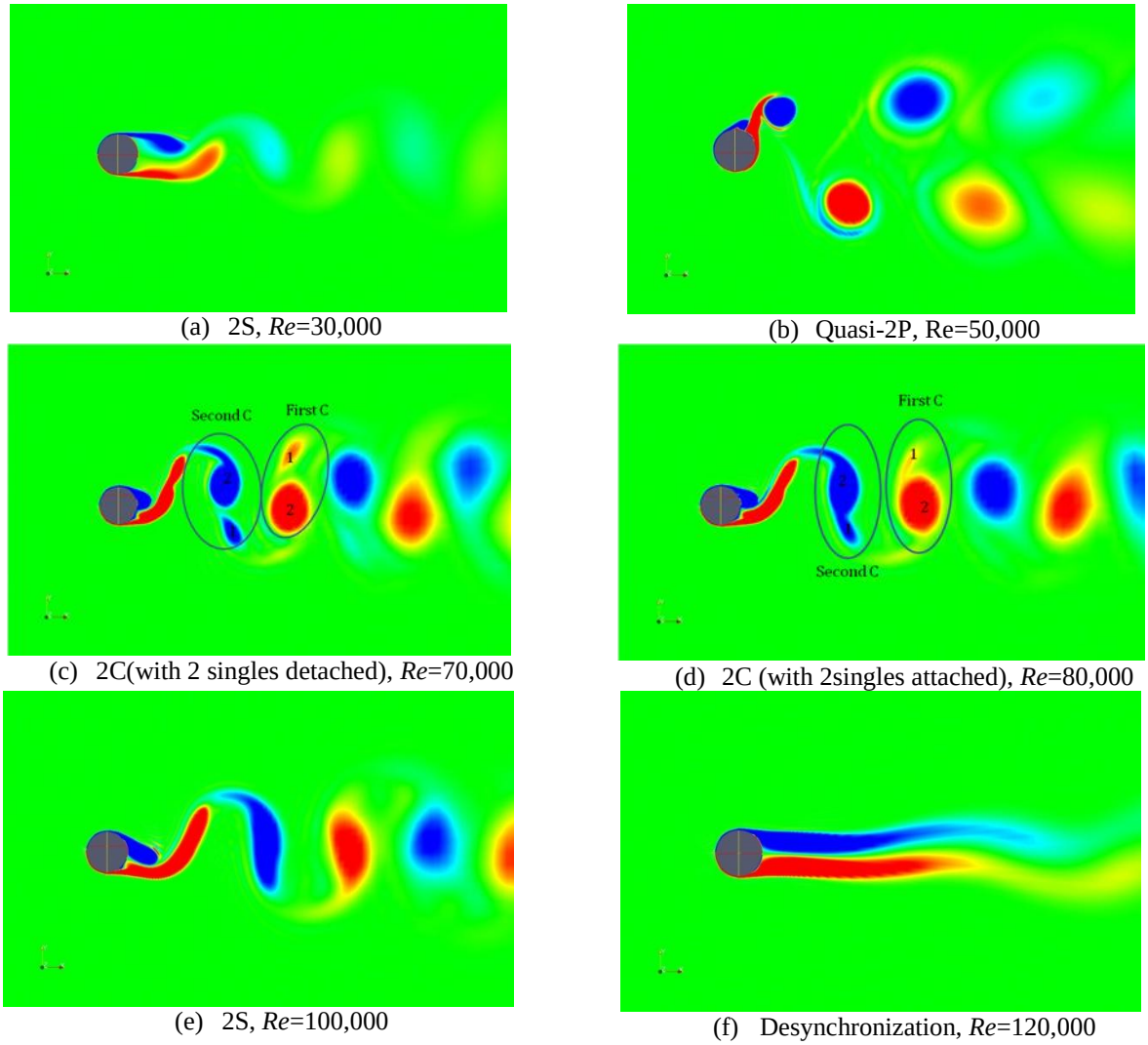

(a) 2S, *Re*=30,000

(b) Quasi-2P, Re=50,000

(c) 2C(with 2 singles detached), *Re*=70,000

(d) 2C (with 2singles attached), *Re*=80,000

(e) 2S, *Re*=100,000

(f) Desynchronization, *Re*=120,000

Figure 7.12. Different vortex patterns associate with various flow regime for FIM suppression (α_{PTC}=114^o, *K*=1600N/m, ζ_{harn}=0.08)

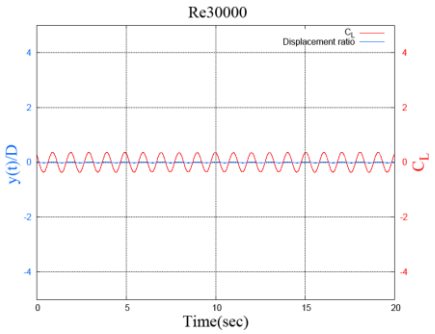

(a1) Lift coefficient and displacement ratio history, *Re*=30,000

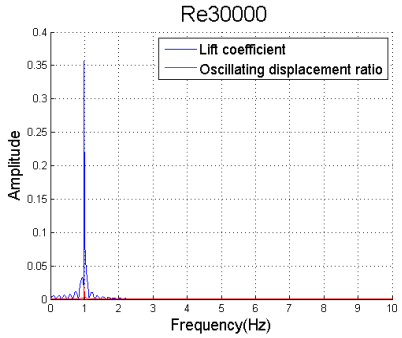

(a2) FFT analysis for lift coefficient and displacement ratio, *Re*=30,000

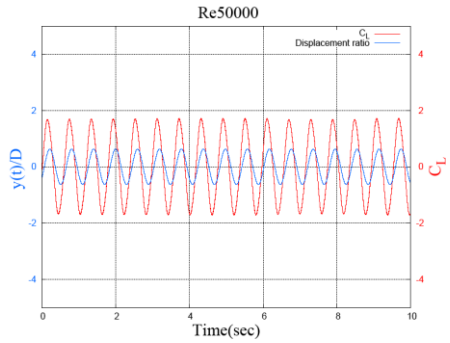

(b1) Lift coefficient and displacement ratio history, *Re*=50,000

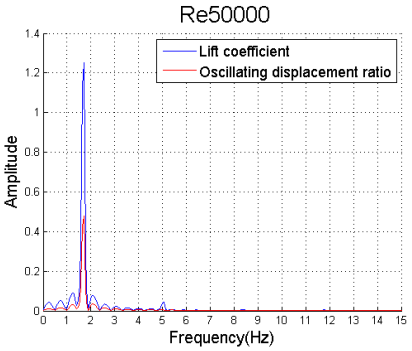

(b2) FFT analysis for lift coefficient and displacement ratio, *Re*=50,000

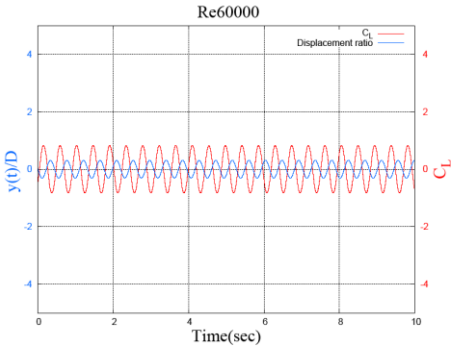

(c1) Lift coefficient and displacement ratio history, *Re*=60,000

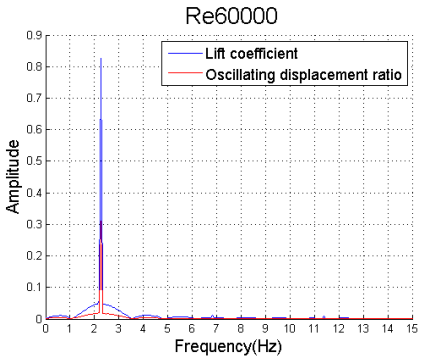

(c2) FFT analysis for lift coefficient and displacement ratio, *Re*=60,000

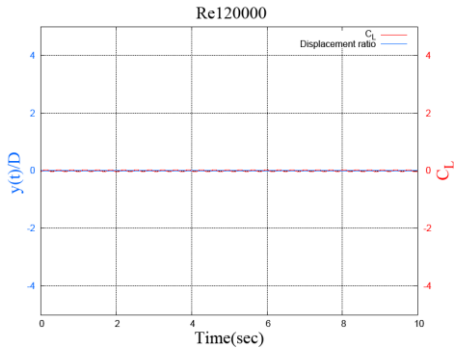

(d1) Lift coefficient and displacement ratio history, *Re*=120,000

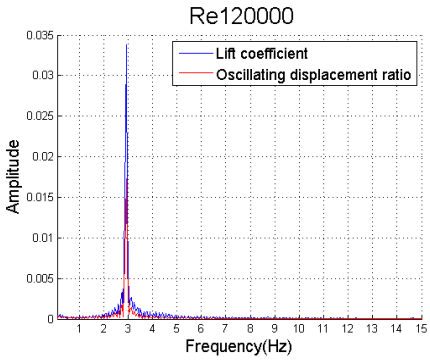

(d2) FFT analysis for lift coefficient and displacement ratio, *Re*=120,000

Figure 7.13. Time history and spectra of lift coefficient (C_L) and displacement ratio($y(t)/D$) for different *Re* cases (30,000≤*Re*≤120,000) (α_{PTC}=114°, *K*=1600N/m, ζ_{harn}=0.08)

7.2.4. Phase angle

Phase angle is the angle by which the lift leads the displacement when the cylinder undergoes FIM. In the present study, for the cylinder with PTC, the lift in most cases is non-sinusoidal and therefore for those cases the phase angle is defined as the angle by which the maximum lift point leads the maximum displacement. As noted before, in the FIM enhancement cases, the displacement is always well in phase with the lift, especially for those cases in the galloping branch. This can be easily observed by plotting the lift and displacement history together (see Figures 5.5, 5.9(a), 5.10(a), 6.5(a1)-(l1), 6.16 (a1)-(i1), 7.4 (a1)-(d1)). The maximum points of each cycle from both curves are always synchronized. In Figure 7.14, the phase angle is presented together with the RMS amplitudes over *Re* and different PTC placement angles are compared side by side. In Figure 7.14(a), this is the case for α_{PTC} = 20^o, which is in the FIM galloping zone. The phase angle is relatively small in the initial branch, less than 20^o, and it keeps growing when stepping into the upper branch. However, after transition to the galloping branch which is around *Re*= 110,000-120,000, the phase angle decreases and drops to nearly 0^o when the fully developed galloping is reached at *Re*= 130,000, which means the displacement is perfectly in phase with the lift in the galloping branch. Due to this well synchronized lift and displacement, the energy absorted from the flow can be best utilized by the moving cylinder and in return yields a much higher amplitude as expected. In Figure 7.14(b)(c) and (d), the phase angle for α_{PTC} = 70^o, 90^o, 114^o are plotted. In the initial branch, the phase angle in all three curves is small and less than 40^o. As Re grows, however, the phase angle eventually reaches aound 180^o, which demonstrates that the displacements are almost entirely out of phase with the lift. Comparing all those three FIM suppression cases, one common feature becomes quite prominent, that is the small *Re* range where the phase angle jumps up is also the turning point where the oscillating amplitude starts to drop. That also makes sense since when the motion is out of phase with the lift, the effective lift that contributes directly to the vertical motion will reduce due to this phase difference, which will eventually result in the amplitude decrement. The phase angle curves for FIM enhancement and suppression are compared side by side in Figure 7.15.

In Figures 7.16, 7.17 and 7.18 the lift and displacement time histories are presented for different *Re* cases with PTC placement angle 70°, 90° and 114°, respectively. How the phase angle changes during the increment of *Re* can be easily observed from the plots.

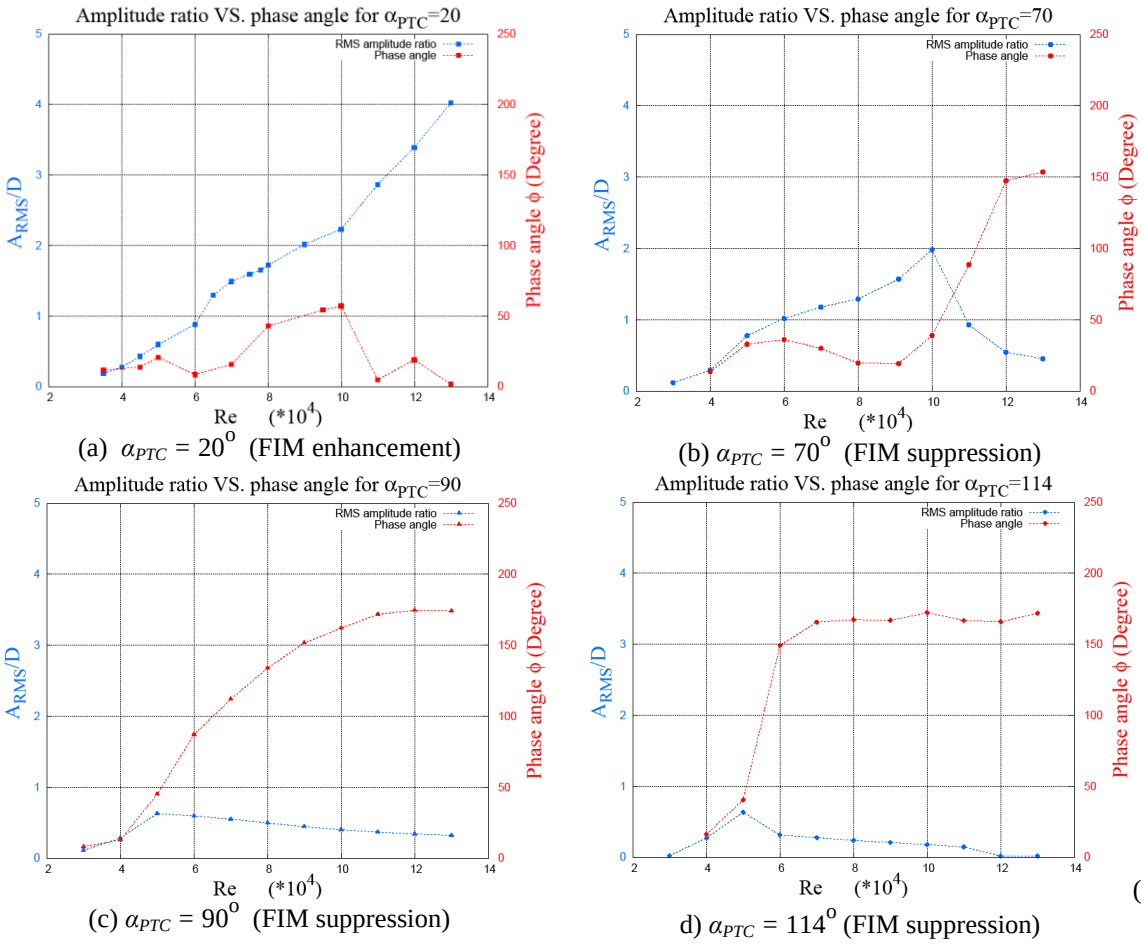

Figure 7.14. Relation between phase angle and displacement for different PTC placement angles

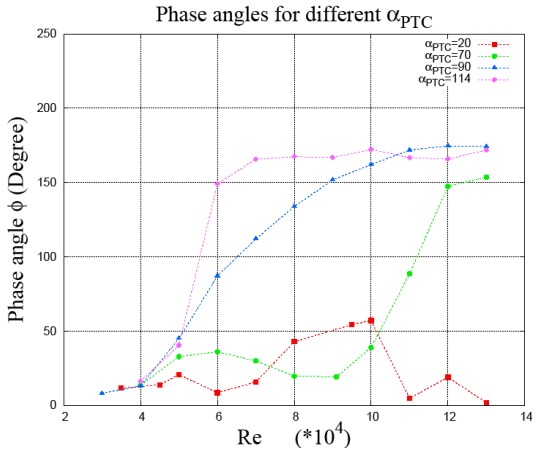

Figure 7.15. Phase angle curves comparison for different α_{PTC} values

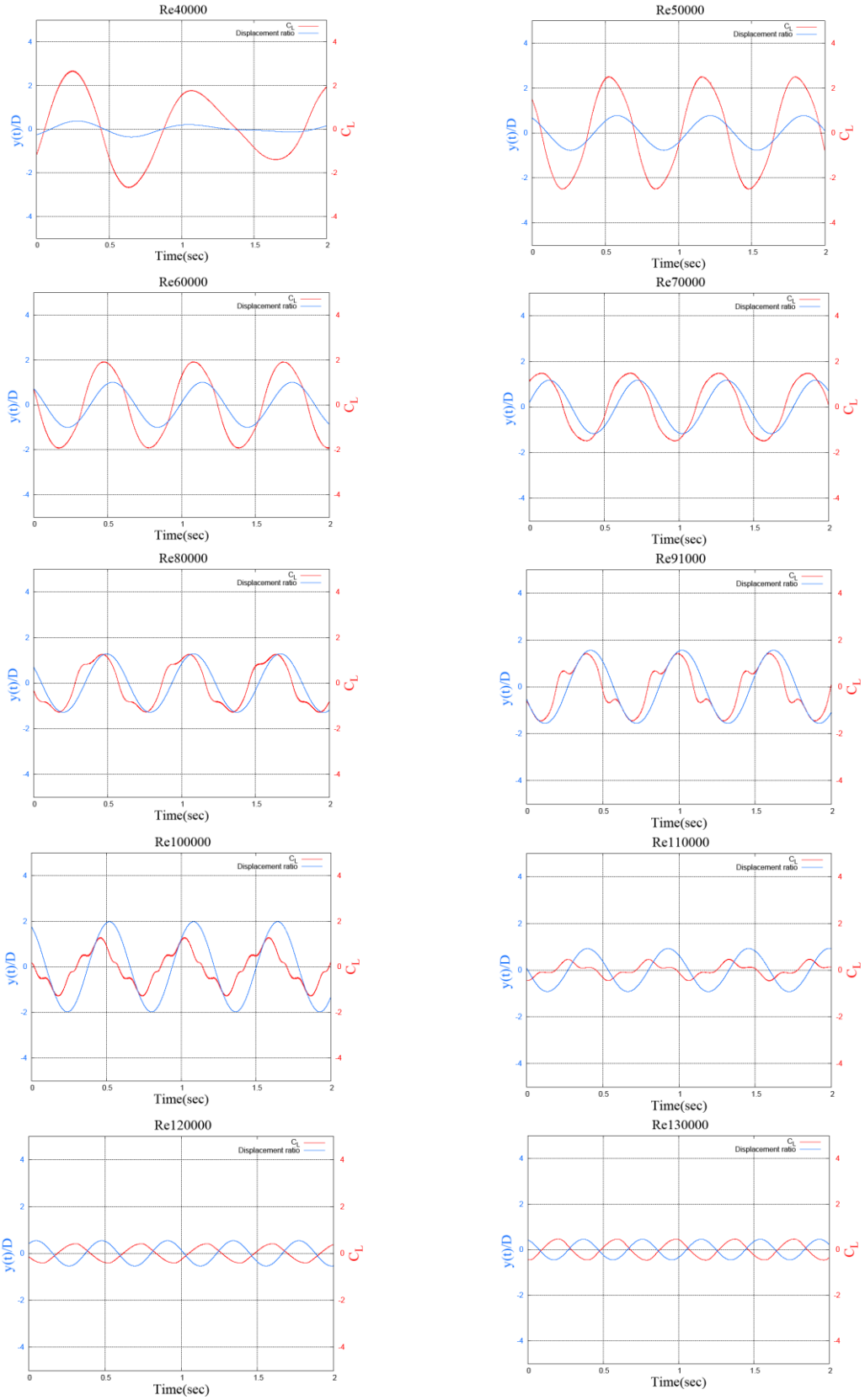

Figure 7.16. Variations of relative position (phase angle) between lift and displacement as *Re* changes (40,000≤*Re*≤130,000) (α_{PTC}=70^{o}, *K*=1600N/m, ζ_{harn}=0.08)

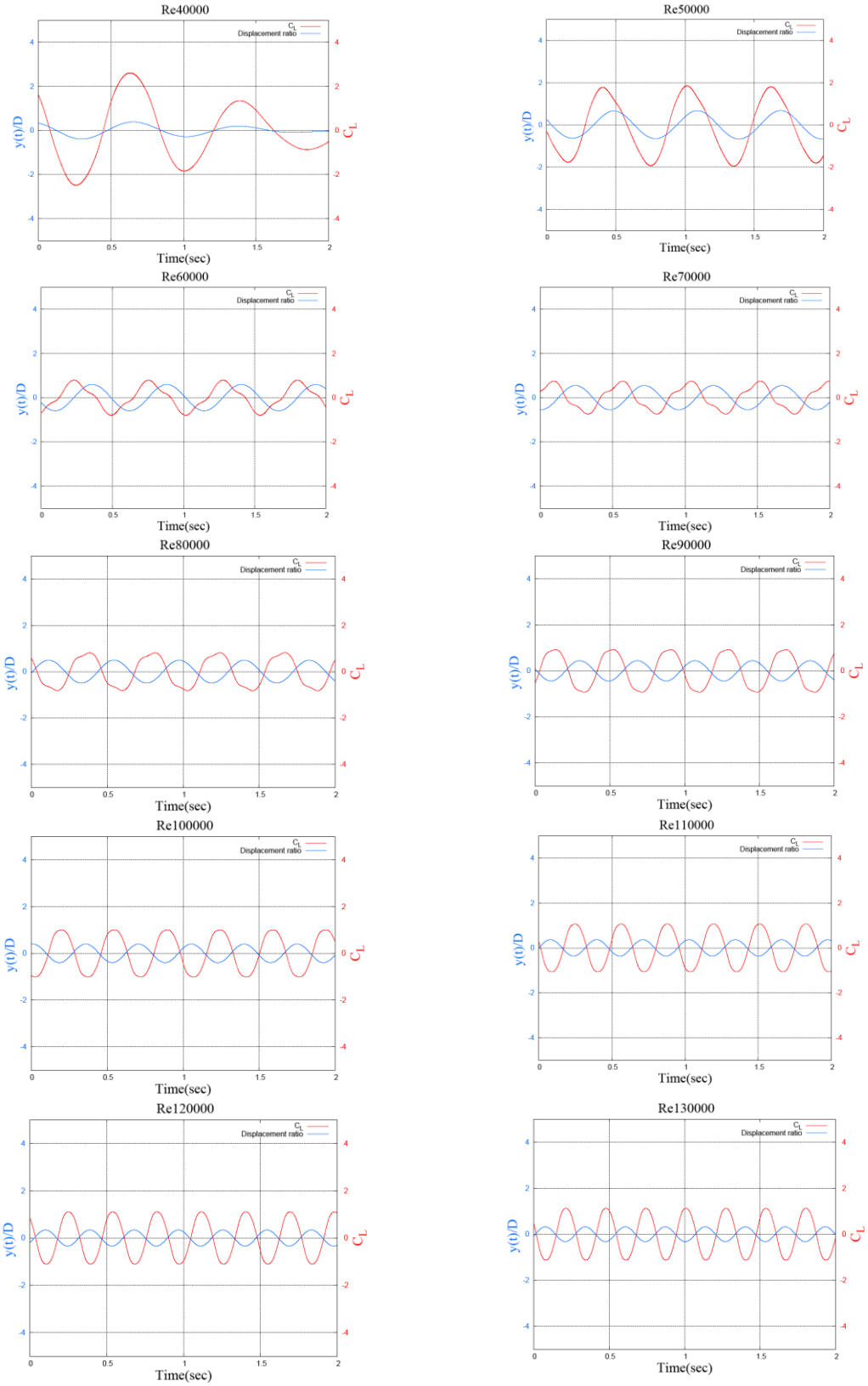

Figure 7.17. Variations of relative position (phase angle) between lift and displacement as *Re* changes (40,000≤*Re*≤130,000) (α_{PTC}=90°, *K*=1600N/m, ζ_{harn}=0.08)

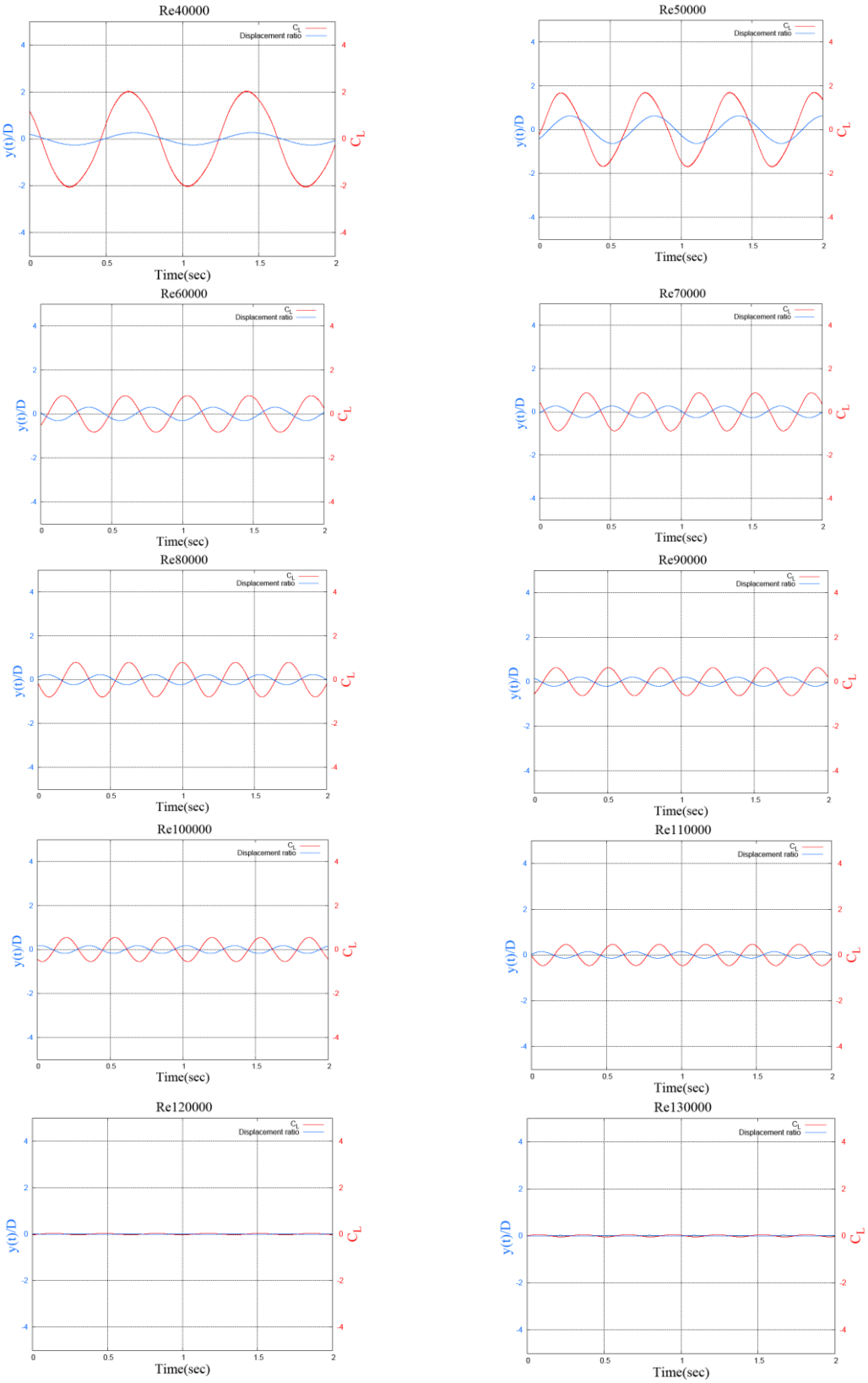

Figure 7.18. Variations of relative position (phase angle) between lift and displacement as *Re* changes (40,000≤*Re*≤130,000) (α_{PTC}=114^{o}, *K*=1600N/m, ζ_{harn}=0.08)

7.3. Conclusions

From the results presented in this chapter, it is concluded that the PTC placement angle is a very an important factor in the VIVACE design and that its value has significant effect on the motion dynamics including amplitude, frequency, vortex pattern, and phase angle. The conclusions can be summarized as follows:

1. Two entirely opposite types of motion behavior, FIM enhancement and FIM suppression, are discovered by varying the location of the passive turbulence control devices. The results match well the PTC-to-FIM map. The numerical results, however, are not capable of distinguishing the specific weak suppression and the strong suppression zones.

2. These two completely different motion types are found compatible with the phase angle values. For every specific α_{PTC} value tested in the suppression zone, the place where the phase angle starts to jump up rapidly is the very point where the amplitude drops most quickly. For the FIM enhancement case, the phase angle is reduced to less than 5^o in the galloping branch, which is even much smaller than that in the upper branch. It is because of this perfectly synchronized lift and motion pattern that the cylinder is able to absorb the energy in such an efficient way and finally reach galloping with remarkable motion amplitude.

3. As for the oscillation frequency, there is no obvious reduction found in the the transition region between different branches. On the contrary, the frequency increases continuously while the slope of the frequency curves vary as α_{PTC} changes.

4. The vortex structures are significantly changed and show strong dependency on the sandpaper (PTC) location. New vortex patterns including 2C, 2T, T+S are found while the placement angle located in the FIM suppression zone.

Chapter 8

CONCLUSIONS AND RECOMMENDATIONS FOR FUTURE WORK

8.1. Conclusions

In the present study, a numerical tool based on OpenFOAM has been developed and verified to predict flow properties pass a smooth cylinder and a roughness-modified cylinder. Best working range as well as limitations are also indentified. Two dimensional RANS method with Spalart-Allmaras turbulence model is selected to solve for the flow fields. The study covers stationary cylinder flow, elastically mounted cylinder in VIV working in lower and higher *Re* ranges respectively, and elastically mounted cylinder with PTC in flow induced motion. Parameters in extensive simulations are: the system damping and stiffness effects and different PTC locations. FIM suppression and enhancement are studied. The main findings and conclusions are:

1. **Grid Analysis**: A few investigations regarding the grid structure/resolution and initial conditions were conducted in order to set a baseline for the studies conducted in this thesis. The wall integration grids resolving the boundary layer are adopted over the smooth stationary cylinder case. From the first grid spacing study, the conclusions can be drawn that in order to resolve the near wall flow structure correctly, in combining with the non-slip wall boundary condition, the first grid spacing need to be fine enough and the wall unit $y+$ should be O(1) or less. From the grid resolution study of three grids with different grid numbers, the results show that the dependency of results on the grid resolution is limited as long as the total cell number is above $\sim 3\times10^4$. This conclusion is suitable for *Re* less than 1.4×10^5 since the coarse grid (S1) is only tested for the *Re* range up to 1.4×10^5, where the results have negligible differences with those from higher resolution grids. From present study, as far as a higher density grid like S3 is concerned, the computational time for *Re* over 1.4×10^5

is much longer compared with S2 (medium grid size), which makes it undesirable in view of limited improvements in accuracy. Comparing with the grid density, the first grid spacing is a factor deserving more attention in the grid design since it may potentially have huge effects on convergence and accuracy.

2. **Initial Conditions**: More sensitivity studies on the initial conditions are conducted in order to make sure proper initial conditions are adopted. Following Shur (1996) and Travin (1999) guidance, a "trip-less" initial condition is applied to achieve reasonable solutions in the subcritical flow regime. The results further confirmed that they have very weak dependency on the regional setups, as well as the initial turbulence level given that the initial values are within a reasonable range recommended by previous documents. From the values tested in current study, for LS, the initial eddy viscosity in the non-zero zone could be 0.1~1 times the molecular viscosity. While for the TS case, the value of more than 5 times the amount of molecular viscosity should be appropriate for the entire domain to avoid nonconvergent behavior due to the insufficient amount of turbulence introduced in the high *Re* cases.

3. **Smooth Stationary Cylinder**: Studies with 4 different grids conducted in this thesis, show the capability of 2D RANS in deriving comparable results with other numerical simulations published. Comparing with experiments, however, the obvious differences still exist and exhibit the weakness and limitations of this 2D method in handling such an inherently 3D problem. The drag is over-predicted in the *Re* range lower than 2×10^4 while underpredicted afterwards until flow transition is reached. The best property that has been predicted is the Strouhal numerical which is a quantity associated with frequency. This fact leaves the question open whether 2D RANS will work better in cylinder body in FIM problem since the frequency is such a dominant factor in this complex phenomenon. The good prediction on the frequency is promising in this sense.

4. **Smooth Cylinder in Low *Re* FIM**: An elastically mounted smooth cylinder in VIV was investigated in Chapter 4 and two Re working ranges are discussed. The relatively lower Reynolds number range (3,000~12,000) is studied first with a "from

rest" initial condition. In comparison with experiments from Khalak and Williamson as well as other numerical simulations for the same problem, results of maximum amplitude ratio, frequency ratio and vortex pattern are well presented. Although the peak-values of the amplitude in the upper branch are not well captured (experimental values are about 20% higher), the amplitudes in the remaining test range are well predicted. The wake structure and branch coverage for different branches and transitional behavior between branches are all predicted correctly. In addition, the results are encouraging in the sense that the frequency of oscillation follows the same trend as in the experiments and periodic as well as quasi-periodic branches are well captured.

5. **Smooth Cylinder in High *Re* FIM**: An elastically mounted smooth cylinder in VIV was investigated for higher *Re* numbers in the range 25,000<*Re*<80,000. It has been further study under the same protocol. Two sets of system parameters with different damping were investigated. Compared with the lower *Re* number range, much higher *Re* working range (in TrSL3 flow regime) makes this problem much more challenging for a 2D method due to the presence of the complicated three dimensional transitional eddies in the shear layer. The numerical results cannot predict well the amplitude, which was expected from similar studies in the literature. The onset and coverage for different branches are not well captured as well and the entire amplitude curve including all branches tend to shift to the lower *Re* direction. As a result, early synchronization as well as early flow transitions are found numerically. Maximum values in amplitude was found to occur at *Re*=~25,000, not in the range of Re=~40,000-50,000 where the upper branch is supposed to be. Regarding the frequency of oscillation, a relatively flatter slope is found in the frequency ratio plot, although the frequencies are well located in the range covered by experimental results. Inherently, 2D-RANS is not capable of capturing flow properties with strong three dimensional effects. Therefore 2D-RANS applies much better in the *Re* range well below TrSL3 regime for smooth cylinder in VIV. Accordingly, it is recommended for higher *Re* ranges, where three-dimensional eddies start to dominate, as in the TrSL3 regime.

6. **PTC Cylinder in FIM**: By introducing PTC, which is made of two straight strips of sand paper, the correlation length of vortices is set close to the spanwise dimension of the cylinder. This makes two-dimensional RANS works better in such a high *Re* range, which is normally very challenging for 2D methods. R.M.S. value of oscillating amplitude and frequency ratio are compared with results conducted by the VIVACE converter group in the MRELab. The three branches in the amplitude curve are well captured as derived in the experiments. However, the numerical results tend to over-predict the amplitude throughout the simulation range. This was anticipated because in the lab the free surface and bottom boundary effects in the experimental facility, the LTFSW Channel induce blocking effects are not considered in present study. The frequency ratio curve also shows variations according to different branches as measured in experiments.

7. **Stiffness and Damping Variation in PTC Cylinder in FIM**: System parameters such as stiffness and damping effects are studied in detail. Three spring stiffness values were used in simulations. For a given *Re* number, higher values of *K* tend to yield lower response amplitude. The lower *K* tends to have earlier transition to the VIV upper branch and to galloping as well. That is, the entire range if FIM synchronization shifts to higher *Re* for higher *K* values. In addition, for higher *K*, it takes longer for the transition regime to transit from the VIV upper branch to fully developed galloping. Beyond these differences caused by *K*, many resemblances can be found in the same branch for different *K* values. Similar wake structures, and frequency spectra for lift and displacements can be easily observed in the same branch. Regarding the damping effects, the most obvious and straightforward effect is on the amplitude of oscillation. The higher the damping level, the lower amplitude. The initial branch is not sensitive to the damping level, but the upper branch and transitional region to galloping are affected by the damping variations. The higher damping is, the longer the upper branch lasts and the shorter the transition to galloping is. When damping is low, the beating behavior is remarkable, and the spectra of lift and displacement show successive multiple harmonic peaks. As the damping increases, the peaks tend to get closer and merge gradually until single-

peaked lift and displacement spectra are presented and the beating phenomenon finally disappears.

8. **PTC Location on Cylinder in FIM**: The location of PTC as defined by the placement angle is also investigated at the end of this study. Under the guidance of PTC-to-FIM-Map developed in the MRELab, different PTC positioning angles within various zones are studied. Two entirely opposite amplitude tendencies have been discovered. In the FIM enhancing zone, roughly within the range α_{PTC}=60 deg, the amplitude curves share similar features. Three branches are present in the amplitude curve. The galloping branch is finally reached where amplitude becomes multiple-times the cylinder diameter with no synchronization end found in the test range. However, the angle varying within the FIM enhancement zone also affects in the branch form, wake pattern, and major oscillation frequencies in different branches. How those quantities are changed is still under investigation with more simulations.

Three angles within the range α_{PTC}>60 deg were studied for the suppression effects. Different levels of suppression effects are found. At α_{PTC}=70 deg, the suppression is not obvious until the region starting around *Re*=90,000 where normally the galloping branch resides. No increments but reductions in amplitude are found in this range, and the suppression branch replaces the galloping branch instead. As the angle α_{PTC} increases, suppression effects become stronger with suppression starting at lower Reynolds numbers and lower values in amplitudes. In the case of α_{PTC}=114 deg, desynchronization is finally reached without showing oscillatory wakes this time. By comparing the displacements and phase angles side by side, the observation can be easily made that, the phase angle has determining effects in the amplitude behavior. The point where the amplitude drops fast is the very point where the phase angle jumps up with large steps, which makes the displacement out of phase with the lift. Unlike the FIM enhancement cases, the frequency keeps climbing within the test range and finally the frequency level of the Strouhal frequency is reached. Wake structures are very sensitive to the location of the placement angle where the turbulence boundary layer is triggered. Different wake patterns are

observed, and some of them are never present in the VIV enhancement cases, like 2C, 2T and T+S.

8.2. Suggestions and recommendations for future work

1. **Boundary Effects:** One of the limitations of the present study is that the boundary blocking effects from free surface and bottom are not considered and modeled. On one hand, we can benefit from the results that it allows us to estimate the potential maximum amplitude the cylinder could achieve without the boundary limitations. On the other hand, in a long run, from design point of view, the boundary effects should be analyzed and quantified especially for the bottom effects to provide meaningful guidance in design.

2. **Initial Conditions**: Another limitation in the present numerical simulations relates to the moving cylinder case. The initial conditions used for the cylinder in VIV and FIM problems are zero velocity and zero displacement for all cases. From the current study as well as other literature on experiments and numerical simulations, different initial conditions, such as from rest, increasing flow speed or decreasing flow speed, could result in different amplitude behavior. Hysteresis phenomenon can be found by changing this condition. More development in the code allowing different initial conditions could be useful to investigate these effects.

3. **PTC Parameters**: PTC effects were studied in this thesis in terms of the placement angle. Other parameters could be studied such as the roughness height of sand grid k as well as sandpaper thickness P.

4. **Hydrokinetic Energy Conversion**: Based on the numerical results of amplitudes and frequencies, the harnessed energy as well as power density could be further evaluated. In addition, the optimal power envelope curve can be computed.

5. **Galloping**: A numerical tool has been developed and verified in the current study based on experimental data. This tool can be used to conduct the following

research. The galloping phenomenon is reached in the results, however, the physics and reasons that drive this instability are not fully understood. The time-varying forces, cylinder motion variables, and other flow field properties like velocity components, pressure field oscillations, shear layer motion, etc can be easily achieved from numerical results, and they can be further used to estimate the lift force slope with respect to the angle of attack which is an important factor in triggering this instability (Chang 2010). The variation in pressure distributions on cylinder surface could be further investigated for the VIV and galloping branches to study the transition from VIV to galloping which has not been studied as yet.

6. **Multiple Cylinder VIVACE Converters**: In the current study the single cylinder module case is considered. However, in reality, the VIVACE converter will be assembled and installed in arrays and farms to enhance the energy generation capacity and efficiency. The presence of multiple bodies will complicate the system dynamics and bring in other problems. How does one cylinder affect and is affected the motion of the others in the group? How to choose the additional system parameters such as the distances among cylinders, configurations such as staggered or inline? How could these geometric parameters be better selected to make cylinders work synergetically and finally reach the optimal energy level as a group? These questions open a new line of research to improve the VIVACE converter and when answered will make the developed code an effective and useful tool in research and design. Current 2D-RANS is only applicable to a single body motion due to the rigid mesh motion property. More development in the code is need in order to work with two or multiple-body systems.

7. **Turbulence Model**: Other numerical methods with other turbulence models could possibly be another option to make it possible design large VIVACE dynamic systems with better accuracy. DES or other modified versions of it like DDES and other hybrid RANS/LES approaches could be expected to have better agreement with experiments, albeit at increased computational time.

BIBLIOGRAPHY

1. Achenbach, E., (1971), "Influence of surface roughness on the cross-flow around a circular cylinder," *Journal of Fluid Mechanics,* 46, 321-335.
2. Achenbach, E., (1977), "The effect of surface roughness on the heat transfer from a circular cylinder to the cross flow of air," *International Journal of Heat and Mass Transfer,* 20, 359-369.
3. Achenbach, E., Heinecke, E., (1981), "On vortex shedding from smooth and rough cylinders in the range of Reynolds numbers $6x10^3$ to $5x10^6$," *Journal of Fluid Mechanics,* 109, 239-251.
4. Batcho, P., Karniadakis, G.E., (1991), "Chaotic transport in two- and three-dimensional flow past a cylinder," *Physics of Fluids, A3,* 1051–1062.
5. Batham, J.P., (1973), "Pressure distributions on circular cylinders at critical Reynolds numbers," *Journal of Fluid Mechanics,* 57, 209-228.
6. Beaudan,P., Moin, P.,(1994), "Numerical experiments on the flow past a cylinder at sub-critical Reynolds number," report No.TF-62, Department of Engineering, Stanford University.
7. Bernitsas M. M., Raghavan K., (2007), "Enhancement of Vortex Induced Forces & Motion through Surface Roughness Control," U.S. Provisional Patent Application, United States Patent and Trademark Office Patent UofM#3737. May 05, 2007.
8. Bernitsas M. M., Raghavan K., Duchene G., (2008), "Induced Separation and Vorticity Using Roughness in VIV of Circular Cylinders at $8\times103 < Re < 1.5\times105$," OMAE'08. Estoril, Portugal, 2008. 15-20.
9. Bernitsas M.M., Raghavan k., 2009, "Converter of Current, Tide, or Wave Energy," U.S. Provisional Patent Application, United States Patent and Trademark Office Patent 7,493,759 B2. February 24, 2009.
10. Bernitsas M.M., Raghavan K., Maroulis D., (2007), "Effect of Free-Surface on VIV for Energy Harnessing at 8x103<Re<1.5x105," *International Conference on Offshore Mechanics and Arctic Engineering,* SanDiego, 2007.
11. Bernitsas, M. M. and Raghavan, K., (2005), "Fluid motion energy converter," *United States Patent* 60/628,152, 60/244,749. 2005.
12. Bernitsas, M. M., Raghavan, K., and Duchene, G., (2008), "Induced separation and vorticity using roughness in VIV of circular cylinders at $8x10^3 < Re < 1.5x10^5$," *27th International OMAE'08 Conference*. Estoril , 2008.

13. Bishop, R.E.D., Hassan, A.Y., (1964), "The lift and drag forces on a circular cylinder in a flowing fluid," *Proceedings Royal Society (London)*, Series A 277, 32–50
14. Blevins, R.D., (1990), "Flow-Induced Vibration," Van Nostrand Reinhold, New York.
15. Brika,D., Laneville,A., (1993), "Vortex-induced Vibrations of a Long Flexible Circular Cylinder," *Journal of Fluid Mechanics*, vol. 250, pp.481-508.
16. Breuer, M., (1998), "Numerical and modeling influences on large eddy simulations for the flow past a circular cylinder," *International Journal of Heat and Fluid Flow, 19*, 512–521.
17. Breuer, M., (2000), "A challenging test case for large eddy simulation: high Reynolds number circular cylinder flow," *International Journal of Heat and Fluid Flow, 21*, 648–654.
18. Catalano, P., Wang, M., Iaccarino, G., Moin, P., (2003), "Numerical simulation of the flow around a circular cylinder at high Reynolds numbers," *International Journal of Heat and Fluid Flow*, 24, 463–469.
19. Chang, C. C., (2010), "Hydrokinetic energy harnessing by enhancement of Flow Induced Motion using Passive Turbulence Control," *Ph.D thesis*, University of Michigan, Ann Arbor, 2010.
20. Chang, C. C., Bernitsas, M. M.,(2011), "Hydrokinetic energy harnessing using the VIVACE converter with Passtive Turbulence Control," *Proceedings of the 30th international conference on ocean, offshore and arctic*, June 19-24, 2011, Rotterdam, The Netherlands.
21. Dong, S., Karniadakis, G.E., (2005), "DNS of flow past a stationary and oscillating cylinder at Re = 10,000," *Journal of Fluids and Structures 20*, 519–531
22. Farell, C., Carrasquel, S., Güven, O., and Patel, V.C., (1977), "Effects of wind-tunnel walls on the flow past circular cylinders and cooling towers models," *Journal of Fluids Engineering*, 99, 470-479.
23. Farell, C., and Blessmann, J., (1983), "On critical flow around smooth circular cylinders," *Journal of Fluid Mechanics*, 136, 375-391.
24. Fedeniuk, S.K., (1982), "An investigation of the effect of end plates on the flow behavior around a rough circular cylinder," *Master's Thesis*, Faculty of Graduate School of the University of Minnesota, Minneapolis, MN, 1982.
25. Flemming, F., Williamson, C. H. K., (2005), "Vortex-induced vibrations of a pivoted cylinder," *Journal of Fluid Mechanics*, vol. 522, pp. 215–252.
26. Govardhan, R., Williamson, C.H.K., (2005), "Revealing the effect of Reynolds number on vortex-induced vibrations using controlled negative and positive damping," *Conference on Bluff Body Wakes and Vortex-Induced Vibrations (BBVIV4)*, 21–24 June, Greece.

27. Govardhan, R., and Williamson, C. H. K., (2000), "Modes of Vortex Formation and Frequency Response of a Freely Vibrating Cylinder," *Journal of Fluid Mechanics*, 420, 85-130

28. Gopalkrishnan, R., (1993), "Vortex-induced forces on oscillating bluff cylinders." *Ph.D. Thesis,* Department of Ocean Engineering, MIT, Cambridge, MA, USA.

29. Güven, O., (1975), "An experimental and analytical study of surface-roughness effects on the mean flow past circular cylinders," *Doctoral Thesis*, University of Iowa, Iowa City, IA, 1975.

30. Guilmineau,E.,Queutey, P., (2004), "Numerical simulation of vortex-induced vibration of a circular cylinder with low mass-damping in a turbulent flow," *Journal of Fluids and Structures*, 19 (2004) 449–466.

31. Hansen, R. P., and Forsythe, J. R., (2003), "Large and Detached Eddy simulations of flow over a circular cylinder using unstructured grids," *AIAA Paper 2003-0775*, Jan. 2003

32. Herfjord, K., (1995), "A study of two-dimensional separated flow by a combination of the finite element method and Navier-Stokes Equations." *Dr. Eng. Theses,* The Norwegian Institute of Technology, Trondheim, Norway.

33. Hove, D.T., Shih, W.C.L., and Curtis, R.J., (1978), "Roughness effects on cylinder flows," *paper presented at the 8th. U.S. National Congress of Applied Mechanics,* University of California, Los Angeles, CA, June 26-30, 1978 (Science Applications Inc., E1 Segundo, CA).

34. Isaacs, J.D., and Seymour, R.J., (1973), "The Ocean as a power resource," *International Journal of Environmental Studies,* vol. 4(3), pp 201-205.

35. Jauvtis, N., and Williamson, C. H. K., (2003), "Vortex-Induced vibration of a cylinder with two degrees of freedom," *Journal of Fluids and Structures*, 17(7), 1035-1042

36. Khalak, A., Williamson, C.H.K., (1996), "Dynamics of a hydroelastic cylinder with very low mass and damping." *Journal of Fluids and Structures* 10: 455-472

37. Khalak, A., Williamson, C.H.K., (1997), "Fluid forces and dynamics of a hydroelastic structure with very low mass and damping." *Journal of Fluids and Mechanics* 11: 973-982.

38. Khalak, A., Wliamson, C.H.K., (1999), "Motions forces and mode transitions in vortex induced vibrations at low mass-damping," *Journal of Fluids and Structures*, 13 (1999): 813-851.

39. Ko, N., Leung, Y., and Chen, J. , (1987) "Flow past v-groove circular cylinders." *AIAA Journal*, 25 (6) 806-811.

40. Lee, J.H., Bernitsas, M.M., (2010) "High-damping, high-Reynolds VIV tests for energy harnessing using the VIVACE converter." *Ocean Engineering*, in press.

41. Lee, J.H., (2010), "Hydrokinetic power harnessing utilizing Vortex Induced Vibrations through a virtual c-K VIVACE model," *Ph.D thesis*, University of Michigan, Ann Arbor, 2010.

42. Lo, S.C., Hoffmann, K. A., and Dietiker, J.F., (2005), "Numerical investigation of high Reynolds number flows over square and circular cylinders," *Journal of Thermophysics and Heat Transfer*, Vol. 19, No. 1, January–March 2005, 72-80.

43. Ma, X., Karamanos, G.-S., Karniadakis, G.E., (2000), "Dynamics and low-dimensionality of a turbulent near wake," *Journal of Fluid Mechanics* 410, 29–65.

44. Mittal, R., Balachandar, S., (1995), "Effect of three-dimensionality on the lift and drag of nominally two-dimensional cylinders," *Physics of Fluids 7*, 1841–1865.

45. Moeller, M.J., Leehey, P., (1984), "Unsteady forces on a cylinder in cross flow at subcritical Reynolds numbers. In: Païdoussis, M.P.Griffin, O.M., Sevik, M. (Eds.)," *ASME Symposium on Flow-Induced Vibrations*, Vol. 1, NewOrleans, 1984. ASME, NewYork, pp. 57–71.

46. Morgan, P. E., Visbal, M. R., (2006), "Application of hybrid RANS/ILES to geometries with separated flows," *3rd AIAA Flow Control Conference* 5 - 8 June 2006, San Francisco, California.

47. Nakamura, Y., Tomonari, Y., (1982), "The effects of surface roughness on the flow past circular cylinder at high Reynolds numbers," *Journal of Fluid Mechanics* 123, 363-378.

48. Nichols, R. H., Nelson, C. C., (2003), "Applications of hybrid RANS/LES turbulence models," *41st Aerospace Sciences Meeting and Exhibit* January 6-9, 2003/Reno, Nevada, AIAA 2003-0083.

49. Nichols, R. H., (2005), "Comparison of hybrid rans/les turbulence models on a circular cylinder at high Reynolds number," *3rd AIAA Aerospace Sciences Meeting and Exhibit* 10 - 13 January 2005, Reno, Nevada.

50. Nichols, R. H., (2006), "Comparison of hybrid turbulence models for a circular cylinder and a cavity," *AIAA Journal* Vol. 44, No. 6, June 2006.

51. Norberg, C. (2000) "Flow around a circular cylinder: aspects of fluctuating lift" *Journal of Fluids and Structures* 15, 459- 469.

52. Norberg, C., (2003). "Fluctuating lift on a circular cylinder: review and new measurements." *Journal of Fluids and Structures*, 17:57-96.

53. Park, H., Bernitsas, M. M., (2011), "Selective roughness in the boundary layer to suppress flow-induced motions of circular cylinder at 30,000<re<120,000," *Proceedings of the 30th international conference on ocean*, offshore and arctic, June 19-24, 2011, Rotterdam, The Netherlands.

54. Raghavan, A.K., Sohn, C.H., and Lakshmana Gowda, B.H.L., (2008), "Passive Control of vortex-induced vibrations: An overview." *Recent Patents on Mechanical Eng*., 1, 1-11.

55. Raghavan,K., (2007) “Energy extraction from a steady flow using Vortex Induced Vibration,” *Ph.D thesis*, University of Michigan, Ann Arbor, 2007.

56. Rengel, J.E., Sphaier, S.H., (1999), “A projection method for unsteady Navier-Stokes equation with finite volume method and collocated grid,” *Hybrid Methods in Heat and Mass Transfer* 1, 4.

57. Ribeiro, J.L.D., (1991), “Effects of surface roughness on the two dimensional flow past circular cylinders I: mean forces and pressures,” *Journal of Wind Engineering and Industrial Aerodynamics*, 37, 299-309.

58. Roulle, C., (1980), “Reproduction des régimes hypercritiques sur formes rondes en soufflerie atmosphérique,” Doctoral Thesis, Centre Scientifique et Technique du Bâtiment, Nantes, 1980.

59. Roshko, A., (1961) “Experiments on the flow past a circular cylinder at very high Reynolds number,” *Journal of Fluid Mechanics*, Vol. 10, No. 3, 1961, pp. 345–356.

60. Sarpkaya, T., (2004), "A critical review of the intrinsic nature of Vortex-induced vibrations," *Journal of Fluids and Structures*, 19(4), 389-447.

61. Shih, W.C.L., Wang, C., Coles, D., Roshko, A., (1993), “Experiments on flow past rough circular cylinders at large Reynolds numbers.” *Journal of Wind Engineering and Industrial Aerodynamics*, 49, 351–368.

62. Shimizu,K., and Kawamura, M., (1972), “Spanwise correlation measurement behind circular cylinder in subcritical Reynolds number region,” *Journal Physical Society Japan*, 32, 1454.

63. Shur, M., Spalart, P. R. , Squires , K.D., Strelets, M., Travin, A., (2005), “Three dimensionality in Reynolds-Averaged Navier–Stokes solutions around two-dimensional geometries,” *AIAA Journal*, Vol. 43, No. 6, June 2005.

64. Shur, M. L., Spalart,P. R., Strelets, M. K., Travin, A. K., (2008), “A hybrid RANS-LES approach with delayed-DES and wall-modelled LES capabilities,” *International Journal of Heat and Fluid Flow* Volume 29, Issue 6, December 2008, Pages 1638-1649.

65. Singh, S. P., Mittal, S., (2005), “Flow past a cylinder: shear layer instability and drag crisis,” *International Journal for Numerical Methods in Fluids*, 47:75–98.

66. Spalart, P. R., and Allmaras, S. R., (1994), “A one-equation turbulence model for aerodynamic flows,” *La Recherche Aérospatiale*, No. 1, 1994, p. 5.

67. Spalart, P. R., Jou,W.-H., Strelets, M., and Allmaras, S. R., (1997), “Comments on the feasibility of LES for wings, and on a hybrid RANS/LES approach,” *Advance in DNS/LES, 1st AFOSR International Conference on DNS/LES*, Greyden Press, Columbus, OH, 1997.

68. Travin, A., Shur, M., Strelets, M., Spalart, P.R., (1999), “Detached-Eddy Simulations past a circular cylinder,” *Flow, Turbulence and Combustion* **63:** 293–313, 1999.

69. Vatsa, V. N., and Singer, B. A., (2003) "Evaluation of a second-order accurate Navier–Stokes code for Detached Eddy simulation past a circular cylinder," *AIAA Paper* 2003-4085.

70. Wanderley, J.B.V, LabOceano, S. H. S., LabOceano, C. L., "A numerical investigation of vortex induced vibration on an elastically mounted rigid cylinder", *Proceedings of the ASME 27th International Conference on Offshore Mechanics and Arctic Engineering OMAE2008*, OMAE2008-57344.

71. Wanderley, J. B. V., Souza, G. H. B., Sphaier, S. H., and Levi, C. A., (2008), "Vortex-induced vibration of an elastically mounted circular cylinder using an upwind tvd two-dimensional numerical scheme," *Ocean Engineering*, V. 35, pp. 1533-1544.

72. West, G.S., Apelt, C.J., (1993), "Measurements of fluctuating pressures and forces on a circular cylinder in the Reynolds number range 10^4 to 2.5×10^5," *Journal of Fluids and Structures* 7, 227–244.

73. White, F.M., (2005) "Viscous fluid flow," Third edition, Mcgraw Hill Series in Mechanical Engineering, 2005.

74. Williamson, C. H. K., (1985), "Sinusoidal flow relative to circular cylinders," *Journal of Fluid Mechanics*, 155, 141-174.

75. Williamson, C.H.K., Roshko, A., (1988) "Vortex formation in the wake of an oscillating cylinder," *Journal of Fluids and Structures*, Vol. 2, pp. 355–381.

76. Williamson, C.H.K., Jauvtis, N., (2004), "A high-amplitude 2T mode of vortex-induced vibration for a light body in *XY* motion," *European Journal of Mechanics B/Fluids* 23 107–114.

77. Wieselsberger, C., (1921) "New data on the laws of fluid resistance," *Physikalische Zeitschrift*, 22, 321-328.

78. Xu, J., Zhu, R., (2009), "Numerical simulation of VIV for an elastic cylinder mounted on the spring supports with low mass-ratio," *Journal of Marine Science and Application* 8: 237-245.

79. Zdravkovich, M. M., (1997), "Flow around circular cylinders Volume 1: Fundamentals," Oxford University Press, England.

80. Zdravkovich, M. M., (1981), "Review and classification of various aerodynamic and hydrodynamic means for suppressing vortex shedding," *Journal of Wind Engineering and Industrial Aerodynamics* 7, 145-189.